The University Of Sheffield.

Contact Mechanics at the Molecular Scale

Oscar Siles Brügge

A thesis submitted in partial fulfillment of the requirements for the degree of

Doctor of Philosophy

The University of Sheffield

Faculty Of Science

Department of Chemistry

July 2017

God created the bulk, but its surface was made by the devil.

Wolfgang Pauli

Declaration

This thesis, unless otherwise stated, is the work of the author and has not been submitted whole or in part for any other degree or qualification at this or any other institution.

_____

Oscar Siles Brügge

July 2017

Acknowledgements

I would first like to thank my supervisors, Professors Graham J. Leggett and Christopher A. Hunter, for their guidance and patience throughout the years; their support was invaluable to the completion of this thesis.

The technical and moral support from the Leggett Group is also greatly appreciated, with special thanks going to: Robert Ducker, Charlie Smith, Paul Chapman, Omed Qadir Al-jaf, Mar Cardellach, Martin Munz, Deborah Hammond, Osama El-Zubir, Alexander Johnson, Brice Darroch, and Max Chambers. Additionally, many thanks go to Anthony Meijer and Theo Keane for their help with density functional theory calculations, and Eleanor Gardiner for help with using *phasetransfer*. I am also grateful to The University of Sheffield, The University of Leeds, and the EPSRC for funding through the CDT in Molecular-Scale Engineering.

I would like to further thank all my friends, at home and around the world, who helped me keep my sanity for just a little longer. Thank you in particular to Will, who survived living with me for the past 4 years, and suffered through my dilemma on the choice of typeface for this thesis. Special thanks go to my mother, my brother Gabriel, and my aunt and uncle in Spain. You always believed in me and gave me the strength to continue when times were tough.

Last but certainly not least, a heartfelt thank you goes to Ellen; without your love and support all these years I would not have made it this far.

Abstract

A better understanding of the adhesive interactions between surfaces at the molecular scale is of growing importance as miniaturization efforts continue. To this end, Lifshitz theory of continuum mechanics was used to calculate the interaction energies between hydrocarbon surfaces in over 200 liquids, and compared to those obtained from the Hunter model of hydrogen bond solvation thermodynamics. In alkanes, amines, and primary alcohols, both theories yielded comparable results. However, in cases where the refractive index between interacting phases diverges greatly, a large disparity between the Lifshitz work of adhesion and Hunter free energy of complexation was found. In addition to some of the liquids showing differing results between the two theories, binary mixtures of benzyl alcohol and methanol were also identified for further experimental analysis. Slight modifications were applied to Lifshitz to allow for predictions of polar surfaces, and these too were compared to those provided by the Hunter model.

Using force spectroscopy and friction force microscopy the tribological properties of hydrocarbon self-assembled monolayers, in the liquids identified previously, were investigated. While interactions in non-polar liquids were well described by both Lifshitz theory and the Hunter model, the former was found to consistently underestimate the work of adhesion in polar liquids, especially in water ($\Delta W_{ad} > 40\,\mathrm{mJ\,m^{-2}}$). In contrast, good agreement was generally obtained between the Hunter model and the experimentally obtained interaction energies. This was also true for binary mixtures of benzyl alcohol and methanol, where Lifshitz theory was completely unable to predict the form of the interaction. Friction-load plots were also obtained for the same systems of non-polar surfaces, and the form of their relation in different media was found to be dependent on the previously obtained adhesive energies. At interaction energies below $6\,\mathrm{mJ\,m^{-2}}$ linear friction-load relationships were observed, while yielding sublinear plots at work of adhesion values above this, corroborating the idea that friction can be considered to consist of load- and area-dependent terms.

Mechanochemical removal of NPEOC photoprotecting groups from surfaces with adsorbed OEG-NPEOC-APTES monolayers using an AFM probe was also performed, with feature sizes up to 20 nm being achieved. The dependence on the width and depth of the patterned features on the applied load was investigated, with a positive relation being found for both, up to a critical load; no such change was observed with increasing write speeds. Changing the tip chemistry and environment (i.e., via immersion in different liquids) yielded no change in the size and quality of the patterns obtained, suggesting the lithographic process relies solely on the physical interaction between tip and sample surface. Modification of the surface through derivatization using TFAA and GFP indicates that only the NPEOC protecting group is being removed. Density functional theory was employed to investigate possible reaction pathways of the usual photodeprotection pathway of NPEOC-APTES, and how the mechanical interaction of the tip with the surface may promote one of these to occur without a high energy photon. It was discovered that a compression of the NPEOC leads to a shift in the UV/Vis absorbance spectrum towards higher wavelengths, and it is suggested that the mechanochemical deprotection of OEG-NPEOC-APTES SAMs occurs via this mechanism.

Contents

List of Figures

List of Tables

List of Abbreviations

Abbreviation	Definition
AFM	atomic force microscope
APTES	3-aminotriethoxysilane
CFM	chemical force microscopy
CGF	contracted Gaussian function
CM-AFM	contact mode AFM
CSV	comma-separated values
DDPA	n-dodecylphosphonic acid
DDT	1-dodecanethiol
DFT	density functional theory
DMT	Derjaguin, Muller, and Toporov
DPN	dip-pen nanolithography
DTS	n-dodecyltrichlorosilane
EBL	electron-beam lithography
FFM	friction force microscopy
FIB	focussed ion beam
FTIR	fourier transform infrared spectroscopy
FWHM	full width at half maximum
GFE	general fitting equation
GFP	green fluorescent protein
GGA	generalized gradient approximation
GTO	Gaussian-type orbital
GUI	graphical user interface
HF	Hartree-Fock
HOMO	highest occupied molecular orbital
ICT	intramolecular charge-transfer

Abbreviation	Definition
IEFPCM	integral equation formulism polarizable continuum model
IL	interference lithography
JKR	Johnson, Kendall, and Roberts
LCAO	linear combination of atomic orbitals
LDA	local density approximation
LFM	lateral force microscopy
LUMO	lowest unoccupied molecular orbital
μCP	microcontact printing
MD	molecular dynamics
MEMS	microelectromechanical system
MEPS	molecular electrostatic potential surface
MUL	11-mercaptoundecanol
NCM-AFM	non-contact mode AFM
NEMS	nanoelectromechanical system
NIL	nanoimprint lithography
NPEOC	2-(4-nitrophenyl)ethoxycarbonyl
NPPOC	2-nitrophenylpropyloxycarbonyl
***o*NB**	*o*-nitrobenzyl
ODPA	n-octadecylphosphonic acid
ODT	1-octadecanethiol
OEG	oligoethylene glycol
OEG-NPEOC-APTES	meta-heptaethyleneglycol 2-(4-nitrophenyl)ethoxycarbonyl (3-aminopropyl)triethoxysilane
OOP	object-oriented programming
OTMS	n-octadecyltrimethoxysilane
OTS	n-octadecyltrichlorosilane
PBS	phosphate-buffered saline
PDMS	poly(dimethylsiloxane)
PMMA	poly(methyl methacrylate)

Abbreviation	Definition
PSD	power spectral density
QED	quantum electrodynamics
QFT	quantum field theory
RCA	Radio Corporation of America cleaning solution
RMS	root mean square
SAM	self-assembled monolayer
SCRF	self-consistent reaction field
SEM	scanning electron microscope
SFA	surface force apparatus
SIMS	secondary ion mass spectrometry
SNOM	scanning near-field optical microscopy
SPL	scanning probe lithography
SPM	scanning probe microscopy
SSIP	surface site interaction point
STM	scanning tunneling microscope
STO	Slater-type orbital
TCCM	thin coating contact mechanics
TD-DFT	time-dependent DFT
TD-SCF	time-dependent self-consistent field
TFAA	trifluoroacetic anhydride
TISE	time-independent Schrödinger equation
TM-AFM	tapping mode AFM
TMR	trace-minus-retrace
VM	virtual machine
XPS	X-ray photoelectron spectroscopy

List of Symbols

Symbol	Description	Unit
A	Hamaker constant; area; adhesion; absorbance	J; m^2; $J\,m^{-2}$; —
a	Contact radius	m^2
α	Polarizability; hydrogen bonding donor parameter	$C\,m^2\,V^{-1}$; —
α^H	Hydrogen bonding acidity	—
α_c	Lateral stiffness calibration factor	$N\,V^{-1}$
α_t	General fitting equation transition parameter	—
β	Hydrogen bonding acceptor parameter	—
β^H	Hydrogen bonding basicity	—
c	Concentration	M
c_{max}	Maximum concentration of SSIPs	M
D	Separation	m
D_0	Minimum separation between surfaces	m
D_e	Bond dissociation energy	E_h
Δ_o	Slope torsion loop offset	V
δ_c	Cantilever deflection	m
δ_t	Dugdale stress range	m
E	Energy; Young's modulus	J; Pa
E_h	Hartree energy	E_h, Ha
E_{max}	Energy maximum on MEPS	$kJ\,mol^{-1}$
E_{min}	Energy minimum on MEPS	$kJ\,mol^{-1}$
ϵ	Orbital energy eigenvalue	—
ε	Dielectric constant (relative permittivity); extinction coefficient	—; $M^{-1}\,cm^{-1}$

Symbol	Description	Unit
F	Force	N
$\hat{f}$	Fock operator	—
ΔG	Change in free energy	$\mathrm{kJ\,mol^{-1}}$
γ	Surface free energy	$\mathrm{J\,m^{-2}}$
$\hat{H}$	Hamiltonian operator	—
h	Planck constant; film thickness	J s; m
$\hbar$	Reduced Planck constant	J s
η	Basis functional	—
I	Intensity	$\mathrm{W\,m^{-2}}$
$\hat{J}$	Coulomb integral	—
K	Equilibrium constant; bulk modulus	varies; Pa
$\hat{K}$	Exchange interaction integral	—
k	Spring constant	$\mathrm{N\,m^{-1}}$
k_B	Boltzmann constant	$\mathrm{J\,K^{-1}}$
L	Applied load; path length	N; cm
λ	Maugis parameter; wavelength	—; m
m	Mass	kg
μ	Coefficient of friction; magnetic permeability; dipole moment	—; $\mathrm{H\,m^{-1}}$; D
μ_T	Tabor coefficient	—
n	Refractive index	—
ν	Frequency; Poisson's ratio	Hz; —
ν_e	Main electronic absorption frequency in UV	Hz
ω	Radial frequency	$\mathrm{rad\,s^{-1}}$
p	Pressure	Pa
Φ, Θ	Slater determinants	—
Ψ, ψ	Wavefunction	—
q	Electric charge	C
R	Radius; separation; ideal gas constant	m; m; $\mathrm{J\,K^{-1}\,mol^{-1}}$

Symbol	Description	Unit
R_a	Average roughness	m
R_q	Root-mean-square roughness	m
r	Radius; separation	m; m
ρ	Mass density; electron density	$\mathrm{kg\,m^{-3}}$; $e\,{a_0}^{-3}$
σ_0	Dugdale constant adhesion stress	N
T	Absolute temperature; thickness	K; m
$\hat{T}$	Kinetic energy operator	—
τ	Shear strength	Pa
θ	Angle; fractional occupancy	deg, rad; —
V	Volume; potential energy	$\mathrm{m^3}$; J
$\hat{V}$	Potential energy operator	—
υ	Velocity	$\mathrm{m\,s^{-1}}$
W	Work of adhesion per unit area	$\mathrm{J\,m^{-2}}$
W_o	Torsion loop half-width	$\mathrm{J\,m^{-2}}$
x	Displacement	m
χ, ϕ	Spin orbital wavefunction	—
Z	Atomic unit	—
z_0	Equilibrium separation between atomic planes	m
ζ	Imaginary frequency; TCCM transition parameter	Hz; —

CHAPTER 1

Introduction

1.1 General Introduction

The race towards miniaturization, sparked by Richard Feynman's renowned 1959 lecture "There's plenty of room at the bottom", has been an integral part the technological advances of the past few decades. Less than a decade after Feynman's talk, the first mass produced microelectromechanical system (MEMS) device, the resonant gate transistor, was created.[1] As these MEMS, and more recently nanoelectromechanical system (NEMS), decrease in size, their components are becoming increasingly affected by interfacial properties: adhesion and friction. It is therefore crucial to improve our understanding of these properties in order to reduce wear and improve the performance of M/NEMS and other technologies such as hard drive heads. Tribology has thus become an increasingly important element of numerous device fabrication industries, as well as a driving force towards greater efficiency in an increasingly environmentally conscious world.

Tribology is the science of "two interacting surfaces in relative motion",[2] being derived from the Greek word *tribos*, meaning "to rub"; simply put, it is the science of friction, lubrication, and wear. It may seem self-evident that, through continuous usage, machinery begins to show signs of wear. However, it wasn't until the publication of the Jost Report in 1964, which outlined how upwards of 1 % of the UK's GNP was continuously lost due to corrosion and wear[3] that research in these areas greatly increased. While the term tribology was not officially adopted until this time as the field's scientific name, this does not mean that a lot of the groundwork had not been done already.

Guillaume Amontons (1663-1705) was one of the first pioneers in the field of tribology, centuries before financial considerations incentivized much of the current research. Life as we know it would not be possible without the effects of friction, much less the technology of our day, and indeed that of Amontons' time. In his seminal paper on friction, Amontons stated that "of all authors that have written about moving forces, there may not even be one who paid sufficient attention to the effect of friction inside machines or on the resistance caused by the stiffness of ropes, nor one who gave us the rules to know one or the other, and to reduce them to calculations".[4] Amontons clearly understood the importance of friction that his fellow scientists seemed to ignore, and motivated by these frustrations took it

upon himself to correct these omissions. Like Amontons, we must strive to understand the phenomena of the world around us, aided by the technology of our time, and the insights of those before us.

Classical theories alone cannot explain the fundamental nature behind the intrinsically linked friction and adhesion. Macroscale contacts consist of multi asperity contacts, and therefore an understanding of the sliding interactions of each single asperity contact is vital. As the contacts are increasingly dominated by interfacial adhesion and friction interactions, due to their relative surface area to volume ratios, conventional lubricants are becoming progressively obsolete. Due to the increase in viscous drag in these systems, traditional lubricants are being replaced in favor of alternatives such as self-assembled monolayers (SAMs).[5] Research into friction and adhesion for such systems of single asperity contact has been greatly aided by the advent of techniques such as atomic force microscope (AFM) and friction force microscopy (FFM). Additionally, the dissipation of mechanical energy at the molecular-scale in these contacts has provided an opportunity to produce nanoscale structures through a combination of bottom-up and top-down lithographic techniques.

A short account of the theory of the intermolecular forces involved in interfacial adhesion is presented in this chapter, from conventional approaches to novel applications of solution-phase thermodynamics. Various theories of contact-mechanics will also be described, in addition to methods in which self-assembled monolayers can be used to modify surface properties, and have their interfacial interactions probed with AFM techniques. Finally, recent advances in nanopatterning will be put into context of the project, including how density functional theory (DFT) may be used to calculate the electronic structure of molecules involved.

1.2 Intermolecular Forces

The four fundamental forces found in nature are: the strong and weak nuclear forces which act between elementary particles, and the electromagnetic and gravitational forces, responsible for interactions between atoms and molecules. Intramolecular forces—those responsible for interactions between atoms within molecules, including covalent and ionic bonding—are much stronger than intermolecular forces, and are unlikely to be involved in the interactions of sliding surfaces. Therefore, the forces acting between molecules are of interest in tribological investigations of adhesion and friction.

There exist several types intermolecular force, including the charge–charge (Coulomb), charge–dipole, charge–induced dipole, dipole–dipole (Keesom), dipole–induced dipole (Debye), and induced dipole–induced dipole (London dispersion) forces. Separation dependent interaction free energies, $W(r)$, of two unconstrained molecules (1, 2) at a separation r in vacuum can be described by the following equations:[6]

$$\begin{aligned}
&\text{charge–charge:} && W(r) \sim \frac{q_1 q_2}{r} && \text{dipole–dipole:} && W(r) \sim \frac{{\mu_1}^2 {\mu_2}^2}{r^6} \\
&\text{charge–dipole:} && W(r) \sim \frac{q_1 \mu_2}{r^2} && \text{dipole–induced:} && W(r) \sim \frac{{\mu_1}^2 \alpha_2}{r^6} \\
&\text{charge–induced:} && W(r) \sim \frac{{q_1}^2 \alpha_2}{r^4} && \text{induced–induced:} && W(r) \sim \frac{\alpha_1 \alpha_2}{r^6}
\end{aligned} \tag{1.1}$$

where, for a given molecule, q is its electric charge, μ its permanent electric dipole moment, and α its polarizability.

Additionally, there exist some special forces such as the hydrogen bond (a special case of the dipole–dipole interaction) and hydrophilic/hydrophobic interactions (largely due to the anomalous nature of water), as well as quantum mechanical ones like the repulsive steric or exchange interactions. Of interest in this project, due to their pervasiveness across all interfacial interactions, are the Keesom, Debye, and London forces which are collectively described as van der Waals interactions. Hydrogen bonding, and how it may be applied to the calculation of interfacial adhesion, will also be investigated.

1.2.1 van der Waals Interactions

Before applying intermolecular forces to large collections of atoms and molecules (as is the case for surfaces in close proximity), it may be beneficial to consider a system of ideal gases. It is basic knowledge that, based on the work of Boyle and Boltzmann, the equation of state for an ideal (non-interacting) gas is:

$$pV = nRT = Nk_{\mathrm{B}}T \tag{1.2}$$

where p is the pressure, N is the number of molecules within a volume V, n is the number of moles, k_{B} is the Boltzmann constant ($1.38 \times 10^{-23}\,\mathrm{J\,K^{-1}}$), and T is the absolute temperature.

However, in 1873 Johannes Diderik van der Waals demonstrated in his PhD thesis that this relation does not hold for more realistic gas systems. Instead, van der Waals had to account for the space occupied by each gas particle, b, and added an attractive interaction between particles by means of reducing the expected pressure, $p_{\mathrm{vdW}} = p_{\mathrm{Boyle}} - a/V^2$, leading to a new real gas equation:[7]

$$Nk_{\mathrm{B}}T = \left(p + \frac{an^2}{V^2}\right)(V - nb) \tag{1.3}$$

Critically, this led to the revelation that uncharged particles are able to attract each other, albeit weakly, in the order of $1\,k_{\mathrm{B}}T$. Indeed, it is an uneven distribution or fluctuation of charges within polarizable atoms and molecules that gives rise to the attractive interactions between electrically neutral bodies.[6,7] Attractive van der Waals interactions are observed from three main sources: between two molecules with aligned permanent dipoles (Keesom interaction[8]), between a molecule with a permanent dipole inducing a dipole in a nearby non-polar molecule (Debye interaction[9]), and between temporary dipoles of polarizable molecules (London dispersion interaction[10]). Of note is that all three components of the van der Waals interaction vary as the inverse sixth power of separation, $-1/r^6$, as seen from the corresponding interaction free energies in Eq. 1.1, and are thus expected to act across short distances only.

1.2.2 Surface Forces

While the interactions between gaseous particles is generally well understood, the same models cannot be directly applied to larger bodies consisting of many atoms or molecules in close proximity—as is the case for surfaces. The *pairwise summation approximation*, originally described by Hugo Hamaker in 1937,[11] allows one to calculate the energy between two large bodies through integration of infinitesimal volumes, dV_1 and dV_2, over both volumes, V_1 and V_2, interacting by energies proportional to $-1/r^6$. A key assumption in this approach is that for each interaction between dV_1 and dV_2, the remaining volume is absent. The strength of the interaction between two objects can therefore be summarized by the coefficient aptly named the *Hamaker constant*, A_{H}. However, a problem remains in that the approach originally followed by Hamaker is best suited for less dense systems,[7] as the interaction between particles in close proximity cannot be approximated simply by an additive approach.

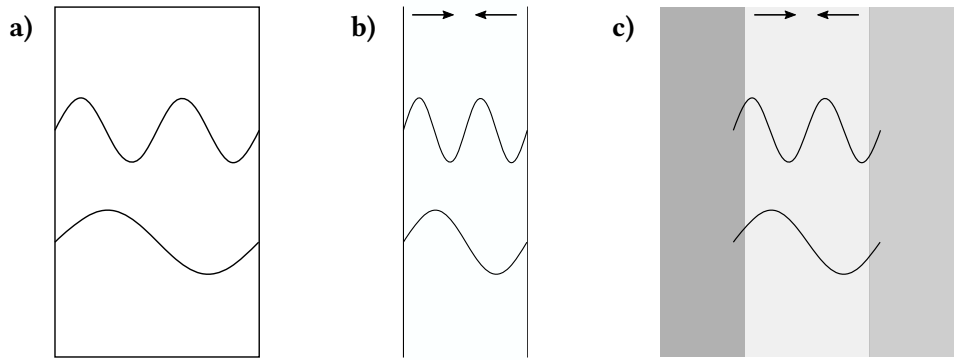

Figure 1.1: Diagrams showing steps in the development of continuum models of van der Waals interactions. **a)** Planck's "black box" radiator, absorbing all incident radiation and emitting energy corresponding to the box's temperature. **b)** Casimir forces between ideally conducting plates. **c)** Lifshitz theory of two media interacting across a third.

In 1900 Max Planck introduced the notion of quantized (discrete) energies in electromagnetic radiation in his famous papers on black-body radiation,[12,13] laying the groundwork for later quantum theories (despite being seen as a mathematical trick until Einstein's Nobel Prize winning paper in 1905 on the photoelectric effect[14]). By the summation of the discrete oscillations permitted within a "black box" with ideally conducting walls (Figure 1.1a), Planck was able to determine the heat capacity of the system. Using a similar approach, Hendrik Casimir in 1948 predicted an attractive

force between uncharged conductive (ideal) surfaces separated by a few nanometers in a vacuum (Figure 1.1b).[15] This force results from the electrodynamic pressure created by quantum vacuum fluctuations described by quantum field theory (QFT), and has been experimentally demonstrated since its initial postulation.[16]

As these forces are determined by fluctuations of electromagnetic waves, Casimir and Polder showed in a later paper how *retardation*—the delay caused as the wave propagates through space—leads to the interaction energy being reduced by $1/r$ (resulting in an energy proportional to $-1/r^7$).[17] However, as the retardation effect is related to the speed of wave propagation (i.e., light), it is not significant at distances shorter than 3 nm.[18] A logical expansion of the Casimir force is to allow the penetration of the interacting surfaces by the electromagnetic "surface modes", and is the basis of Lifshitz theory (Figure 1.1c),[7] which will be discussed at greater length in the following section. It must also be stressed that continuum theories are unable to account for imperfections or surface roughness, as they assume smooth and perfect interacting media (a potential problem at shorter separations). Nevertheless, they have been shown to provide calculated results with extraordinary levels of accuracy for some systems, well within the limits of experimental error.[3,6,7]

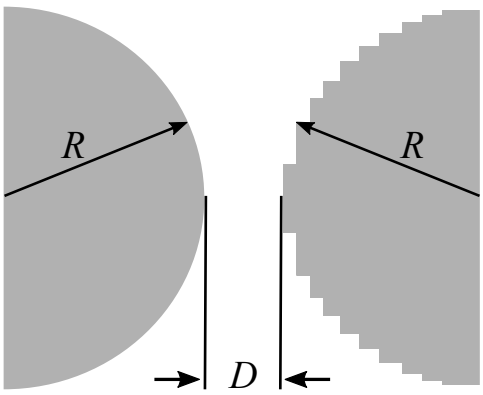

Figure 1.2: Diagram showing basis of Derjaguin Approximation, with two spheres of equal radius separated by a distance D. Right sphere has been broken into a series of steps on the curved surface as per Derjaguin's method.

One final problem exists in the calculation of real-world interactions: surfaces are generally not infinite half-spaces, their geometries being better approximated by archetypical shapes such as spheres or cylinders. To this end, Boris Derjaguin published in 1934 (predating the work by Hamaker on pairwise additivity) a method for approximating

the interaction between any combination of curved and flat surfaces,[19] now known as the *Derjaguin approximation*. This approach relies on the integration of infinitely small plane-parallel surfaces over each curved surface, as seen in Figure 1.2, and the interactions of different systems are then governed by various power-laws. The power-law interaction free energies for various systems of surfaces separated by a distance, D, are given by:[6,7]

Two Half-Spaces

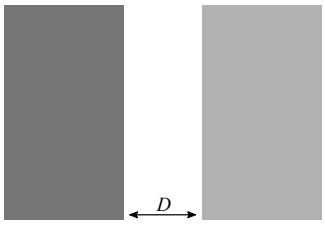

$$W(D) = -\frac{A_{\mathrm{H}}}{12\pi D^2} \tag{1.4}$$

Half-space and Sphere

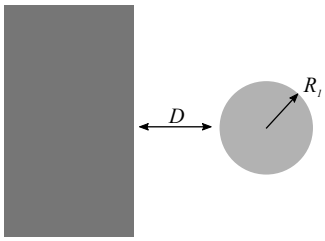

$$W(D) = -\frac{A_{\mathrm{H}} R}{6D} \tag{1.5}$$

Two Spheres

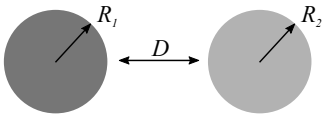

$$W(D) = -\frac{A_{\mathrm{H}} R_1 R_2}{6(R_1 + R_2)D} \tag{1.6}$$

In all three systems, the separation is assumed to be much smaller than the radii ($D \ll R, R_1, R_2$). Taking the case of a sphere (radius R) and a half-space as an example, the force per unit area, $F(D)$, experienced by the two bodies is obtained from the interaction free energy per unit area between two half-spaces, $W_{\mathrm{flat}}(D)$, of equivalent materials using the relation:[6]

$$F(D) = 2\pi R W_{\mathrm{flat}}(D) \tag{1.7}$$

1.2.3 Lifshitz Theory

An approach to solve some of the limitations of pairwise additivity of interactions was provided by Evgeny Lifshitz in 1954,[20] following the work of Planck and Casimir. By treating the interacting bodies and intermediate medium as continuous phases, the problems associated with additive approaches (e.g., the change in the polarizability of individual atoms when surrounded by other particles) are circumvented. As with the Casimir effect, van der Waals interactions in Lifshitz theory are a result of the fluctuations in the electric and magnetic fields, inducing a force between interacting bodies. In a system of electrically neutral bodies various processes can lead to the movement of charges, which in turn generate electromagnetic waves, such as: molecular rotations and vibrations, electronic movements (e.g., in metals), ion displacements, etc. These waves propagate through space (while interacting with the medium), causing a response in the electromagnetic configuration of the opposing body, and vice-versa. Ultimately, a force is experienced by the bodies that aims to minimize the energy of the system—by repulsive or attractive means—bringing them to a separation of minimum energy (see Lennard-Jones potential).

A full derivation of Lifshitz's work requires a deep understanding of quantum electrodynamics (QED) and QFT, and therefore the basic principles behind the continuum theory will be briefly summarized to give the reader sufficient background on the origin of the formulas used in this study. The two interacting phases are assumed to consist of a set of (purely sinusoidal) quantum oscillators generating and responding to fluctuations in the electromagnetic field. These oscillators interact with electromagnetic waves according to the the frequency dependent electric permittivity, $\varepsilon(\omega)$, and magnetic susceptibility, $\mu(\omega)$, of the bulk material (obtained experimentally from the absorption spectra across all frequencies). The electric permittivity can then be used to determine a set of discrete imaginary frequencies, also called *Matsubara frequencies*, $\zeta_n = 2\pi k_B T n/\hbar$ (where $n = 0, 1, 2, \ldots$), which correspond to the allowed oscillations within the interacting medium.

To determine the total free energy of the system as a function of surface separation, $W(D)$, the free energies of each oscillation involved, $g(\omega_j)$, are summated. Not every oscillation within the bodies is involved in the interaction between the two, but instead

there exists a set of oscillatory modes whose waves exist between the two surfaces, exponentially decaying outside this region. These are hence called *surface modes*, dependent on the interfacial separation and are described by a radial frequency, $\omega_j = \omega_j(D)$ with the set of all possible modes labelled as $\{\omega_j\}$. It is solely the perturbation of these discrete surface modes which causes an attractive (or repulsive) force, and therefore the origin of dispersion interactions is purely quantum mechanical. Still remaining in determining the total free energy of the system is therefore a description of the form of $g(\omega_j)$ and of the whole set of surface modes, $\{\omega_j\}$.

As the system consists of a series of quantum oscillators whose energy levels increase in quantized steps ($\hbar\omega$) from the zero-point energy ($\frac{1}{2}\hbar\omega$), the free energy of each oscillator, $g(\omega_j)$, is calculated via the corresponding partition function, $Z(\omega_j)$:[7]

$$Z(\omega_j) = \sum_{\eta=0}^{\infty} e^{-\hbar\omega_j\left(\eta+\frac{1}{2}\right)/k_\mathrm{B}T} \tag{1.8}$$

$$\begin{aligned} g(\omega_j) &= -k_\mathrm{B}T \ln Z(\omega_j) \\ &= -k_\mathrm{B}T \ln[e^{-\hbar\omega_j/2k_\mathrm{B}T}/(1-e^{-\hbar\omega_j/k_\mathrm{B}T})] \\ &= k_\mathrm{B}T \ln[2\sinh\left(\hbar\omega_j/2k_\mathrm{B}T\right)] \end{aligned} \tag{1.9}$$

To determine the surface modes, $\{\omega_j\}$, one can apply the knowledge that these modes decay rapidly within the materials to the boundary conditions of Maxwell's equations, providing the desired frequencies. These surface modes are a subset of the Matsubara frequencies which are given by:

$$\omega_j = i\zeta = i\frac{2\pi k_\mathrm{B}T}{\hbar}n, \quad n = 0, 1, 2, \ldots \tag{1.10}$$

Due to the boundary conditions of Maxwell's equations, the frequencies obtained are dependent on the separation between the surfaces, as well as the dielectric properties of all three interacting media (the two bodies, 1 and 2, and intermediate phase, 3): the electric permittivity, $\varepsilon_{1,2,3}(i\zeta)$, and the magnetic permeability, $\mu_{1,2,3}(i\zeta)$. Thus, the free energy of each quantum oscillator surface mode is also dependent on the dielectric properties of each

material, and the total free energy of the system is obtained via summation:

$$W(D) = \sum_{\omega_j} g(\omega_j[\varepsilon_{1,2,3}(i\zeta), \mu_{1,2,3}(i\zeta), D]) \tag{1.11}$$

This expression can be combined with Eq. 1.4 to give the free energy as a function of separation of two half-spaces in terms of a Hamaker constant:

$$W(D) = -\frac{A_{\mathrm{H}}[\varepsilon_{1,2,3}(i\zeta), \mu_{1,2,3}(i\zeta), T, D]}{12\pi D^2} \tag{1.12}$$

Of course, one is not limited to planar geometries, and the Derjaguin approximation can be used to provide expressions for various other configurations. This shows the power of Lifshitz theory, which allows the Hamaker coefficient of a system to be calculated solely from the dielectric and optical properties (obtained experimentally) of the interacting media.

Naturally, Lifshitz theory concerns itself predominantly with ubiquitous dispersion forces arising through the mutual polarization of electrically neutral surfaces, and therefore cannot explain the nature of interactions in more complex systems. For example, forces arising from ion-correlation or the electrostatic repulsion from electric double layers are not accounted for. Not accounted for either are interactions due to hydrogen bonding, which are important in many systems; these will be discussed in a further section. Despite these shortcomings, it has been shown to offer remarkably accurate predictions on the interactions of many systems[3,6,7,21,22] and was thus chosen for further investigation, albeit with some modifications as described in Section 3.1.1.

1.2.4 Hydrogen Bonding

Hydrogen bonding, as its name suggests, describes the interaction between a hydrogen atom covalently bonded to an electronegative atom of the first four halogens, O, or N. As alluded to earlier, a hydrogen bond is a special type of dipole–dipole interaction and hence is electrostatic and directional in nature. Its importance in biological systems is exceptional, leading Jeffrey and Saenger to preface their book on the subject with:[23] “The discovery of the hydrogen bond could have won someone the Nobel prize, but it

didn't". Hydrogen bonds tend to have bond strengths between $10 - 40\,\mathrm{kJ\,mol^{-1}}$, making them considerably stronger than van der Waals interactions ($\approx 1\,\mathrm{kJ\,mol^{-1}}$), yet weaker than covalent or ionic bonds ($> 200\,\mathrm{kJ\,mol^{-1}}$).[24]

Early descriptions of hydrogen bonding by Werner[25] and Hantzsch[26] in 1902 and 1910 mention the involvement of a "Nebenvalenz" or "secondary valence" of the hydrogen atom. The first formalized concept of hydrogen bonding (the first to call it a "bond") was proposed by Latimer and Rodebush a decade later,[27] based on the work done by Huggins as part of his master's thesis,[28] suggesting that hydrogen may sometimes have a valence of two. This was, as per Jeffrey and Saenger, "heresy in the golden age of paired electrons and Lewis's octet rule".[23] It was not until Pauling's 1939 book *The Nature of the Chemical Bond*,[29] which included an influential chapter on hydrogen bonding, that the phenomenon became widely accepted. Since then, there have been many attempts to present a unified theory to describe hydrogen bonding and while none have accomplished this goal, our knowledge of the interaction has been greatly expanded.[3,6,30–33]

To determine whether hydrogen bond interactions can predict the adhesive energy between non-polar surfaces (however unintuitive at first glance!), an improved version of the model initially proposed by Hunter in 2004 was used. This model of solvation thermodynamics has been thoroughly experimentally tested for various solvation effects,[34–36] and has also been used to simulate the adhesive interactions between polar surfaces.[37] A brief description of the original model will be presented in the next section, while an explanation on the modifications applied to the calculations for this study can be found in Section 3.1.2.

1.2.5 Hunter Model

Many intermolecular interactions (e.g., hydrogen bonding, hydrophobic interactions) have generally been partitioned into separate fields, and therefore Hunter's goal was to adopt a unified thermodynamic point of view to explain these.[32] The basic principle of the model relies on describing the strength of each hydrogen bond donor and acceptor by a set of parameters which are obtained either experimentally or via calculation. Using these, it is then possible to determine various thermodynamic properties of a system of solvated molecules in equilibrium.

The first use of hydrogen bond parameters to calculate the association constant of a system (a type of equilibrium constant, popular amongst physical organic chemists) was introduced by Abraham et al.[38] In their study it was shown that the equilibrium constant, K, of an interacting system can be determined with remarkable accuracy as simple pairwise hydrogen bond interactions by the relation:

$$\log K = c_1 \alpha_2^{\mathrm{H}} \beta_2^{\mathrm{H}} + c_2 \tag{1.13}$$

where α_2^{H} and β_2^{H} are functional group constants that relate to the hydrogen bond acidity (donor) and basicity (acceptor), respectively, c_1 is a solvent-specific term inversely proportional to the polarity of the medium, and c_2 has been found to be a constant with an approximate value of -1.0.

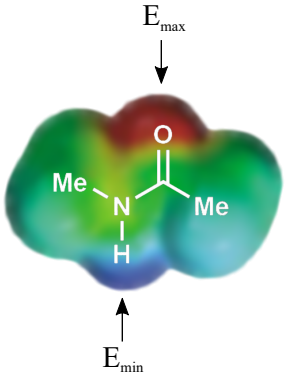

Figure 1.3: MEPS at the van der Waals radius of N-methyl acetamide via AM1, showing sites corresponding to α (E_{max}) and β (E_{min}) parameters. Colors represent increasing electron density from blue to red. Image adapted from Hunter.[32]

The main assumption of the Hunter model is that hydrogen bonding occurs only at specific locations on the interacting molecules. If one determines the molecular electrostatic potential surface (MEPS) at the van der Waals radius (representing the closest approach distance of two non-bonded atoms) for any given molecule, the maximum is often located near a hydrogen while the minimum is usually over a lone pair or other area of high π-electron density. An example of such a surface with labelled maxima and minima can be found in Figure 1.3. Therefore, the dominant electrostatic interactions between molecules are assumed to occur as a pairwise interaction between the maxima and minima of this MEPS. The energy of these maxima and minima, E_{max} and E_{min}, were

found to be relatively well described by a linear correlation to the values of α_2^{H} and β_2^{H}, allowing for new hydrogen bond strength parameters relating the two quantities to be obtained:[32]

$$\alpha = E_{\mathrm{max}}/52\,\mathrm{kJ\,mol^{-1}} = 4.1(\alpha_2^{\mathrm{H}} + 0.33) \tag{1.14}$$

$$\beta = -E_{\mathrm{min}}/52\,\mathrm{kJ\,mol^{-1}} = 10.3(\beta_2^{\mathrm{H}} + 0.06) \tag{1.15}$$

where α is the hydrogen bond donor and β is the hydrogen bond acceptor ability of the corresponding molecule. As can be seen, if either the experimental values of α_2^{H} or β_2^{H} are known, or those of E_{max} or E_{min} obtained from the calculation of the MEPS via AM1 (a semi-empirical calculation method using the AM1 Hamiltonian[39]), the other property can be easily derived.

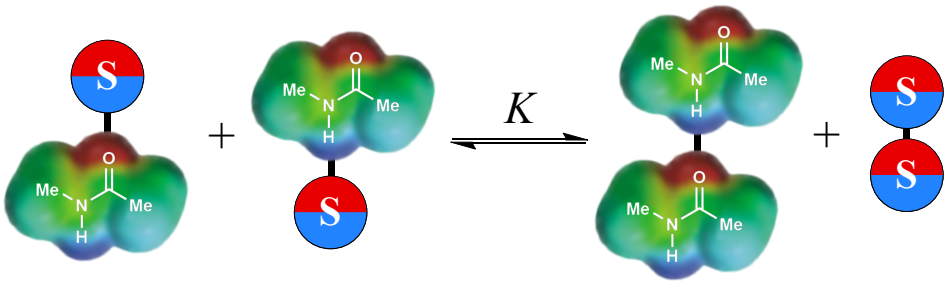

Figure 1.4: Solute–solvent equilibrium with association constant, K, shown for N-methyl acetamide and a solvent S..

Consider now the case of a system of two molecules in solution having reached equilibrium—one a hydrogen bond donor, the other an acceptor. At any given time there will be a competition between solvent–solvent, solute–solvent, and solute–solute interactions, as shown in Figure 1.4. Each of these interacting molecules will possess hydrogen bond parameters, and the free energy of solvation can thus be expressed as:[32]

$$\Delta G^{\circ} = -RT \log K = -(\alpha - \alpha_s)(\beta - \beta_s) + 6\,\mathrm{kJ\,mol^{-1}} \tag{1.16}$$

where α_s and β_s are the Hunter hydrogen bond parameters of the solvent, and the addition of 6 kJ mol^{-1} is due to the adverse free energy of bimolecular complexation. The greater the difference between the hydrogen bond donor and acceptor parameters of the solute and the

solvent, the greater the solute–solute interaction, and the equilibrium is shifted towards the bimolecular complex. Therefore, the stronger the hydrogen bond donor/acceptor parameters, the stronger the bond between the two, and the free energy to form a complex is increased. It should be noted that while α and β are dimensionless, the product of two parameters gives rise to a value of free energy in $\mathrm{kJ\,mol^{-1}}$, a consequence of the normalization performed to obtain their values.[32]

This approach has been used in numerous studies and found to offer robust results in determining the interactions of mixed solvents,[34] the role of functional group concentration,[36] and has also provided insights into halogen bonding.[40] Finally, it has been used to successfully predict the critical concentration of polar solvent at which adhesion and friction between various polar surfaces changes.[21,37,41] This was achieved by assuming that the interacting maxima and minima of a MEPS are localized to the end groups of a surface, an approach similar to the one taken in this study. For this reason, and the ability of the expanded model to predict non-polar interactions,[42] the Hunter model is of interest in describing surface forces.

1.3 Nanotribology

The effects of friction are felt all around us, vital in processes from the continental scale of stick-slip friction in earthquakes[43] to the micro- and nano-scale as seen in biomolecular motors[44] and NEMS.[45] Friction is just one form of energy dissipation between surfaces in moving contact and is a large contributor to the wear of moving parts, a matter of great concern for many industries (e.g., the automotive sector). The study of friction, as well as associated processes such as adhesion, lubrication, and wear—or more generally the study of surfaces in motion relative to one another—can be found under the comprehensive field of "tribology". Utilising the many new experimental and theoretical techniques provided by the (then) budding field of nanotechnology, the study of interfacial interactions at the molecular-scale became possible, leading to the new field of *nanotribology*.[2,46,47]

Despite the recent increase of interest in the subject, studies on friction have been carried out for centuries, the earliest account of which can be found in renowned polymath Leonardo Da Vinci's notebooks.[48] While Da Vinci noted that the weight required to move a

block down a slope was independent of the surface contact area, it was not until Guillaume Amontons confirmed these findings in 1699 that a more robust theory of friction became available.[4] Amontons proposed two laws of friction, which are expressed mathematically as a single relation, in which the force experienced due to friction, F_{fr}, is given by:

$$F_{\text{fr}} = \mu F_{\text{N}} \tag{1.17}$$

where F_{N} is the load applied perpendicular to the plane of contact, and μ is the coefficient of friction, a term dependent on the materials in contact. As with many new discoveries, it was met with ambivalence by contemporary scientists, until it was once again confirmed by Coulomb in 1781.[48,49] It had been previously hypothesized by Antoine Parent and Leonard Euler that surfaces can be assumed to consist of a number of microscopic "ramps" (or *asperities*), and that these interlock at the interface between surfaces in contact. While the simple model presented by Parent and Euler would struggle to predict the behavior of many systems,[49] it presented the idea of two types of friction: static friction, the force arising due to the need to overcome the interlocked asperities of two bodies at rest, and kinetic friction, the force resisting the sliding of two surfaces. Therefore, in addition to verifying the results obtained by Da Vinci and Amontons, Coulomb investigated the effect of sliding velocity on the force of friction, culminating in the discovery that kinetic friction is independent of the rate of surface motion.[50] This completes the three classical laws of friction:

1. The force of friction increases linearly with the normal force
2. The force of friction is independent of the size of the contact area
3. (Coulomb) Kinetic friction is independent of the sliding velocity

The theory of friction as presented by Amontons, Parent, Euler, and Coulomb has been used for centuries, and is still prevalent today. However, a full understanding of the underlying nature of the interactions involved remains elusive. Indeed, there are several issues with the classical model: what is the process of energy dissipation, how do intermolecular and surface forces affect friction, and is the friction force truly independent of contact area?

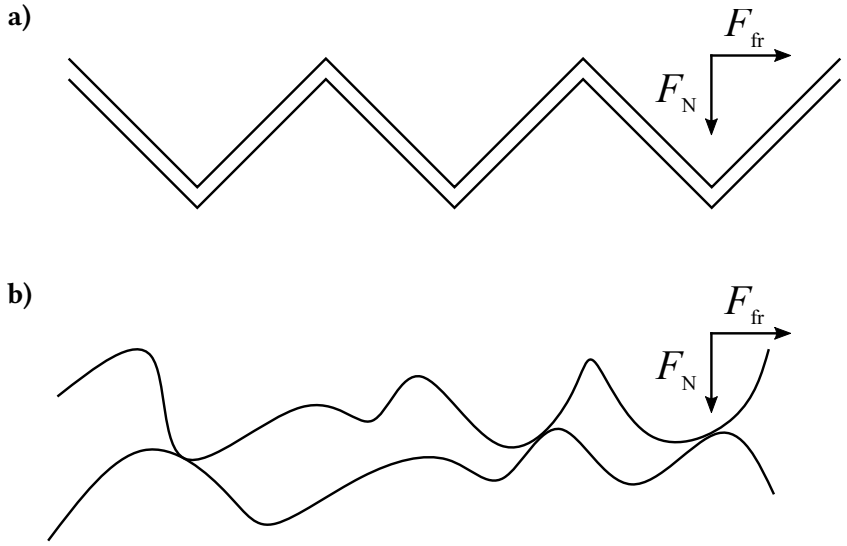

Figure 1.5: Illustrations showing **a)** smooth and regular asperities proposed by Parent and Euler and **b)** irregular surfaces in contact more representative of real systems.

To address these, one must return to the original justification by Parent and Euler for the source of the friction force, in which the surfaces consist of a series of sloped asperities. While this may explain the source of the friction force (and its linear dependence on the applied load), it also suggests that the asperities slide down on the opposite side (Figure 1.5). There would therefore be little to no energy dissipation as the energy required to move up the asperity would be regained upon sliding down, and no additional work would be required for the objects to continue sliding against each other. Ultimately, the initial model presented centuries ago fails to account for any surface deformation and adhesion which dominate the energy loss processes of sliding contacts,[51] as well as the fact that surfaces consist of irregular asperities (Figure 1.5b). The first recorded work on the effect of adhesion on friction was by J. T. Desaguliers, who showed that highly polished surfaces experienced high friction forces. In his 1745 book, Desaguliers attributed this to the adhesive interactions between surfaces, and postulated that the friction force was proportional to the true contact area,[52] contradicting the second law of friction.

Derjaguin proposed in 1934 a modified version of Amontons' laws, accounting for the adhesive forces between surfaces through the inclusion of an internal load, L_0:[53]

$$F_{\text{fr}} = \mu(L + L_0) \tag{1.18}$$

where $L = F_{\text{N}}$. Additionally, the coefficient of friction, μ, was now defined as the gradient of the friction-load plot, rather than by Eq. 1.17:

$$\mu = \frac{dF_{\text{fr}}}{dF_{\text{N}}} \tag{1.19}$$

It was not until 1950 that the ideas of adhesion and asperity contacts were married by F. P. Bowden and D. Tabor,[49] who furthered the critical observation (which Desaguliers had hinted at) that friction was proportional to the real—and not apparent—area of contact. In a series of studies, Bowden and Tabor showed that the electrical conductivity at the interface between metal contacts was proportional to the normal force applied.[54] From this they concluded that the real area of contact between two bodies must be proportional to the applied load ($A \propto L$), and thus the friction force is also proportional to the real contact area. This may seem inconsistent with established Hertz theory in which $A \propto L^{2/3}$ for a sphere in contact with a flat surface, however by assuming plastic deformations of the asperities to be occurring, Amontons laws were preserved.[55] Therefore, as increasing pressure is exerted on each asperity, the area of contact of each asperity rises linearly.

This would later be corrected for Hertz theory by Greenwood and Williamson, who suggested an exponential distribution of asperities.[46] These asperities were assigned spherical apexes of equal radius and while the real area of contact of each asperity obeyed Hertz ($A \propto L^{2/3}$), the sum of all real areas is linearly proportional to the applied load.[56] However, understanding the interactions of single asperity contacts (rather than of an accumulation of these contact points), is of great interest, especially since the advent of apparatus capable of probing such contacts.

1.3.1 Single Asperity Contact Mechanics

Defined as the study of "stresses and deformations which arise when the surfaces of two solid bodies are brought into contact",[57] contact mechanics is an integral aspect of tribology. Several models for the contact mechanics of single asperity contacts exist, the first of which was developed by Heinrich Hertz in 1881.[58] His paper titled *Über die Berührung fester elastischer Körper* (On the contact of elastic bodies), considered to be the origin of contact mechanics, describes the contact between two glass lenses.

1.3.2 Classical Theories

While investigating the optical interference between glass lenses, Hertz questioned whether a deformation of the lenses, caused by the pressure of two lenses in contact, would show a significant change in the observed interference pattern. With this in mind, he created a model of the lenses in contact, constrained by certain assumptions: the two solids are perfectly elastic, only small strains that are within the elastic limit are considered, the contact area is much smaller than the radius of curvature, and contact is frictionless.[58]

From these assumptions, it is possible to calculate the stress experienced by elastic solids in contact for various different physical systems, such as sphere on elastic half-space or sphere on sphere. The Hertz contact radius, a, of a sphere (radius R) on a half-space is defined as:[59]

$$a = \left(\frac{3LR}{4E^*}\right)^{1/3} \tag{1.20}$$

$$E^* = \left(\frac{1-\nu_1^2}{E_1} + \frac{1-\nu_2^2}{E_2}\right)^{-1} \tag{1.21}$$

where L is the applied load, E_1 and E_2 the Young's Moduli of the two materials, and ν_1, ν_2 their Poisson's ratios. Consequently, the area of contact is given by the relation for the area of a circle, $A = \pi a^2$, and therefore $A \propto L^{2/3}$. Being an elastic contact the deformation is fully reversible and, for a retracting sphere, upon reaching a contact radius of exactly zero (reducing the contact area to a single point), zero force is required to separate the two bodies, as adhesion is ignored.

While it would be convenient to simply combine Hertz's model with Amontons law for use in FFM experiments (although it has been shown to hold true for non-adhering surfaces[60]), one cannot ignore the importance of adhesion. The Bradley model of rigid contact was the first contact mechanics model to include adhesive interactions.[61] Adhesion at zero load for a sphere and half-space is expressed by the Bradley model:

$$F_{\text{ad}} = -2\pi WR \tag{1.22}$$

where W is the work of adhesion per unit area (or surface interaction energy), and R the radius of the sphere. The work of adhesion represents the work done in separating two surfaces completely, for a unit area of interface. However, unlike the Hertz model, Bradley assumed perfectly rigid bodies unable to deform, making it unsuitable for most contacts. This model would soon be followed by the JKR and DMT models for elastic single asperity contacts, which incorporate either short- or long-range adhesive interactions between surfaces in contact.

1.3.3 JKR & DMT

A solution to the problem of adhesion in elastic contacts was first proposed by Johnson, Kendall, and Roberts (JKR) in 1971.[62] In their study, experimentally obtained contact areas were found to be larger than expected from Hertz theory, and a finite contact area existed at zero applied load. From these observations, the following modified Hertz radius was derived for the contact between a sphere (radius R) and and a half-space:[57]

$$a = \left[\frac{3R}{4E^*}\left(L + 3\pi WR + \sqrt{6\pi WRL + (3\pi WR)^2}\right)\right]^{1/3} \tag{1.23}$$

Of note is the fact that as the work of adhesion per unit area, W, approaches zero, the area of contact reduces to Hertz's result.

In essence, JKR theory states that the compressive stress within the contact area is enhanced by the presence of short-range adhesive interactions solely within this area. This has the effect of expanding the contact area beyond that predicted by the Hertz model, leading to characteristic "neck" contact profiles as shown in Figure 1.6. Additionally, this

causes a hysteresis in the loading and unloading, as the contact area at pull-off is no longer zero. From Eq. 1.23 one can obtain the formula for the contact area at zero applied load:

$$a_0 = \left(\frac{6\pi W R^2}{E^*}\right)^{1/3} \tag{1.24}$$

The (tensile) load required to fully separate from the surface, i.e., the critical load, L_c, or pull-off force, F_{po}, is therefore:

$$L_c = F_{po} = -\frac{3}{2}\pi W R \tag{1.25}$$

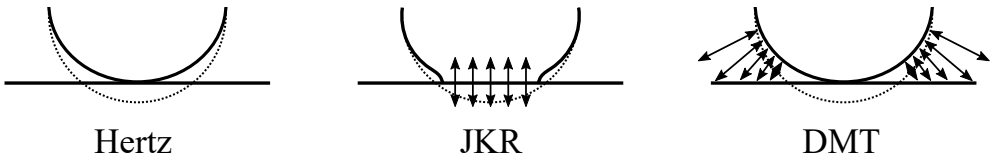

Figure 1.6: Comparison between the contact profiles and adhesive interactions in the Hertz, JKR, and DMT contact mechanics models. In all three cases a spherical indenter is being compressed into a rigid plane, with arrows showing interfacial forces and dotted lines the shape of an undeformed sphere.

Originating from the intial work by Derjaguin in 1934, the Derjaguin, Muller, and Toporov (DMT) model introduced in 1975[63] (and expanded further since[64]) takes a different approach to adhesion in elastic contacts. Unlike the JKR model, DMT theory expands on the Derjaguin approximation (see Section 1.2.2) by including Hertzian contact stresses. The total free energy of a system at any given state is therefore the sum of the elastic energy of the deformation and energy due to the longer range interfacial interactions. Essentially, this has the effect of increasing the effective load on the system by the critical (or pull-off) load. Therefore, the contact radius as per DMT mechanics for a sphere (radius R) and a half-space is given by:

$$a = \left[\frac{R}{E^*}(L + L_c)\right]^{1/3} \tag{1.26}$$

where the critical load is given by:

$$L_c = F_{po} = -2\pi WR \tag{1.27}$$

the same result as given by the Bradley model.

In contrast to JKR, the DMT model does not have a finite contact area at the point of separation, instead behaving like Hertz theory by having a point contact at the moment of separation. This leads to the entire load/unload process to be fully reversible, without any hysteresis in the forces observed. Additionally, the adhesive interaction is entirely independent of the load, a departure from JKR theory as seen in Eq. 1.23.

One might therefore be inclined to assume that the two models are incompatible with one another, and that one theory is closer to reality than the other. This was the subject of much debate, until a suggestion was made that the two models may in fact be correct at different ends of a spectrum, with a transition regime between the two. Therefore, neither JKR or DMT are the panacea for the problem of adhesion in single asperity contacts, but instead describe the behavior of different real systems.

1.3.4 Transition Regime

Both JKR and DMT models have been successfully applied to a number of real scenarios,[65–67] but neither is able to predict the behavior of all possible systems. Instead, they describe the behavior of systems on opposite sides of a spectrum, depending on a number of factors. For systems with spheres of large radii made of compliant materials able to be easily deformed by strong and infinitely short-range forces, JKR is able to accurately describe the contact area. Conversely, if the materials are stiff, with small sphere radii, and long-range adhesion forces outside the contact area are dominant, the opposite side of the asperity contact spectrum is reached, and DMT mechanics apply. The interactions per unit area as a function of separation for the Hertz, JKR, and DMT models can be seen visually in Figure 1.7, which includes a real interaction for comparison. The transition regime between the two extremes of either JKR or DMT mechanics is therefore described by a *transition parameter*.

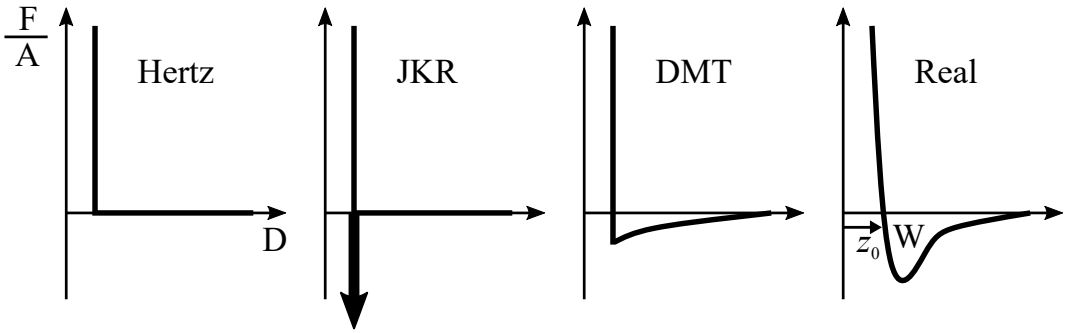

Figure 1.7: Interaction force per unit area for Hertz, JKR, and DMT models, compared to a more realistic system.[68]

Many transition parameters exist,[69] but the most common is perhaps the Tabor coefficient, μ_{T}, defined as:[70]

$$\mu_{\mathrm{T}} = \left(\frac{16RW^2}{9E^* z_0^3}\right)^{1/3} \tag{1.28}$$

where W is the work of adhesion per unit area, R is the radius of the sphere, E^* is the reduced Young's modulus, and z_0 is the equilibrium separation between atomic planes. This parameter gives the ratio of the deformation due to adhesion versus the spatial range of these adhesive forces. Therefore, values of μ_{T} close to zero correspond to DMT mechanics (as the deformation due to adhesion is zero), and greater values are expected to lead to JKR character.

An improvement on this parameter was proposed by Maugis in 1992,[71] which also allowed for a better explanation of the more common regime between the pure JKR and DMT extremes. Describing the attractive force between spheres in contact by using a Dugdale square-well potential (Figure 1.8), the work of adhesion was defined as:

$$\gamma = \sigma_0 \delta_{\mathrm{t}} \tag{1.29}$$

where σ_0 is a constant adhesion stress and δ_t is the range this stress acts over. Using this modified work of adhesion, the Maugis parameter, λ, is given by:

$$\lambda = 2\sigma_0 \left(\frac{R}{\pi \gamma E^*}\right)^{1/3} \tag{1.30}$$

Setting σ_0 to be equal to the minimum of a Lennard-Jones potential with equilibrium separation of z_0, the range becomes $\delta_t = 0.97z_0$ and therefore the two parameters can be related:[68]

$$\lambda = 1.1570\mu_T \tag{1.31}$$

As with the Tabor parameter, JKR can be attributed to systems with greater values of the Maugis parameter, $\lambda > 5$, while DMT corresponds to $\lambda < 0.1$. Any values that fall between these are best described by the Maugis-Dugdale model. The use of a square-well potential was shown to be an appropriate assumption in 1998 by Barthel[72] who showed that the contact is largely uninfluenced by the shape of the interaction potential. However, this requires only interactions of a single length-scale, with the inclusion of multiple intermolecular forces (e.g., electrostatic, van der Waals, etc. See Section 1.2) requiring a simultaneous approach.[73] Despite its improvements, the Maugis-Dugdale model is difficult to use, due to its lack of equations relating simply to the contact radius, requiring solutions to simultaneous equations at each step, with parameters bound between limits set by the value of λ. Additionally, if λ is unknown (as it is usually determined experimentally), it must be obtained iteratively,[74] adding to the computational complexity.

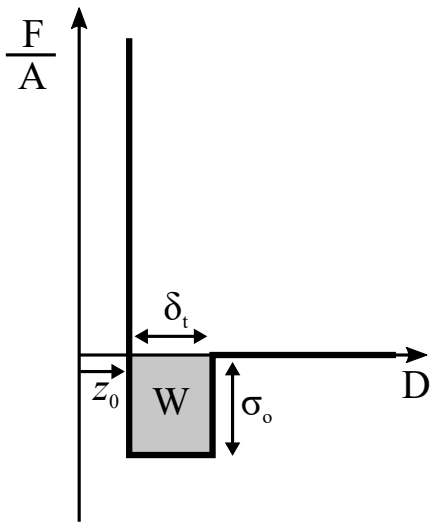

Figure 1.8: Force per unit area against distance for the Dugdale square-well potential.

To aid with this, Carpick, Ogletree, and Salmeron in 1999 proposed a solution in the form of the *General Fitting Equation*,[68] an approximation of the Maugis formulations. Easy to incorporate into modern curve fitting software, the equation relates the applied load, L to the contact area, $a(L)$, with a transition parameter, α_t:

$$\frac{a(L)}{a_0} = \left(\frac{1 + \sqrt{1 - L/L_c}}{1 + \alpha_t} \right)^{2/3} \tag{1.32}$$

where L_c is the critical load, and a_0 is the contact radius at zero applied load. The equation is normalized such that $\alpha_t = 1$ corresponds to the exact JKR case, while $\alpha_t = 0$ gives pure DMT mechanics. Carpick et al. showed that for the transition regime ($0 < \alpha_t < 1$) the generalized equation gave results very close to those of the Maugis-Dugdale transition.[75] The two parameters are related by the equation:

$$\lambda = -0.924 \ln(1 - 1.02\alpha_t) \tag{1.33}$$

while the critical load, L_c, and contact radius at zero applied load, a_0, are given by:

$$L_c = -\frac{7}{4} + \frac{1}{4} \left(\frac{4.04\lambda^{1.4} - 1}{4.04\lambda^{1.4} + 1} \right) \tag{1.34}$$

$$a_0 = 1.54 + 0.279 \left(\frac{2.28\lambda^{1.3} - 1}{2.28\lambda^{1.3} + 1} \right) \tag{1.35}$$

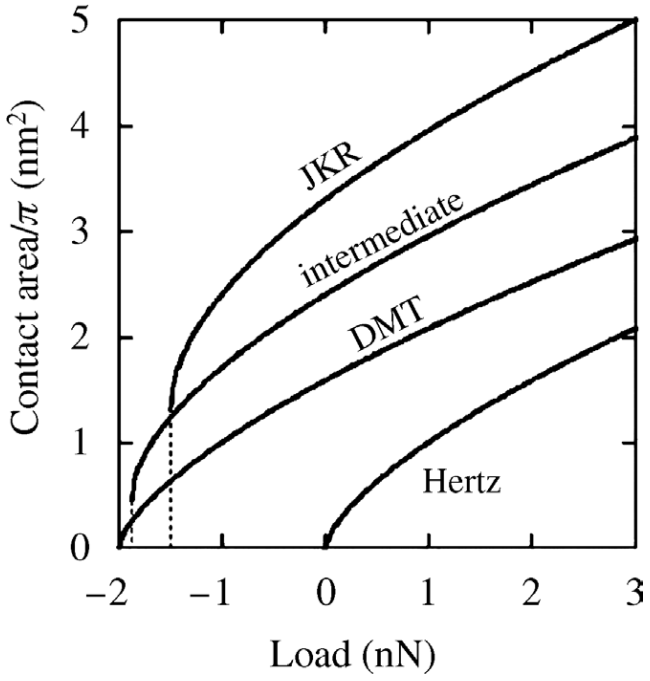

Figure 1.9: Area-load curves of pure Hertz, JKR, and DMT models, as well as Maugis transition region. In limit of no adhesion ($W \rightarrow 0$), Hertz curve is obtained.[68]

1.3.5 Thin Coating Contact Mechanics

The contact mechanics discussed until now have been for homogeneous elastic bodies, but many real systems have their surface properties (e.g., lubrication[76,77] and corrosion resistance[78,79]) modified via the adsorption of thin chemical layers. Certain physical properties of these layers, such as the elastic moduli, are often different enough from the bulk substrate material's that the contact stress and strain fields within and in close proximity to the contact area are affected. This was suggested by Barthel et al.,[80] who stated that the geometries and physical properties of all materials, as well as the chemical interactions between surfaces, must be known to accurately describe a system consisting of at least one thin layer. As such, the JKR and DMT models described previously are not completely suitable for use in explaining the behavior of the contacts experienced in this study, as the atomic force microscope (AFM) probes used have been modified with a layer of self-assembled monolayers.

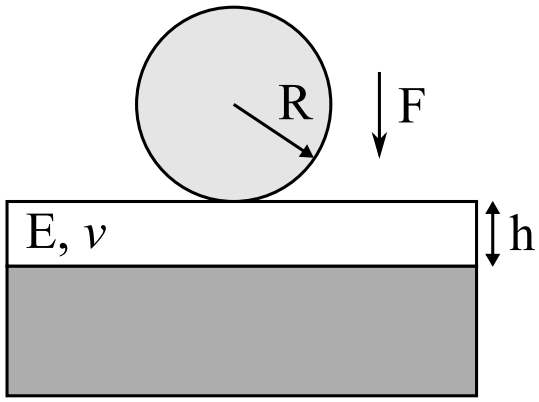

Figure 1.10: Illustration showing the TCCM model for a rigid sphere about to compress into a thin film adsorbed onto a rigid substrate. Not to scale, as $R \gg h$ required by model.

The most notable attempt to resolve this limitation of the contact mechanical theories, the thin coating contact mechanics (TCCM) model, was initially proposed in 2006 by Reedy,[81] and was modified soon after to better suit a greater number of possible scenarios.[82] Since its inception, it has also seen use in several AFM studies,[83,84] as well as molecular dynamics simulations.[85] The model, seen illustrated in Figure 1.10, can be applied as long as the thickness-to-indenter radius ratio is below 0.1 and the Poisson's ratio of the coating is less than 0.45. Assuming a coating of thickness h with an elastic modulus E and Poisson's ratio ν, the compressive normal strain, $\epsilon_z(r)$, as a function of radial distance along the surface, r, by a spherical indenter (radius R) is given by:[81]

$$\epsilon_z(r) = \frac{a^2}{2Rh}\left[1 - \left(\frac{r}{a}\right)^2\right] \tag{1.36}$$

where a is the contact radius. Assuming $R, a \gg h$, the compressive stress is $\sigma_z = E_u \epsilon_z$ where the the uniaxial reduced Young's modulus of the coating is:

$$E_u = \frac{(1-\nu)E}{(1+\nu)(1-2\nu)} \tag{1.37}$$

Finally, the applied load, L is determined from the equation:

$$L = \frac{E_u A^2}{4\pi Rh} \tag{1.38}$$

where A is the contact area. Compared to models that do not account for surface coatings, the TCCM model has a contact area related to the applied load by $A \propto L^{1/2}$ as opposed to $L^{2/3}$. Reedy accounted for the transition regime in his modification of the original TCCM model, introducing a further transition parameter, ζ. As with the Carpick, Ogletree, and Salmeron transition parameter, $\zeta = 0$ relates to pure DMT and $\zeta = 1$ to JKR mechanics, with any value in between corresponding to the transition regime. Using this parameter, the applied load is described by the relation:[82]

$$\frac{L}{2E_{\mathrm{u}}RT} = \frac{\pi}{4(2RT)^2}a^4 - \frac{\pi}{2RT}\left(\frac{\zeta W}{E_{\mathrm{u}}T}\right)^{1/2}a^2 - \frac{\pi W}{E_{\mathrm{u}}T}(1-\zeta) \tag{1.39}$$

where W is the work of adhesion and T is the absolute temperature. Unfortunately, Eq. 1.39 is not well suited to the fitting of friction-load plots, due to the numerous parameters that would need to be left free as their values are uncertain, and instead the General Fitting Equation is used in this study. However, the TCCM model provides an equation for the critical load, L_{c}, at which separation of the two surfaces is achieved, independent of the transition parameter ζ:

$$L_{\mathrm{c}} = -2\pi WR \tag{1.40}$$

1.3.6 Surface Roughness

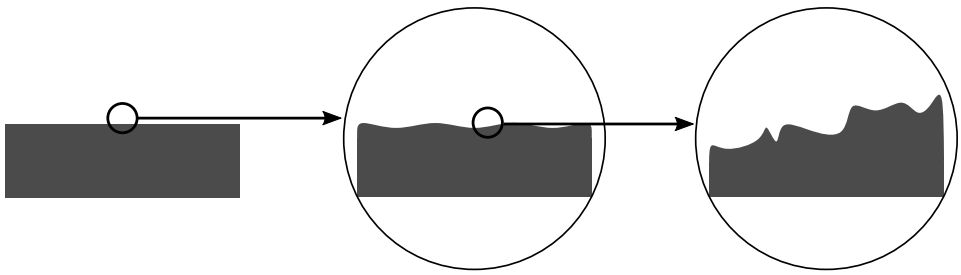

Figure 1.11: Importance of measurement scale showing surface profile at macroscale, mesoscale, and microscale.

Surfaces are very rarely as flat as they appear at first glance, their roughness becoming increasingly apparent as the scale of measurements decreases. The field studying roughness and other geometrical surface features is called surface metrology, and is strongly associated with tribology due to the role of topography on the wear of sliding contacts.[86] While a surface may be flat at the macroscopic scale, it conceals more complex surface profiles at smaller length scales, as shown in Figure 1.11.

Throughout the years there have been several programmes focussed on parameterizing the surface texture of a material, the first of which was led by K. J. Stout. It lead to the publishing of the de facto standard "Blue Book"[87] in 1993, which contained the definition of the "Birmingham 14" parameters. However, these were considered to be impractical and lacking in empirical evidence, and were eventually replaced with two core sets—field and feature parameters—contained within the 2003 "Green Book" by Blunt and Jiang.[88] These have formed the basis of the ISO 25178 standard[89,90] "Geometric Product Specifications (GPS) – Surface texture: Areal". This study is not concerned with a detailed analysis of surface roughness, and thus not all parameters are required.

The main reason for determining the roughness of the samples in this study is to ensure that the asperity distribution is consistent across all surfaces analyzed. In particular, determining whether the roughness profile follows a Gaussian or sinusoidal distribution and comparing this between samples is of importance. Only two parameters are required to determine this: the average roughness, R_a, and the root mean square (RMS) roughness, R_q. These are straightforward to determine from an appropriately sized (e.g., $1\,\mu m^2$) topographical image, easily obtainable via AFM. For a height profile in one dimension, $z(x)$, over a distance l, the parameters are given by:

$$R_a = \frac{1}{l}\int_0^l |z(x)|dx \tag{1.41}$$

$$R_q = \sqrt{\frac{1}{l}\int_0^l z^2(x)dx} \tag{1.42}$$

where a Gaussian distribution results in $R_q/R_a = \sqrt{\pi/2} \sim 1.25$ and for a sinusoidal distribution $R_q/R_a = \pi/2\sqrt{2} \sim 1.11$,[91] with the parameters usually being determined from AFM analysis software.

1.4 Scanning Probe Microscopy

The rapid development of nanofabrication techniques in the late 20th century brought with it the requirement for analytical tools with ever increasing spatial resolution. While methods existed to profile the topography and chemical composition of surfaces in the form of SIMS and SEM (from the late 1960s and early 1970s), they were limited to resolving features in the micro-scale. IBM researchers Gerd Binnig and Heinrich Rohrer transformed the field of nanoscience with the introduction of the scanning tunneling microscope (STM) in 1981, allowing for measurements with sub-nanometer precision.[92,93] A probe with an extremely sharp tip is rastered, just out of contact, across an electrically conductive surface, with the tunnelling current measured at each x and y tip position. Since its inception, STM has been used in a host of different studies and has been shown to achieve atomic resolution under the right conditions,[94] ultimately leading Binnig and Rohrer to win the Nobel Prize in 1986 for its invention.[95] However, STM is only viable for conductive samples (or those modified with a conductive coating), and thus techniques suited for different situations were developed.[96] Collectively, the family of techniques based on the basic principles of scanning a probe across a surface is known as scanning probe microscopy (SPM), with AFM being one of the most common types found in the literature.

1.4.1 Atomic Force Microscopy

In 1985, shortly after the invention of the scanning tunneling microscope, Binnig, Quate, and Gerber developed the atomic force microscope (AFM), using the deflection of an ultralight cantilever rather than a tunneling current to interrogate the surface.[97] Like its predecessor STM, atomic resolutions have been achieved using AFM,[98] relying on the force between surface and tip atoms—hence its name. The principle of operation is straightforward, with a sharp tip on the underside of a flexible cantilever being scanned across a surface. The interaction of the tip apex with the surface causes a deflection of the cantilever which is monitored and recorded. As in other SPM techniques, the cantilever is kept at a known distance from the surface using a 3-axis piezoelectric feedback loop system, which is also used to move the tip (or sample) in the x- and y-axis. The deflection is measured using a laser beam reflected off of the end of the cantilever

into a four-quadrant photodetector[99,100] (although other methods of detecting cantilever movement do exist[97,101,102]). Essentially, the cantilever acts as a tiny spring, and thus the force required to bend the cantilever by a displacement distance x is given by Hooke's law:[103]

$$F = -kx \tag{1.43}$$

where k is the spring constant of the cantilever normal to the surface. As the piezoelectric system moves the cantilever across the surface, the signal at each position is recorded by a computer, creating a topographical image of the scanned area. Since it is the interactions between the tip and the surface which govern the cantilever deflection, AFM is perfectly suited to measure not only the height profile of the surface, but a number of different physical properties. This flexibility has made it a popular tool in nanoscience and has enabled, but not been limited to, the investigation of biomolecules,[104] polymers,[105–107] and magnetic nanostructures.[108,109]

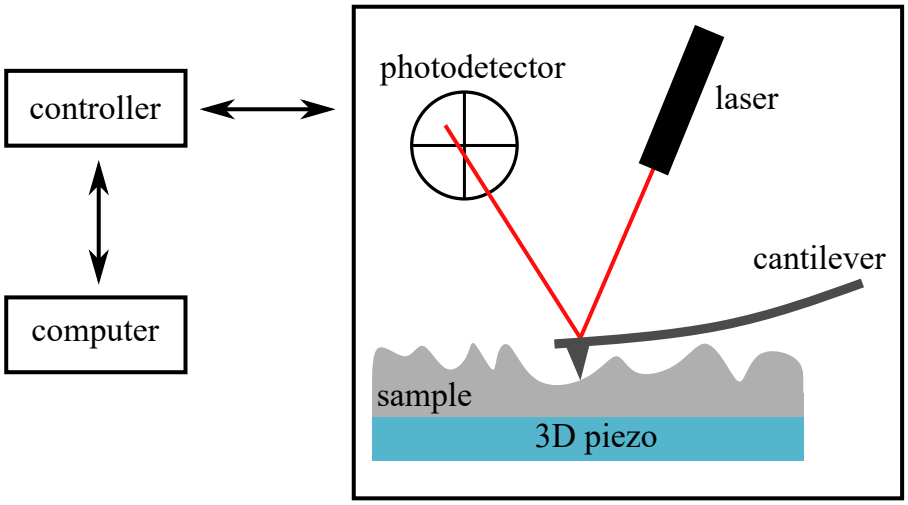

Figure 1.12: Illustration of contact mode AFM in operation.

As the forces experienced by the cantilever are often in the order of 0.1 – 100 nN (and much smaller in some cases[110]), it is desirable for the cantilever to be sensitive enough to detect these. This is easily achieved by using a softer cantilever, with as low a spring constant as possible. However, a spring constant that is too low can introduce unwanted mechanical noise, due to a change in the cantilever resonant frequency ($\omega_r = \sqrt{k/m}$).[111]

By optimizing the spring constant, k, and mass, m, of the cantilevers, AFM probe manufacturers are able to provide the best possible cantilevers for a number of different operational modes.

The features of the Lennard-Jones potential (Figure 1.13) are exploited to provide several instrumental modes for the AFM, by measuring the deflection of the cantilever in the repulsive or attractive regimes. Most common among these is contact mode AFM (CM-AFM) which employs the repulsive region to cause an upwards deflection as the probe is pressed into the surface.[112] The simplest way to visualize this mode is to consider a record player moving its stylus across the surface of a record, translating height changes into the desired information; in this case height rather than sound. The feedback loop can also be set up so as to maintain a fixed compressive load into, or height from, the surface (as determined from the vertical deflection), adjusting the z-piezoelectric element accordingly. This keeps the deflection constant, with the height signal originating from the movement of the z-axis piezo (via its input voltage) rather than the position of the reflected laser spot on the photodetector. However, as a constant compressive force is required in this mode it is not well suited to investigating soft samples (e.g., biological systems), as these can be damaged or moved during the imaging process.[113]

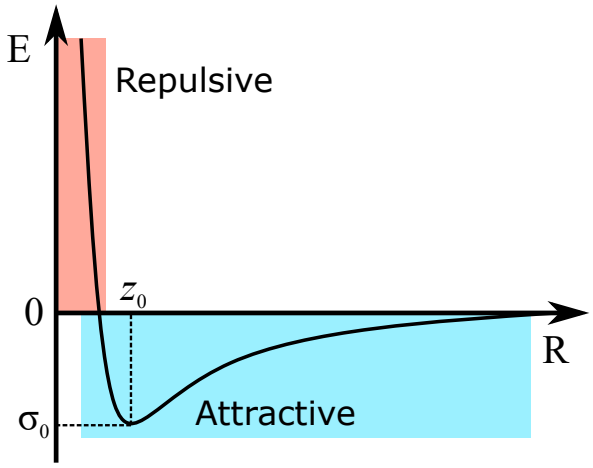

Figure 1.13: Energy–distance plot showing Lennard-Jones potential.

A non-destructive method exists in the form of non-contact mode AFM (NCM-AFM), which uses the attractive portion of the Lennard-Jones potential to measure surface profiles. In this mode, the cantilever is oscillated at its eigenfrequency just above the surface (out of contact), the frequency of the oscillation being measured via the reflected laser on the photodetector.[114] As the cantilever approaches the surface it enters the attractive regime of the Lennard-Jones potential, causing a change in its oscillation frequency as the intermolecular interactions between tip and sample increase. The feedback system then adjusts the vertical distance of the tip relative to the surface via the z-piezo, thus creating a topographical map as in contact mode. The technique is extremely sensitive, allowing for the detection of point defects on the surface[112] and true atomic resolution,[115] but is not as straightforward in practice as other modes. A narrow range in which intermolecular forces affect the cantilever oscillations, and preventing tips from being captured by the surface liquid layer[116] are considerations which have kept NCM-AFM from becoming more commonly used.

An extremely common variation on NCM-AFM is tapping mode AFM (TM-AFM).[104,113,116–119] Similarly to non-contact mode, tapping mode works by oscillating a cantilever just off-resonance, but instead of remaining a few nanometers above the surface the tip makes intermittent contact with the surface,[112,120] effectively "tapping" it. As the tip makes contact with the surface, the oscillating and driving frequencies fall out of phase, causing the feedback loop system to correct the distance from the surface to regain the desired signal. While the movement of the z-piezo is used to record the height of the sample, the frequency phase difference can be used to identify differences in surface stiffness.[121] The latter is possible due to the fact that surfaces with a lower Young's modulus are able to yield further to the applied force of the AFM tip, leading to a larger time delay between input and detected oscillations. A lack of lateral forces applied to the surface allows TM-AFM to be well suited for the imaging of biological or other "soft" samples that would otherwise be damaged by shearing or plowing by the tip.

Many other instrumental AFM modes exist, but are not directly relevant to this study, and will therefore not be covered. So far the assumption has been that measurements are made in air or vacuum conditions, however as previously mentioned, in normal conditions a thin layer of water forms on most surfaces causing a meniscus to form between surface

and tip.[122] This has an effect on all measurements taken, and therefore control over the solvent environment between tip and sample is an important consideration. Marti et al.[123] showed that AFM imaging was possible while completely immersed in mineral oil, and has since been shown to be possible under other liquids such as water[124] and ethanol.[125] Beyond changing the solvent environment, researchers have been able to modify the chemistry of the tip, enabling the investigation of numerous chemical interactions at the molecular-scale.

1.4.2 Chemical Force Microscopy

The interactions between tip and surface play a vital role in AFM measurements, and are directly influenced by the intermolecular forces discussed in Section 1.2. Standard probes are usually manufactured from silicon or silicon nitride, and are thus covered in a thin layer of native oxide, causing the surface to be polar. By modifying the surface coating of the tips and sample, information on a variety of different interfacial properties can be probed. The first demonstrations of this were by Nakagawa et al.[126] and Frisbie et al.[127] who investigated the interactions between alkane- and alcohol-terminated surfaces through the adsorption of self-assembled monolayers on tip and sample, and was given the name of chemical force microscopy (CFM). Not long after these initial studies, the technique was being used to investigate phenomena such as of friction,[128–130] force titrations,[131,132] the mechanical properties of DNA,[133] and many others.[125,127,134,135]

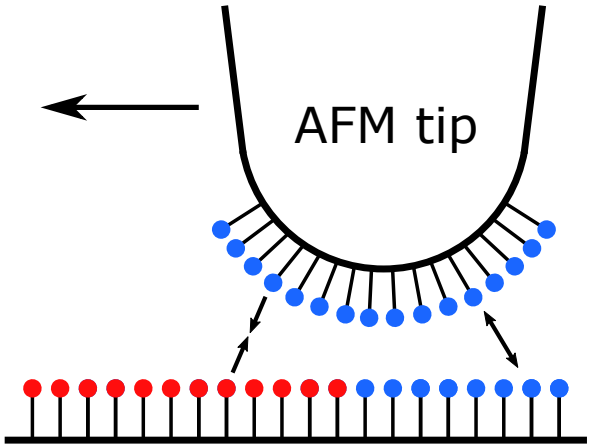

Figure 1.14: Illustration of chemically functionalized AFM probe being rastered across a surface with different monolayers. Difference in adhesive interactions between the tip and the two monolayer regions will create a contrast in the recorded image, despite no change in topography, showing some of the capabilities of CFM.

Thanks to the rapid development of self-assembled monolayers (more details of which can be found in Section 1.5), it has become trivial to modify the interacting surfaces in AFM with any desired functional group or combination thereof. In this study, contact mode probes and samples are modified using non-polar monolayers, and their surface energetics investigated using force spectroscopy and friction force microscopy, which will be described in the next few sections.

1.4.3 Force Spectroscopy

In addition to capturing height images, AFM can be used to measure the forces involved with surfaces approaching and retracting. This process is called force spectroscopy and is also possible via other techniques such as optical tweezers[136] and magnetic beads.[137] It has the ability to measure intermolecular forces between individual atoms and molecules when combined with CFM, and has been used for many years to measure the mechanical properties of biological systems.[138,139] In this project it is used to determine the adhesive properties of various non-polar surfaces.

Unlike in normal imaging mode, force spectroscopy is performed on an AFM without movement in the x- and y-axes during data collection. To collect information about the interactions between tip and sample, the probe is moved into the desired position above the

surface; far enough to ensure no appreciable force exists between the two. The z-piezo is then actuated at a constant rate to bring the tip into contact with the surface, and continues to do so until a critical deflection is reached, as measured by the reflected laser spot on the photodetector. Once this point has been reached, the tip can be held for a set amount of time if desired (it is not required), and the piezoelectric system is then run in reverse, maintaining the same speed on retract as on approach. This retraction is maintained until the cantilever returns to its starting position, before the measurement began. At every position step the deflection of the cantilever is recorded in volts, as obtained from the photodetector signal, and the data is split into approach and retract curves. These are then presented as characteristic force curves, an example of which can be seen in Figure 1.15, from which valuable information about the tip-surface interaction can be determined.

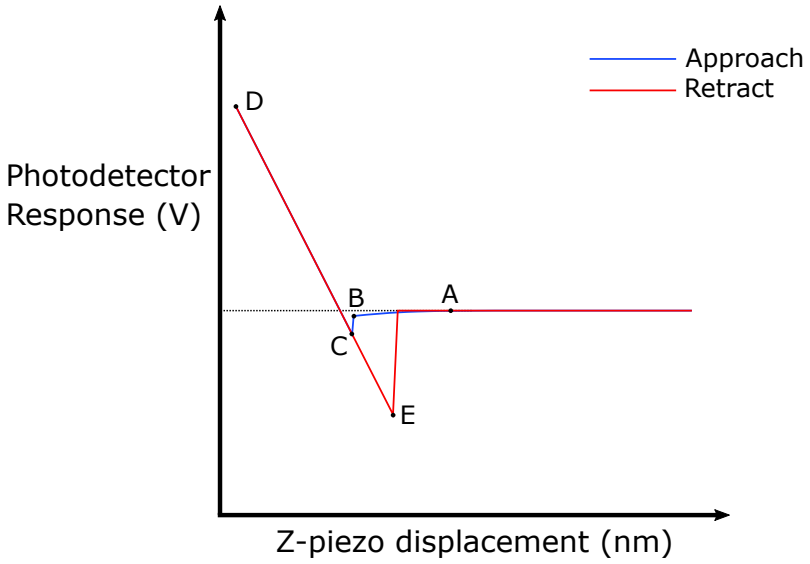

Figure 1.15: Example of a force curve obtained via force spectroscopy.

There are several key stages during a full approach-retract cycle that are shown on the force curve above. As the tip approaches the surface, it eventually reaches a point (**A**) where an attractive force—or repulsive in some cases—is experienced, due to electrostatic or dispersion interactions. Thus, a deflection towards the surface begins to form in the cantilever, which increases as the distance between tip and sample decreases, until the force in sufficient (point **B**) to cause the tip to suddenly "snap" into contact with the surface (point **C**). The mechanical instability causing this rapid snap-in is visible for any systems

in which the cantilever spring constant is lower than the tip-sample force gradient.[69,140] However, even if the cantilever is infinitely stiff, a snap-in will occur at the atomic scale due to the finite cohesive strengths of atoms at the surface, as shown by Pethica and Sutton[141] using Lennard-Jones potential calculations and later by Landman et al.[142] via the use of molecular dynamics simulations. As such, a complete force-distance plot cannot be obtained using AFM.

With snap-in having occurred, further expansion of the z-piezo towards the surface causes the cantilever to straighten and bend in the opposite direction, leading to a positive signal in the photodetector. This continues until a critical deflection (set as a parameter in the AFM controller software) is reached (point **D**), and the approach portion of the load/unload cycle is complete. The controller then instructs the z-piezo to retract the tip from the sample at the same speed as on approach, commencing the retract/unload section.

The measured deflection follows the same path as on the approach for the compressive region of the curve until reaching the initial "snap-in" point (**C**), although in some cases hysteresis effects may occur (e.g., due to experimental drift). After this point, the tip remains in contact with the surface, causing a greater negative deflection of the cantilever as the piezo is retracted, until a critical point (**E**) where the tip separates fully from the surface. This pull-off point will always be at a greater separation than the snap-in point for a number of reasons.[69] Firstly, adhesive or chemical bonds may be formed which generate non-conservative forces, leading to differences in energy dissipation.[143] Additionally, contact with the surface will have lead to a deformation in the surface by the indenting tip, therefore increasing the effective contact area (as discussed in the contact mechanics section). This causes greater force to be experienced between tip and sample than before contact, in particular for softer samples (e.g., biological materials), where gradual separation is observed rather than just a single discontinuity.[144] Finally, meniscus forces by liquids such as water have been shown to increase the pull-off force experienced,[124] a predominant reason for liquid AFM being an essential tool in the determination of surface forces.

The force required to cause this pull-off is the same as the critical load (L_c) presented in Section 1.3, and is determined from the maximum deflection of the cantilever, $(\delta_c)_{po}$, using Hooke's Law:

$$L_c = F_{po} = -k(\delta_c)_{po} \tag{1.44}$$

The greater the deflection measured, the greater the adhesive force between surfaces. In order to be statistically significant, however, a great number of force curves are required to create a histogram of obtained forces, from which the mean force and standard error can be derived. Additionally, the conversion from volts into deflection requires a photodetector sensitivity value, and the normal spring constant must also be determined. The methods used to obtain these parameters are provided in Section 1.4.5.

1.4.4 Friction Force Microscopy

The frictional resistance to motion in contact mode causes a lateral torsion of the cantilever, resulting in a lateral deflection of the reflected laser spot on the photodetector. The mode has since been referred to as friction force microscopy (FFM), and assumes a linear relationship between the torsion of the cantilever and the friction force experienced for a constant applied load. This phenomenon was first exploited by Mate et al.,[145] who used an interferometer to measure the lateral deflection of a tungsten tip, enabling measurement of the frictional force as it slid across a graphite surface.

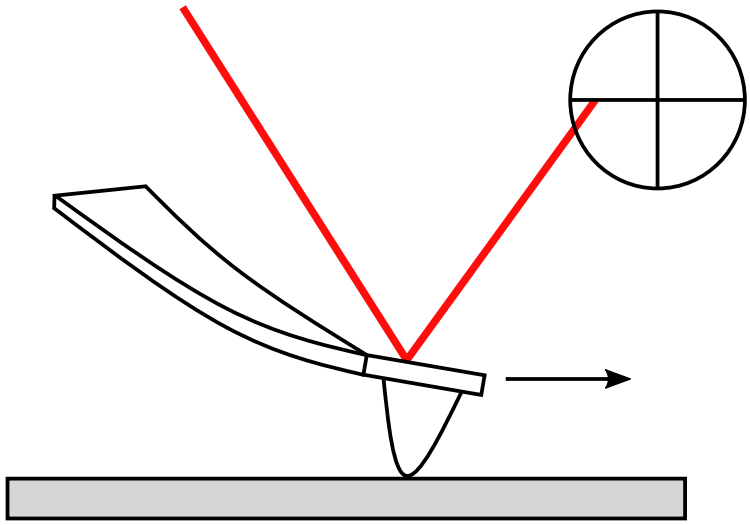

Figure 1.16: Diagram showing principle of cantilever torsion behind FFM.

Conventional height imaging is performed by setting the fast-scan axis parallel to the long side of the cantilever. However, in friction force microscopy (FFM) data is collected while scanning perpendicular to the direction of the cantilever (90° compared to imaging[146]), causing the probe to bend side to side (see Figure 1.16). Thus, the reflected laser spot moves laterally which is recorded alongside the vertical deflection in two separate channels: trace is the forward scan line, while retrace refers to the line recorded in the backwards direction over the same path. The topography of the surface has an effect on the measured friction force. Upwards and downwards slopes increase and decrease, respectively, the torsion experienced by the AFM cantilever. It is therefore important to deconvolute friction forces from topographical effects by subtraction of the trace and retrace signals.[147,148]

In the case of a perfectly flat surface, the lateral signal observed is directly linked to the friction forces due to changes in intermolecular forces or other factors, with trace and retrace signals being mirrored across positive and negative photodetector voltages. In reality, the lateral signal is no longer solely affected by interfacial interactions, as the topography causes trace and retrace signals to be affected by equal amounts instead of

being reversed (Figure 1.17). By subtracting trace from retrace signals (for the same scan lines), the topographical contribution is greatly diminished, and the resulting value is double the desired friction.

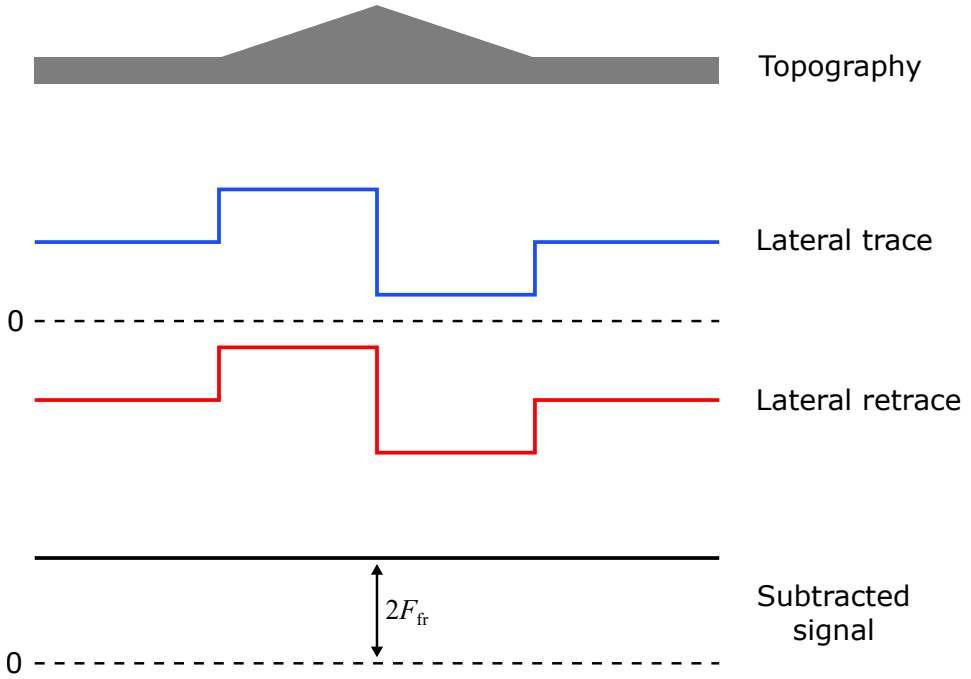

Figure 1.17: Contribution from topography on trace and retrace signals and its neutralization by subtraction of the two.

Friction-load plots can then be created through the collection of friction loops at various applied loads, providing information on the dependence of friction forces on the compressive—or tensile—load, as predicted by contact mechanical models. However, calibration is required in order to determine the conversion factor of lateral photodetector voltage into newtons, which is unique to each cantilever. Further details on this procedure is given in the following section.

1.4.5 Calibration of Forces

Due to the variable physical properties of different AFM probes, and the fact that signals are recorded in volts from the photodetector, calibration of these parameters is essential for quantitative experiments. The procedures used in this study for calibration and their underlying theoretical basis are presented in the following paragraphs.

Normal Forces

The force required to move a spring by a given distance is provided by Hooke's law, Eq. 1.43, which also requires knowledge of the spring's characteristic constant, k. In an AFM experiment, particularly a force spectroscopy measurement, neither the spring constant nor the vertical deflection (in units of distance) of the cantilever are known from the outset. The former is usually determined from the thermal fluctuations of the cantilever at room temperature using the method developed by Hutter and Bechhoeffer.[149] The deflection is converted into distance units from the photodetector voltage via the use of a conversion factor commonly referred to as the *normal deflection sensitivity*, which relates the photodetector response to the z-piezo displacement. This deflection sensitivity is derived from a force curve obtained on flat surface of much greater stiffness than that of the AFM probe, and as such mica sheets are frequently used.[150] If the stiffness of the tip and sample are comparable, it is impossible to definitively separate the deformations of the cantilever and flat surface. Therefore, if the flat surface is considerably stiffer, the magnitude of the z-piezo movement can be assumed to be equal to that of the cantilever deflection, and thus the recorded photodetector voltage corresponds linearly to the deflection of the cantilever. This linear relationship can be extracted from the gradient of the force curve, V/nm, in the repulsive regime as the tip is pressed into the surface (see Figure 1.15), and is usually used in its inverse form, nm/V. Multiplication of the deflection sensitivity and the vertical photodetector response thus gives the deflection distance required by Eq. 1.43.

Many methods exist to determine the spring constant of AFM cantilevers, such as using finite element analysis,[151,152] attaching pendulums,[153] and forced oscillations.[154] However, most of these procedures are cumbersome,[155] especially with chemically modified probes as used in this study, and therefore the thermal fluctuation technique introduced by Hutter

and Bechhoeffer in 1993 was preferred.[149] The technique is easy to use, and prone to errors between 5 – 10 % as shown by Matei et al.,[156] who also found that the variation between probes with identical quoted spring constants (by the manufacturer) could be as high as 20 %.

In the thermal fluctuation method, the cantilever is approximated as a simple harmonic oscillator with one degree of freedom, with an associated Hamiltonian containing kinetic and potential energy terms. This is possible since, for a cantilever with an assumed spring constant of 0.05 N/m, the expected thermal deflection at room temperature is expected to be in the order of 3 Å,[149] easily detectable by modern AFM instruments. According to the equipartition theorem, the thermal energy, $k_\mathrm{B}T$, is split evenly amongst both terms of the cantilever's Hamiltonian, and thus the potential energy can be written as:

$$\left\langle \tfrac{1}{2}kx^2 \right\rangle = \tfrac{1}{2}k_\mathrm{B}T \tag{1.45}$$

where x is the displacement of the oscillator/cantilever and k is its normal spring constant, k_B is the Boltzmann constant, and T the absolute temperature. A rearrangement of Eq. 1.45 leads to:

$$k = \frac{k_\mathrm{B}T}{\langle x^2 \rangle} \tag{1.46}$$

This equation suggests that by simply measuring the RMS of the cantilever oscillation one can easily calculate the spring constant, k. However, even though the cantilever's other elastic modes only contribute a negligible amount to the total fluctuation, other sources of error exist and consequently using the RMS displacement measurement is not appropriate.[149] The voltage fluctuations of the photodetector signal are recorded over time, and converted into the frequency domain via a Fourier transform, providing a power spectrum; a relationship between frequency and the power spectral density (PSD), the latter being a description of the spectral energy distribution per unit time. Thanks to Parseval's theorem, which describes the unitary nature of Fourier transforms,[157] the integral of the first mode, P, is equal to the RMS deflection in the time domain, $\left\langle x^2 \right\rangle$. Therefore, the spring constant can be calculated from the integral of the PSD at the cantilever's resonant frequency:

$$k = \frac{k_\mathrm{B}T}{P} \tag{1.47}$$

Some of the assumptions made are not fully correct, however, and other factors have also been omitted, necessitating a correction factor depending on the shape of cantilever being used. While the initial method ignores all but the resonant mode, Butt and Jaschke showed that further vibrational modes should be considered.[158] For tipless force-calibration cantilevers a factor of 0.972 is required,[156] while for V-shaped cantilevers the value was found to be closer to 0.963 by Stark et al.[159] (although more recent studies have shown it to vary between 0.93 – 0.99[160]). These correction factors have been determined with high experimental accuracy using laser Doppler vibrometry,[161] and account for other considerations such as the change in position of the laser spot on the cantilever as it deflects.[162] In practice, most modern AFM controller software allows for quick and effortless determination of the cantilever spring constant, incorporating many of the corrections in the literature and allowing users to modify parameters as needed.

Lateral Forces

As with normal forces, a conversion factor is required to obtain a friction force in newtons from the lateral photodetector signal in volts. Just as the normal spring constant, the lateral calibration factor, α_c (N/V), is unique for each cantilever used and is dependent on its shape and stiffness. There exist a multitude of different lateral stiffness calibration techniques,[163] but the one selected for use in this study is the *wedge calibration method*. It was chosen mainly due to its ease of implementation, as it requires no detailed information of the tip geometry, and has been used in numerous studies since its inception.[164] However, it is important to note that while a linear friction-load relationship is assumed by the model, this is not always reflected by reality[37,165,166] and is therefore a potential source of systematic error.

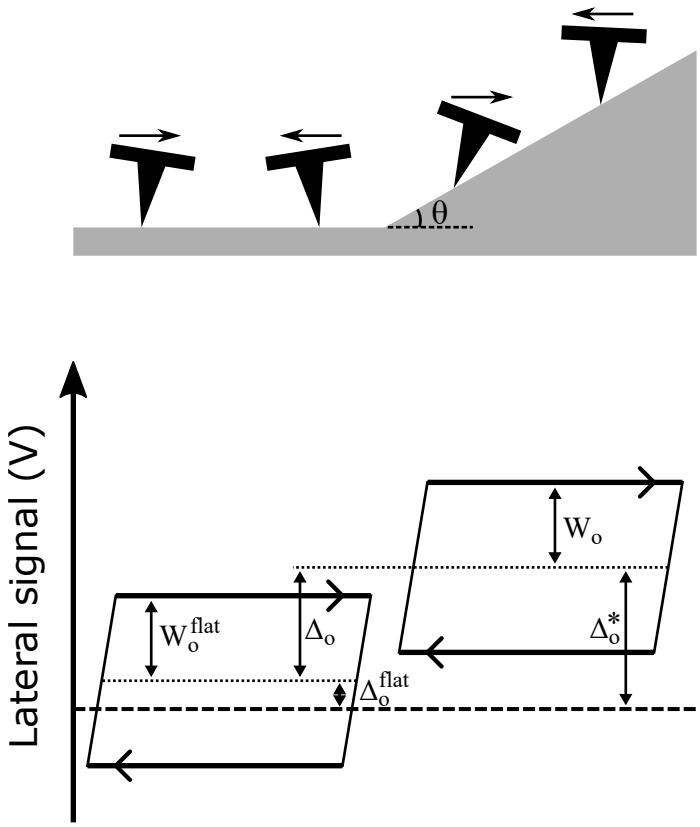

Figure 1.18: Idealized friction loops obtained on flat and sloped regions of TGF11 test grating, showing source of parameters used to calculate lateral calibration factor.

Originally developed by Ogletree et al.,[167] and improved by Varenberg et al.[168] to simplify the experimental procedure, the wedge calibration method uses the topographical effects discussed in Section 1.4.4 to obtain α_c. Using a commercially available silicon test grating, friction loops are generated across flat and angled sections of the surface, where the slope of the latter is precisely known (54.7°, between the silicon 100 and 111 planes). As the cantilever is translated horizontally across the surface of the test grating, the lateral torsion measured is dependent on the slope of the surface and the direction of travel, resulting in the force curve shown in Figure 1.18. From this information, the improvements provided by Varenberg et al.[168] allow one to amend the inaccurate measured sloped torsion offset, Δ_o^*, by subtraction of the equivalent measured torsion offset from the flat section, Δ_o^{flat}:

$$\Delta_o = \Delta_o^* - \Delta_o^{flat} \tag{1.48}$$

where Δ_o is the corrected torsion loop offset. Using the the torsion loop's half-width at the sloped facets, W_o, the load applied to the tip, L, and the adhesion of the system (obtained using force spectroscopy), A, the lateral calibration factor is given by:

$$\alpha_c = \frac{\mu(L + A\cos\theta)}{W_o(\cos^2\theta - \mu^2\sin^2\theta)} \tag{1.49}$$

where μ is the coefficient of friction for the sloped regions, and $\theta = 54.7°$. To solve for the unknown μ, the following quadratic must be solved:

$$\sin\theta(L\cos\theta + A)\mu^2 - \frac{\Delta_o}{W_o}(L + A\cos\theta)\mu + L\sin\cos\theta = 0 \tag{1.50}$$

Realistically, two solutions for μ will be obtained (a null set would occur due to poor input data or user error, while a single solution is highly improbable) from which one must be identified as the correct solution. The real solution must satisfy the condition $0 < \mu < \tan^{-1}\theta$, and if only one solution passes this test, the lateral calibration factor can be simply obtained from Eq. 1.49. If both solutions remain, then the value of μ that is closest in magnitude to that of the flat region, μ^{flat}, is the desired solution. To determine this, both possible values of α_c are obtained using Eq. 1.49 and substituted into the following equation (obtained by setting $\theta = 0$ in Eq. 1.49):

$$\mu^{flat} = \frac{\alpha_c W_o^{flat}}{L + A} \tag{1.51}$$

Whichever μ gives the lowest value for $|\mu - \mu^{flat}|$ is then used to determine the lateral calibration factor, α_c. This process should be repeated for several loads within the range of applied values used to obtain friction-load plots. Calculated values of α_c at these different loads should be compared to ensure no significant deviation exists that might indicate a non-linear torsional response by the cantilever.

1.4.6 Tip Radius Determination

Interactions between surfaces are dependent on the shape and size of the interacting media, as discussed in previous sections, and therefore knowledge of the AFM tip geometry is vital. Since the contact mode tips used in the investigation of non-polar surface contact

mechanics are assumed to have spherical apices, a method for determining the tip radius is required. All AFM images are in reality a convolution of the tip profile and surface topography,[169,170] a fact that may be exploited to reconstruct the profile of a tip by using a well-defined test structure. While many different techniques exist for the determination of the tip radius,[171] the blind tip reconstruction method is simple and cost-effective compared to using specialized equipment (e.g., SEM).

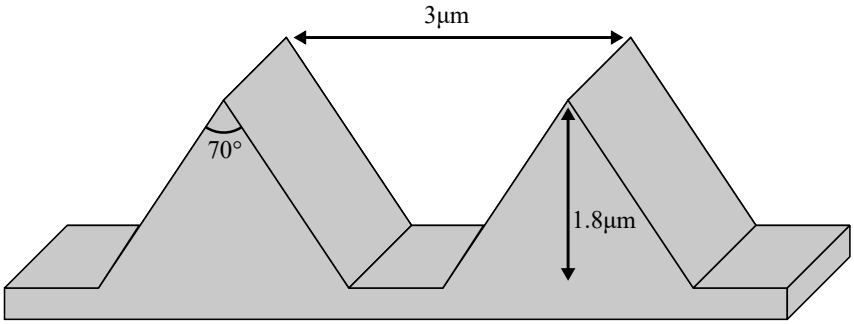

Figure 1.19: Cartoon of TGG01 test grating and a few of its features.

Many such test structures exist but the one used in this study is the TGG01 structure (MikroMasch, Sofia, Bulgaria), whose surface profile is illustrated in Figure 1.19. Use of sharp structures such as TGG01 has been shown by Martin and Wickramashinghe[172] to obtain radii with uncertainties of approximately 3 nm. Two main deconvolution models exist, the Zenhausern[169] and Garcia models,[173] the applicability of which depends on the relative size of the tip radius and feature being imaged. As the contact mode tips used in this study have significantly larger tip radii (≈ 50 nm) than those of the TGG01 test grating's feature peaks (< 10 nm), the Zenhausern model was the most appropriate to use.

Obtaining the tip radius requires the imaging of the test structure using the tip of interest, where the recorded image is a convolution of the tip geometry and test structure. This has the effect of increasing the measured topography of the test grating, as is shown diagramatically in Figure 1.20. By using the Zenhausern model, using the known radius of the (assumed) spherical feature curvature, one can then deconvolute the image and hence reconstruct the radius of curvature of the tip.

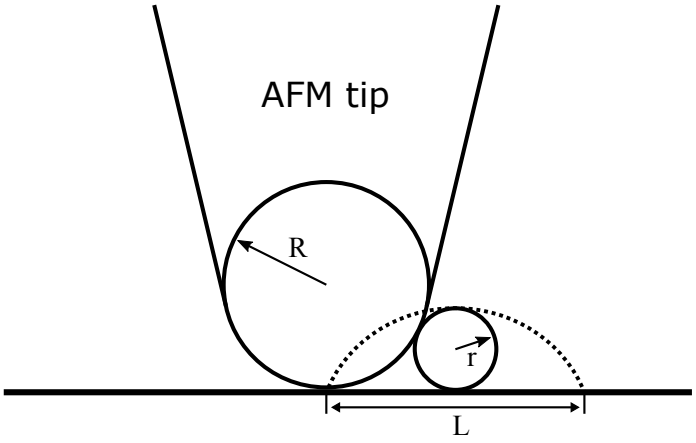

Figure 1.20: Convoluted image (dotted line, radius $L/2$) of a molecule adhered to the surface of cross-section radius r, obtained with an AFM tip with a spherical apex of radius R.

As mentioned previously, the Zenhausern model assumes that the radius of the feature imaged, r, is smaller than that of the tip used to image it, R, leading to only a contribution of the lower hemisphere of the tip on the convolution. The size of the convoluted feature, L, is then:[169]

$$L = 4(Rr)^{1/2} \tag{1.52}$$

Using commercial software, such as SPIP by Image Metrology, makes the blind reconstruction process simple to perform. The process should, however, be repeated in both scanning axes (ensuring one rotates the sample by 90° between measurements), to build a profile of the tip in more than one direction, using the geometrical mean as the final tip radius.

1.5 Self-Assembled Monolayers

Self-assembled monolayers (SAMs) have been an incredibly popular system of surface functionalization for many years, allowing for the modification of surface properties across a plethora of different substrates.[78,174–178] An extensive review on the formation and structure of SAMs was published in 1996 by Abraham Ulman,[179] with the field gaining ever increasing popularity. More recent review articles have since emerged.[180–182] Categorized

according to their head and tail groups, the former determining the substrate and the latter its chemical functionality, SAMs have found a wide variety of uses, including lubrication,[5,183] sensing,[184] as lithographic resists,[185,186] and to catalyze bulk reactions.[187] In particular, they offer an incredibly simple and cost-effective method for AFM tip functionalization, and are therefore frequently used in CFM studies.[125,130,131,150,188–190]

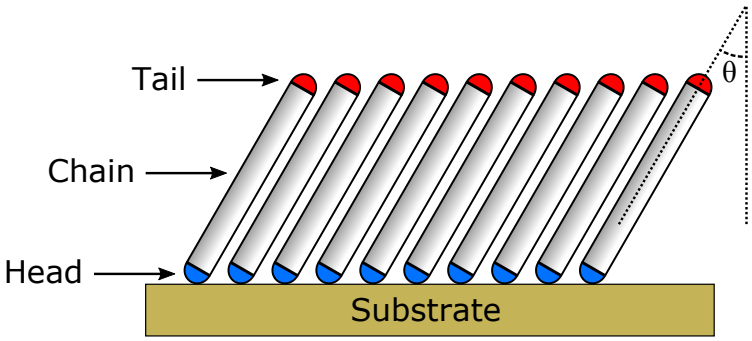

Figure 1.21: Schematic diagram of a typical self-assembled monolayer on a substrate with a tilt angle θ.

A schematic diagram of a representative self-assembled monolayer is presented in Figure 1.21 above, displaying its three main components: the head and tail groups, and a chain linking the two together (predominantly hydrocarbon). The head group is responsible for the chemisorption of the SAM to the substrate, e.g., thiol ($-$SH) on gold or silver, the strength of which depends on the relative energy of the final bond formed. The linking chain determines the bulk of the intermolecular interactions between neighboring molecules, and therefore affect the mechanical properties of the monolayer such as its elastic modulus.[179,191] Additionally, the length of the chain can have a measurable impact on various interfacial properties.[192–194] Finally, the tail group defines the chemical nature of the SAM, which can be tailored for the desired surface interactions: hydrophobic ($-CH_3$, $-CF_3$), acidic ($-$COOH), basic ($-NH_2$), etc. Provided that the tail group does not compete strongly with the head group to adsorb onto the surface, react with the head group, nor prevent packing due to steric effects, any functional group can be chosen to attach to the end of the chain.[195]

1.5.1 Thiols

By far the most common type of self-assembled monolayer are thiols on gold,[196] due to their ease of preparation and use, high lateral order (including average orientation), and in the case of alkanethiols a high resistance to hydrolysis by water.[179,195] The relative inertness of gold surfaces is a large contributor to this, allowing the physisorption of the thiol head group via intermolecular forces directly onto the (usually) Au(111) surface. The thiol is converted to a gold thiol in a reductive elimination of the hydrogen:[179]

$$\mathrm{R{-}S{-}H} + \mathrm{Au_n^0} \longrightarrow \mathrm{R{-}S^-Au^+ \cdot Au_n^0} + \tfrac{1}{2}\,\mathrm{H_2}$$

However, while molecular hydrogen has been shown to be produced in the gaseous phase in the absence of oxygen,[197–199] Hasan et al. demonstrated that the monolayer can still be formed while retaining the hydrogen–sulfur bond, albeit for relatively small (2 – 5 nm) gold clusters rather than for a planar gold surface.[200] Despite the controversy surrounding the hydrogen atom, thiol SAMs remain a solid choice for surface modification for the reasons listed above, as well as their flexibility in choice of tail group functional group. Thiol SAMs formed on crystalline Au(111) plane tend to be densely packed in a c(4×2) superlattice on top of the gold's standard $\sqrt{3} \times \sqrt{3}\mathrm{R}30^\circ$ lattice structure (see Figure 1.22).[179,201] This superlattice has unit cell dimensions four times greater than that of Au(111), with each monolayer molecule of an alkanethiol occupying a surface area of 21.4 $\mathrm{Å}^2$ on average.[202] This is greater than the cross-sectional area of an individual molecule, and is due to a tilt of each molecule by ~30° (the precise value depends on the exact composition of the monolayer) in order to maximize stabilizing intermolecular interactions between chains.[203]

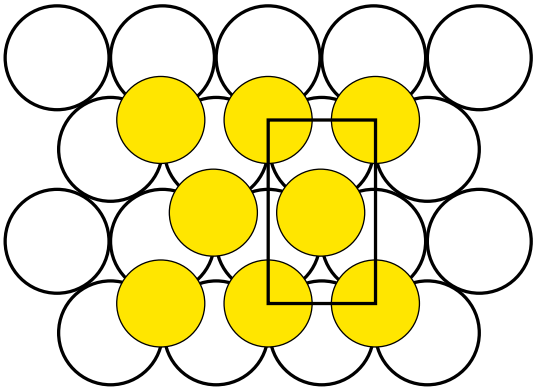

Figure 1.22: Diagram demonstrating c(4×2) superlattice (unit cell marked by rectangle) of sulfur atoms (yellow circles) on a crystalline Au(111) surface (hollow circles).

Formation of thiol SAMs is trivial in a standard laboratory, and while the quality of the final monolayer is dependent on the solvent environment[204] and surface cleanliness, it is largely independent of other factors such as temperature and concentration. Despite this, thiol monolayers tend to be sensitive to light and are prone to photooxidation in the presence of oxygen,[205] and must thus be kept in a dark oxygen-free environment and preferably used within 48 h.

1.5.2 Phosphonic Acids

Phosphonic acids adsorb onto oxide surfaces to form monolayers which, while less commonly studied than thiols and silanes,[189] offer high degrees of order and chemical stability.[206–208] Organophosphonates ($RPO(OH)_2$) have a head group phosphorus atom bonded to three oxygen atoms (two of which are hydroxyls) and a carbon attached to the rest of the chain, binding more strongly to oxide surfaces than equivalent carboxylic acid SAMs.[209] The monolayers that alkylphosphonic acids form tend to be dense and well-ordered,[206,210] and as such they have seen increased use in the fabrication of micro- and nano-devices such as digital micromirror devices, used in many optical projectors.[178,211]

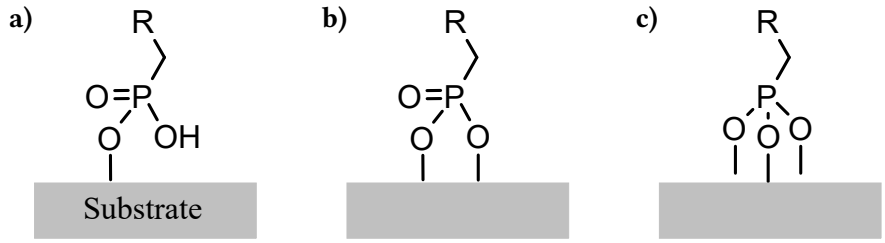

Figure 1.23: Diagram showing the different binding methods of phosphonic acids on metal oxides: **a)** monodentate **b)** bidentate and **c)** tridentate.

There are three bonding modes of phosphonic acids on metal oxides, involving the covalent bonding of one, two, or all three of the phosphonate head group as shown in Figure 1.23. DFT calculations by Luschtinetz et al. suggest that there is little effect on ordering by any particular binding mode.[212] For alkylphosphonic acids on alumina, the system used in this project, previous studies have shown that the binding on the Al_2O_3(0001) plane is predominantly bidentate. This was proposed by Thissen et al.[213] who used fourier transform infrared spectroscopy (FTIR) to detect the disappearance of the P−OH vibrational modes, which in turn likely reduces the stability of said monolayers. The tilt angle of alkylphosphonic acids is ~30° on average,[208,214] with molecular dynamics calculations predicting average tilt angles of 15° – 45° , depending on the number of *gauche* defects.[215] Formation of phosphonic acid SAMs on metal oxide surfaces follows much of the same procedure as for thiols, usually via immersion in a solution of the desired molecules.

1.5.3 Silanes

Silane SAMs made up from organosilane molecules are commonly used to modify the properties of various oxide surfaces such as glass or mica.[179,216–218] Of interest to this study are alkylsilanes, a subset of organosilanes with a general chemical formula of R−Si−R'_3 where R is the alkyl chain (with tail group) and R′ can consist of Cl (–trichlorosilane), OMe (–trimethoxysilane), OEt (–triethoxysilane), and others. While the precise mechanism of formation for silane monolayers has been the subject of much debate,[219] the overall pathway for oxide surfaces is generally well accepted. The role of water in the formation of silane SAMs has been thoroughly investigated, and it has been

shown that greater hydration at the surface can lead to higher quality monolayers.[220,221] Water, either at the surface or in solution,[222] helps hydrolize the individual head groups to $R-Si-O_3^{3-}$ (silanol). Next, the activated head groups partially cross-link to form small clusters of molecules connected by Si−O−Si bonds via condensation reactions. Finally, these aggregates react with the silanol groups on the surface through further condensation reactions, covalently bonding themselves to the surface and forming small "islands". This process continues until full surface coverage is reached (see Figure 1.24), although not all head groups may be chemically attached to the surface.

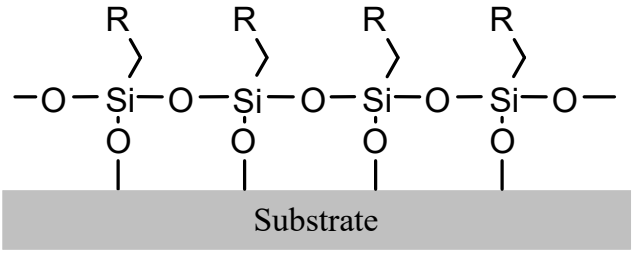

Figure 1.24: Crosslinking in silane SAMs.

As a result of the mechanism of formation, silane self-assembled monolayers tend to be of lower quality (i.e., lower order) than their thiol or phosphonic acid counterparts. However, due to their stronger bonds to the surface and the cross-linking of neighboring molecules, they display greater mechanical and thermal stability than either of the previously described monolayer types. Additionally, they are much more sensitive to the environmental conditions during their formation, and as such greater care has to be taken to select the appropriate solvent, concentration, temperature, and formation time. Just as with other monolayers, modifying the tail group allows for the modification of surface properties.

1.6 Nanolithography

Concerned with the fabrication of patterned functional structures at length-scales below 100 nm, nanolithography (derived from the Greek words *lithos* and *graphein*, meaning 'stone' and 'to write') is an important branch of nanotechnology. In the following

paragraphs a brief overview of some nanolithographic techniques will be presented, from conventional optical and particle beam methods to slightly more recent advances involving scanning probes and contact printing.

1.6.1 Photolithography

Perhaps the most common form of nanolithography, predominantly due to its pervasiveness in the ever expanding semiconductor industry, photolithography is a "conventional" form of nanofabrication.[223] It is a type of *top-down* nanolithography (where structures are formed by removing material by carving or etching) in which light is passed through a photomask to selectively expose an image onto a surface coated in a chemical photoresist. This light (of high enough energy, e.g., UV) reacts with the photoresist to either weaken (positive resist) or strengthen (negative resist) the exposed regions, eventually leaving behind the same or inverse pattern as the photomask on the surface after subsequent washing and etching. By washing away the weaker regions of photoresist with an appropriate solvent, a pattern can then be etched or deposited onto the exposed material while the remaining photoresist protects its underlying substrate from modification. A schematic of the overall process for a single photolithographic step in the fabrication of a larger (i.e., micro-scale) device can be seen in Figure 1.25.

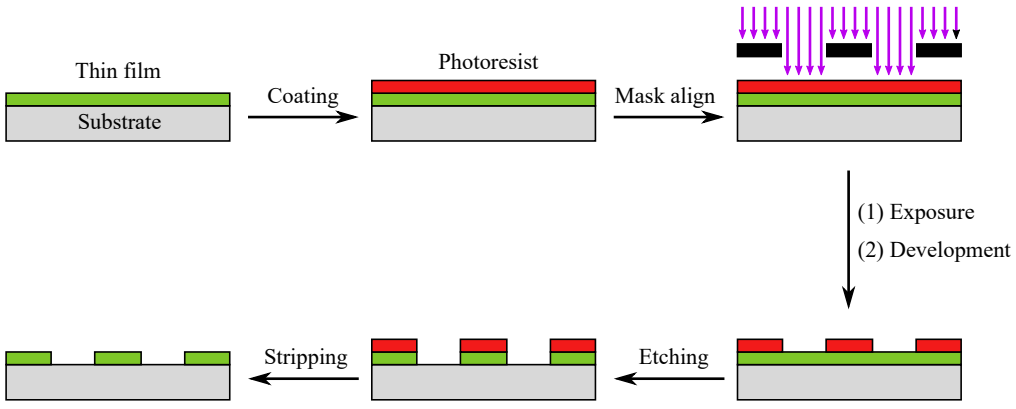

Figure 1.25: Steps followed in a sample photolithographic process. For nanoscale features to be achieved, several other processes are required (e.g., double exposures, dual tone resists, etc.) due to being diffraction-limited.

Capable of mass-producing devices with 10 nm feature sizes (as seen by the recent collaboration between Samsung and Qualcomm[224]), photolithography remains the most popular nanolithographic technique due to its higher throughput compared to others (≥275 wafers per hour for 193 nm and ≥125 for EUV[225]) by exposing the entire feature area at once. However, the significant cost associated with the equipment (e.g., the light source and photomask), as well as the time required to produce the latter have made conventional photolithography unsuitable for many applications and research groups.[223] An exception to this would be interference lithography (IL), which uses the properties of constructive and destructive interference of coherent light to generate patterned arrays,[226] with sub-10 nm resolutions having been attained.[227]

1.6.2 Charged-Particle Beam Lithography

Another "conventional" top-down technique, charged-particle beam lithography is a serial process (unlike photolithography), and therefore a much slower nanofabrication technique. As the name suggests, it consists of focussing a beam of charged-particles, such as electrons (electron-beam lithography, EBL) or ions (focussed ion beam, FIB), and scanning across the surface to expose the surface in the desired pattern. This is accomplished through the use of electrostatic or magnetic lenses to focus and move the particle beam on the surface,[228] where the particles react with a resist, e.g., poly(methyl methacrylate) (PMMA) for EBL, or actively mill the substrate through ion bombardment.[223] One of the main uses of particle beam lithography is in the production of photomasks used in optical lithography techniques, as it is capable of resolutions ≤5 nm using electron[229] or ion[230] beams. Just as with conventional photolithography, the techniques can be prohibitively expensive due to the highly specialized equipment required and the relatively slow write speeds. Additionally, the requirement of ultra-high vacuum systems increases the complexity of the process.

In recent years, traditional top-down approaches have been combined with *bottom-up* approaches (where individual atoms or molecules are used to build up the desired structure) such as self-assembly. Particle beam lithography has been used in conjunction with self-assembled monolayers—due to their ability to act as positive or negative

resists[231]—to form patterns of biological molecules such as proteins[232,233] and DNA.[234,235] Mendes et al.[236] used EBL to modify the tail group chemistry of a SAM on the surface, allowing the immobilization of gold nanoparticles onto the exposed areas.

1.6.3 Soft Lithography

Developed more recently than photolithography and particle beam lithography, the use of physical contact by elastomeric molds or stamps in transferring patterns to a surface is known collectively as *soft lithography*.[237] Such nanofabrication techniques include microcontact printing (μCP) and nanoimprint lithography (NIL) (if using a soft mold), the former employing self-assembly to "print" molecular layers onto a substrate and the latter physically deforming the surface resist.

The printing of patterns and symbols through physical contact of an ink-coated stamp with textiles or paper has been common practice for millenia, and is the basis of microcontact printing. Master stamps used in μCP are commonly produced out of poly(dimethylsiloxane) (PDMS), an optically transparent and chemically inert elastomer that conforms to the topography of the surface over large areas.[237] Rather than conventional ink, however, a solution of self-assembling molecules is coated onto the PDMS stamp, which is brought into contact with an appropriate substrate.[223] After enough time has been allowed for the ink to adsorb to the surface the stamp is removed, leaving behind a stable self-assembled monolayer in the same pattern as the master. In addition to the SAMs mentioned above, the technique has been used to successfully fabricate structures containing biological molecules,[238,239] polymers,[240–242] and magnetic compounds,[243,244] with sub-50 nm feature sizes having been achieved.[245]

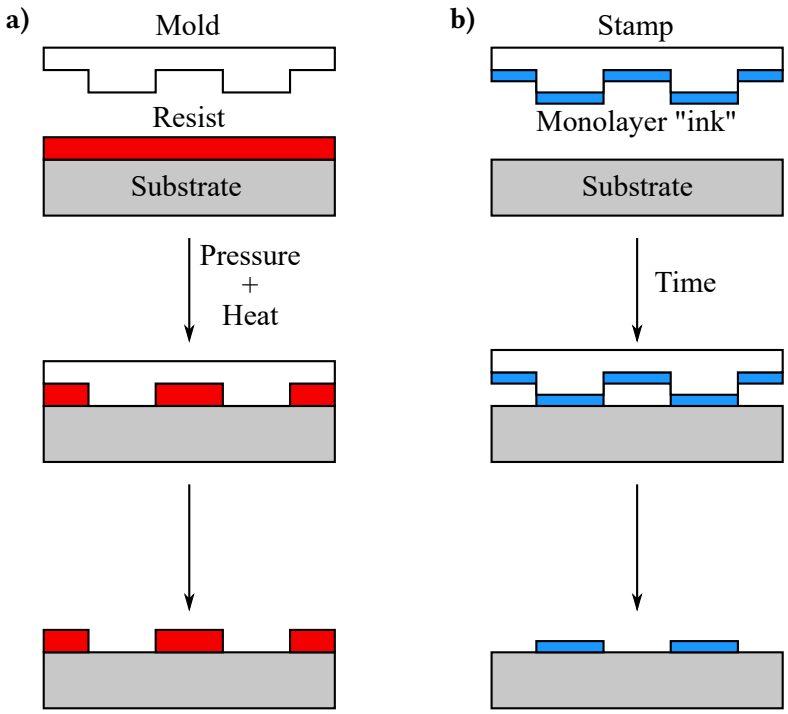

Figure 1.26: Diagrams showing the basic operating procedures of **a)** thermal NIL and **b)** μCP.

Similar to μCP, nanoimprint lithography uses a mold (made from PDMS or another elastomer to qualify as soft lithography, although silicon is common as well[223]) to deform a soft resist on the surface. The resist can then be hardened through curing with heat or light, allowing it to retain the inverse pattern of the mold when this is removed. Using soft molds structures with comparable resolutions to those achieved by nano/microcontact printing have been achieved,[246] while hard molds have enabled feature sizes an order of magnitude smaller at 5 nm.[247] In both cases, the stamps and molds can be used to manufacture copies of themselves, reducing the cost of subsequent master patterns. Notwitshstanding its ease of use and lower operational costs, soft lithography has limiting factors of its own, namely surrounding the elastomeric mold or stamp itself. The initial master has to be fabricated using other, usually conventional, nanolithographic techniques which can suppose a high upfront cost. Additionally, the mold or stamp can swell and deform in different solvent environments, fail to mold the resist completely, not contact the surface properly, or distort under high pressures,[223] all of which can negatively impact the quality of the final pattern.

1.6.4 Scanning Probe Lithography

While scanning probe techniques were originally developed for imaging purposes (discussed in further detail in Section 1.4), they have since been modified for nanofabrication and are classed under the term scanning probe lithography (SPL).[248] The exceptional control on the motion and position of probes on or near a surface afforded through SPM techniques are a large reason for this, with improvements in imaging methods being widely transferrable to fabrication, and vice versa. With STM being the first scanning probe imaging technique, it is not surprising that only a few years later the same instrumentation had been modified to produce linear features less than 20 nm apart.[249] Compared to other established techniques such as EBL, methods based off of scanning probe apparatus possess significant advantages, such as not requiring costly vacuum systems and offering greater resolutions by being inherently closer to the target surface.[248]

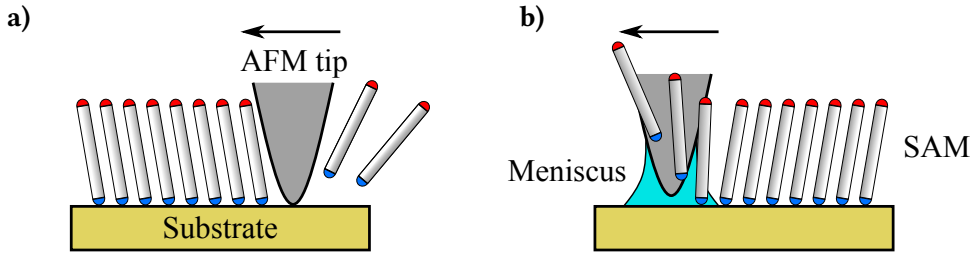

Figure 1.27: Schematic showing scanning probe lithography techniques that include **a)** removal of material through nanoshaving and **b)** monolayer deposition through dip-pen nanolithography.

Overall, there is a great variety of techniques within SPL and can be categorized by the general method of surface patterning: material removal, deposition, or modification.[250] In the former, material is removed from the surface, e.g., through shaving by physical contact of an AFM probe with the surface (nanoshaving)[120] or by thermal decomposition due to localized heating caused by an electron beam.[251] Material deposition involves the creation of surface structures by transferring atoms or molecules onto the surface, and includes techniques such as dip-pen nanolithography (DPN). Much like a conventional pen, DPN uses an AFM probe connected to a reservoir containing a solution of self-assembling molecules. As the probe is moved across the surface, the capillary action draws the “ink”

out of the reservoir and onto the surface, attaching the molecules to the substrate by self-assembly in the desired pattern.[252] Finally, the surface chemistry can be modified through electrically induced oxidation,[253,254] exposure to UV light through near-field optics,[255] using a heated probe,[256] etc.

1.7 Quantum Chemistry

Quantum chemistry is a subfield of computational chemistry with the primary focus of determining the electronic structure of atoms and molecules through the application of quantum theory.[257] Responsible for a vast amount of chemical properties and reactivities, the development of methods to accurately describe this electronic structure—for systems more complex than the hydrogen atom—has been a major goal in physics and chemistry. Numerous algorithms exist for approximately calculating many-body systems, providing valuable information to guide current or future experimental work. With the rise of computational power these tools have become increasingly popular, in which density functional theory (DFT) is among the most common. Here, the base principles behind DFT are introduced, beginning with the Schrödinger equation. Unless stated otherwise, equations will be given in atomic units. That is, electron mass (m_e), elementary charge (e), and the reduced Planck constant ($\hbar$) are all set to unity.

1.7.1 Basic Quantum Mechanics

Solving the non-relativistic Schrödinger equation is the ultimate aim in the vast majority of quantum mechanical approaches. Using the system's wavefunction $\Psi(\mathbf{r}, t)$—a description of the probability distribution of the quantum system, where $\int_{-\infty}^{\infty} \mathrm{d}\mathbf{r}\, |\Psi(\mathbf{r}, t)|^2 = 1$ for a normalized wavefunction—the time-dependent, non-relativistic Schrödinger equation is given by:

$$i\hbar \frac{\partial}{\partial t} \Psi(\mathbf{r}, t) = \hat{H} \Psi(\mathbf{r}, t) \tag{1.53}$$

where $\hbar$ is the reduced Planck constant ($h/2\pi$), and $\hat{H}$ is the Hamiltonian of the system. The Hamiltonian is an operator, which is to say that it maps one state vector, $|\psi\rangle$, into another, $|\phi\rangle$, i.e., $\hat{H}\,|\psi\rangle = |\phi\rangle$. In the case that $\hat{H}\,|\psi\rangle = a\,|\psi\rangle$, where a is a real number, then $|\psi\rangle$ is considered to be an eigenstate/function of $\hat{H}$ with an eigenvalue a.

As the ground-state of a static system is often the target for calculations, one can separate the time and spatial dependent parts of the wavefunction, giving the time-independent Schrödinger equation (TISE) in its familiar form:

$$\hat{H}\Psi(\mathbf{r}) = E\Psi(\mathbf{r}) \tag{1.54}$$

where E is the energy eigenvalue of the system. While analytically solvable for simple problems such as the hydrogen atom, the vast majority of systems necessitate approximate numerical solutions, commonly referred to as the many-body problem.

The Hamiltonian is the sum of kinetic energy, $\hat{T}$, and potential energy, $\hat{V}$, operators, which for a system containing M nuclei and N electrons can be written as:[258]

$$\begin{aligned}\hat{H} &= \hat{T}_\mathrm{e} + \hat{T}_\mathrm{n} + \hat{V}_\mathrm{ne} + \hat{V}_\mathrm{ee} + \hat{V}_\mathrm{nn} \\ &= -\frac{1}{2}\sum_{i=1}^{N}\nabla_i^2 - \frac{1}{2}\sum_{A=1}^{M}\frac{1}{m_A}\nabla_A^2 - \sum_{i=1}^{N}\sum_{A=1}^{M}\frac{Z_A}{r_{iA}} + \sum_{i=1}^{N}\sum_{j>i}^{N}\frac{1}{r_{ij}} + \sum_{A=1}^{M}\sum_{B>A}^{M}\frac{Z_A Z_B}{R_{AB}}\end{aligned} \tag{1.55}$$

where ∇^2 is equivalent to the Laplace operator (which returns the sum of second-order differentials in all cartesian axes), m is the nuclear mass, Z is the atomic number, and r_{ij}, r_{iA}, and R_{AB} are the distances between particles: electron–electron, electron–nucleus, and nucleus–nucleus, respectively. The first two terms of the Hamiltonian represent the kinetic energy while the latter three describe the electrostatic interactions between all charged particles, both attractive and repulsive.

The vast number of possible interactions can be greatly simplified by using the Born-Oppenheimer approximation. As nuclei have masses at least 1800 times larger than individual electrons, and the net momentum of a system of particles in equilibrium is zero ($\sum \mathbf{p} = 0$), the velocity of the nuclei in relation to the electrons must be reduced by an equivalent factor ($\mathbf{p} = m_\mathrm{n}\mathbf{v}_\mathrm{n} = m_\mathrm{e}\mathbf{v}_\mathrm{e}, m_\mathrm{n} \gg m_\mathrm{e}, \therefore \mathbf{v}_\mathrm{n} \ll \mathbf{v}_\mathrm{e}$). Effectively this allows for the assumption that nuclei are stationary with respect to the electrons (reducing their kinetic energy to zero), and thus the Born-Oppenheimer approximation states that as a result, the wavefunction of the system can be expressed as a product of the nuclear and electronic wavefunctions:

$$\Psi_\mathrm{total} = \Psi_\mathrm{elec} \times \Psi_\mathrm{nucl} \tag{1.56}$$

Therefore, the Hamiltonian for a group of electrons moving in the electric field of static nuclei, known as the electronic Hamiltonian, is:

$$\begin{aligned}\hat{H}_{\text{elec}} &= \hat{T} + \hat{V}_{ne} + \hat{V}_{ee} \\ &= -\frac{1}{2}\sum_{i=1}^{N}\nabla_i^2 - \sum_{i=1}^{N}\sum_{A=1}^{M}\frac{Z_A}{r_{iA}} + \sum_{i=1}^{N}\sum_{j>i}^{N}\frac{1}{r_{ij}}\end{aligned} \tag{1.57}$$

The electronic energy of the system can then be derived from the TISE, and added to the nuclear energy to give the total energy of the system:

$$\hat{H}_{\text{elec}}\Psi_{\text{elec}} = E_{\text{elec}}\Psi_{\text{elec}} \tag{1.58}$$

$$E_{\text{nucl}} = \sum_{A=1}^{M}\sum_{B>A}^{M}\frac{Z_A Z_B}{R_{AB}} \tag{1.59}$$

$$E_{\text{total}} = E_{\text{elec}} + E_{\text{nucl}} \tag{1.60}$$

The attractive potential arising between electrons and nuclei from the eigenvalue of Ψ_{elec} with $\hat{V}_{\text{ne}}$ is frequently referred to as the external potential, V_{ext}. As only the electronic problem is of interest from this point forward the "elec" subscript will be dropped in future equations, and any wavefunction is assumed to be electronic unless stated otherwise.

In quantum mechanics the expected value to be obtained through measurement for a particular property (e.g., energy) is called the *expectation value*, equal to the probability-weighted average. Using bra-ket notation, the expectation value of energy, $\langle E \rangle$, would be expressed as:

$$\langle E \rangle_\psi = \langle \psi | E | \psi \rangle = \int_{-\infty}^{\infty} \mathrm{d}\mathbf{r}\, \psi^*(\mathbf{r}) \hat{H} \psi(\mathbf{r})$$

where ψ^* is the complex conjugate of ψ.

An approach for determining the expectation value of the energy of a system from the TISE is provided by the variational principle. Since the wavefunction of a system is not an observable quantity, a guessed trial wavefunction is often used as a starting point. The variational principle states that the expectation value of the energy from any trial

wavefunction, Ψ_{trial}, is an upper bound to the true ground state energy, E_0, of the system:[258]

$$\langle E \rangle_{\Psi_{\text{trial}}} = E_{\text{trial}} \geq E_0 \tag{1.61}$$

By minimizing the energy value through testing a large amount of trial wavefunctions, the closest approximation to the true wavefunction can therefore be obtained.

Despite this, calculation of $\hat{V}_{\text{ee}}$ for many-body systems remains difficult, largely due to the Pauli exclusion principle requiring the total wavefunction to remain antisymmetric ($\Psi = -\Psi$). To reduce the possible number of wavefunctions to calculate while maintaining antisymmmetry, mean-field theories such as Hartree-Fock (HF) and density functional theory make a few assumptions. Firstly, electrons are assumed to move in an average potential field of all other electrons (hence the qualifier mean-field), greatly simplifying the necessary Hamiltonian and consequently wavefunction.[259] The next shared assumption is to use a set of Slater determinants to describe the system's wavefunction which allows antisymmetry to be maintained while avoiding the complex nature of an N-body wavefunction. These determinants can be used for any multi-fermionic system, and describe an N-electron system as:[258]

$$\Psi_0 \approx \Phi_{\text{SD}} = \frac{1}{\sqrt{N!}} \begin{vmatrix} \chi_1(\mathbf{x}_1) & \chi_2(\mathbf{x}_1) & \cdots & \chi_N(\mathbf{x}_1) \\ \chi_1(\mathbf{x}_2) & \chi_2(\mathbf{x}_2) & \cdots & \chi_N(\mathbf{x}_2) \\ \vdots & \vdots & \ddots & \vdots \\ \chi_1(\mathbf{x}_N) & \chi_2(\mathbf{x}_N) & \cdots & \chi_N(\mathbf{x}_N) \end{vmatrix} \tag{1.62}$$

where each one-electron function $\chi_i(\mathbf{x}_i)$ is called a *spin orbital*, composed of the product of a spatial orbital, $\phi_i(\mathbf{r})$, and a spin function, $\alpha(s)$ or $\beta(s)$:

$$\chi(\mathbf{x}) = \phi(\mathbf{r})\sigma(s), \quad \sigma = \alpha, \beta \tag{1.63}$$

From here the HF and DFT methods diverge, with the former concentrating on the system's total wavefunction and the latter focussing on the electron density, as its name suggests.

1.7.2 Hartree-Fock

The Hartree-Fock method seeks to determine the ground state of a system by modifying its wavefunction into a more manageable form, and then minimizing its energy using the variational principle. As a first step in HF, the Hamiltonian is separated into single- and multi-electron terms:

$$\hat{H} = \sum_{i=1} h(i) + \frac{1}{2} \sum_{i<j} v(i,j) + V_{\text{nn}} \tag{1.64}$$

$$h(i) = -\frac{1}{2}\nabla_i^2 - V_{\text{ext}}(\mathbf{x}) \tag{1.65}$$

$$v(i,j) = \frac{1}{r_{ij}} \tag{1.66}$$

where V_{nn} is a constant associated with the energy contribution due to nucleus–nucleus interactions.

The next assumption of the HF method is the use of Slater determinants to describe the system's wavefunction as a set of spin orbitals which allow it to obey the Pauli exclusion principle of antisymmetry. This greatly simplifies the number of calculations necessary during minimization compared to an N-body wavefunction, and also implicitly defines the system as a set of independent electrons moving in the electric field created by the average position of all particles. Using this information, the Hartree-Fock energy can be written as:[258]

$$E_{\text{HF}} = \sum_i \langle i|h|i\rangle + \frac{1}{2} \sum_{ij} [ii|jj] - [ij|ji] \tag{1.67}$$

with the shorthand two-electron notation expressing the integral:

$$[ij|kl] = \int \mathrm{d}\mathbf{x}_1 \, \mathrm{d}\mathbf{x}_2 \, \chi_i^*(\mathbf{x}_1)\chi_j(\mathbf{x}_1)\frac{1}{r_{12}}\chi_k^*(\mathbf{x}_2)\chi_l(\mathbf{x}_2) \tag{1.68}$$

Assuming orbitals are orthonormal, i.e., $\left\langle \chi_i \middle| \chi_j \right\rangle = \delta_{ij}$ where δ_{ij} is the Kronecker delta, the canonical orbital form of the HF equation can be attained through the use of Lagrange multipliers:[257]

$$\left[h(\mathbf{x}_1) + \sum_{j \neq i} \hat{J}_j(\mathbf{x}_1) - \sum_{j \neq i} \hat{K}_j(\mathbf{x}_1) \right] \chi_i(\mathbf{x}_1) = \epsilon_i \chi_i(\mathbf{x}_1) \tag{1.69}$$

where ϵ_i is the set of Lagrange multipliers which become orbital energy eigenvalues. $\hat{J}$ is the Coulomb integral, defining the interaction of each electron in the electronic mean-field, while $\hat{K}$ is the integral describing the exchange interaction (Pauli repulsion in the case of fermions):

$$\hat{J}_j(\mathbf{x}_1) = \int \mathrm{d}\mathbf{x}_2 \, \chi_j^*(\mathbf{x}_2) \frac{1}{r_{12}} \chi_j(\mathbf{x}_2) \tag{1.70}$$

$$\hat{K}_j(\mathbf{x}_1) = \int \mathrm{d}\mathbf{x}_2 \, \chi_j^*(\mathbf{x}_2) \frac{1}{r_{12}} \chi_i(\mathbf{x}_2) \tag{1.71}$$

A further simplification is possible when considering that $\hat{J}$ and $\hat{K}$ are identical if $i = j$. By introducing the *Fock operator*, $\hat{f}$, as:

$$\hat{f}(\mathbf{x}_1) = h(\mathbf{x}_1) + \sum_j \hat{J}_j(\mathbf{x}_1) - \hat{K}_j(\mathbf{x}_1) \tag{1.72}$$

Eq. 1.69 can now be rewritten:

$$\hat{f}(\mathbf{x}_1)\chi_i(\mathbf{x}_1) = \epsilon_i \chi_i(\mathbf{x}_1) \tag{1.73}$$

Using a basis set to represent the spin orbitals, the eigenvalue energies of the orbitals can now be attained using computational methods. However, a major disadvantage to the Hartree-Fock methods is the rapidly rising computational complexity as N increases. Referred to as the *exponential wall* by Walter Kohn in his Nobel Lecture,[260] he stated that for a system consisting of N interacting electrons, the required number of parameters to calculate, M, to minimize the energy is:

$$M = p^{3N}, \quad 3 \leq p \leq 10 \tag{1.74}$$

Therefore, in a system containing 100 electrons the value of M is $\gtrsim 10^{150}$, rising rapidly with a greater number of interacting electrons. Even with ever increasing computational power, HF methods remain time consuming. Additionally, due to the wavefunction of an N-body system being approximated by a single Slater determinant, E_{HF} will always be greater than the true ground state energy, with the difference between the two being called

the *correlation energy*:[261]

$$E_{\text{corr}} = E_0 - E_{\text{HF}} \tag{1.75}$$

1.7.3 Density Functional Theory

Closely related to the Hartree-Fock approximation described in the previous section, density functional theory uses similar self-consistent field methods to solve the TISE and determine the ground state of a desired system. The main focus of DFT is to replace the complex many-body wavefunction (a function of $3N$ variables[260]) with a less complicated description of the system's electron density. The electron density function, $\rho(\mathbf{r})$, for a system of N electrons is defined as the multiple integral of the spins of all electrons and the spatial coordinates of all but one electron:[258]

$$\rho(\mathbf{r}) = N \int \dots \int \mathrm{d}s_1 \, \mathrm{d}\mathbf{x}_2 \dots \mathrm{d}\mathbf{x}_N \, |\Psi(\mathbf{x}_1, \mathbf{x}_2, \dots, \mathbf{x}_N)|^2 \tag{1.76}$$

and must obey certain boundary conditions:

$$\rho(\mathbf{r}) \geq 0 \tag{1.77}$$

$$\rho(\mathbf{r} \to \infty) = 0 \tag{1.78}$$

$$\int \mathrm{d}\mathbf{r} \, \rho(\mathbf{r}) = N \tag{1.79}$$

The question remaining is how the ground state of a system may be described solely by the electron density, which was resolved by the Hohenberg-Kohn theorems.

Hohenberg-Kohn Theorems

The first of the theorems confirms that the basic assumption in DFT of using the electron density to determine the properties of a many-body system is physically justified. Following an elegant *reductio ad absurdum* proof, Hohenberg and Kohn showed in their influential 1964 paper that "[the external potential] $V_{\text{ext}}(\mathbf{r})$ is (to within a constant) a unique functional of $\rho(\mathbf{r})$; since, in turn, $V_{\text{ext}}(\mathbf{r})$ fixes $\hat{H}$ we see that the full many-particle ground state is a unique functional of $\rho(\mathbf{r})$".[262]

In other words, the Hamiltonian—used to determine the total energy a system—is entirely determined by the electron density and can therefore be re-stated in terms of $\rho(\mathbf{r})$:

$$\hat{H} = \hat{H}_{\text{int}} + V_{\text{ext}} \tag{1.80}$$

$$\begin{aligned} E[\rho] &= \langle \Psi | \hat{H} | \Psi \rangle \\ &= F_{\text{HK}}[\rho] + \int \mathrm{d}\mathbf{r}\, V_{\text{ext}}(\mathbf{r})\rho(\mathbf{r}) \end{aligned} \tag{1.81}$$

where $F_{\text{HK}}[\rho]$ is a functional (a mathematical operator which takes a function as an input and returns a number), valid for any number of particles and any $V_{\text{ext}}(\mathbf{r})$.[262] This universal functional is the core of density functional theory and can be applied to any system, from the humble hydrogen atom to complex macromolecules such as DNA. It includes functionals for both the kinetic energy, $T[\rho]$, and electron–electron interactions, $E_{\text{ee}}[\rho]$, the latter of which can be futher split into classical and non-classical terms:

$$F_{\text{HK}}[\rho] = T[\rho] + E_{\text{ee}}[\rho] \tag{1.82}$$

$$\begin{aligned} E_{\text{ee}}[\rho] &= J[\rho] + E_{\text{nc}}[\rho] \\ &= \frac{1}{2} \int \int \mathrm{d}\mathbf{r}_1\, \mathrm{d}\mathbf{r}_2\, \frac{\rho(\mathbf{r}_1)\rho(\mathbf{r}_2)}{r_{12}} + E_{\text{nc}}[\rho] \end{aligned} \tag{1.83}$$

where E_{nc} is the non-classical contribution to the electronic interactions, including exchange, Coulombic correlation, and self-interaction corrections.[258] This non-classical functional, in conjunction with the kinetic energy functional, is the main obstacle in DFT.

The second Hohenberg-Kohn theorem is essentially a rephrased version of the variational principle used to determine the ground state energy through the minimization of trial wavefunctions: the functional that determines the ground state energy, $F_{\text{HK}}[\rho]$, returns the lowest possible energy if and only if the input density function is the true ground state density.[258] Modifying Eq. 1.61 to reflect this for a trial density function:

$$E_0 \leq E[\rho_{\text{trial}}] \tag{1.84}$$

As with the variational principle, the energy obtained from the energy functional in Eq. 1.81 is the upper bound of the true ground state energy, which can therefore be determined through minimization of the chosen functionals. With these theorems, what remains is an explicit description of the various functionals in order to allow computer algorithms to minimize the ground state energy of a system.

Kohn-Sham Equations

While the framework provided by Hohenberg and Kohn allows for the exact solution of the TISE, it does not give the precise form of the required functionals. With this in mind, Kohn and Sham proposed in 1965 a way to compute the ground state energy of the system with great accuracy, borrowing some of the ideas in the Hartree-Fock self-consistent field method.[263] They considered a system of non-interacting reference system from which the kinetic energy could be easily computed, upon which a mean-field is then applied to determine the electron–electron interactions. Using this approach a large portion of the ground state energy is exactly obtained, leaving a relatively minor non-classical contribution to be approximated.[258]

A local potential, V_{KS}, is introduced to give the Hamiltonian of a non-interacting reference system:

$$\hat{H}_{\mathrm{KS}} = \sum_{i}^{N} \left[-\frac{1}{2}\nabla_i^2 + V_{\mathrm{KS}}(\mathbf{r}_i) \right] = \sum_{i}^{N} h(\mathbf{r}_i) \tag{1.85}$$

Using a similar approach to the HF method, the ground state wavefunction is represented by a Slater determinant, Θ_{KS}, made up of spin orbitals, φ_i. Just as in Eq. 1.73, the energy eigenvalues can be extracted using the relation:

$$h(\mathbf{r}_i)\varphi_i(\mathbf{r}_i) = \epsilon_i \varphi_i(\mathbf{r}_i) \tag{1.86}$$

In addition, the electron density can be defined in terms of the spin orbitals:

$$\rho(\mathbf{r}) = \sum_{i}^{N/2} |\varphi_i(\mathbf{r})|^2 \tag{1.87}$$

To calculate the ground state energy of the system, V_{KS} needs to be defined. By separating the functional $F[\rho]$:

$$F_{KS}[\rho] = T_{KS}[\rho] + J[\rho] + E_{XC}[\rho] \tag{1.88}$$

$$E_{XC}[\rho] \equiv (T[\rho] - T_{KS}[\rho]) + (E_{ee}[\rho] - J[\rho]) \tag{1.89}$$

$T_{KS}[\rho]$ and $J[\rho]$ can be computed exactly, and the functional $E_{XC}[\rho]$ contains all unknowns, including non-classical interactions and parts of the kinetic energy. Therefore, the local potential can be expanded into:[258]

$$V_{KS}(\mathbf{r}) = \int \mathrm{d}\mathbf{r}_2 \, \frac{\rho(\mathbf{r}_2)}{r_{12}} + V_{XC}(\mathbf{r}_1) - \sum_{A}^{M} \frac{Z_A}{r_{1A}} \tag{1.90}$$

where V_{XC} is related to E_{XC} by:

$$V_{XC} = \frac{\delta E_{XC}}{\delta \rho} \tag{1.91}$$

Once again, calculating an exact solution to the TISE would be possible if the explicit form of one of the functionals involved were known (either V_{XC} or E_{XC}), albeit for a much smaller part of the total energy. Methods for the approximation of this exchange-correlation energy have been crucial in the success of DFT, and will be the focus of the next few paragraphs.

Exchange-Correlation Functionals

Until now, exact solutions to the TISE have been presented, provided that the exact form of all terms were known. Kohn-Sham separated as much of the energy functional, $E[\rho]$, into known terms and left the elusive exchange-correlation functional, containing all unknown interactions, to be approximated. When presented with a "failure of DFT" in the literature, it should be made clear that it is not a failure of the theory itself, but a deficiency in the exchange-correlation functional. There currently exists no universal functional to accurately represent every system or property of interest, and thus the correct choice of functional is critical. For brevity's sake, the term "functional" will henceforth be used to refer to the exchange-correlation functional alone.

The simplest functional—and the basis for all approximate functionals—is the local density approximation (LDA).[258] The most successful approach is to consider the system as jellium, or a *uniform electron gas*, in which positive charges (nuclei) are evenly distributed and electrons move freely within the potential created, much like in crystalline solids. The functional in the LDA is given by:

$$E_{\mathrm{XC}}[\rho] = \int \mathrm{d}\mathbf{r}\, \epsilon_{\mathrm{XC}}(\rho(\mathbf{r})) \tag{1.92}$$

where $\epsilon_{\mathrm{XC}}(\rho(\mathbf{r}))$ is the exchange-correlation energy per particle of jellium. This can be further subdivided into individual exchange and correlation components:

$$\epsilon_{\mathrm{XC}}^{\mathrm{LDA}}(\rho(\mathbf{r})) = \epsilon_{\mathrm{X}}(\rho(\mathbf{r})) + \epsilon_{\mathrm{C}}(\rho(\mathbf{r})) \tag{1.93}$$

The exchange component has an exact solution, as originally derived by Dirac and Bloch:[264]

$$\epsilon_{\mathrm{X}} = -\frac{3}{4}\left(\frac{3\rho}{\pi}\right)^{1/3} \tag{1.94}$$

While the correlation term, ϵ_{C}, has no exact form, it can be derived from Monte-Carlo simulations.[265]

An extension of the LDA is the generalized gradient approximation (GGA), which attempts to account for the inhomogeneity of a true electronic system by introducing the gradient of the electron density, $\nabla\rho(\mathbf{r})$. Therefore, the function given by the GGA has the form:

$$E_{\mathrm{XC}}^{\mathrm{GGA}}[\rho] = \int \mathrm{d}\mathbf{r}\, \epsilon_{\mathrm{XC}}(\rho(\mathbf{r}), \nabla\rho(\mathbf{r})) \tag{1.95}$$

Unlike the LDA, however, there is no single form of GGA functional, with several different forms having been proposed These include PW91 (the first GGA functional to be useable over a range of materials),[266] PBE (most commonly used),[267] and WC (a reparameterized version of PBE).[268]

A common technique in attempting to minimize the shortcomings of each functional used is the use of so-called *hybrid functionals*, which incorporate any number of different GGA, LDA, correlation functionals, and empirical corrections. All functionals used in this study are classed as hybrid functionals. Introduced in 1993 by Axel Becke,[269] B3LYP is by

far the most commonly used functional in DFT calculations, and is expressed as:

$$E_{\mathrm{XC}}^{\mathrm{B3LYP}} = (1-a)E_{\mathrm{X}}^{\mathrm{LSDA}} + aE_{\mathrm{X}}^{\mathrm{HF}} + bE_{\mathrm{X}}^{\mathrm{B88}} + (1-c)E_{\mathrm{C}}^{\mathrm{VWN}} + cE_{\mathrm{C}}^{\mathrm{LYP}} \tag{1.96}$$

where LSDA is a modification of LDA to incorporate spin, B88 is the Becke 88 functional, LYP is a correlation functional that includes local and non-local terms, and VWN is a further correlation functional. The factors a, b, and c are constants which are chosen empirically to best approximate the system in question.

A careful choice of functional is therefore crucial in obtaining reliable results via DFT calculations, and will be different depending on the nature of the system, e.g., gas or solid. The final requirement for use of density functional theory is the choice of a valid basis set, which describes the system as a set of atomic orbitals.

Basis Sets

In order to simplify the required calculations from a set of non-linear problems into easily optimizable linear ones, the linear combination of atomic orbitals (LCAO) ansatz of the Kohn-Sham equations is applied.[258] This approach leads to the expansion of the Kohn-Sham molecular orbitals, φ_i, into a more easily digestible set of atomic orbitals:

$$\varphi_i = \sum_{\mu=1}^{L} c_{i\mu}\eta_{i\mu} \tag{1.97}$$

where L is the number of members (finite in practice) in the sets of basis functionals, $\{\eta_i\}$, and related parameters, $\{c_i\}$, the latter being the only variables. Therefore, by using a set of pre-defined basis functionals, or *basis set*, the computation has been converted into matrix equation which computer algorithms are adept at solving efficiently. Each basis functional attempts to best represent the wavefunctions of each atomic orbital, and thus it would be expected that the more complex a basis set is chosen, the more accurate the resulting calculation, albeit at an equivalent computational cost. So, just as with the choice of functional, selecting the most appropriate basis set for the system being investigated is critical in attaining chemically meaningful results.

The most prevalent form of basis functional used in quantum chemistry is the Gaussian-type orbital (GTO), largely due to the computational advantages it provides (e.g., the product of two GTOs can be linearly expanded). A base GTO takes the form (in Cartesian coordinates):[258]

$$\eta^{\mathrm{GTO}} = Nx^k y^m z^n \exp\left(-\zeta \mathbf{r}^2\right) \tag{1.98}$$

where ζ defines how diffuse the orbital is, N is a normalization factor such that $\langle \eta_\mu | \eta_\mu \rangle = 1$, and $L = k + m + n$ is used to classify the orbital as an s-function ($L = 0$), p-function ($L = 1$), d-function ($L = 2$), f-function ($L = 3$), etc. Less commonly used, but more accurate than GTOs, are Slater-type orbitals (STOs) which are expressed as:

$$\eta^{\mathrm{STO}} = N\mathbf{r}^{n-1} \exp(-\zeta \mathbf{r}) Y_{\mathrm{lm}}(\Theta, \phi) \tag{1.99}$$

in which n is the principal quantum number, and Y_{lm} describes the spherical harmonics of the angular elements of the functional. By using a linear combination of GTOs and contraction coefficients (d_τ), known as a contracted Gaussian function (CGF), the wavefunction provided by the STO can be approximated (and remain computationally cheaper):

$$\eta_\tau^{\mathrm{CGF}} = \sum_a^A d_{a\tau} \eta_a^{\mathrm{GTO}} \tag{1.100}$$

Using $A = 3$ gives a reasonable approximation to a STO, but remains unsatisfactory in describing the overall wavefunction of an atomic orbital. Instead, several of these orbitals are combined to provide so-called correlation-consistent "double zeta" or "triple zeta" basis sets (more than one CGF per atomic orbital), and split-valence (or Pople) basis sets which contain varying amounts of CGFs for core and valence orbitals.

Once the appropriate functional and basis set have been selected, DFT offers a whole host of different properties that can be calculated, such as the ground state energy, vibrational modes, spatial locations of the individual atomic orbitals, etc. Deriving a similar set of Kohn-Sham equations for the time-dependent Schrödinger equation allows for an even greater amount of molecular properties to be calculated through what is known as time-dependent DFT (TD-DFT). In particular, by exciting the optimized ground state

of a system and observing the path it takes during relaxation can provide information on the expected UV-Vis absorption spectrum,[270,271] or elucidating a proton transfer mechanism.[272]

1.8 Project Aims

Tribological phenomena are increasingly important in modern technologies, from increasing the read/write capabilities of hard drive heads to miniaturized devices in the form of MEMS and NEMS. This thesis examines two aspects of tribology on the molecular scale. First, a fundamental study is carried out on the relationship between friction and intermolecular forces for hydrocarbon surfaces. Second is an examination of the mechanochemical modification of a molecular surface.

Chapter 3 will present the results of calculations from Lifshitz theory and the Hunter model as applied to a system of non-polar SAMs. The work of adhesion and free energy of complexation is calculated for over 200 solvents located between the interacting surfaces and compared to each other, highlighting any potential shortcomings of either approach. Finally, the calculations are expanded to approximate various systems of polar monolayers.

The predicted values obtained in the previous chapter were investigated experimentally using an AFM, the results of which are found in Chapter 4. Using force spectroscopy, the work of adhesion between non-polar SAM-coated tip and sample is collected and compared to the predicted values previously obtained, for a subset of solvents. The contact mechanics of the system are further explored using friction force microscopy for the same set of solvents (obtaining a friction-load plot for each), identifying the effect of adhesion on the frictional properties. These experiments are repeated for SAMs of varying chain length and substrate.

Chapter 5 demonstrates the mechanochemical removal of the NPEOC protecting group using a sharp AFM tip. Lines are written into monolayers of the protecting group under varying conditions, their widths and depths being recorded as a function of the applied load. Through control experiments and reactions with the exposed functional groups in the exposed regions it is demonstrated that the lithographic process involves the cleavage of a specific bond. The effect of the environment is investigated, under polar and non-polar liquids and by modifying the tip-chemistry with non-polar SAMs. Finally, a short DFT study is presented, identifying possible pathways for the observed mechanochemical deprotection.

CHAPTER 2

Experimental

2.1 TToolbox

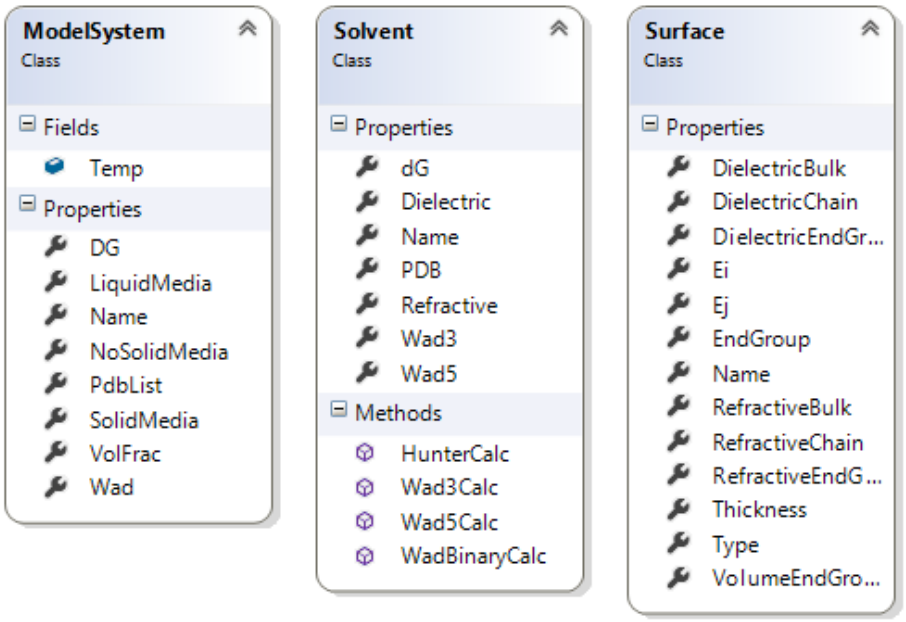

Figure 2.1: Class diagrams of three TToolbox classes responsible for the calculation of the Lifshitz work of adhesion and the free energy of complexation of the Hunter model.

Due to the need to calculate the interaction between surfaces according to both Lifshitz theory and the Hunter model, for a large number of solvents, a custom piece of software was written in C# to perform these, and was named "TToolbox" (short for Tribology Toolbox). This allowed for input parameters to be easily modified in a graphical user interface (GUI) by the user, greatly accelerating the usual workflow of calculating interfacial properties. Additionally, TToolbox was written following the object-oriented programming (OOP) paradigm, allowing for code to be modular and re-usable. Figure 2.1 shows three classes which are instantiated in order to calculate the Lifshitz work of adhesion and the free energy of complexation of the Hunter model. As a result of this modularity, TToolbox was expanded to allow for the bulk processing of atomic force microscopy files, as well as basic statistical analysis of these. MATLAB scripts were originally written for this purpose, and form the basis of the algorithms used in TToolbox.

A shared database of surfaces and solvents is used by TToolbox to perform its calculations, which is stored in a comma-separated values (CSV) file for simple access and modification. Information on where the source code for all software written by the author can be found in Appendix B.

2.2 Modelling

All modelling calculations were performed using TToolbox or MATLAB scripts and phasetransfer, in conjunction with a number of different Python scripts written by the author to aid with batch processing of data. Figure 2.2 shows the computational workflow used to calculate various interaction properties.

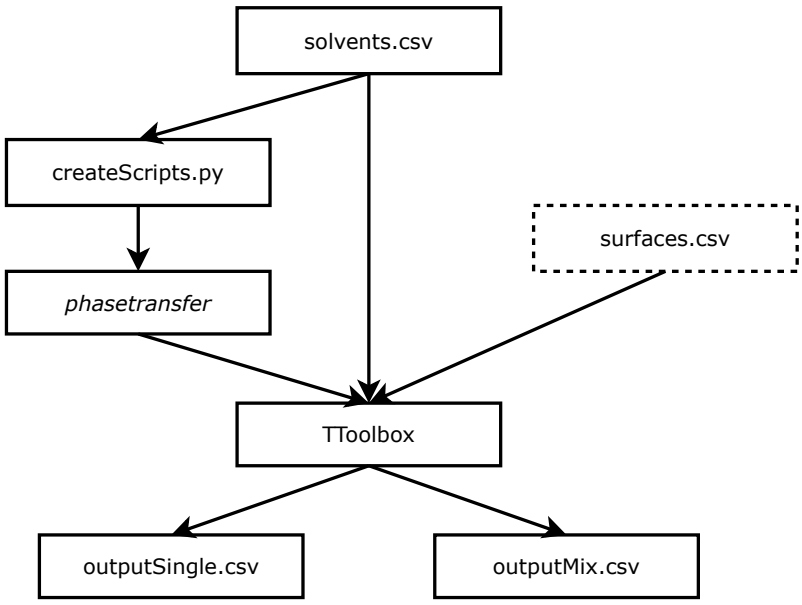

Figure 2.2: Diagram of workflow for calculations of work of adhesion and free energy of complexation using parameters found in shared databases solvents.csv and surfaces.csv. Outputs for single solvents, and binary mixtures are saved in separate files.

2.2.1 3-Medium Systems

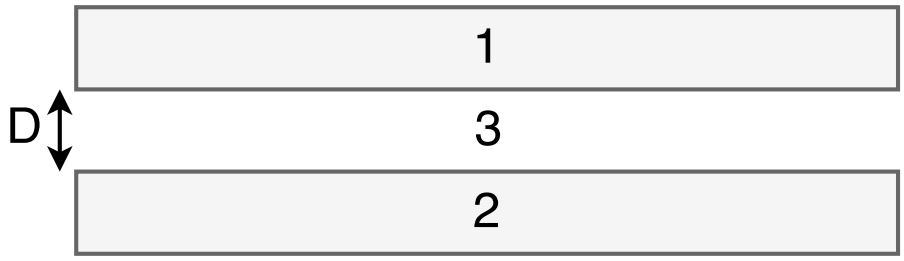

Figure 2.3: Schematic diagram showing a 3-medium system of two surfaces (1, 2) separated by a distance D, interacting through a medium (3).

To calculate the work of adhesion of a 3-medium system comprising two planar surfaces interacting through a medium at a separation D (see Figure 2.3), the Hamaker constant (a measure of the strength of the Van der Waals interaction) is calculated from the respective bulk properties using:

$$\begin{aligned} A_{132} =& A_{\nu=0} + A_{\nu>0} \\ \approx& \frac{3}{4} kT \left(\frac{\varepsilon_1 - \varepsilon_3}{\varepsilon_1 + \varepsilon_3}\right)\left(\frac{\varepsilon_2 - \varepsilon_3}{\varepsilon_2 + \varepsilon_3}\right) \\ &+ \frac{3h\nu_e}{8\sqrt{2}} \frac{(n_1^2 - n_3^2)(n_2^2 - n_3^2)}{(n_1^2 + n_3^2)^{1/2}(n_2^2 + n_3^2)^{1/2}[(n_1^2 + n_3^2)^{1/2} + (n_2^2 + n_3^2)^{1/2}]} \end{aligned} \tag{2.1}$$

where k is the Boltzmann constant ($1.3805 \times 10^{-23}\,\mathrm{J\,K^{-1}}$), T is the absolute temperature, a value of 298.15 K was used here, ε_x and n_x are the static dielectric constant and refractive index of medium x, h is the Planck constant ($6.626 \times 10^{-34}\,\mathrm{J\,s}$), and ν_e is the main electronic absorption frequency in the UV (assumed to be $3 \times 10^{15}\,\mathrm{s^{-1}}$). Once obtained, the Hamaker constant was used to calculate the work of adhesion based on the cutoff separation value D_0 of 0.165 nm based on Israelachvili's work:[6]

$$W_{\mathrm{ad}} = \frac{A}{12\pi D_0^2} = 2\gamma \tag{2.2}$$

All values were obtained using the shared surface and solvent database found in TToolbox, and all combinations of surface and solvent were calculated by TToolbox and results exported to a CSV file.

2.2.2 5-Medium Systems

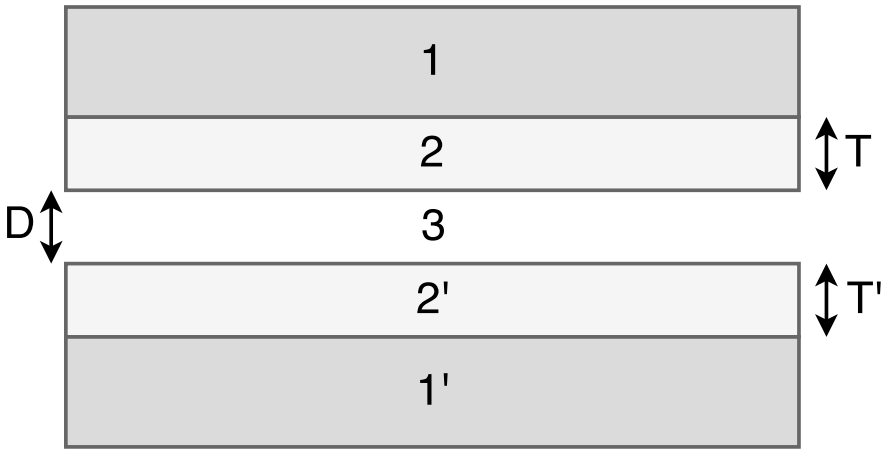

Figure 2.4: Schematic diagram showing a 5-medium system of two bulk surfaces (1, 1') with thin surface film (2, 2') of corresponding thicknesses (T, T') across a medium (3) at a separation distance D.

In order to determine the Lifshitz work of adhesion for a system consisting of two bulk surfaces, each with a thin surface film of a specific thickness, interacting across a medium at a separation D (see Figure 2.4), a slightly amended calculation is required that takes into account all the different interactions:[6]

$$F(D) = \frac{1}{6\pi}\left[\frac{A_{232'}}{D^3} - \frac{\sqrt{A_{121}A_{32'3}}}{(D+T)^3} - \frac{\sqrt{A_{1'2'1'}A_{323}}}{(D+T')^3} + \frac{\sqrt{A_{1'2'1'}A_{121}}}{(D+T+T')^3}\right] \tag{2.3}$$

where $F(D)$ is the non-retarded van der Waals force at a separation D, and all individual Hamaker constants are calculated using the method described in Section 2.2.1. In order to determine the work of adhesion, the force function was integrated over all separations:

$$W_{\text{ad}} = \int_{D_0}^{\infty} F(D)dD \tag{2.4}$$

For systems other than 1-dodecanethiol (DDT), the SAM molecule was split into two constituents — the backbone chain (bulk medium) and the end group (thin adsorbed layer). The thickness of the end group layer was calculated from the molecular volume of the closest relative molecule. The bulk properties of the bulk and adsorbed layer were therefore known, and the above calculations could be performed. For example, in the case

of 11-mercaptoundecanol (MUL) the end group and therefore thin layer was assumed to be similar to methanol and assigned the corresponding dielectric constant and refractive index, while the bulk solid was given the bulk properties of n-decane.

2.2.3 Hunter Model

The free energy of complexation for an equivalent system of interacting surfaces is obtained from the model discussed in Section 3.1.2. The surface site interaction points (SSIPs) of the non-polar surfaces were assigned hydrogen bond donor and acceptor constants, α and β, of 0.5 (corresponding to alkane solvents). These, and all other hydrogen bond parameters used in the free energy calculations were either obtained experimentally or derived from experimentally obtained parameters, α^H and β^H,[32,38] and the equations discussed in Section 1.2.5:

$$\alpha = 4.1(\alpha_2^H + 0.33) \tag{1.14}$$

$$\beta = 10.3(\beta_2^H + 0.06) \tag{1.15}$$

Using these parameters it is possible to calculate the free energy of complexation between two surfaces with an even distribution of SSIPs using:

$$\Delta G^\circ = \Delta G_b + \Delta G_c - \Delta G_S(i) - \Delta G_S(j) + RT \ln c_{\max} \tag{2.5}$$

where $\Delta G_S(i)$ and $\Delta G_S(j)$ are the solvation free energies of the two sets of SSIP surfaces, $c_{\max}$ is the maximum concentration of SSIPs (300 M), ΔG_c is a confinement energy term to account for an overestimation of the net free energy, and ΔG_b is the change in binding energy. The solvation free energies are calculated by a custom piece of software, *phasetransfer*, written by members of the Hunter group. As *phasetransfer* was written to run on UNIX based systems, a virtual machine (VM) running Ubuntu Linux was set up to run all the calculations, using a shared folder to transfer data between guest and host. A script was written in Python to generate all the run commands required to run all combinations of surface and solvent through *phasetransfer*. Finally, the confinement and

binding energies were obtained using TToolbox, using:

$$\Delta G_c = -2RT \ln\left(\frac{\sqrt{1+8\theta}-1}{4\theta}\right) \tag{2.6}$$

$$\Delta G_b = 2RT \ln\left(\frac{\sqrt{1+8K\theta}-1}{4K\theta}\right) \tag{2.7}$$

$$K = \frac{K_{ii}+K_{ij}+K_{ji}+K_{jj}}{4} \tag{2.8}$$

$$K_{ij} = 0.5e^{-E_{ij}/RT} \tag{2.9}$$

$$E_{ij} = \frac{\varepsilon_i \varepsilon_j}{1+e^{-\varepsilon_i \varepsilon_j/RT}} - 5.6\,\mathrm{kJ\,mol^{-1}} \tag{2.10}$$

$$E_{ii,jj} = \varepsilon_{i,j}^2 - 5.6\,\mathrm{kJ\,mol^{-1}} \tag{2.11}$$

where θ is the fractional occupancy of the phase, and $\varepsilon_{i,j}$ are the H-bond parameters of SSIPs on surfaces i and j, equivalent to the dimensionless α and $-\beta$ parameters whose product is normalized to give an energy in $\mathrm{kJ\,mol^{-1}}$. Using all these results, TToolbox calculated the final free energy of complexation for the different systems of interest. Results were normalized by subtraction from $RT \ln c_{\max}$ to give a positive correlation between calculated values and interaction between surfaces.

2.2.4 Binary Mixtures

The free energy of complexation for binary mixtures was calculated in the same manner as for pure liquids, but specifying which liquids were to be mixed and in what proportion in the *phasetransfer* input file. All possible liquid combinations and corresponding fractions' input files were programmatically generated using a Python script. While solvent mixtures are natively possible in Hunter's model, for Lifshitz theory the bulk dielectric constant and refractive index are required.

The dielectric constant of a non-polar mixture can be calculated using the Clausius-Mosotti equation:[273]

$$\frac{\varepsilon'_m - 1}{\varepsilon'_m + 2} = \sum_i \frac{4\pi \nu_i \rho_i N_A \alpha_i}{3M_i} \tag{2.12}$$

where ε'_m is the dielectric constant of the mixture, N_A is Avogadro's number, and for each i-th component of the mixture v_i is the volume fraction, ρ_i is the mass density, α_i is the electric polarizability, and M_i is the molecular weight. The values of these parameters can be obtained from literature,[274] but has been found to cause a mostly linear relationship in the dielectric constant of mixtures with one or two non-polar liquids.[275] For mixtures between two polar solvents, a linear relation for the dielectric constant was shown to give average deviations of up to 5 % at 25 °C.[276] As such, a linear relation was assumed when determining the dielectric constant of the resulting mixtures. For the refractive index, the Lorentz-Lorenz mixing rule was used, as it has been previously shown to give average percentage deviations below 2 % for binary systems of mixtures of several types of liquids:[277,278]

$$\frac{n_{12}^2 - 1}{n_{12}^2 + 2} = \phi_1 \frac{n_1^2 - 1}{n_1^2 + 2} + \phi_2 \frac{n_2^2 - 1}{n_2^2 + 2} \tag{2.13}$$

where n_{12} is the refractive index of the mixture, n_1 and n_2 are the refractive indices of the two pure components, and ϕ_1 and ϕ_2 are the volume fractions. For mixtures of benzyl alcohol and methanol, experimentally obtained values for the refractive index of the mixture were used.[279]

2.3 Sample Preparation

All samples prepared on glass or silicon substrates were first cleaned using piranha solution, followed by immersion in Radio Corporation of America cleaning solution (RCA), in order to eliminate any source of contamination. To prepare the piranha solution, hydrogen peroxide (H_2O_2, 30 %, Sigma) and sulfuric acid (H_2SO_4, 95 %, Sigma) were mixed in a volume ratio of 30:70 (warning: piranha is a strong oxidizing agent!). RCA solution consists of a mixture of hydrogen peroxide (H_2O_2, 30 %, Sigma), ammonium hydroxide (NH_4OH, 30 %, Sigma), and deionized water in a 1:1:5 volume ratio kept at 80 °C. All glass and silicon wafers were first immersed in an aqueous solution containing the anionic surfactant sodium dodecyl sulfate ($CH_3(CH_2)_{11}OSO_3Na$, 90 %, Sigma), to remove any excess contamination that could be potentially hazardous if exposed to piranha solution, and then rinsed with deionized water. All substrates were then fully immersed in piranha solution for at least 2 h, until the generated heat had dissipated and the containers were

safe to handle. After rinsing with large amounts of deionized water, the substrates were immersed in boiling RCA solution for 30 minutes. After further thorough rinsing with deionized water, the substrates were kept overnight in a clean oven at ca. 120 °C to dry.

2.3.1 Thiol SAMs

Self-assembled monolayers of 1-dodecanethiol ($CH_3(CH_2)_{11}SH$, ≥98 %, Sigma) and 1-octadecanethiol ($CH_3(CH_2)_{17}SH$, 98 %, Sigma) were formed on gold-coated glass slides. These slides were prepared using an Edwards Auto 306 thermal evaporator with bell jar and diffusion pump to reach an operating pressure of 10^{-6} mbar. Gold wire (Au, 99.999 %, Goodfellow metals) and chromium chips (Cr, 99.5 %, Sigma) were placed in 40 A Mo boats and 20 A W baskets (Agar Scientific), respectively, and were resistively heated to allow for thermal evaporation onto pre-cleaned glass slides (Menzel-Gläser, 22 × 50 mm, #1,5). First, a thin (10 nm) adhesive layer of chromium was evaporated onto the bare glass, to promote better deposition of the gold film, at a rate of 0.01 nm s^{-1}. After 15 min of cooling, a 50 nm layer of gold was deposited at a rate of 0.02 nm s^{-1}. These deposition rates were chosen so as to promote the growth of polycrystalline gold films with the (111) crystal plane exposed, preferred for thiol SAMs.[182] After preparation, the gold-coated slides were immediately rinsed with degassed HPLC grade ethanol, and placed in clean 30 mL glass vials containing 1 mM solutions of thiol dissolved in degassed HPLC grade ethanol. The vials were sealed with polyethylene stoppers, and stored at room temperature away from direct sunlight for a minimum of 24 h and a maximum of 72 h before use to prevent formation of multilayers and degradation of the SAM.

2.3.2 Phosphonic Acid SAMs

Self-assembled monolayers of n-dodecylphosphonic acid ($CH_3(CH_2)_{11}P(O)(OH)_2$, 95 %, Alfa) and n-octadecylphosphonic acid ($CH_3(CH_2)_{17}P(O)(OH)_2$, 97 %, Alfa Aesar) were formed on aluminium-coated glass slides. To prepare the slides, an Edwards 306 thermal evaporator was used to deposit a thin (10 nm) adhesive layer of chromium on clean glass slides at a rate of 0.01 nm s^{-1}. After 15 min of cooling, a 30 nm layer of aluminium (Al, 99.5 %, Goodfellow metals) was deposited at a rate of 0.03 nm s^{-1}. After cooling and removal from the evaporator, the aluminium coated slides were left exposed to the

laboratory air for 30 min to allow the native aluminium oxide layer, required for surface functionalization, to grow. Once the native oxide layer had grown, the slides were rinsed with HPLC grade ethanol, and immersed in 30 mL vials containing 1 mM solutions of phosphonic acid in degassed HPLC grade ethanol. After sealing with polyethylene stoppers, the vials were stored at room temperature for at least 24 h to ensure monolayer formation. Before use, samples were sonicated for 10 min, rinsed with fresh ethanol, and dried under a stream of N_2.

2.3.3 Silane SAMs

Self-assembled monolayers of n-dodecyltrichlorosilane ($CH_3(CH_2)_{11}SiCl_3$, 95 %, Fluorochem) and n-octadecyltrimethoxysilane ($CH_3(CH_2)_{17}Si(OCH_3)_3$, 95 %, Fluorochem) were prepared on pre-treated glass slides. Before use, all silanes were filtered and stored in clean vials filled with an inert nitrogen atmosphere. Glass slides were piranha and RCA cleaned as described in Section 2.3, ensuring the glass surface is properly hydroxylated.[280] The glass slides were immersed in 1 % by volume solution of silane in degassed dry toluene (obtained from the Grubbs dry solvent service). The slides were inserted into clean glass vials and an inert atmosphere was created by evacuating the gas within the vials and filling them with nitrogen via the use of a Schlenk line. A cannula was then used to transfer dry toluene to each sample vial. The appropriate amount of silane was inserted into each sample vial with a glass syringe, and left under nitrogen for 2 h to ensure proper monolayer formation.[281,282] After this time, the slides were rinsed with toluene, followed by sonication in pure toluene, 1:1 toluene/ethanol mixture, and pure ethanol sequentially for 10 min in each solution. Following the final sonication step, the slides were rinsed in ethanol and dried in a vacuum oven (Technico) at 120 °C for 1 h. Once cooled, the slides were stored in 30 mL vials stoppered with polyethylene lids. The silane samples were stored at room temperature and used within a month of preparation. Before use, the samples were rinsed with ethanol and dried under a stream of N_2.

2.3.4 OEG-NPEOC-APTES SAMs

SAMs of meta-heptaethyleneglycol 2-(4-nitrophenyl)ethoxycarbonyl (3-aminopropyl)triethoxysilane (m−OEG_7NPEOC-APTES or OEG-NPEOC-APTES, custom synthesis from AFChemPharm, Sheffield, UK) were prepared on pre-treated silicon wafers using the method used by Alang Ahmad et al.[283] Due to the light sensitive nature of the aminosilanes used, special precautions were taken to ensure all procedures were performed under UV-filtered light. Dry toluene was degassed for 20 min and inserted into sample tubes with an inert nitrogen atmosphere. A glass syringe was then used to inject the OEG-NPEOC-APTES to create a 1 mM solution, and the tube was sonicated for 5 min to ensure proper mixing. The samples were left inside this solution for 48 h in a dark place at room temperature, ensuring the formation of a complete monolayer of minimum roughness.[283] After this time, the slides were rinsed thoroughly in toluene, followed by sonication in pure toluene, 1:1 toluene/ethanol mixture, and pure ethanol sequentially for 10 min each. The samples were then rinsed in ethanol and placed in a vacuum oven for 120 °C for 1 h, and allowed to cool to room temperature. Once cooled, the sample tubes were wrapped in aluminum foil and stoppered with polyethylene lids. The OEG-NPEOC-APTES samples were stored at room temperature and used within two weeks of preparation. Before use, the samples were rinsed with ethanol and dried under a stream of N_2.

2.3.5 Sample Derivatization with TFAA

Surface reactions on deprotected APTES regions of the OEG-NPEOC-APTES monolayers were performed following a method slightly modified from that used by Alang Ahmad et al.[283] After being rinsed with copious amounts of HPLC grade ethanol and dried under a stream of N_2, the selectively deprotected samples were positioned into clean sample vials and placed under inert nitrogen environment via the use of a Schlenk line. The reagent mixture was prepared in a clean round bottom flask under inert conditions, where a 20 mM solution of trifluoroacetic anhydride (TFAA, >99 %, Sigma) was prepared in dry tetrahydrofuran (THF, Grubbs dry solvent system), to which twice the volume (with respect to TFAA) of trimethylamine (TEA, >99 %, Sigma) was added as a catalyst. Enough of the reaction mixture was transferred into each vial for each sample to be fully immersed,

with each vial being left under flowing nitrogen. After an immersion time of 2 h, the samples were thoroughly rinsed with ethanol and dried under a stream of N_2 and stored in a sealed clean sample vial, ready for further analysis.

2.4 AFM Probe Functionalization

AFM probes supplied by the manufacturer are stored and transported in gel packs that introduce PDMS contamination. To eliminate this contamination, the probes were cleaned before functionalization. Initially cold piranha solution was used, but this was found to cause the reflective gold film on the rear of the cantilevers to peel and cause instability in AFM measurements. Instead, probes were cleaned in a ProCleaner Plus UV/Ozone cleaner (BioForce, Salt Lake City, USA) for 30 min. After exposure to ozone, the probes were rinsed in ethanol and dried in a stream of N_2. The clean probes were then stored in petri dishes before functionalization.

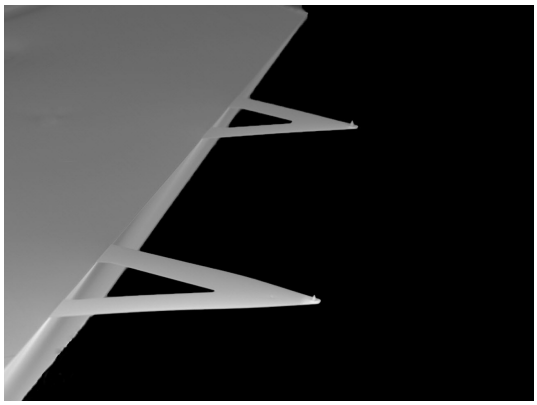

Figure 2.5: SEM image of DNP-10 cantilevers (Source: Bruker AFM Probes, 2016).

2.4.1 Thiol SAMs

Silicon nitride probes (DNP-10, Bruker AFM Probes) were functionalized by forming a self-assembled monolayer of the same thiols as in Section 2.3.1. To deposit a film of gold (Au) onto the tips of the AFM probes, an Edwards 306 thermal evaporator was used. A thin (2 nm) layer of chromium (Cr) was deposited at a rate of $0.03\,\mathrm{nm\,s^{-1}}$; a faster rate was used as a compromise between forming a better layer at a slower rate and the cantilevers bending due to prolonged thermal exposure. Once the probes had been allowed to cool

for 10 min, a 10 nm layer of gold was deposited on top of the adhesive chromium layer at a rate of 0.03 nm s^{-1}. After cooling, the cantilevers were rinsed in HPLC grade ethanol, and immersed in a 1 mM solution of 1-dodecanethiol ($CH_3(CH_2)_{11}SH$, ≥98 %, Sigma) or 1-octadecanethiol ($CH_3(CH_2)_{17}SH$, 98 %, Sigma) in degassed HPLC grade ethanol. These were left for a minimum of 24 h and a maximum of 72 h before use to prevent the formation of multilayers and degradation of the SAM. Prior to use, the functionalized probes were rinsed with ethanol, and very carefully dried under a gentle stream of N_2.

2.4.2 Phosphonic Acid SAMs

Silicon nitride probes (DNP-10, Bruker AFM Probes) were functionalized by forming a self-assembled monolayer of the same phosphonic acids as in Section 2.3.2. To deposit a film of aluminium (Al) onto the tips of the AFM probes, an Edwards 306 thermal evaporator was used. A thin (2 nm) layer of chromium (Cr) was deposited at a rate of 0.03 nm s^{-1}; a faster rate was used as a compromise between forming a better layer at a slower rate and the cantilevers bending due to prolonged thermal exposure. Once the probes had been allowed to cool for 10 min, a 10 nm layer of aluminium was deposited at a rate of 0.03 nm s^{-1}. After cooling, the cantilevers were rinsed in HPLC grade ethanol, and immersed in a 1 mM solution of n-dodecylphosphonic acid ($CH_3(CH_2)_{11}P(O)(OH)_2$, 95 %, Alfa Aesar) or n-octadecylphosphonic acid ($CH_3(CH_2)_{17}P(O)(OH)_2$, 97 %, Alfa Aesar) in degassed HPLC grade ethanol. These were left for a minimum of 24 h and a maximum of 72 h before use to prevent the formation of multilayers and degradation of the SAM. Prior to use, the functionalized probes were rinsed with ethanol, and very carefully dried under a gentle stream of N_2.

2.4.3 Silane SAMs

Silane self-assembled monolayers of the same silanes as used in Section 2.3.3 were formed on silicon nitride probes (DNP-10, Bruker AFM Probes) in order to functionalize them. AFM probes were immersed in 1 % by volume solution of silane in degassed dry toluene (obtained from the Grubbs dry solvent service). Due to the fragile nature of the AFM probes, this was not performed on a Schlenk line. After 60 min, the probes were gently rinsed in toluene, followed by a rinse in 1:1 toluene/ethanol mixture, and finally in pure

ethanol. As for the probes functionalized with thiols and phosphonic acids, exposure to prolonged high temperatures would lead to the cantilevers bending, and so the probes were not dried in a vacuum oven at 120 °C. Instead, they were dried with a gentle stream of N_2, and stored at room temperature for a maximum of two weeks before use.

2.5 Atomic And Friction Force Microscopy

A Bruker NanoScope V MultiMode 8 (Bruker UK Ltd, Coventry, UK) in conjunction with a J-scanner was used for all atomic force and friction force measurements, unless stated otherwise. For OEG-NPEOC-APTES mechanochemical removal experiments, a Digital Instruments NanoScope III MultiMode instrument (Veeco Instruments Ltd, Cambridge, UK) was used. In order to perform measurements in a liquid environment, a MTFML-V2 fluid cell (Bruker AFM Probes) was employed, using either silicone, fluorosilicone rubber, or Viton polymer O-rings depending on the suitability for the liquid being investigated. All AFM probes used for pull-off and friction force measurements had triangular silicon nitride contact mode cantilevers (DNP-10, Bruker AFM Probes) with a nominal normal spring constant of $0.12\,\mathrm{N\,m^{-1}}$. Surface roughness determination and OEG-NPEOC-APTES mechanochemical removal experiments were performed using rectangular silicon tapping mode cantilevers (OTESPA-R3, Bruker AFM Probes) with a nominal normal spring constant of $26\,\mathrm{N\,m^{-1}}$. All calibration steps were performed after all experiments had been finished, in order to prevent contamination of the tip prior to use.

2.5.1 Pull-off Force Determination

To obtain a measure of the adhesive interaction between two SAM functionalized surfaces, an AFM was used to collect force curves between functionalized sample and AFM tip. Force curves plot the vertical deflection of a cantilever against the vertical displacement of the cantilever/tip (the same as the z-piezo displacement). The retract signal is then used to determine the nature of the adhesion between sample and tip. This was achieved by using the “Ramp” mode in the NanoScope software after setting the microscope to contact mode.

Unless stated otherwise, a 500 nm scan range was used, a trigger displacement of 30 nm, and a rate of 0.5 Hz to achieve approach and retract speeds of 500 nm s^{-1} as any faster scan rates would lead to unstable readings.

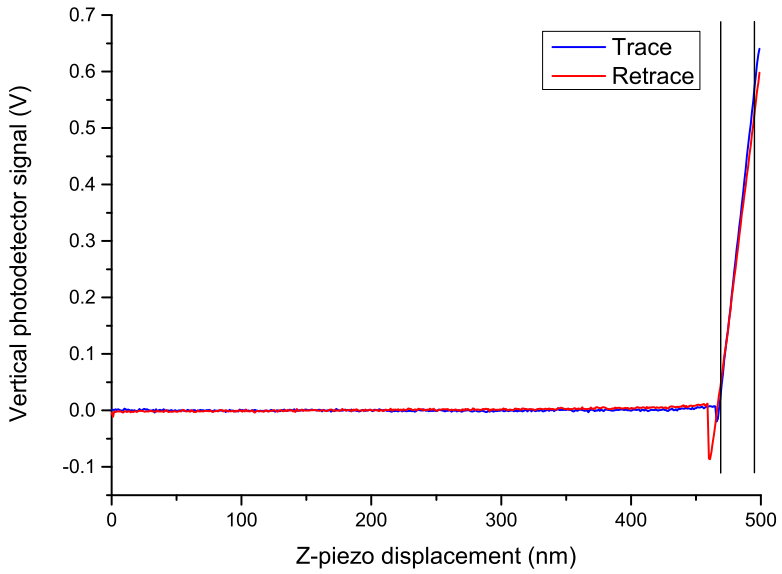

Figure 2.6: Force curve obtained with 1-dodecanethiol SAM functionalized AFM probe and sample in ethanol. The blue line shows the approach signal, while the red shows the retract signal used for determination of the pull-off force. Marked region used for calculation of photodetector deflection sensitivity.

To obtain statistically significant results, force curves were obtained at 400 locations on each sample, repeated a minimum of 3 times with different samples and probes in each liquid. The raw NanoScope force curve data files were then imported into TToolbox for analysis. This allowed for easy batch processing of force curve files with all required tip parameters for calculation of the pull-off force. The algorithm follows the same steps as Carpick's Toolbox force curve Matlab routine, but has been heavily optimized to speed up the calculations by 100x (or more, depending on number of CPU threads available).

TToolbox calculates the magnitude of the difference in the photodetector signal between the approach and retract signal in the region of negative (adhesive) signal. Using the force curve in Figure 2.6 as an example, it was found to be 0.0865 V. This is then multiplied by the photodetector deflection sensitivity and the normal spring constant to

calculate the amount of force required to separate the tip from the surface:

$$F_{\mathrm{po}} = 0.0865\,\mathrm{V} \times 0.1230\,\mathrm{N\,m^{-1}} \times 48.75\,\mathrm{nm\,V^{-1}} = 0.5187\,\mathrm{nN}$$

This calculation was be performed for each force curve, and the average pull-off for the sample was then determined.

2.5.2 Friction Force Microscopy

Friction force measurements were obtained in contact mode, with the scan angle set to 90° from the fast scan axis to create horizontal torsion of the cantilever in order to deflect the laser horizontally. Scans were performed over an area of $1 \times 0.03\,\mu\mathrm{m}$ (16 lines) and at a rate of 1 Hz ($2\,\mu\mathrm{m\,s^{-1}}$). The friction force was recorded at various applied loads in decrements of 0.6 nN, from a starting load of 10 nN until the tip was no longer in contact with the surface. A minimum of ten friction-load plots were recorded at different points of the sample. For each friction file, the absolute value of the trace-minus-retrace (TMR) signal was divided in half for each line, and the average for the entire file calculated.

An example for a particularly rough sample can be seen in Figure 2.7, where the TMR calculation eliminates any topographical dependence of the friction, as well as any sharp increases and decreases in the trace and retrace signals. As the example TMR signal shown is for a single scan line, there are exaggerated features and noise, which are reduced by determining the mean TMR for each scan file. These calculations were performed in a batch process by TToolbox, which extracted the scan parameters from the NanoScope raw data file, and using the lateral conversion factor (post-calibration) determined the friction force at each applied load. This was then exported as a CSV file in order to construct a friction-load plot to be analyzed further.

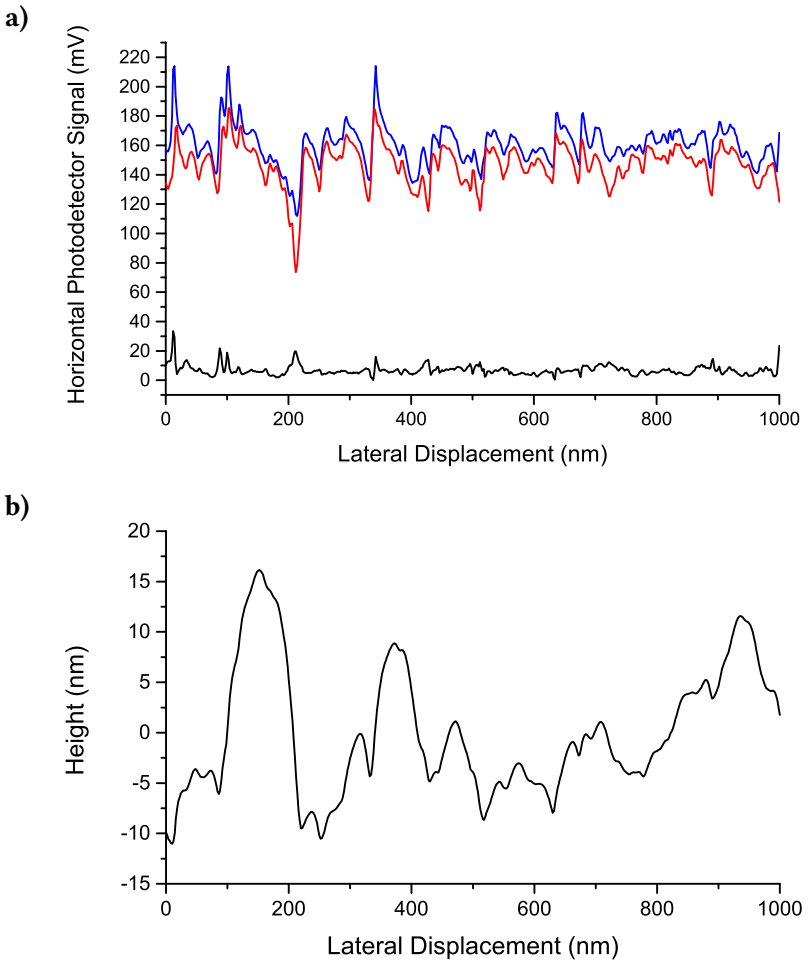

Figure 2.7: **a)** Friction loop for a probe and sample, both coated with a DDT SAM, at an applied load of 9 nN, showing trace signal in blue and retrace in red. Trace-minus-retrace (TMR) is shown in black. **b)** Topographical data acquired along the same scan line.

2.5.3 Mechanochemical NPEOC Removal

All OEG-NPEOC-APTES scratching experiments were performed on a Digital Instruments NanoScope III MultiMode instrument loaded with the nanolithography module in contact mode. To determine accurately the applied load to be used in the mechanochemical deprotection of the OEG-NPEOC-APTES layer, the normal force and deflection sensitivity were obtained as described in Section 2.5.4. Once known, the correct force to be applied

to the surface could be calculated as follows:

$$\begin{aligned}&\text{Applied force(nN)}\\&\quad = \text{spring constant}(\mathrm{N\,m^{-1}}) \times \text{deflection sensitivity}(\mathrm{nm\,V^{-1}}) \times \text{setpoint(V)}\end{aligned}$$

The correct applied force was then set by adjusting the setpoint, and the nanolithography module was activated to begin writing features using input files generated by a piece of software written by the author. Features were written at applied loads varying from $100 - 19{,}000\,\mathrm{nN}$, at write speeds varying from $0.1 - 1.000\,\mu\mathrm{m\,s^{-1}}$, and at a typical feature size of $10 \times 10\,\mu\mathrm{m}$. Following deprotection, the samples were washed with ethanol and dried in a stream of N_2, and imaged in tapping mode with a fresh tip. Originally conducted in air, this process was repeated in water and heptane. A program written by the author, AFMdraw, was used to generate scripts for use by the AFM instrument software, allowing the generation of complex patterns beyond arrays of lines using the same procedure outlined above.

2.5.4 Normal Force Calibration

In order to convert the signal observed during pull-off force measurements into a force value, the sensitivity of the photodetector as well as the spring constant of the cantilever in the normal direction are required. To determine the sensitivity of the photodetector ($\mathrm{nm\,V^{-1}}$), force curves were obtained on a freshly cleaved mica surface, with a trigger displacement of 30 nm. Due to the much greater relative stiffness of the mica compared to that of the silicon nitride or silicon cantilevers, the detected signal can be assumed to be entirely due to the deflection of the cantilever. Therefore, the displacement in nanometers of the z-piezo corresponds to the amount of deflection in the cantilever when in contact with the surface. The photodetector's sensitivity can then be obtained by calculating the inverse slope of the force curve between the trigger point and the point of contact (marked region in Figure 2.6).

The normal spring constant is obtained by the thermal noise calibration technique.[149] The equipartition allows for the spring constant to be determined by the thermal fluctuations in the root mean squared of the position of the cantilever. However, due

to factors such as laser spot position, approach angle, and cantilever shape, a correction factor is required.[161] The MultiMode 8 system used applies a correction factor, χ, of 1.09 by default, which was changed to 0.93 due to the use of triangular (V-shaped) cantilevers.[160] The resonant frequency in air of the cantilevers was measured using the MultiMode 8 thermal tuning mode, and a simple harmonic oscillator fit was then used to determine the normal spring constant of the cantilever.

2.5.5 Lateral Force Calibration

In lateral force microscopy, the lateral deflection of the cantilever gives rise to a change in the photodetector signal. This deflection is proportional to the lateral force. To determine the lateral force from the photodetector signal, a lateral conversion factor must be obtained. This was achieved using the improved wedge detection method,[168] a modified form of an earlier model,[167] but with an adjustment to account for adhesion. The method requires measurements of friction loops across flat and tilted surfaces, so a commercially available silicon test structure was used. The structure was the TGF11 grid (Mikromasch) which has a pitch of 10 µm and an edge angle of 54.74° between the (100) and (111) crystallographic planes ($\cos^{-1}(1/\sqrt{3}) = 54.74°$). All calibrations of the lateral force were performed in ethanol for consistency, as the TGF11 surface was too small for an O-ring to contain the liquid being investigated.

The friction loops required for the wedge calibration method were obtained with a scan size of 2×0.25 µm with 512 samples being recorded per slow-scan axis line, at a scan rate of 1 Hz. To check for any dependence of applied load on the lateral conversion factor, scans were obtained at applied loads of 3 nN, 6 nN, 9 nN, and 12 nN. The resulting 64 friction loops were averaged to obtain the friction loop to be used in the final lateral conversion factor calculation for each applied load. In order to calculate the adhesion between tip and surface, 100 force curves were obtained from the flat region of the TGF11 test structure and the adhesive force was calculated using TToolbox.

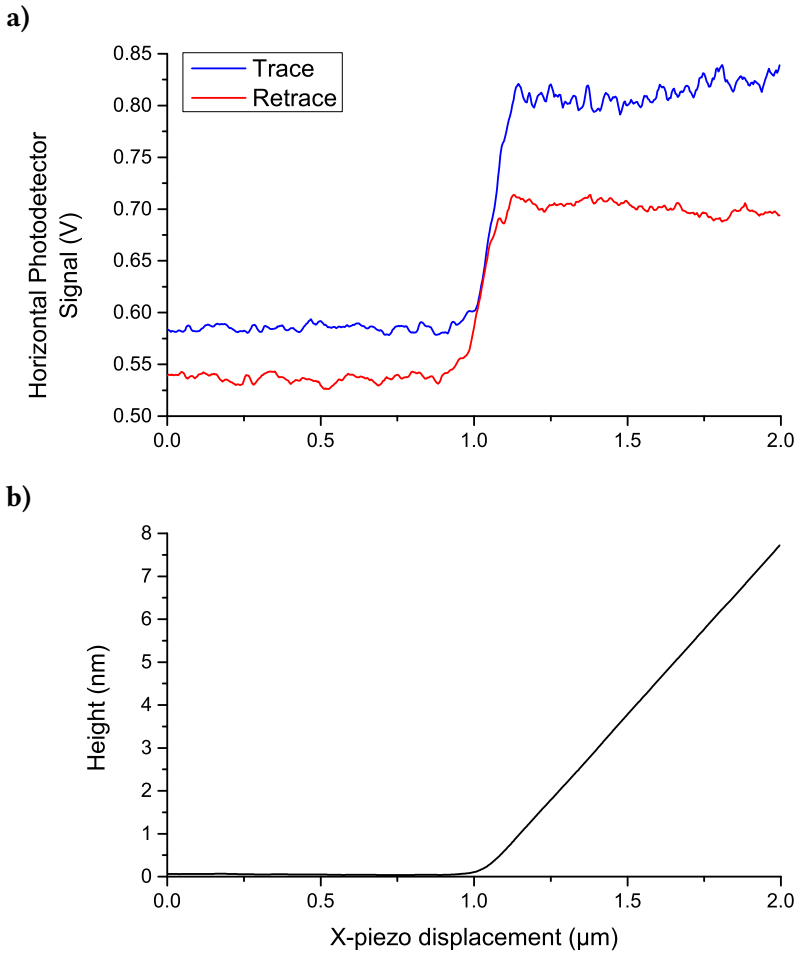

Figure 2.8: Average friction loop and topography measurements obtained on the TGF11 test structure with 1-dodecanethiol functionalized gold-coated DNP-10 probe at 12 nN applied load. **a)** Average trace (blue) and retrace (red) signal of 64 scan lines. Vertical lines are used by TToolbox user to select segments to use to calculate lateral conversion factors. **b)** Height signal average of the same 64 lines.

TToolbox is responsible for the calculation of the lateral conversion factor, α_c, allowing the user to determine which sections of the averaged friction loops to use for the calculation (in case of a slight drift from the center of the image). Using the data from the friction loop in Figure 2.8 as an example, TToolbox calculates values of W_0, Δ_0^*, and Δ_0^{flat}. From these, it calculates the solutions to the quadratic equation:

$$\sin\theta(L\cos\theta + A)\mu^2 - \left(\frac{\Delta_0^{flat} - \Delta_0^*}{W_0}\right)(L + A\cos\theta)\mu + L\sin\theta\cos\theta = 0 \tag{2.14}$$

which for this example were $\mu_1 = 7.8417$ and $\mu_2 = 0.1257$. The former result of is discarded as it has a value greater than $tan^{-1}\theta = 0.7149$, and therefore the latter result is used to calculate α_c using Eqs. 1.49 to 1.51. The lateral conversion factor for this probe was calculated to be $9.0248 \times 10^{-8}\,\mathrm{N\,V^{-1}}$.

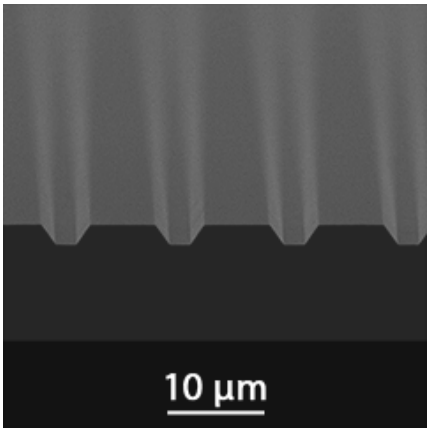

Figure 2.9: Scanning electron microscope image of TGF11 grating used in determination of lateral conversion factor, α_c (Source: MikroMasch, 2015).

2.5.6 Determination of Tip Radius

After all AFM experiments, the tip radius was determined in order to normalize the results properly. This was achieved by first imaging a well-defined grating TGG01 (Mikromasch, Sofia, Bulgaria) at 0° and 90° scan angles. This grating has well defined triangular steps with a pitch of 3 µm and apex radii of less than 10 nm, much lower than the expected radius of curvature of the AFM tips used for friction measurements. By deconvoluting the images using SPIP software by Image Metrology it was possible to determine the tip radius from the images. The deconvolution algorithm used by SPIP is based on the blind reconstruction method described by J.S. Villarubia and P.M. Williams et al.[284,285]

Images of the TGG01 grating were obtained at a scan size of 10×1.25 µm with 512 samples being recorded per slow-scan axis line, at a scan rate of 0.5 Hz. Three images were collected at different locations on the sample at an applied load of ca. 5 nN at the first scan angle. Once complete, the grating was rotated 90° and three more images were acquired at a scan angle perpendicular to the first.

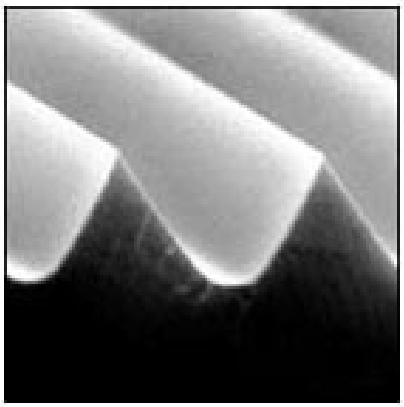

Figure 2.10: TGG01 grating used in blind-tip reconstruction to measure tip radius (Source: MikroMasch, 2014).

SPIP was then used to determine the worst case tip — the radius of the tip that would be able to scan all parts of the surface, but whose actual radius may actually be smaller. For each scan direction, the arithmetic mean radius was calculated from the three images. The final tip radius was calculated as the geometric mean of the average radius in each scan direction.

2.5.7 Surface Roughness Determination

All surface roughness measurements were performed by imaging the sample using a silicon tapping mode AFM probes (OTESPA/OTESPA-R3, Bruker AFM Probes). Topographical images were recorded at 1 Hz scan rates, with a minimum of 512 sample points per line, and scan areas between 1×1 µm and 0.5×1 µm. These were then flattened using a first-order plane fit command in the AFM analysis software to eliminate any sample tilt, as well as a first-order flatten to improve their presentation. Roughness parameters were then obtained using the AFM analysis software, namely the average roughness (R_a) and the root mean square deviation (R_q). Using the ratio of the two (R_q/R_a), it is possible to determine if the asperity height more closely resembles a Gaussian ($(\pi/2)^{1/2} \approx 1.253$) or sinusoidal ($\pi/(2\sqrt{2}) \approx 1.111$) distribution.

2.6 Supplementary Techniques

Throughout the study, several analysis techniques were used to verify the results of the experimental procedure, determine the quality of samples before use, and to help identify the appropriate basis set and functional to use for DFT calculations. A brief overview of these and their theoretical background will be provided in the following sections.

2.6.1 Contact Angle Goniometry

A simple method for determining the surface free energy of a sample is to exploit its interaction with a droplet of water. Instead of wetting the surface completely (except for extraordinarily hydrophilic systems), the equilibrium between the solid, liquid, and vapor phases will cause the water droplet to reach a stable conformation with a measurable contact angle, θ, as shown in Figure 2.11. This contact angle is dependent on the surface free energy of the solid surface, and is given by the Young equation:[286]

$$\gamma_{LG} \cos\theta = \gamma_{SG} - \gamma_{SL} \tag{2.15}$$

where γ is the surface free energy for the respective liquid–gas, solid–gas, and solid–liquid interfaces. Thus, measurement of the contact angle between different samples can be used to compare effective surface free energies, or ascertain the quality of prepared samples by ensuring θ is close to the expected value. Surfaces displaying $\theta > 90°$ are classed as hydrophobic, while systems with $\theta < 90°$ are deemed hydrophilic.

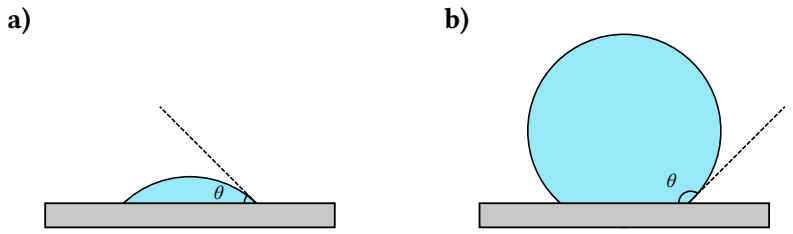

Figure 2.11: Schematic diagram of water droplets showing example contact angles for **a)** hydrophilic surfaces and **b)** hydrophobic surfaces.

Water contact angle measurements of samples and AFM probes were performed using the sessile drop technique with a ramé-hart goniometer with an attached microlite syringe. A droplet (≈1 µL) of ultrapure water (18.2 MΩ) was extruded from the syringe, and the sample stage was slowly brought upwards until full contact was made with the water droplet. The stage was then brought downwards, detaching the droplet from the syringe. The advancing water contact angle was then measured at several points along each sample. To prevent AFM probes to lift off from the stage during retraction of the stage a small amount of adhesive was used on the unfunctionalized end.

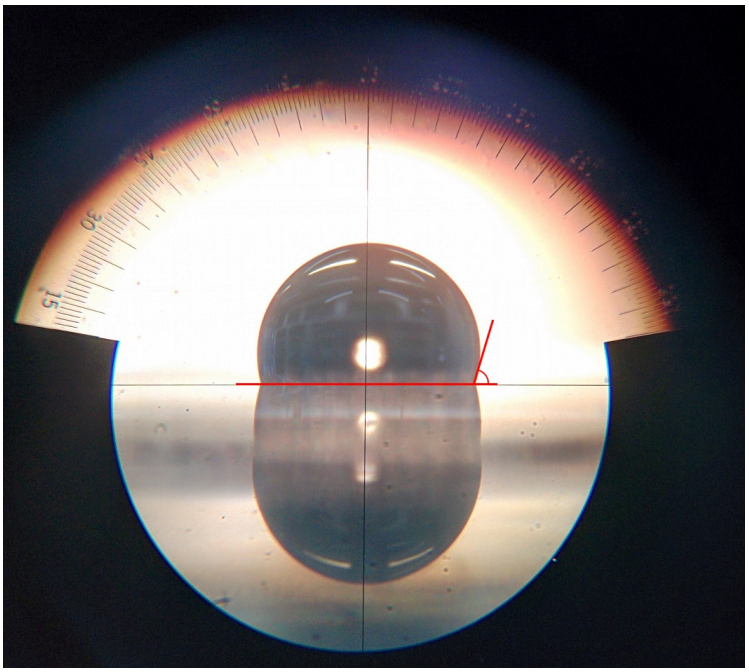

Figure 2.12: Photograph of water droplet on fresh 1-dodecanethiol sample as seen through the lens, centered at the point of contact with the surface. Image has been flipped vertically and the contact angle measured with ImageJ software to be 107°.

2.6.2 XPS

Based upon the photoelectric effect, X-ray photoelectron spectroscopy (XPS) is a powerful analytical technique capable of providing elemental and chemical information on the species existing at a given surface, up to a depth of several nanometers. It is a particularly useful surface analysis technique in being non-destructive (in most cases, some exceptions exist as in this study), and can be used for both qualitative[287] and quantitative[288,289] investigations.

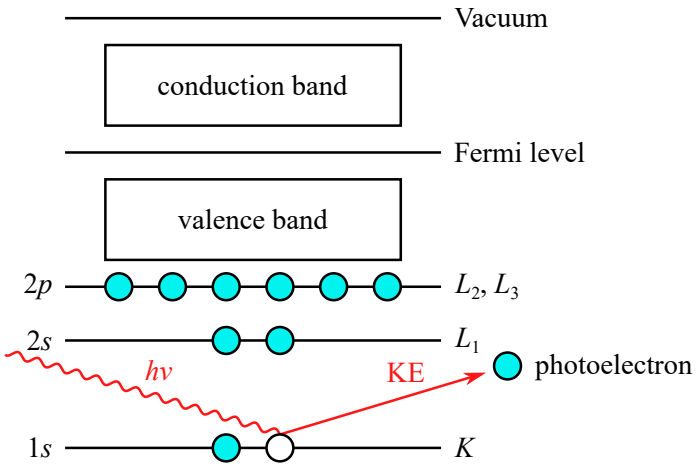

Figure 2.13: Diagram showing photoemission process in XPS.

In XPS, the surface is bombarded with low energy X-rays which lead to the ejection of electrons from atoms at the surface. If this occurs as a single photo-emission step, it is deemed to be an XPS event, but if valence electrons are ejected through a two-step process (i.e., relaxation of a higher energy electron to a lower level causing ejection of a valence electron) these are due to the Auger effect.[287] The kinetic energy of the emitted electrons is measured by the spectrometer and plotted as a function of intensity, with each element at the surface generating characteristic peaks from their "core" electrons (e.g., 1*s*, 2*s*, 2*p*, etc.). Assuming no loss of energy during or after the emission process, the binding energy (specific to the element and atomic energy level) is given by:[287]

$$\mathrm{BE} = h\nu - \mathrm{KE} - \Phi \tag{2.16}$$

where $h\nu$ is the energy of the incident x-ray photon and Φ is the work function of the spectrometer. Since all three terms on the right hand side of the equation are known, the binding energy is trivial to calculate.

While initially used for the elemental analysis of a surface, it was discovered that photoelectrons exhibited shifts in their binding energy compared to pure samples. This was attributed to atoms being in different chemical environments, and thus these "chemical shifts" provide valuable information on the chemical—in addition to elemental—composition of the surface.[287] Originally coined as electron spectroscopy for

chemical analysis (ESCA) by Siegbahn et al.,[290] the term has fallen out of favor as a description of the technique and is simply known as a subset of XPS. As these chemical shifts can be under 1 eV,[287] a properly calibrated high-resolution spectrometer is essential.

XPS measurements were performed using either a Kratos Axis Ultra DLD or a Kratos Supra (Kratos Analytical Ltd, Manchester, UK) X-ray photoelectron spectrometer using an AlK_a X-ray source and operating current and voltage of 6 mA and 10 kV, respectively. Ion pumps were used to maintain ultra-high vacuum levels of 10^{-8} mbar, and an electron flood gun helped achieve charge neutralization.

Samples were cut into 1×0.5 cm sizes, rinsed thoroughly in ethanol, and dried in a stream of N_2 before being mounted onto the instrument's integrated sample stage. Exposure times of 240 s were used for to obtain all spectra, and pass energies used for survey and narrow scans were 160 eV and 20 eV, respectively. Step sizes of 1.0 eV were used for survey spectra, while 0.1 eV steps were used for core level spectra.

XPS data were analyzed using CASA XPS (Casa Software Ltd), ensuring all data was corrected for any loss of kinetic energy due to charge build up by using the C1s peak at 285 eV. Positions and shapes of peaks were obtained from standard XPS spectra. To fit peaks in the high-resolution spectra, a linear baseline was applied before fitting intensity peaks with Gaussian-Lorentzian mixed functions.

2.6.3 SIMS

Mass spectrometry is a common analytical tool used by chemists for the better part of the last century, providing valuable information on the chemical composition of a sample through ionization and measurement of the resulting mass fragments. However, the technique is ill suited for in situ measurements of surface composition, as samples must be vaporised and therefore lose all spatial information. This problem was solved with the development of secondary ion mass spectrometry (SIMS) in the early 1960s by Castaing and Slodzian,[291] using a high-energy beam of ions to eject *secondary ions* from the surface.

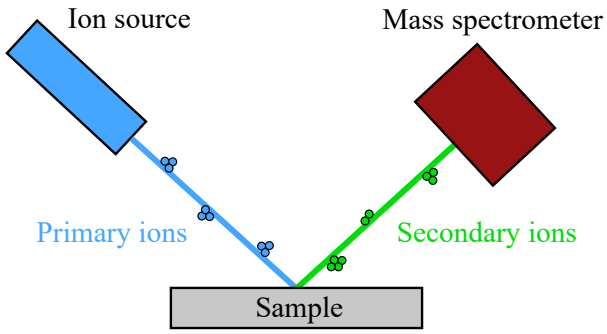

Figure 2.14: Schematic diagram of SIMS instrument.

The secondary ions emitted from the surface are captured and analysed by conventional means, e.g., by using a time-of-flight (TOF) mass spectrometer. The principle behind TOF-SIMS is remarkably simple, and uses the fact that particles possessing equal kinetic energy have velocities dependent on their mass. For a particle of mass m, its kinetic energy is given by:

$$\mathrm{KE} = \frac{1}{2}mv^2 \tag{2.17}$$

and therefore its velocity v is inversely proportional to the square root of its mass. As the particles travel across a set distance before landing on the detector, those with greater velocities will arrive at a time proportional to their mass. By then rastering the primary beam of ions across the surface, detecting the resulting mass fragments at each "pixel", an image of chemical composition can be obtained, with a full mass spectrum available at each point. The technique has seen increased use in the analysis of biological samples,[292,293] including the imaging of cells,[294] quantification of DNA components,[295] and characterization of protein films.[296,297]

SIMS measurements were performed on an ION-TOF TOF-SIMS IV (ION-TOF GmbH, Münster, Germany), with a Bi_3^{2+} focused liquid metal ion gun. Positive and negative ion spectra were obtained at energies of 50 keV, with charge compensation achieved through the use of an electron flood gun, and total ion dose never surpassing 10^{16} ions/m^2 at any time. Before mounting in the instrument's sample stage, the samples were cut into 1.5×1.0 cm portions, rinsed with ethanol, and dried in a stream of N_2. Spectra were

obtained with a 128×128 pixel raster and a field of view of $100 \times 100\,\mu m$. The resulting data were then analyzed until the ION-TOF software, ensuring any shifts in the data were calibrated using known low-mass peaks.

2.6.4 UV-Visible Spectroscopy

Ultraviolet-visible spectroscopy (or just UV-Vis) is a common form of absorption spectroscopy using the UV (>200 nm) and visible portions of the electromagnetic spectrum to probe samples, usually in solution. In UV-Vis, a monochromatic beam of photons is directed at the sample to be analysed, which causes electrons from the ground state to be excited into one of the excited state levels (e.g., $S_0 \rightarrow S_1$). This only occurs if the energy of the incident photon is equal to the difference in energy between the lower and upper energy level, which are characteristic to the elemental and chemical structure of the sample. The promotion of electrons causes photons to be absorbed, and thus the intensity of the beam is decreased as it passes through the sample solution. To determine the absorbance, A, at a given wavelength, λ, the Beer-Lambert law is used:[286]

$$A(\lambda) = \log_{10}\left(\frac{I_0(\lambda)}{I(\lambda)}\right) = \varepsilon(\lambda)cL \tag{2.18}$$

where I_0 is the intensity of the incident light, I is the intensity of the transmitted light, ε is the extinction coefficient, c is the concentration of the absorbing species, and L is the path length of the sample. By scanning through the desired range of wavelength, an absorption spectrum of the sample can be obtained.

UV-Vis spectra of OEG-NPEOC-APTES were obtained in order to identify the most suitable parameters in the DFT calculations. A 0.1 mM solution of m$-$OEG$_7$NPEOC-APTES in acetonitrile was prepared in a pre-cleaned 30 mL sample vial and wrapped in aluminum foil to avoid degradation during storage and transport. A Cary 300 UV-Vis spectrophotometer (Agilent Technologies, Santa Clara, USA) was used to collect UV-Vis spectra, using a UV-compatible cuvette (UVette, 220 – 1600 nm, Eppendorf AG, Hamburg, Germany) with a 10 mm path length. Spectra were collected between 220 – 450 nm and exported to a CSV file for processing in conventional data analysis software.

2.7 DFT

All DFT calculations were performed with Gaussian 09[298] on a supercomputer cluster. Calculations were run on 2 CPU threads, with a maximum memory limit of 3 GB. Unless stated otherwise, all calculations used the ω-B97XD functional with the 6-311++G(d,p) basis set and the added keyword "int=ultrafine". The functional and basis set were chosen based on experimental UV-Vis data obtained for OEG-NPEOC-APTES in acetonitrile, and using the parameters which most closely approximated the UV-Vis spectrum obtained. The ω-B97XD functional includes long-range corrections and empirical dispersion parameters not used in the ubiquitous B3LYP functional,[299] and the basis set includes diffuse functions for light atoms as first described by Clark et al.[300]

GaussView 5.0.8 was run via SSH to generate all COM files and submit jobs to the cluster, as well as to open completed calculations and extract the results. Ground state geometries were obtained using the "Opt+Freq" job type and "Ground State" job type, while excited state geometries and energies were obtained using "Optimization" or "Energy" job type, respectively, and "TD-SCF" method. Geometry optimizations at varying frozen bond lengths were performed using the "modredundant" keyword and "Scan" job type. Where possible, checkpoint files were saved alongside the output.

CHAPTER 3

Theoretical Approaches To Interfacial Adhesion

Calculating Adhesion Between Hydrocarbon Surfaces Using Lifshitz Theory And Hydrogen bond Thermodynamics

The strengths of van der Waals interactions between hydrocarbon surfaces have been calculated using two different approaches: Lifshitz theory, which treats the interacting bodies as continuous media, and Hunter's model, based on the thermodynamics of a system of pairwise hydrogen bonding interactions in equilibrium. These were applied to systems with different intermediate media chosen from a set of over 200 liquids, with the resulting values from either theory compared. Interactions of potential interest for further investigation using experimental methods were identified, and the possible shortcomings of each approach are discussed. In addition, the Lifshitz calculations were modified to allow for the prediction of interfacial forces between various classes of polar surfaces (acid, alcohol, amine) and contrasted against results obtained from the Hunter model.

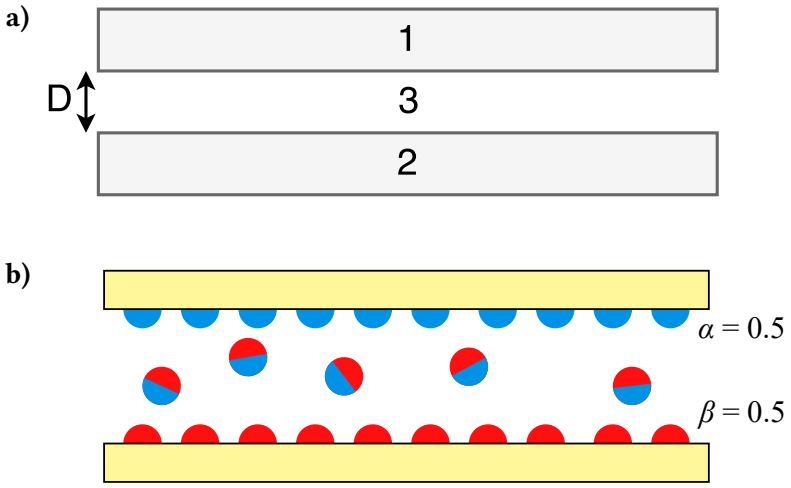

Figure 3.1: Diagram showing the 1-dodecanethiol SAM systems being analyzed by **a)** Lifshitz theory, between solid (1 and 2) and liquid (3) phases **b)** the Hunter model. Hydrogen bond acceptor (red) and donor (blue) SSIPs are evenly distributed across each surface and assigned α and β values for alkanes of 0.5.

3.1 Introduction

SAMs have been widely used to model a diversity of interfacial phenomena including wetting,[301] friction,[302] and surface charge.[303] With nanotechnology advancing at breakneck speed, applications of these SAMs have been seen in biosensors,[304] bio-antifouling coatings,[305,306] microcontact printing,[307] and as lubricants.[308] However, as these structures are further miniaturized, the surface area to volume ratio also increases

causing interactions between surfaces to become increasingly important. On small length scales there are problems with stiction, friction, and hence wear in microelectromechanical and nanoelectromechanical systems (N/MEMS).[5,309,310] This stiction arises due to capillary, van der Waals, and electrostatic adhesive forces[311,312] which, while pervasive in all surface contacts, dominate at the molecular-scale. A better understanding of these intermolecular forces and how they relate to surface interactions, especially in liquids, is therefore crucial to develop improved coatings in order to improve the performance and longevity of these micro- and nanoscale devices or materials.

The two main forces involved in surface interactions in liquids are van der Waals interactions and ionic electrostatic forces.[6] Van der Waals forces encompass all intermolecular forces (either attractive or repulsive) other than those involved with bond formation or the electrostatic interaction between ions with other molecules.[313] This includes dipole–dipole (Keesom), dipole–induced dipole (Debye), and dispersion forces (London). Other electrostatic intermolecular forces include the interactions between ions and dipoles or induced dipoles. Hydrogen bonding, the interaction between an electronegative atom and hydrogen attached to another electronegative atom, is a special case in that it is a particularly strong dipole-dipole interaction which can also be considered electrostatic in nature.[314] For this project, we are interested in the role of van der Waals interactions (especially dispersion forces) and hydrogen bonding on the adhesive energies between interacting bodies in liquids, in particular between non-polar surfaces.

The determination of the van der Waals force between surfaces using Lifshitz theory (as described in Section 1.2.3) is advantageous as it discards the need for pairwise interactions between all atoms present, and instead assumes the interacting bodies as continuous media.[6,20] Lifshitz theory has been adapted and used for many years to predict the attractive forces between molecules[315,316] and surfaces[70,317–319] in a liquid medium. More recently it has been used in experimental studies to calculate accurately the contact angles of several non-polar liquids on alkanethiol SAMs on gold.[22] Previous experiments have also demonstrated that Lifshitz theory of interactions can accurately predict the magnitude of pull-off forces in a number of different liquids.[21] However, in the same study, deviations between calculated and experimental results were found in systems with hydrogen bonding media.

3.1.1 Modification of Lifshitz Theory

While the equations described in Section 1.2.3 describe perfectly continuous interacting media, such conditions are impossible to achieve in practice. The system used to investigate the interactions between non-polar surfaces consists of a sample surface and AFM probe made up of a number of different materials, each with different dielectric properties (see Figure 3.2). There exist a few problems to solve in order to use Lifshitz theory in order to calculate the interaction between the AFM probe and the sample: what contact geometry should be assumed, will the underlying materials affect the calculations, and how will the interaction free energy be calculated?

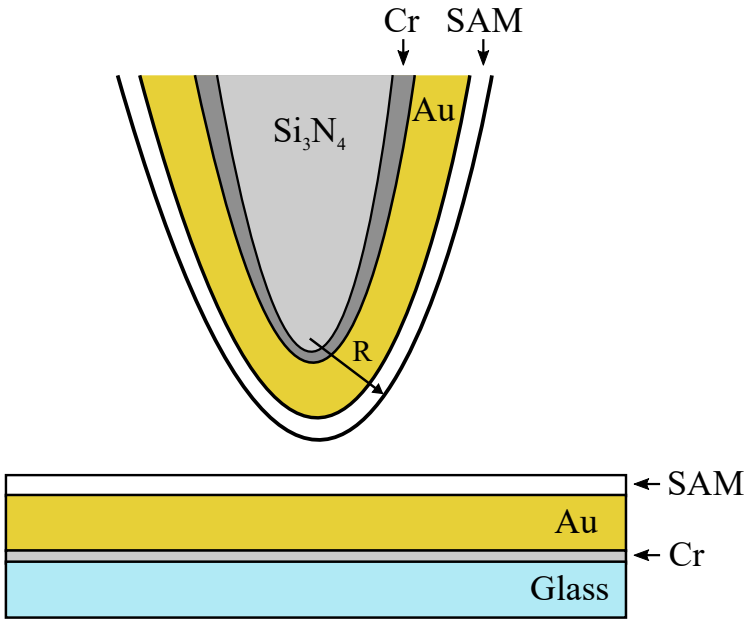

Figure 3.2: Schematic diagram of an AFM probe and glass slide coated with chrome and gold and functionalized with non-polar SAMs. Native oxide layer on AFM probe not pictured. Not to scale.

With respect to the first problem, the average shape of the AFM probes used is known to be parabaloid and can thus be assumed to have a spherical tip profile. The average tip radius is approximately 60 nm, and therefore any part of the tip beyond this spherical section is likely too distant from the sample to couple with its fluctuating electromagnetic fields.[3,6,7,142,320] Additionally, as the contact separation is expected to be in the sub-nm range, $R \gg D$ and the interaction geometry can be assumed to be similar to that of two half-spaces at close proximity, the force experienced being given by Eq. 1.7.

A lack of homogeneity in the materials of the interacting surfaces is the next consideration. The multi-layered solution of Lifshitz theory[7] suggests that the largest contribution to the dispersion force is due to interactions between the material up to a depth equal to the separation of the two surfaces. Because the thickness of DDT is $\approx$1.3 nm[321] and the separation between AFM probe and sample is assumed to reach 0.165 nm,[6] underlying layers are not expected to exert a significant influence on the interaction energy.

Finally, the Hamaker constant and interaction free energy need to be calculated. As described in Section 1.2.3, the complete absorption spectrum of each interacting medium is required to facilitate this. However the data is not easily obtainable for the large number of liquids (or even surfaces) to be investigated. Therefore, an approximated version of the exact solution developed by Jacob Israelachvili[6] can be used. In this simplified relation, the interactions are described entirely by the dielectric constants, ε, and refractive indices, n, of the materials involved. As the systems being investigated are not expected to be greatly influenced by magnetic fields (being mostly organic), ignoring the magnetic permeability of each phase should have a negligible effect on the final result.

The Hamaker constant, A_{132}, for a system of two planar bodies (1 and 2) across a third medium (3) is given as as the sum of the infinite series of allowed imaginary frequencies, ζ_n, by:[6]

$$A_{132} = \frac{3}{2} k_B T \sum_{n=0,1,\ldots}^{\infty} \left[\frac{\varepsilon_1(i\zeta_n) - \varepsilon_3(i\zeta_n)}{\varepsilon_1(i\zeta_n) + \varepsilon_3(i\zeta_n)}\right]\left[\frac{\varepsilon_2(i\zeta_n) - \varepsilon_3(i\zeta_n)}{\varepsilon_2(i\zeta_n) + \varepsilon_3(i\zeta_n)}\right] \tag{3.1}$$

The first term in the series expansion is sometimes called the "zero frequency contribution", and includes interactions due to dipoles (Keesom and Debye). The remaining frequency terms can be combined into an integral (due to each step being much smaller than a typical absorption frequency) and expressed in a single term, describing the interactions due to London dispersion forces:

$$\begin{aligned} A_{132} \approx & \frac{3}{4} k_B T \left(\frac{\varepsilon_1 - \varepsilon_3}{\varepsilon_1 + \varepsilon_3}\right)\left(\frac{\varepsilon_2 - \varepsilon_3}{\varepsilon_2 + \varepsilon_3}\right) \\ & + \frac{3h}{4\pi} \int_{\zeta_1}^{\infty} \left(\frac{\varepsilon_1(i\zeta_n) - \varepsilon_3(i\zeta_n)}{\varepsilon_1(i\zeta_n) + \varepsilon_3(i\zeta_n)}\right)\left(\frac{\varepsilon_2(i\zeta_n) - \varepsilon_3(i\zeta_n)}{\varepsilon_2(i\zeta_n) + \varepsilon_3(i\zeta_n)}\right) d\zeta \end{aligned} \tag{3.2}$$

While not an exact formula, the excluded terms are generally insignificant, contributing less than 5 %.[6] Since $\zeta_1 \approx 4 \times 10^{13}\,\mathrm{s}^{-1}$, the dispersion energy can be said to be purely affected by electronic absorption processes. Thus, by expressing $\varepsilon(i\zeta)$ in the form:[322]

$$\varepsilon(i\zeta) = 1 + \frac{(n^2 - 1)}{1 + \zeta^2/\nu_e} \tag{3.3}$$

and substituting into Eq. 3.2, one can solve the definite integral to arrive at the final form of the approximated Hamaker constant:[6]

$$\begin{aligned} A_{132} =& A_{\nu=0} + A_{\nu>0} \\ \approx& \frac{3}{4} k_\mathrm{B} T \left(\frac{\varepsilon_1 - \varepsilon_3}{\varepsilon_1 + \varepsilon_3}\right)\left(\frac{\varepsilon_2 - \varepsilon_3}{\varepsilon_2 + \varepsilon_3}\right) \\ &+ \frac{3h\nu_e}{8\sqrt{2}} \frac{(n_1^2 - n_3^2)(n_2^2 - n_3^2)}{(n_1^2 + n_3^2)^{1/2}(n_2^2 + n_3^2)^{1/2}[(n_1^2 + n_3^2)^{1/2} + (n_2^2 + n_3^2)^{1/2}]} \end{aligned} \tag{3.4}$$

where k_B is the Boltzmann constant ($1.3805 \times 10^{-23}\,\mathrm{J\,K^{-1}}$), T is the absolute temperature (298.15 K was used), ε_x and n_x are the static dielectric constant and refractive index of medium x, h is the Planck constant ($6.626 \times 10^{-34}\,\mathrm{J\,s}$), and ν_e is the main electronic absorption frequency in the UV (assumed to be $3 \times 10^{15}\,\mathrm{s}^{-1}$).

3.1.2 Surface Site Interaction Model

Hunter's model of solvation thermodynamics[32] has been shown to give accurate predictions for the pairwise interactions between molecules in solution.[34,35,40] It assumes the dominant interactions between molecules are those between the maxima and minima on the MEPS, with specific interaction parameters for hydrogen bond donors and acceptors. The equilibrium between solute and solvent associations can then be calculated using Eq. 1.16. The interactions between hydrogen bonding surfaces in various media have been previously investigated,[37,41,190] and have been found to be remarkably well described by the Hunter model. However, its exclusion of dispersion forces has been shown to limit the accuracy of prediction of binding in certain supramolecular systems,[323,324] and could potentially lead to its being a poor predictor of the interactions between non-polar

surfaces, where dispersion forces are expected to dominate. Hunter has recently developed a new model[42] which incorporates dispersion forces and introduces surface site interaction points (SSIPs) on each interacting molecule.

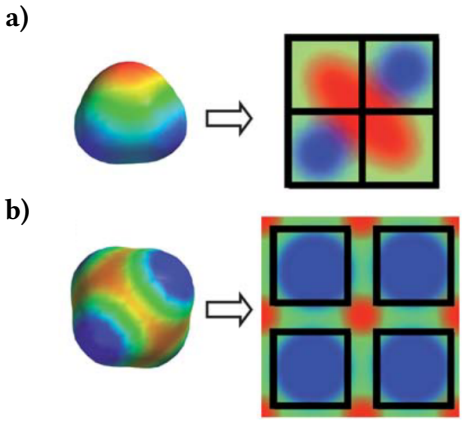

Figure 3.3: Demonstration of how the MEPS of **a)** water and **b)** methane is converted into a collection of SSIPs.[42] Black squares and area in-between represent the locations of SSIPs on the flatted surface.

Rather than focussing simply on the maxima and minima of the molecular electrostatic potential surface, a set of SSIPs are defined that fully describe the binding properties of the molecules. Each SSIP has a surface area of 9.5 $Å^2$ and volume of 5 $Å^3$, the former being derived from water as a reference and the latter being the volume of a zero-point void.[42] The basis behind this process is shown in Figure 3.3 for water (a) and methane (b), and involves mapping the sites of minimum and maximum potential to the MEPS. For water, the surface corresponds to exactly four SSIPs as marked by the black squares, with an equal amount of positive and negative sites. These sites are assigned interaction parameters, ε_i, equal to the hydrogen bond donor (α) and acceptor ($-\beta$) parameters discussed in Section 1.2.5, which are obtained from E_{max} and E_{min} within the specific region of the calculated potential surface or from experimental data (if available). The parameters are dimensionless as in Hunter's original model, where the product of two values is equal to the energy in kJ mol^{-1} of a point contact between two SSIPs.[42] In the case of methane, the surface area corresponds to a 5.4 interaction points (to be rounded to the nearest integer[42]) of which 4 arise from the maxima near the hydrogen atoms. The area between these corresponds to a fifth, negative, site. Thus, instead of only having two points at which

binding can occur, the number of interaction sites has more than doubled in methane and is increased even further for larger molecules. The free energy of interaction is now calculated from the equilibrium of all the pairwise interactions between all available SSIPs in the system, with the caveat that all structure and relationships between nearby binding sites are ignored.[42]

Hunter's newer model also expands on the original formulism by the inclusion of unbound states, in which an SSIP is not bound to another site but with void space. In a real liquid, there exist a non-zero amount of unbound states, IR spectroscopy showing a considerable amount of void space in room temperature water.[325] For non-polar molecules with $\varepsilon_i \approx 0$, the competition between the binding of one site to another or to a void space is entirely dependent on van der Waals interactions. Therefore, the inclusion of unbound states in the SSIP model potentially allows for accurate predictions in a larger number of scenarios than using Hunter's original model.

The binding equilibrium between two SSIPs is provided by association constant, K_{ij}, in the following equation:[42]

$$K_{ij} = \tfrac{1}{2} e^{-(\varepsilon_i \varepsilon_j + E_{\mathrm{vdW}})/RT} \tag{3.5}$$

where R is the ideal gas equation, T the temperature of the system, and E_{vdW} is an estimation of the contribution purely due to van der Waals interactions between a pair of SSIPs, having a fixed value of $-5.6\,\mathrm{kJ\,mol^{-1}}$. The concentration of the complex formed by two separate SSIPs, [ij], is expressed in terms of the association constant:

$$[\mathrm{ij}] = K_{\mathrm{ij}}[\mathrm{i_{free}}][\mathrm{j_{free}}] \tag{3.6}$$

where $[\mathrm{i_{free}}]$ and $[\mathrm{j_{free}}]$ are the concentrations of the unbound states of i and j, and the concentration of an individual SSIP (also referred to as the *fractional occupancy*) is:

$$[\mathrm{i}] = \theta = [\mathrm{i_{free}}] + \sum_{j=1}^{n} ([\mathrm{ij}] + [\mathrm{ji}]) \tag{3.7}$$

The maximum concentration of SSIPs, c_{max}, is attained by assuming that a zero-point liquid is the densest medium possible (filling 90 % of space[326]) and using the volume occupied by a mole of interaction sites:

$$c_{max} = \frac{0.9}{N_A V_{SSIP}} \tag{3.8}$$

If the chemical potential of an SSIP is equal in two different liquid phases (1 and 2) at equilibrium, then the concentrations of unbound states are assumed to be equal in both phases.[42] The *binding energy*, ΔG_b, of transferring a molecule completely from phase 1 to 2 is then given by:

$$\Delta G_b = -\sum_{i=1}^{N} RT \ln\left(\frac{f_2^i}{f_1^i}\right) \tag{3.9}$$

in which f^i is the fraction of unbound SSIPs for the given phases, and N is the total number of SSIPs on the molecule. Due to the overestimation of the free energy of complexation in the model, a *confinement energy* term, ΔG_c, is included which increases as the difference in densities (and thus the concentration of unbound states) between phases grows:

$$\Delta G_c = -NRT \ln\left(\frac{\sqrt{1+8\theta}}{4\theta}\right) \tag{3.10}$$

where N is the total number of SSIPs on the molecule and θ is the total concentration of SSIPs in the phase. The complete free energy of complexation between two interaction sites, i and j, is then given by:

$$\Delta G^\circ = \Delta G_b + \Delta G_c - \Delta G_S(i) - \Delta G_S(j) + RT \ln c_{max} \tag{2.5}$$

where $\Delta G_S(i)$ and $\Delta G_S(j)$ are the solvation energies of the molecule's SSIPs in the pure phases.

This expanded SSIP model of solvation thermodynamics developed by Hunter has not yet been applied to model any surface interactions. In order to do so for this project, the surfaces were assumed to consist of evenly distributed SSIPs with hydrogen bond donor and acceptor values corresponding to the surface functional group (in the case of hydrocarbon surfaces: $\alpha, \beta = 0.5$). This was achieved by using a test molecule consisting of exactly 2 SSIPs, of opposite charges corresponding to the aforementioned α and β

values. Using test molecules with 2:1 or 3:1 ratios of positive to negative surface area (corresponding to greater numbers of α sites, as on a methyl surface) showed no qualitative difference in the trends observed. The set of SSIPs for the liquid were obtained from their MEPS or from experimental values as described previously. The free energy of complexation between the surface interaction sites was then calculated using Eq. 2.5.

The aim of this chapter is therefore to compare Lifshitz theory and Hunter's model, and to identify any potential shortcomings of either approach for non-polar surfaces (where dispersion forces are expected to dominate) as well as some polar surfaces in a large number of different liquids.

3.2 Experimental

3.2.1 Lifshitz Theory

All Lifshitz calculations were done by means of the method described in (Sections 2.2.1 and 2.2.2), using a shared solvent and surface database in CSV format. Different systems were constructed using TToolbox, including the number of media interacting, and the results collated alongside free energy values from the Hunter model calculations.

3.2.2 Hunter's Model

Free energies were calculated using a combination of TToolbox and *phasetransfer*, details of which can be found in (Section 2.2.3). As *phasetransfer* runs on UNIX systems and the author used Windows 7/8/10 throughout the duration of the project, a VirtualBox VM running Ubuntu 16.04 was created with a shared folder between host and guest OS. Output files from *phasetransfer* were then imported into TToolbox to calculate the binding and confinement free energies, and the final free energy of complexation output to CSV along with the Lifshitz work of adhesion values. Values of kJ mol^{-1} were converted into mJ m^{-2} through division of the known area of the test molecule (2 SSIPs) and Avogadro's constant.

3.2.3 Binary Mixtures

Binary mixture graphs were obtained by creating 11 different solvent media, with fractions between 0 and 1 (inclusive) in 0.1 intervals, the properties being calculated using the method described in Section 2.2.4. The predicted interactions in each fraction were obtained using the same methods as above, and the results plotted as a function of liquid composition.

3.3 Results and Discussion

3.3.1 Non-Polar Surfaces

Values for the work of adhesion based on Lifshitz theory were calculated using the method described in Section 3.1.1 for two solid phases at a fixed separation with a third intermediate liquid medium (Figure 3.1), and the values of free energy were calculated as described in Section 3.1.2. Figure 3.4 shows the results of these calculations in the pure solvents investigated.

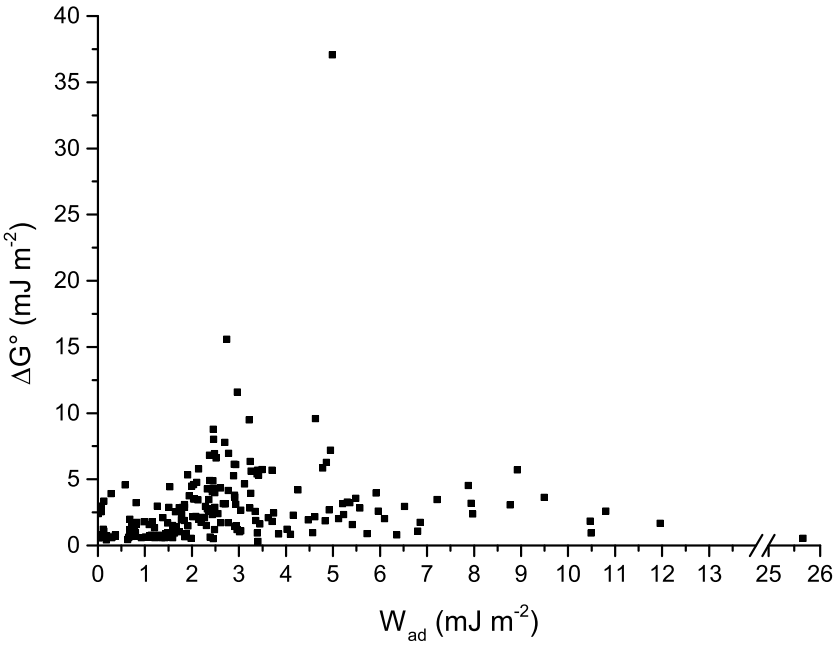

Figure 3.4: Graph showing all calculated values of the work of adhesion given by Lifshitz theory 3-medium calculations against the normalized free energy of complexation provided by the Hunter model for over 200 solvents investigated in the systems shown in Figure 3.1.

A larger value in the work of adhesion indicates that a greater amount of work must be done in separating the two solid phases (effectively creating 2 free surfaces). Greater values in the normalized free energy of complexation describe a stronger solvation between surface SSIPs. A positive correlation between the normalized free energy of complexation and the work of adhesion for different solvents would therefore imply that

both models predict similar behavior. The data in Figure 3.4 shows that ΔG° appears to be comparatively invariant with W_{ad}, with 91.4 % and 97.7 % of free energy values falling within one or two standard deviations of the mean, respectively. However, for certain groups of solvents, a good correlation is observed between the work of adhesion and the free energy. Figure 3.5 shows data for alkanes, primary alcohols, amines, and carboxylic acids.

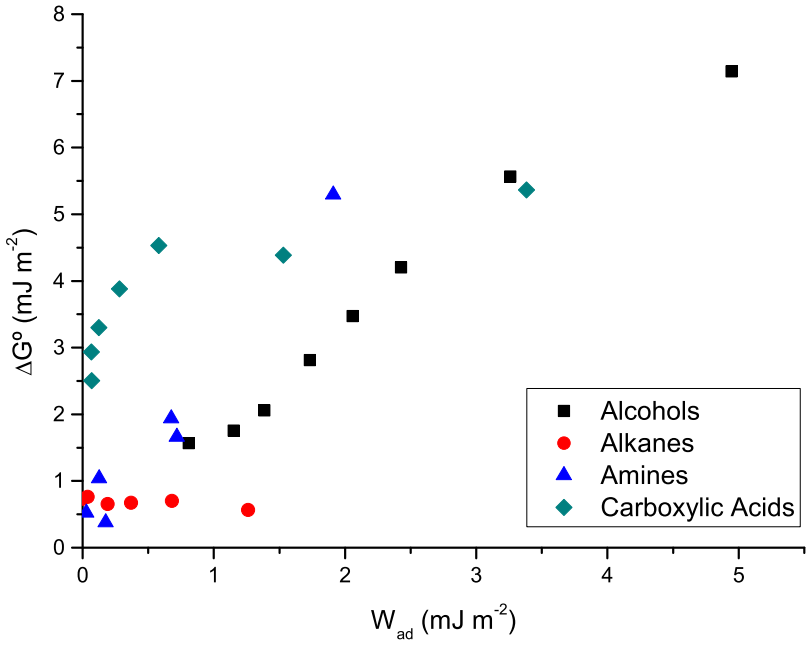

Figure 3.5: Work of adhesion against free energy of complexation for hydrocarbon surfaces in several groups of solvents isolated from all liquids presented in Figure 3.4.

Calculated values for alcohols can be seen to correlate relatively linearly for the two models of surface interaction, as seen in the figure above. Methanol (W_{ad} = 4.95 mJ m^{-2}, ΔG° = 7.19 mJ m^{-2}) is the most polar of the solvents, and is also predicted to yield the greatest interaction energy for hydrocarbon surfaces among the primary alcohols according to both models. As the polarity of the alcohol decreases (with increasing hydrocarbon chain length), so too do the associated free energy and work of adhesion. There also exists a good correlation between the two models for the non-aromatic amines, with the predicted interaction decreasing with polarity just as is observed for

the primary alcohols. In contrast, the two models diverge in their predictions for the behavior in alkanes. Pentane ($W_{ad} = 1.27\,mJ\,m^{-2}$, $\Delta G^\circ = 0.61\,mJ\,m^{-2}$), the shortest of these, yields a calculated work of adhesion between that of 1-decanol ($W_{ad} = 1.15\,mJ\,m^{-2}$, $\Delta G^\circ = 1.80\,mJ\,m^{-2}$) and 1-octanol ($W_{ad} = 1.38\,mJ\,m^{-2}$, $\Delta G^\circ = 2.11\,mJ\,m^{-2}$), but its free energy is similar to that of n-hexadecane ($W_{ad} = 0.04\,mJ\,m^{-2}$, $\Delta G^\circ = 0.81\,mJ\,m^{-2}$). While the Hunter model suggests effectively no change in the interaction between non-polar surfaces in these non-polar solvents, the Lifshitz model shows an increased work of adhesion between surfaces in shorter alkanes, indicating a significant divergence between the two models.

The solvent with the largest predicted free energy of complexation is water ($W_{ad} = 4.98\,mJ\,m^{-2}$, $\Delta G^\circ = 37.08\,mJ\,m^{-2}$), dramatically greater than that of other highly polar solvents such as methanol. Additionally, there are many solvents yielding calculated works of adhesion greater than that in water, but with predicted free energies of complexation within $3\,mJ\,m^{-2}$ of each other. This can be seen in closer detail in Figure 3.6. The majority of these liquids include at least one aromatic ring, such as quinoline ($W_{ad} = 12.0\,mJ\,m^{-2}$, $\Delta G^\circ = 1.68\,mJ\,m^{-2}$, green circle) and benzophenone ($W_{ad} = 10.5\,mJ\,m^{-2}$, $\Delta G^\circ = 1.84\,mJ\,m^{-2}$, red triangle).

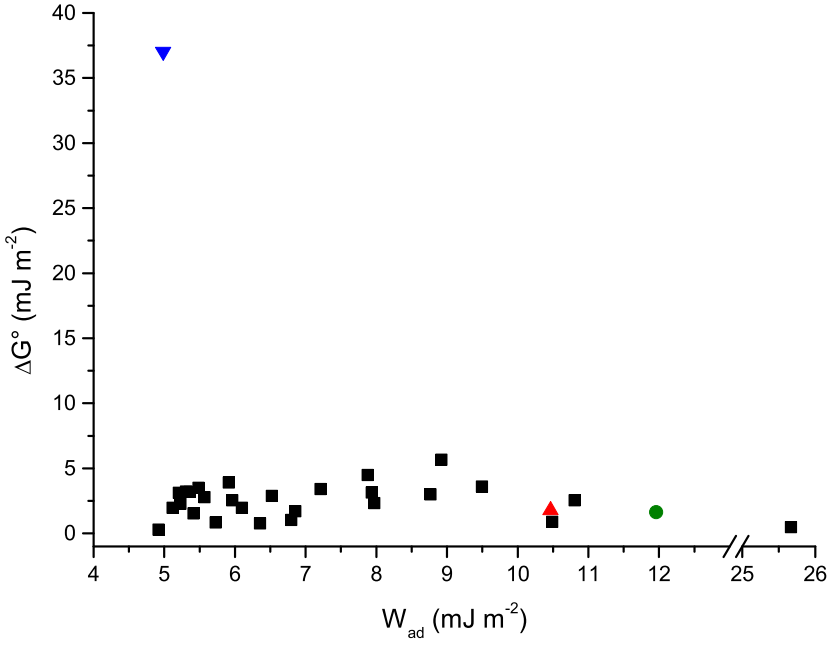

Figure 3.6: Work of adhesion against free energy of complexation for water and liquids with calculated work of adhesion greater than that of water (upside down blue triangle).

Comparing liquids with analogous compounds containing an aromatic ring, as shown in Table 3.1, shows an increase in the refractive index of the latter, as aromatic liquids are known to have higher refractive indices.[327] Molecules with larger atoms such as sulfur and iodine also show an increased refractive index due to their increased polarizability arising from their ability to better stabilize instantaneous dipoles.[328] This increase in the polarizability, α, leads to an increase in the refractive index according to the Lorentz-Lorenz equation:

$$\frac{n^2 - 1}{n^2 + 2} = \frac{4\pi}{3} N\alpha \tag{3.11}$$

where N is the number of molecules per unit volume.

Table 3.1: Dielectric constants (ε), refractive index (n_D, measured at sodium D line), and calculated Lifshitz work of adhesion (W_{ad}) and Hunter free energy of complexation ($\Delta G°$) for a series of related solvents with and without an aromatic ring, as well as dichloromethane and its analogous molecule methylene iodide with heavier iodine atoms replacing chlorine. Dodecane included for reference.

Solvent	ε^*	n_D^*	W_{ad} (mJ m^{-2})	$\Delta G°$ (mJ m^{-2})
ethanol	24.55	1.359	3.25	5.61
2-phenylethanol	12.31	1.533	4.92	2.70
nitromethane	35.87	1.379	2.91	3.80
nitrobenzene	34.78	1.550	6.85	1.75
methanol	32.66	1.327	4.95	7.19
benzyl alcohol	12.70	1.538	5.31	3.28
dichloromethane	8.93	1.421	1.21	0.60
methylene iodide	5.32	1.738	25.70	0.54
cyclohexane	2.02	1.424	0.01	0.60
benzene	2.27	1.498	1.63	0.95
perfluorodecalin	1.98	1.313	3.40	0.31
dodecane	2.00	1.420	0.00	0.78

* ε, n_D: average values at 20 °C obtained from Marcus et al.[329] and Lide et al.[274]

Meanwhile, the free energy for all the solvent pairs shown decreases with the introduction of an aromatic ring. Substituting the chlorine in dichloromethane for iodine in methylene iodide has no effect on the free energy which is negligible for both of these when compared to that calculated for the other solvent pairs highlighted. This accentuates the main differences between the two models, especially the reliance on the properties of bulk liquids on the calculations of Lifshitz interaction energies.

Figure 3.7 shows the relation between the refractive index of the liquids being investigated in this chapter and the resulting work of adhesion calculated using Lifshitz theory. It can be seen that there is a parabolic relationship between the two values, with

the variation in the work of adhesion at any given refractive index being due to differences in the dielectric constants of the liquid. Indeed, as the refractive index deviates more from that of dodecane (1.421), a smaller variation in the interaction is predicted.

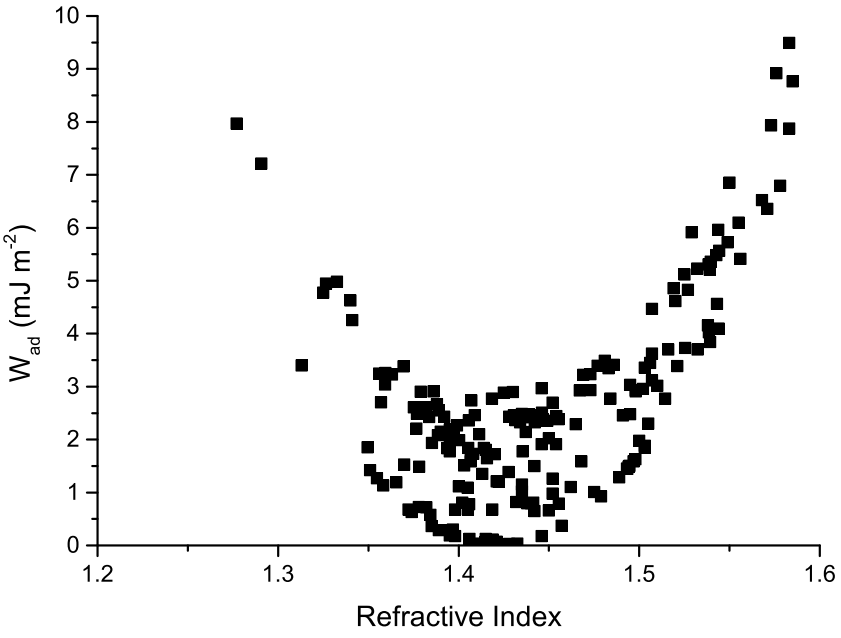

Figure 3.7: Refractive index of bulk liquid compared to the calculated Lifshitz work of adhesion for a system of two alkane surfaces interacting across different liquids.

This arises due to the non-zero frequency term (London dispersion term) of the Hamaker constant calculation, which for a system of two identical surfaces (1) separated by a liquid (3) is given by:[6]

$$A_{\nu>0} \approx \frac{3h\nu_e}{16\sqrt{2}} \frac{(n_1^2 - n_3^2)^2}{(n_1^2 + n_3^2)^{3/2}} \tag{3.12}$$

Similarly, the zero-frequency term (Keesom and Debye), which determines the contribution of the dielectric constant, is:

$$A_{\nu=0} \approx \frac{3k_B T}{4} \left(\frac{\varepsilon_1 - \varepsilon_3}{\varepsilon_1 + \varepsilon_3} \right)^2 \tag{3.13}$$

Finally, the total Hamaker constant is given by the equation:

$$A_{131} = A_{\nu=0} + A_{\nu>0} \tag{3.14}$$

We can infer from Eq. 3.13 that the closer the values of the dielectric constant of the surfaces are to that of the liquid medium, the smaller the contribution of the zero frequency term, and therefore the interaction is dominated by dispersion forces. For non-polar surfaces, where electrostatic forces are not dominant, this is the expected behavior. The variation in the calculated work of adhesion in Figure 3.7 at any given refractive index is therefore due to the increase in Debye (permanent–induced dipoles) and Keesom (permanent–permanent dipoles) interactions as the dielectric constant of the medium increases. Any increase in the dielectric constant of the liquid medium would thus lead to a rising contribution of the zero-frequency term. Alternatively, one can consider the Dupré equation for the separation of two surfaces (S) in a medium (M):[330]

$$W_{\mathrm{SMS}} = 2\gamma_{\mathrm{SM}} - \gamma_{\mathrm{SS}} \tag{3.15}$$

where W_{SMS} is the work done to separate the two surfaces per unit area, while γ_{SM} and γ_{SS} are the interfacial free energies per unit area of the surface-medium and surface-surface interfaces, respectively. The dielectric constant can be seen as an approximate measure of the polarity of a liquid,[329] and is therefore related to γ_{SM} in a system of two non-polar surfaces. The system of interest consists of two hydrophobic dodecane surfaces, and therefore the energy required to separate these two surfaces in increasingly polar liquids is likely to be larger than for non-polar liquids. In other words, the value of $A_{\nu=0}$ is expected to become more significant in systems with a highly polar liquid due to the increased contribution of Debye (dodecane-medium) and Keesom (medium-medium) interactions. However, as seen in Figure 3.7, $A_{\nu>0}$ still dominates in determining the interaction energies between these non-polar surfaces. In the case of polar surfaces, previous studies have shown that an increase in the dielectric constant of the intermediary liquid correlates to a decrease in the interaction between these surfaces.[165,331,332] This is primarily due to the

effect of the solvent medium on the electrostatic interactions (e.g., hydrogen bonding) between the polar surfaces, rather than due to large shifts in the magnitude of van der Waals forces.

Conversely, the Hunter model does not rely on the bulk properties of the liquid or surface media, instead taking a first principles approach in its determination of interaction energies, using instead hydrogen bond donor (α) and acceptor (β) parameters. This model of solution-phase thermodynamics has already been demonstrated to be able to predict the interactions between hydrogen bonding surfaces in liquid mixtures of varying polarity.[37,41,190] In these, one surface was assumed to be a hydrogen bond donor (D) while the other acted as a hydrogen bond acceptor (A). These can form a 1:1 complex with an associated equilibrium constant K_a:[37]

$$\mathrm{D} + \mathrm{A} \rightleftharpoons \mathrm{D} \cdot \mathrm{A} \tag{3.16}$$

Meanwhile, in a non-polar solvent (e.g., a hydrocarbon), labelled S1, the D and A complex may be weakly solvated, and be described by the equilibrium constant K_1:

$$\mathrm{D} \cdot \mathrm{S1} + \mathrm{A} \rightleftharpoons \mathrm{D} \cdot \mathrm{A} + \mathrm{S1} \tag{3.17}$$

Finally, if a second more polar liquid is introduced into the system to act as a hydrogen bond acceptor, this may replace S1 as the solvated molecule, with an equilibrium constant K_S associated to this reaction:

$$\mathrm{D} \cdot \mathrm{S1} + \mathrm{S2} \rightleftharpoons \mathrm{D} \cdot \mathrm{S2} + \mathrm{S1} \tag{3.18}$$

This leads to an equilibrium in which S1, S2, and A are competing to form a complex with the hydrogen bond donor, which lets us describe the equilibrium constant of the formation of the D:A complex, K_a, as:

$$K_a = \frac{K_1}{1 + K_\mathrm{S}[\mathrm{S2}]} \tag{3.19}$$

The nature of the change of $\log K_a$ with respect to log[S2] is remarkably well described by the model when compared to experimental pull-off forces and the variation in the surface shear strength as a function of log[polar solvent].[37] Despite the considerably different conditions between free molecules interacting in a liquid phase and restricted functional groups interacting dynamically between tip and surface in AFM pull-off and friction measurements, the model has been shown to be transferrable to different systems.

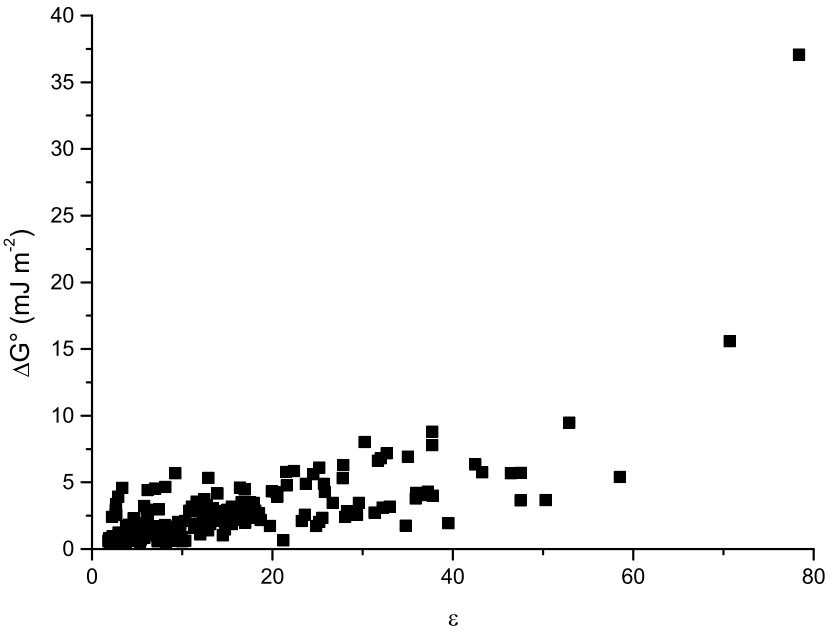

Figure 3.8: Dielectric constant of bulk liquid compared to the calculated Hunter free energy of complexation for a system of two alkane surfaces interacting across different liquids.

The modified SSIP model used in this study is expected to more accurately describe systems involving non-polar surfaces, due to its inclusion of unbound states and van der Waals interactions. It has been shown[42] to predict the hydrophobic effect between non-polar liquids and water, which implies that the solvophobic effect (expected to be present in the interactions between hydrocarbon surfaces in a polar medium) could be understood based upon the thermodynamic equilibrium of the competing interactions

between the SSIPs of D, A, and S. A greater interaction between D and A would therefore describe greater adhesive forces between the two surfaces, which is presented in the results as a greater normalized free energy of complexation.

Since the value of the hydrogen bond donor and acceptor parameters is determined by the maxima and minima on the calculated MEPS of the molecule, which would grow in magnitude as the polarity increases, one might expect a relationship between the dielectric constant of the liquid medium and the normalized free energy of interaction. Indeed, Figure 3.8 shows that there is a linear relationship, albeit a slightly diffuse one. A clear outlier to this relation is water, however. This anomalously large interaction between non-polar surfaces in water has been verified experimentally,[132] and demonstrates the potential importance of solvation effects on adhesive forces.

3.3.2 Binary Mixtures between Non-Polar Surfaces

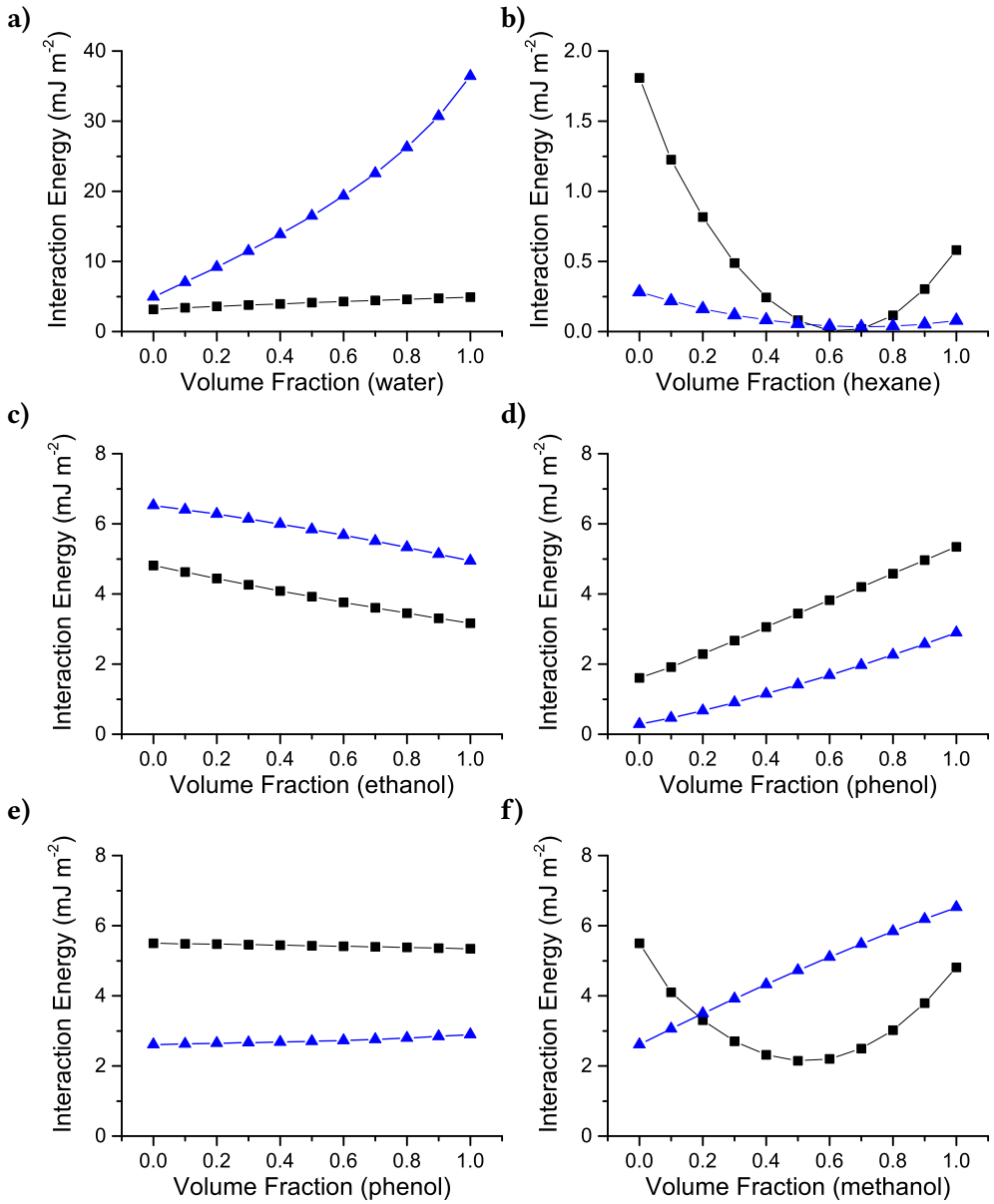

Figure 3.9: Lifshitz work of adhesion (black squares) and free energy of complexation (blue triangles) against volume fraction of **a)** water in ethanol **b)** hexane in benzene **c)** ethanol in methanol **d)** phenol in toluene **e)** phenol in benzyl alcohol **f)** methanol in benzyl alcohol.

Interactions between hydrocarbon surfaces were investigated in a series of binary mixtures of liquids. The works of adhesion and free energies of complexation were calculated. A selection of these can be seen in Figure 3.9, where several differences between the two

approaches can be identified. Due to the error associated with the use of a simple linear relationship in calculating the dielectric constant of each volume fraction,[276,333,334] a slight deviation in the Lifshitz calculations is expected (up to ~5 %).

In the system of water and ethanol mixtures, the two models predict similar trends in the interactions between surfaces, with water causing the greatest adhesive force (as previously seen in Section 3.3.1). However, the order of magnitude increase in the free energy is not mirrored in the calculated work of adhesion, which only increases by 50 %. Lifshitz theory does not account for the molecular structure or ordering of the interacting phases, treating them instead as continuous media. Consequently, it is not suitable for systems of non-polar interacting surfaces immersed in polar liquids, as it grossly underestimates the strength of such interactions when compared to experimental data.[335] For ethanol/methanol mixtures, it can be seen that the two models predict a similar drop in the interaction energy from pure methanol to pure ethanol, with a decrease in the free energy and work of adhesion of 25 % and 35 %, respectively. The Hunter model predicts systematically greater interaction between the surfaces in these mixtures (by approximately 2 mJ m^{-2}), but it still constitutes some of the best agreement between the two approaches in the expected trend.

Binary mixtures of non-polar liquids were also investigated, and of particular interest were ones including aromatic rings that caused dramatic increases in the work of adhesion according to Lifshitz theory. Hexane/benzene mixtures yield a decrease in both W_{ad} and ΔG° with increasing volume fraction of hexane, reaching a minimum at (respectively) 0.6 and 0.7 before increasing again as the hexane volume fraction is increased to unity. However, the calculated work of adhesion in pure hexane is less than half that in pure benzene, highlighting once again the effect of the higher refractive index on the strength of the dispersion force between surfaces. In Lifshitz theory, this can be explained by the fact that the bulk properties of hexane and benzene, in particular the refractive index, lie on either side of that of dodecane (see Figure 3.7). While a similar trend is observed for the Hunter model, possibly due to a minimization of the fractional density of the liquid mixture, the absolute values of the free energy in either pure liquid remain insignificant.

The effect of the aromatic ring was further investigated in the systems seen in Figures 3.9d to 3.9f. For phenol/toluene mixtures a relatively good agreement is found between the two theories, with both W_{ad} and ΔG° increasing with the volume fraction of phenol. A slight disparity is found for phenol/benzyl alcohol mixtures, with Lifshitz theory predicting a 3 % lower interaction and the Hunter model suggesting a 13 % increase. However, due to the low values of W_{ad} and ΔG° for this system, the change is barely appreciable. The largest disparity between the two models was found in mixtures of liquids with aromatic rings and polar liquids such as methanol (and presumably water, which was not investigated as it is not miscible with such solvents). For methanol/benzyl alcohol mixtures, Lifshitz theory predicts a smaller work of adhesion in pure methanol than in pure benzyl alcohol, the opposite result to the Hunter model, with the lowest interaction actually in a 1:1 mixture of the two solvents (just as for the mixtures of hexane and benzene).

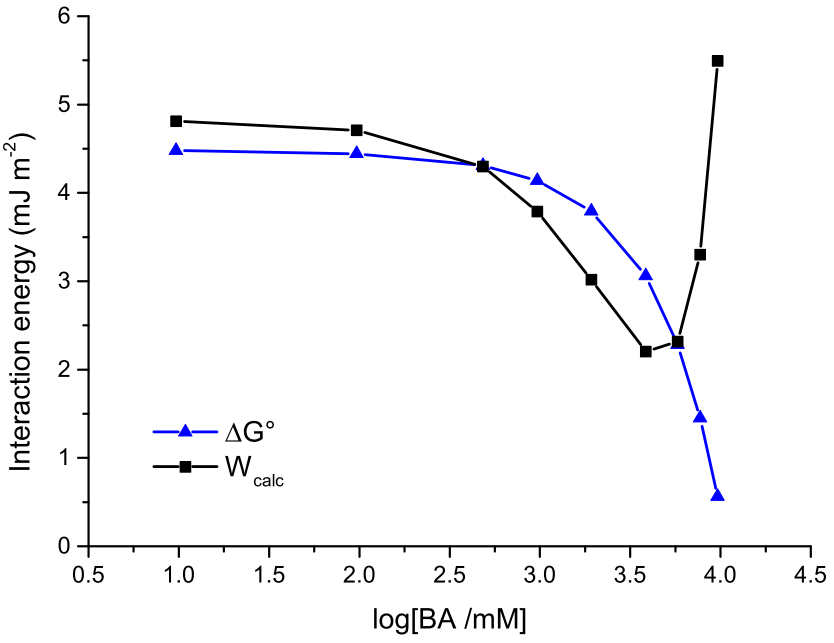

Figure 3.10: Free energy of complexation (black) and work of adhesion (blue) for mixtures of methanol and benzyl alcohol against the concentration of benzyl alcohol.

Figure 3.10 shows the same data as a function of the log of the concentration of benzyl alcohol (log[BA]), ΔG° initially changes little as benzyl alcohol is added to methanol, but at a concentration of ca. 1.5 M, ΔG° begins to decrease as [BA] is increased. The general form of the relationship is similar to that observed for hydrogen bonding surfaces.[37,41,190] The updated SSIP model thus appears to predict a similar decrease in the interaction free energy at higher concentrations of less polar solvent between non-polar surfaces. For reference, the dipole moment of methanol is 2.87 D and that of benzyl alcohol is 1.87 D. At values up to log [BA] $\approx$ 3.5 the general trend of W_{ad} on the concentration of benzyl alcohol is similar, but at higher concentrations a markedly different relationship is observed, with the work of adhesion increasing as [BA] is increased. This system brings the differences between the models into sharp focus, therefore, and provides a good candidate for experimental investigation.

3.3.3 Polar Surfaces

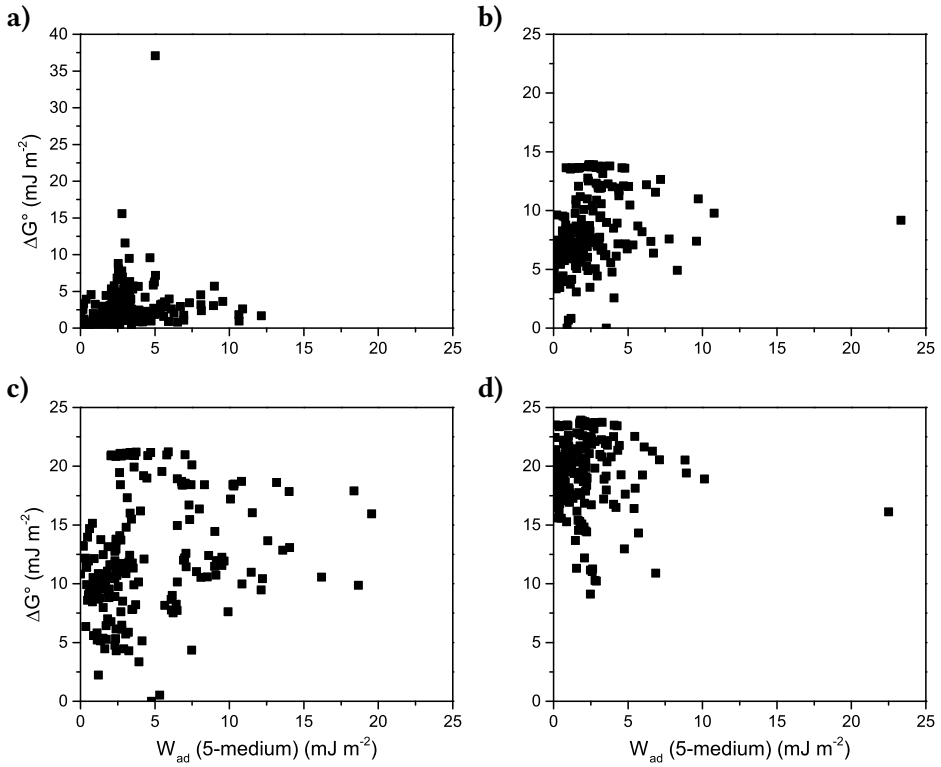

Figure 3.11: Graph showing all calculated values of the work of adhesion given by Lifshitz theory 5-medium calculations against the normalized free energy of complexation provided by the Hunter model for systems of **a)** 1-dodecanethiol (DDT) **b)** 11-mercapto-1-undecanol (MUL) **c)** 11-mercaptoundecanoic acid (MUA) and **d)** 11-amino-1-undecanethiol (AUT) in over 200 solvents.

The same calculations for each model were also performed for a number of polar surfaces with different functional groups: 11-mercapto-1-undecanol (MUL, alcohol), 11-mercaptoundecanoic acid (MUA, acid), and 11-amino-1-undecanethiol (AUT, amine). Due to the bulk properties used in the calculations of Lifshitz theory being obtained in liquid,[274,329] whose molecular orientations are inherently isotropic, a slightly expanded system comprising 5 interacting media was used (see Figure 2.4). This allows for the directionality of the dipole moments in the SAMs to be better accounted for. The Hamaker constant is calculated in exactly the same way as for the 3-medium system used in the previous sections, but for the interactions between the two bulk surfaces 1 and 1', and adsorbed layers 2 and 2' across medium 3. However, in order to determine the work of

adhesion, the van der Waals force experienced between surfaces is integrated over all possible separations, as described in Section 2.2.2:

$$F(D) = \frac{1}{6\pi}\left[\frac{A_{232'}}{D^3} - \frac{\sqrt{A_{121}A_{32'3}}}{(D+T)^3} - \frac{\sqrt{A_{1'2'1'}A_{323}}}{(D+T')^3} + \frac{\sqrt{A_{1'2'1'}A_{121}}}{(D+T+T')^3}\right] \tag{2.3}$$

$$W_{\text{ad}} = \int_{D_0}^{\infty} F(D)dD \tag{2.4}$$

where D_0 is the same minimum separation (0.165 nm) as in the 3-medium system. For the SSIP calculations, the hydrogen bond parameters (α, β) of the surfaces were modified from ±0.5 for alkane surfaces to the corresponding values for the functional groups of the polar surfaces, as obtained by Hunter.[32] The results of the calculations can be seen in Figure 3.11, with the values for a system of non-polar surfaces also included (calculated with the same 5-medium method using methane as the end group, the results of which were within 3 % of those obtained using the 3-medium calculations). As expected, ΔG° values are larger for carboxylic acid-terminated surfaces. However, the value of W_{ad} is only larger for the carboxylic acids in benzene. There is also a broader spread of values for the work of adhesion between acid-terminated surfaces, likely due to the greater dielectric constant value of the formic acid end group causing a greater variation in the possible (combined) Keesom and Debye interactions in different liquids.

If we compare the results obtained by Nikogeorgos et al.[37] for MUL (referred to as HUT) to the data in Table 3.2, we can see that the Hunter SSIP model accurately predicts a smaller interaction free energy between the alcohol-terminated surfaces in a more polar solvent. The original 3-medium calculation suggested the opposite result, but the correction for the anisotropy in the surface polarity appears to give more reasonable results. Similarly for acid-terminated surfaces, work by Busuttil et al.[41] shows a decrease in the adhesion energy for MUA surfaces in polar solvents, which is mirrored in the normalized free energy provided by the SSIP Hunter model, and also in the 5-medium Lifshitz system. According to both models, water would compete very effectively as a hydrogen bond acceptor in much the same way as acetone.

Table 3.2: Dielectric constants (ε), refractive index (n_D, measured at sodium D line), and calculated Lifshitz work of adhesion (W_{ad}) for 3 and 5-medium calculations and Hunter free energy of complexation ($\Delta G°$) for systems of alcohol and acid-terminated surfaces in a number of polar and non-polar solvents.

Surface	Solvent	ε^*	n_D^*	W_{ad}^{3med} (mJ m^{-2})	W_{ad}^{5med} (mJ m^{-2})	$\Delta G°$ (mJ m^{-2})	$F_a/R^\dagger$ (mN m^{-1})
alcohol	acetone	20.56	1.356	3.31	2.28	6.02	5
	heptane	1.92	1.385	1.42	3.31	13.78	78
	water	78.36	1.330	5.82	3.93	4.75	—
	benzene	2.27	1.500	1.20	3.14	11.89	—
							$F_a^\dagger$ (nN)
acid	acetone	20.56	1.356	2.19	0.75	8.89	0.2
	heptane	1.92	1.385	1.21	2.70	21.08	2.9
	water	78.36	1.330	4.58	0.48	8.59	—
	benzene	2.27	1.500	2.15	7.12	18.45	—

* ε, n_D: average values at 20 °C obtained from Marcus et al.[329] and Lide et al.[274]

† F_a/R, F_a: values obtained from Nikogeorgos et al.[37] and Busuttil et al.[41]

Figure 3.12 shows correlations between the work of adhesion and free energy for hydroxyl-terminated surfaces in the same liquids used to generate the data in Figure 3.5. The trends are different to those found for non-polar surfaces. A reversal of the interaction in non-polar liquids such as alkanes when compared to non-polar surfaces is unsurprising, as they are unlikely to compete in the hydrogen bonding between these surfaces, and has been previously experimentally confirmed.[37] These values of the free energy can therefore be assumed to represent the maximum possible interaction between solvents. For the non-polar system, due to the bulk properties of the liquids being used in the Lifshitz calculations, a large (3 mJ m^{-2}) shift results in the values of the work of adhesion. Any solution-phase hydrogen bond donors or acceptors that compete effectively to coordinate to surface sites should result in a lower value of the normalized free energy. This is indeed the case for the series of carboxylic acids in the Hunter model, with formic acid

($W_{ad} = 1.72\,mJ\,m^{-2}$, $\Delta G^\circ = 5.61\,mJ\,m^{-2}$) showing the greatest reduction in the surface adhesion, and slowly increasing values for each consecutive molecule in the series. Apart from formic acid, Lifshitz theory provides the opposite result for the work of adhesion of carboxylic acids of increasing chain length. As reasoned previously, this is due to the dependence of the Lifshitz adhesive interaction on the magnitude of deviation in the bulk properties of the interacting media. The Hunter model provides the same trend for the series of primary alcohols, with decreased polarities resulting in larger interaction values. The peculiar change in the values of the work of adhesion in alcohols is a consequence of the bulk properties of the liquid becoming more similar to those of the surface monolayer (hence decreasing the adhesive interaction), reaching a minimum at 1-pentanol ($W_{ad} = 0.84\,mJ\,m^{-2}$, $\Delta G^\circ = 7.57\,mJ\,m^{-2}$), and then yielding an increase in adhesion (at decreasing polarity) as the bulk property values diverge again.

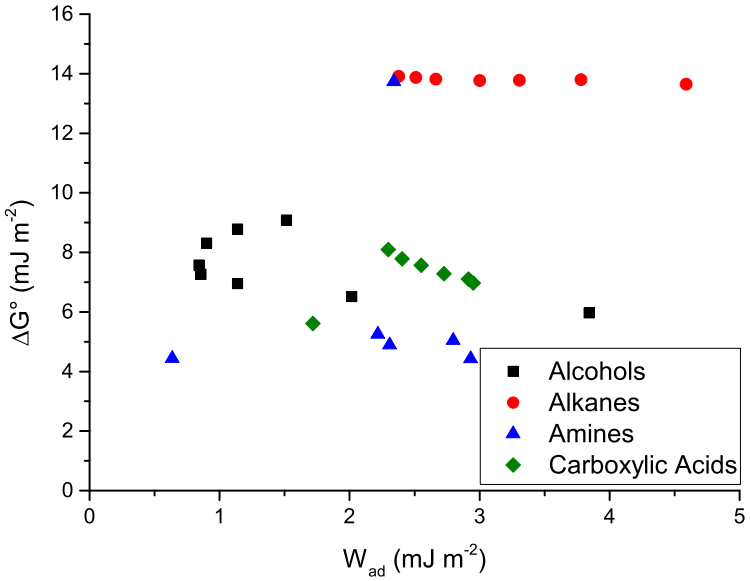

Figure 3.12: 5-medium work of adhesion (W_{ad}) against free energy of complexation (ΔG°) of several groups of solvents for a system of alcohol-terminated (MUL) SAMs.

The group of amines consists of a couple of primary, secondary, and tertiary amines, and shows a further disparity between the two models. For all amines, with the exception of tri-n-butylamine ($W_{ad} = 2.34\,mJ\,m^{-2}$, $\Delta G^\circ = 13.74\,mJ\,m^{-2}$), which is a much weaker hydrogen bond acceptor with $\beta = -1.2$ (comparatively, $\beta \approx -8$ for other amines),

there is a moderate reduction in the adhesive interaction when compared to a system with a non-polar liquid. Finally, values predicted using Lifshitz theory are relatively similar (between $2-3\,\mathrm{mJ\,m^{-2}}$) with the exception of ethylenediamine ($W_{\mathrm{ad}} = 0.65\,\mathrm{mJ\,m^{-2}}$, $\Delta G^{\circ} = 4.44\,\mathrm{mJ\,m^{-2}}$). While the increased dielectric constant of this diamine causes a decrease in the work of adhesion (due to more similar bulk properties to the solid phase), there is not much difference in the free energy of complexation as the hydrogen bond acceptor ability is relatively unchanged ($\beta = -7.4$) according to DFT.

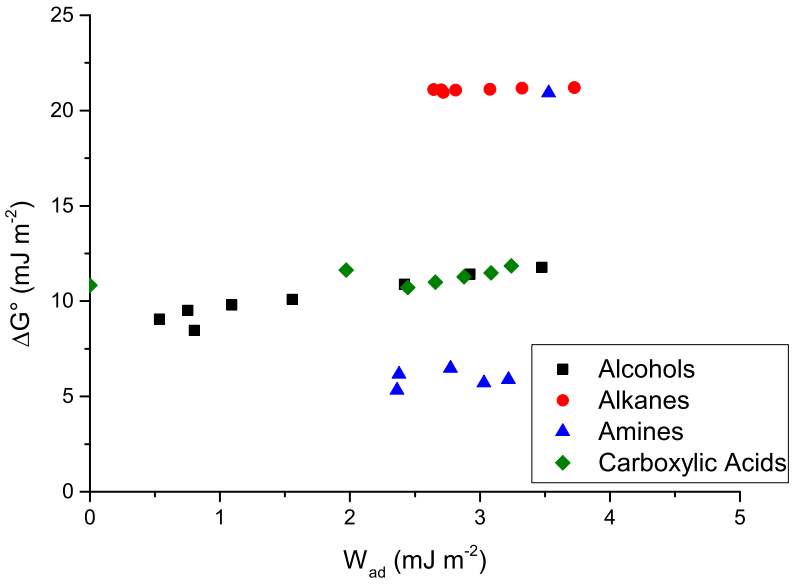

Figure 3.13: 5-medium work of adhesion (W_{ad}) against free energy of complexation (ΔG°) of several groups of solvents for a system of acid-terminated (MUA) SAMs.

For surfaces with acid-terminated SAMs (Figure 3.13), it can be immediately seen that there are three main regions of interaction according to hydrogen bond thermodynamics: high ($21\,\mathrm{mJ\,m^{-2}}$), moderate ($8-12\,\mathrm{mJ\,m^{-2}}$), and low ($5-7\,\mathrm{mJ\,m^{-2}}$) interaction. Interactions in alkanes and tri-n-butylamine are firmly in the high interaction energy region (with a moderate spread of $1.5\,\mathrm{mJ\,m^{-2}}$ according to Lifshitz theory), while in primary alcohols and carboxylic acids moderate interactions are calculated (as for alcohol-terminated surfaces), and the other amines, being particularly strong hydrogen bond acceptors, are found in the

low region. The main trends are similar to those predicted for the alcohol-terminated surfaces, and interactions between surfaces decrease in strength as competition for hydrogen bonding between surface-surface and surface-solvent molecules increases.

While not as clear as for the acid-terminated surfaces, the results for amine-terminated surfaces (Figure 3.14) vary slightly in that the interaction in amines are much greater than in the other polar surfaces. Alkanes, primary alcohols, and carboxylic acids show much the same behavior as in other systems, for both Lifshitz theory and the Hunter model. However, experiments have shown that systems of amine-terminated SAMs show increased interaction in aqueous solutions in a range of pH,[188] and a negligible interaction in vacuum[336] (somewhat comparable to a non-polar surface in terms of hydrogen bond interactions), suggesting that the Hunter model (as implemented here) might not be well suited for this system.

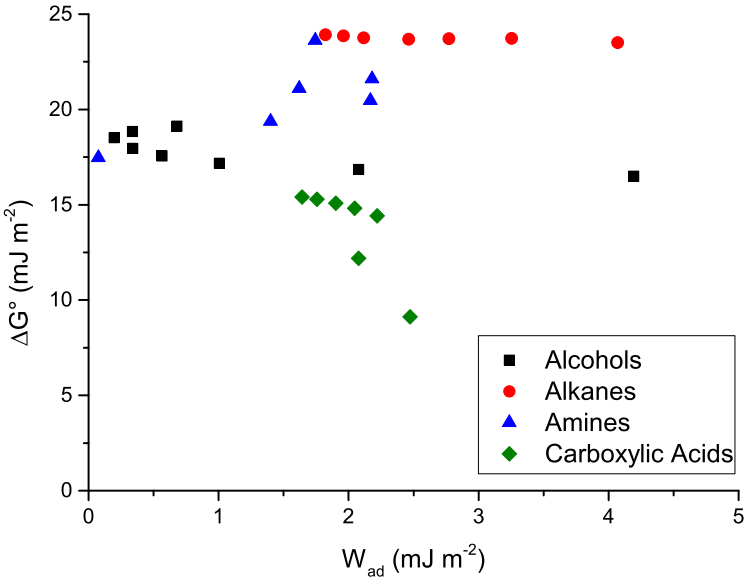

Figure 3.14: 5-medium work of adhesion (W_{ad}) against free energy of complexation ($\Delta G°$) of several groups of solvents for a system of amine-terminated (AUT) SAMs.

3.4 Conclusions

The Lifshitz theory of van der Waals forces and the expanded Hunter model of hydrogen bond thermodynamics using surface site interaction points were compared to each other for a number of different interacting systems. For non-polar 1-dodecanethiol surfaces, the work of adhesion (using a 3-medium construction of the Hamaker constant) and free energy of complexation between surfaces in over 200 liquids were calculated. While both models offered comparable results for a number of different solvent groups such as alkanes, amines, and primary alcohols, there was a large disparity between the two for liquids containing heavier atoms or aromatic rings. These cause the bulk properties, namely the refractive index responsible for dispersion forces, to be drastically different to their non-aromatic counterparts.

This effect was further seen in binary liquid mixtures, where agreement between the two approaches existed for certain groups of polar or non-polar liquids, but the inclusion of an aromatic ring resulted in different predictions by Lifshitz and the Hunter model. Additionally, mixtures of benzyl alcohol and methanol were identified as a good candidate for experimental investigation, due to the extreme disagreement between the two models, and the similarity with results obtained in previous investigations of the dynamics of hydrogen bonding surfaces.

Lifshitz calculations were also expanded to better represent systems of polar surfaces by using 5 interacting media instead of the previous 3. The updated Hunter model was found to predict the same general trends in the interactions between alcohol and acid-terminated surfaces in both polar and non-polar liquids such as acetone and heptane as obtained in previous experimental studies. Lifshitz theory managed to provide similar predictions for two of these solvents as well (when using the 5-medium approach), but this agreement is thought to be serendipitous and discrepancies were found when other more polar solvents were used.

CHAPTER 4

Molecular-Scale Adhesion and Friction of Hydrocarbon Surfaces

The Effect of Solvent Environment on the Interfacial Properties of Non-Polar Surfaces

In this chapter, the results from Chapter 3 are experimentally verified, using AFM probes to measure adhesive and friction interactions. AFM tips and surfaces are functionalized with a variety of non-polar self-assembled monolayers on a number different substrates. This has been illustrated in Figure 4.1 below. Measurements were performed in various liquid environments, including pure solvents and mixtures of benzyl alcohol and methanol.

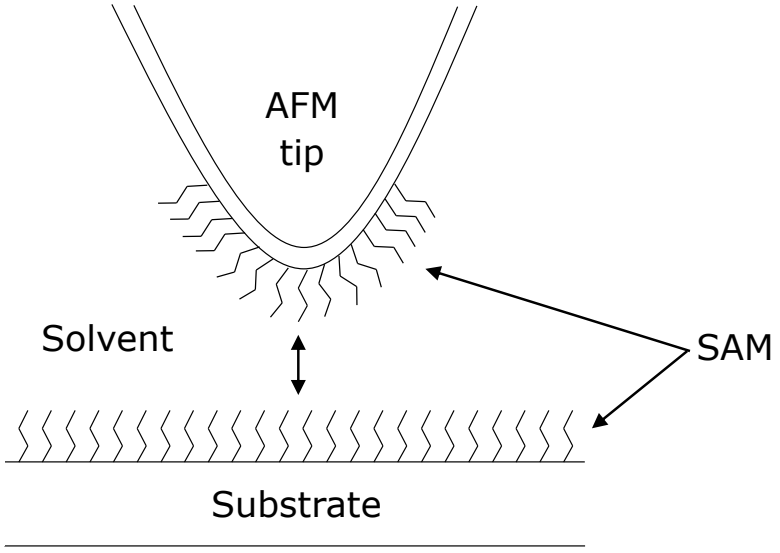

Figure 4.1: Schematic diagram of contact between metal-coated tip and surface with adsorbed molecular monolayers. Not to scale.

4.1 Introduction

Investigations of surface forces and interactions in a number of different systems such as lipid bilayers,[337,338] emulsions,[339] and more recently polymer brushes,[340–342] have been aided by the development of several experimental and theoretical techniques. Experimental data collection was limited until the introduction of the surface force apparatus (SFA) by Tabor and Winterton,[343] which was later improved by Israelachvili and Tabor,[344] and again by Israelachvili and Adams to allow for measurements in liquid.[345] In this technique, two cylindrical surfaces are brought into perpendicular contact with each other. The distance between the two surfaces is determined via optical interferometry, and the forces exerted are obtained from the deflection of a cantilevered spring holding

one of the surfaces. This apparatus allows for the direct measurement of forces (including dispersion forces) for a number of different surfaces which were previously not possible. These were predominantly composed of mica sheets, either unmodified[343–345] or modified with Langmuir-Blodgett films[346,347] or self-assembled monolayers,[348] although some other surface substrates have also been investigated.[349] However, the SFA is subject to limitations, particularly in the measurement of weak forces, as well as in measuring the interaction between single asperities, because the contact area in an SFA experiment is typically micrometer-scale.[47,350] As such, SFA experiments are not well suited for the inspection of single-asperity models of contact mechanics described in further detail in Section 1.3.1.

The introduction of scanning probe microscopy, and more specifically AFM[97] and FFM,[351] has helped shed light on the interaction between single-asperity contacts. This is thanks to the nanometer-scale contact area between tip and surface, as well as the much greater resolution in all three axes when compared to SFA. As a result of these improvements, much work has been done in the field of nanotribology to better understand the properties of adhesion,[134,352,353] friction,[145,350,354] wear,[192,355,356] and lubrication.[112,192,357] These phenomena at the nanoscale are becoming increasingly important to fully understand, in turn aiding in the development of numerous nanotechnological devices, such as micro- and nanoelectromechanical systems (MEMS/NEMS) which are found in an increasing number of applications. When considering the lubrication of these systems, traditional liquid lubricants are unsuitable due to the increase in capillary forces and viscous drag becoming dominant.[358] Non-polar alkyl SAMs have been demonstrated to be particularly effective lubricants,[179,308] and their adhesive and frictional properties have been investigated on a number of different substrates.[308,359–361] This has been possible thanks to the work by Nakagawa et al.[126] in developing what was later named chemical force microscopy, in which AFM probes were functionalized with alkylsilane SAMs of varying lengths and their interactions with silicon substrates investigated.

By changing the chain length,[362] end groups,[128,134] or conformational order,[363] it is possible to change the friction measured in these SAM systems. A previous study by Bain et al.[195] shows that for alkanethiol ($X(CH_2)_nCH_3$, X = SH for thiol monolayers)

SAMs with chains of n > 10 show little effect of the underlying gold substrate on various interfacial properties of the monolayer. This will be further tested in relation to adhesion and friction of alkyl SAMs with n = 11 and n = 17 for alkanethiols on gold, alkylphosphonic acids on aluminium, and alkylsilanes on silicon oxide (glass), the results of which are presented in this chapter. Measurements were performed in liquid, as it allows for easy modification of the interfacial medium, and eliminates any issues with capillary forces leading to erroneous data.

The mechanics behind the tip-sample interaction allowing FFM to produce friction-load plots is not yet thoroughly understood, with several different models of contact and friction being applied in the literature. Amontons' law is also frequently cited, when there may often be no fundamental reason why a multi-asperity (macroscopic) contact model should be used to explain the nanoscale interaction data provided by AFM techniques. Even when considering single-asperity contacts, there exist several competing models, namely the Hertz,[58] JKR[62] and DMT[63] models, taking different approaches in describing the nature of the deformation and adhesion experienced by surfaces in contact (further details can be found in Section 1.3.3). In systems where little adhesive interaction exists, a linear (Amontons-like) friction-load relationship is found, while in cases of strong interfacial interactions a sublinear relationship is usually obtained.[165,332,364] Marti et al.[365] proposed that this could be explained by treating the friction force as the sum of load-dependent and pressure-dependent terms:[112]

$$F_{\mathrm{fr}} = \mu F_{\mathrm{N}} + \tau A \tag{4.1}$$

where μ is the coefficient of friction, F_{N} is the applied load, τ is the surface shear strength, and A is the area of contact. When adhesion is low the shear term becomes insignificant, reducing the relation to Amontons' Law and thus yielding a linear friction plot. In studies of hydrogen bonding surfaces, it has been observed that as the solvation of surfaces was decreased by employing less polar solvents (thus causing greater interfacial adhesion), the friction plots shifted from linear to sublinear and a variation in the surface shear strength was measured.[190] Similar behavior has also been found in systems of non-polar surfaces, with sublinear friction-load plots found for liquids causing greater adhesive interactions.[21]

Combined with calculations from Chapter 3, friction and adhesion data obtained in a number of different liquids, as well as methanol/benzyl alcohol mixtures (which offered stark differences in theoretical values obtained), will be presented in this chapter to verify the merits of Lifshitz theory and the Hunter model in predicting the interactions between non-polar surfaces in liquid media.

4.2 Experimental

4.2.1 Monolayer Formation

Samples were prepared for analysis using the methods described in Section 2.3, on clean substrates in order to eliminate any source of contamination. 1-dodecanethiol (DDT, n = 11) and 1-octadecanethiol (ODT, n = 17), and n-dodecylphosphonic acid (DDPA, n = 11) and n-octadecylphosphonic acid (ODPA, n = 17) SAMs were deposited onto 50 nm gold and 30 nm aluminium films, respectively, on glass substrates with a 10 nm chromium adhesion layer. n-dodecyltrichlorosilane (DTS, n = 11) and n-octadecyltrimethoxysilane (OTMS, n = 17) SAMs were deposited onto cleaned glass substrates and annealed in a vacuum oven.

The AFM probes used for the measurements in this chapter were silicon nitride contact mode probes with triangular cantilevers (Bruker DNP-10). Probes were functionalized using the same methodology, with some changes to prevent damage to the cantilevers and reflective gold layer. Probes were not piranha cleaned, as this was found to cause the reflective backing layer to peel, instead being subjected to ozone treatment. To avoid the destructive bending of the cantilevers at prolonged high temperatures, the amount of metal deposited was minimized: 10 nm gold/aluminium, 2 nm chromium. In the case of silanized probes, the annealing step was omitted for the same reason.

4.2.2 Surface Characterization

XPS was used to determine the composition and electronic state of the elements at the sample surface (see Section 2.6.2), to ensure the correct monolayers had been deposited. As running XPS on every sample would become prohibitively expensive (and redundant with

strong methodology), contact angle measurements (see Section 2.6.1) were also performed on all samples prior to use, testing for contamination and failures in monolayer adsorption. Roughness measurements were taken as described in Section 2.5.7 for each monolayer.

4.2.3 Atomic Force Microscopy

All AFM data in this chapter was collected using a Bruker MultiMode 8 with NanoScope V controller and J-scanner. A liquid cell was employed to maintain an appropriate liquid environment for the AFM experiments with O-rings composed of silicone, Viton, or fluorosilicone being used depending on the chemical suitability for each liquid being investigated. Tip radii were then obtained using the method described in Section 2.5.6.

Pull-off Forces

Once the cantilever's deflection sensitivity and normal spring constant had been determined as per Section 2.5.4, pull-off forces for each system of interest were measured. Several hundred force curves were recorded at different locations on several samples, at a separation of at least 50 nm between measurements. These were then analyzed with TToolbox to determine the mean and standard error in the pull-off forces collected. For more details refer to Section 2.5.1.

Friction Forces

To apply the correct load on the tip in nN, the normal spring constant was first obtained. Friction images were then recorded for a series of decreasing loads, until the tip lost contact with the surface, as covered in Section 2.5.2. This was repeated several times at each load, with trace-minus-retrace signals being averaged across all recorded lines. Friction-load plots were then plotted in Origin Pro, and fitted with either a linear regression or the general fitting equation (GFE) developed by Carpick et al.[68]

4.3 Results and Discussion

4.3.1 X-Ray Photoelectron Spectroscopy

The XPS wide scan spectrum for DDT monolayers on gold can be seen in Figure 4.2 below, displaying the characteristic peaks for gold and carbon (sulfur signal is too weak to be seen at this scale), typical of spectra found in the literature for similar alkanethiols on gold.[301] The spin-orbit splitting for the Au 4f peak was determined to be 3.68 eV at an intensity ratio of 4:3 for the Au $4f_{7/2}$:Au $4f_{5/2}$ peaks. For the S 2p peaks (Figure 4.3b), the splitting is 1.21 eV with an intensity ratio of 2:1 for the S $2p_{3/2}$:S $2p_{1/2}$ sub-orbitals. Values found in the literature for these spin-orbit splittings of Au 4f and S 2p are 3.65 eV and 1.20 eV, respectively, while the ratios obtained match.[118,366]

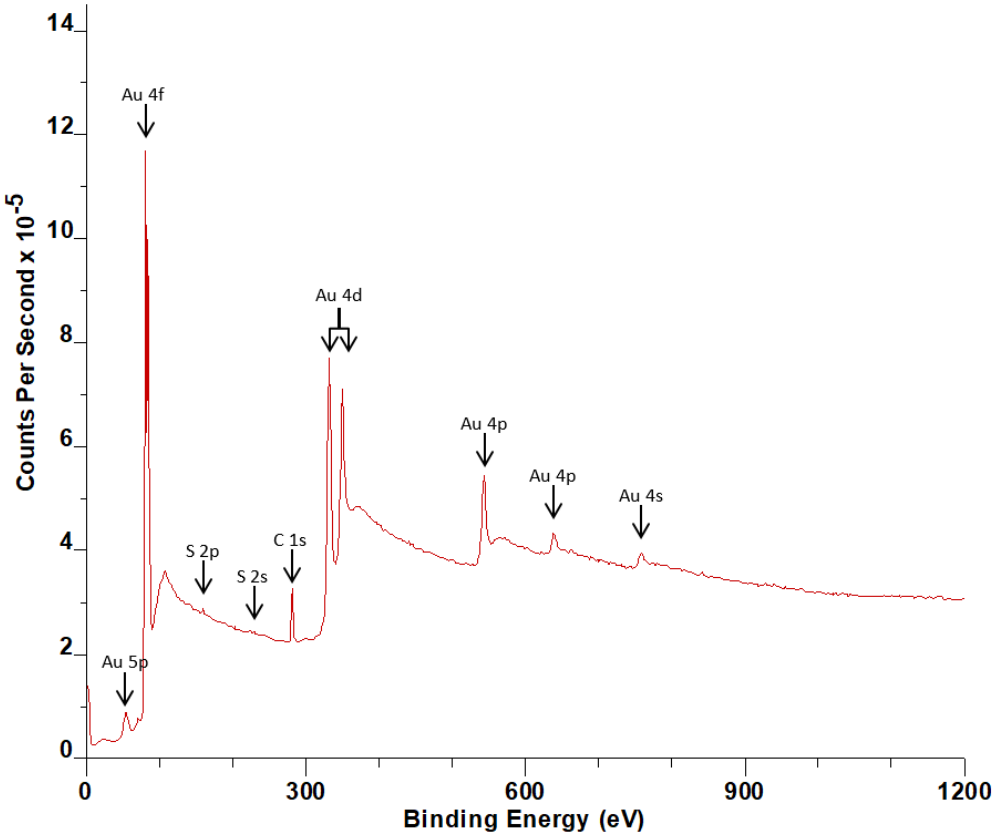

Figure 4.2: XPS wide scan spectrum of gold coated glass slide with dodecanethiol SAM.

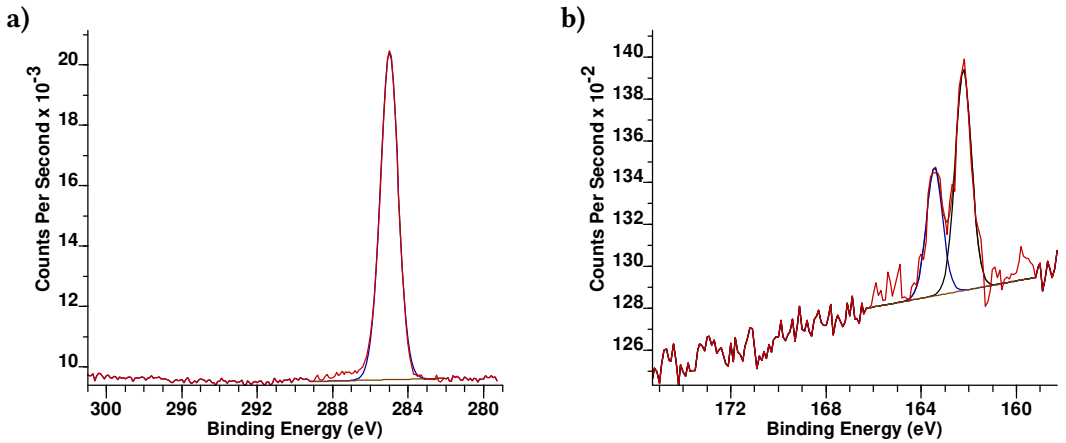

Figure 4.3: High-resolution XPS spectra of **a)** C 1s and **b)** S 2p regions of dodecanethiol SAMs on gold coated glass slides.

Figure 4.3 above shows the high-resolution spectra for the C 1s and S 2p orbitals of DDT. The characteristic C 1s peak at 285 eV for aliphatic carbons is present, while the core S $2p_{3/2}$ peak was found at the binding energy of 162.2 eV, characteristic for thiols chemisorbed to gold.[301,367,368] The absence of a sulfonate peak around 168 – 170 eV demonstrates that the SAMs used for analysis have not been oxidized after deposition and storage.[367] These findings were consistent in ODT samples as well, with a greater signal in the C 1s peak due to the greater presence of carbon atoms in the longer alkyl chains.

Spectra shown in Figures 4.4 and 4.5 (overleaf) are for DTS SAMs on glass substrates, with octadecyl silane SAMs showing greater intensity C 1s peaks as was the case for the alkanethiol SAMs. The wide scan spectrum in Figure 4.4 shows the expected elements at the surface for silane SAMs: silicon, oxygen, and carbon. As before, a sharp peak at 285 eV is present in the C 1s spectrum for the alkyl chain of the monolayer (Figure 4.5a), and a single silicon dioxide (SiO_2) peak in the Si 2p spectrum (Figure 4.5b) at a binding energy of 103.5 eV. Two small peaks are found at roughly 294 eV and 296 eV, most likely due to the presence of a minor amount of potassium in the glass slides used.

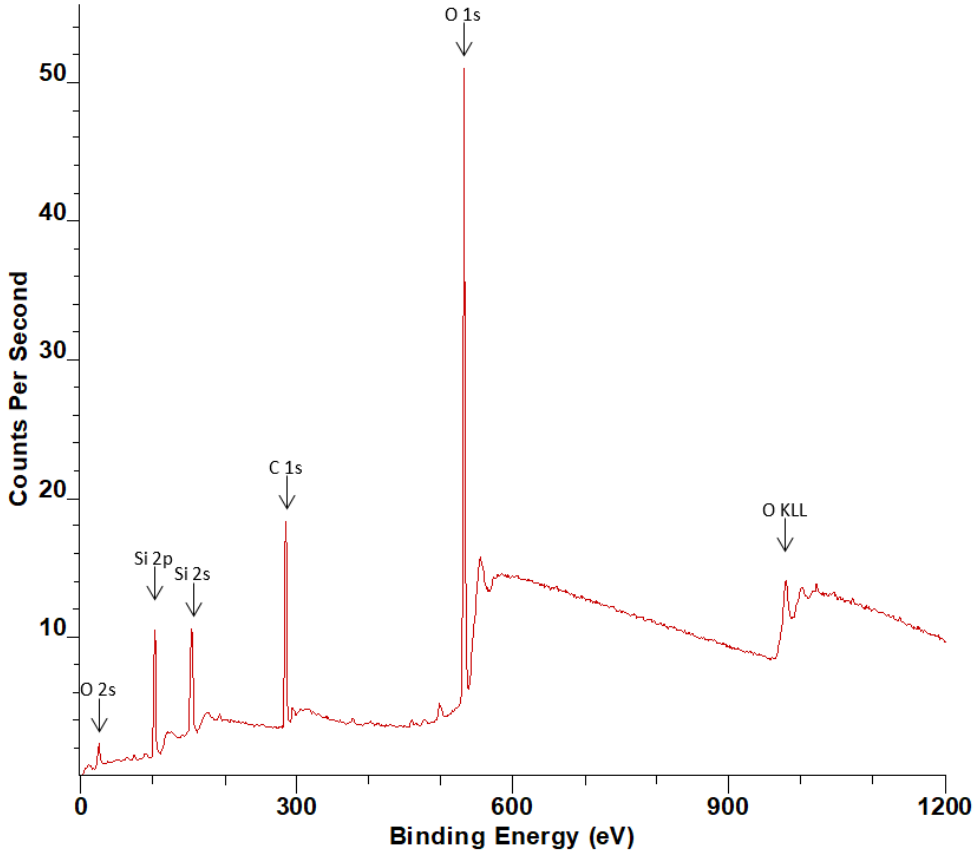

Figure 4.4: XPS wide scan spectrum of clean glass slide with dodecyltrichlorosilane SAM.

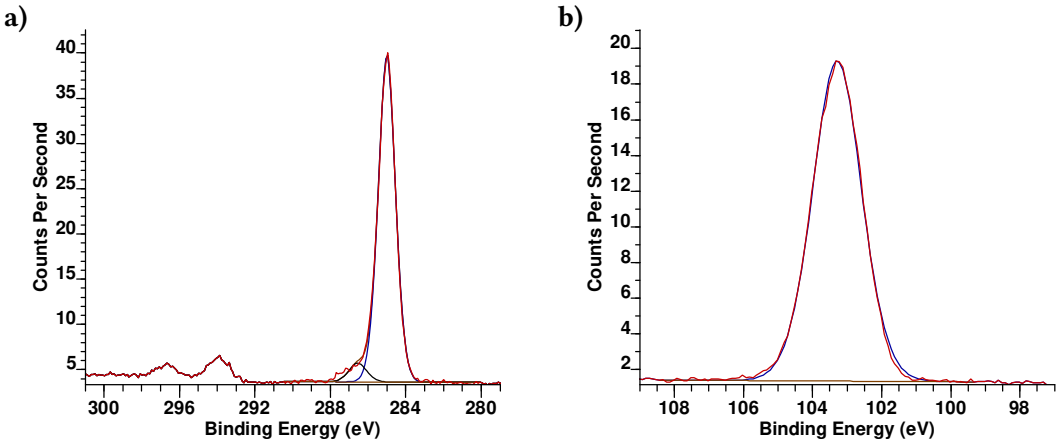

Figure 4.5: High-resolution XPS spectra of **a)** C 1s and **b)** Si 2p regions of dodecyltrichlorosilane SAMs on clean glass slides.

Phosphonic acids on aluminium were also characterized via XPS, and the wide scan spectrum of dodecylphosphonic acid is presented in Figure 4.6 below. The expected carbon, oxygen, phosphorus, and aluminium peaks are visible, with the ratio of the C 1s:O 1s peak intensities changing depending on the number of carbon atoms in the alkyl chain, while all other peaks remain unchanged. The presence of the P 2s and P 2p (Figure 4.7b) peaks demonstrates that a phosphonic acid monolayer has been achieved,[369] the quality of which can be further quantified using contact angle goniometry. Fitting the P 2p peak for overlapping P $2p_{3/2}$ and P $2p_{1/2}$ components gave a spin-orbit peak splitting ratio of 2:1 and a binding energy separation of 0.85 eV. Finally, the characteristic aliphatic C 1s peak at 285 eV is present in the high-resolution C 1s spectrum seen in Figure 4.7a.

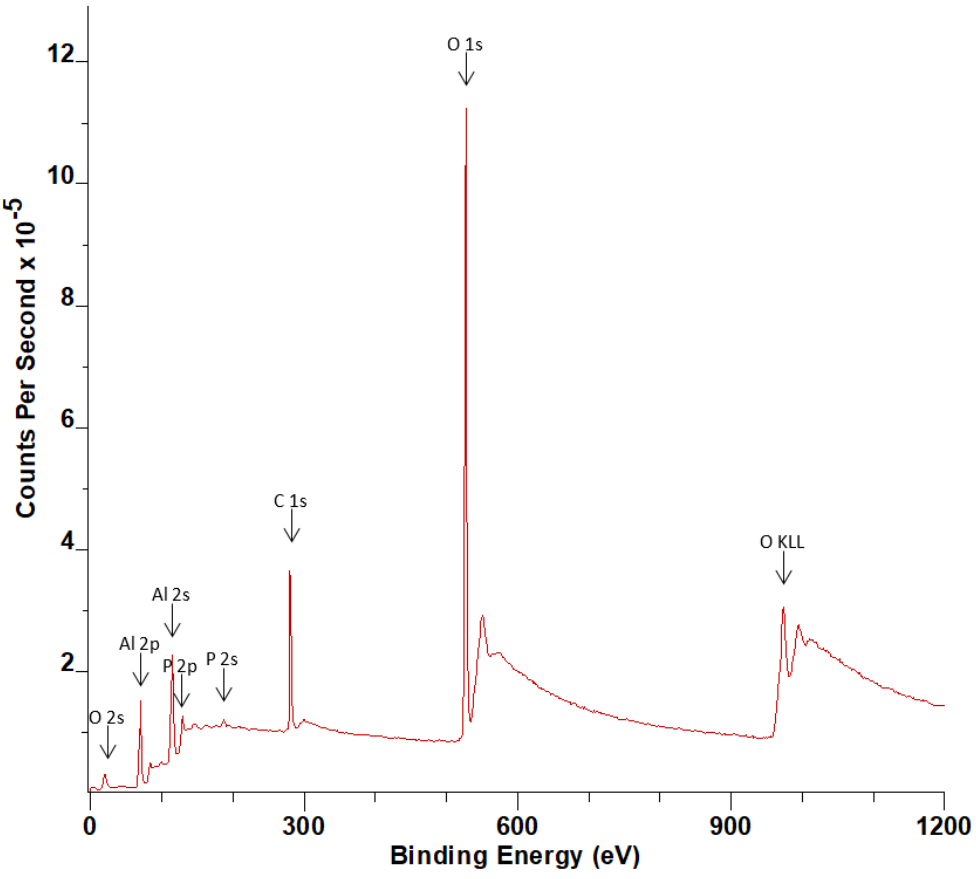

Figure 4.6: XPS wide scan spectrum of dodecylphosphonic acid SAMs on aluminium oxide.

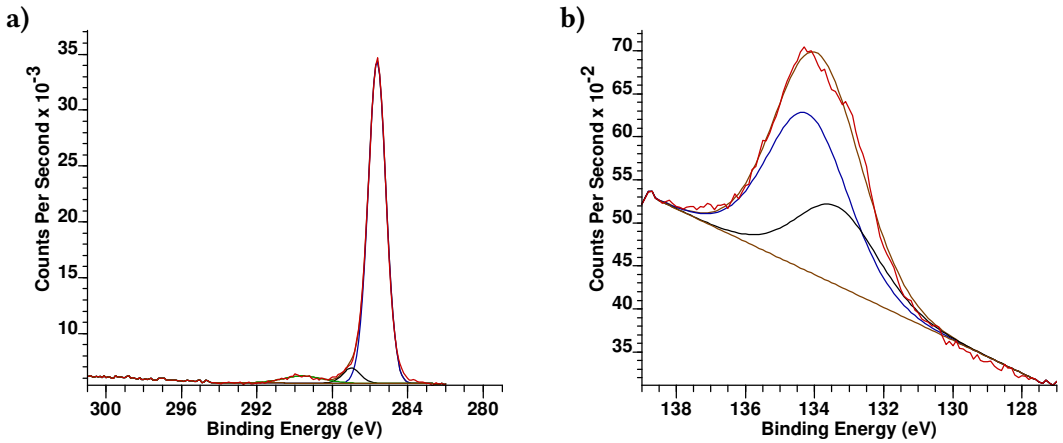

Figure 4.7: High-resolution XPS spectra of **a)** C 1s and **b)** P 2p regions of dodecylphosphonic acid SAMs on aluminium oxide.

4.3.2 Contact Angle Goniometry

All monolayers demonstrated hydrophobic behavior, with measured contact angles (presented in Table 4.1) being in agreement with literature values. Surfaces with advancing water contact angles greater than 90° are labelled as hydrophobic, which is expected from non-polar surfaces. Combined with the XPS results, these confirm that a good surface coverage was achieved using the methodology described. Any samples with contact angles outside of these values (within error) were discarded and not used for further analysis.

Table 4.1: Measured advancing contact angles for different monolayers measured with water, compared to values obtained in literature. Families of SAMs grouped by shading.

Monolayer (substrate)	Contact angle (°)	Literature value (°)*
DDT (Au)	112 ± 2	112
ODT (Au)	113 ± 2	116
DDPA (Al)	116 ± 3	115
ODPA (Al)	117 ± 2	115
DTS (SiO_2)	110 ± 2	110
OTMS (SiO_2)	103 ± 2	105

* : Literature values obtained from Creager et al.,[370] Sondag-Huethorst et al.,[371] Chiou et al.,[372] Wasserman et al.,[373] Dhotel et al.,[374] Sugimura et al.,[375] and Foster et al.[376]

4.3.3 Surface Roughness

The surface roughness of all monolayers was tested using tapping mode AFM. For thiol SAMs, a tip of radius 34 ± 3 nm was used. One of the topographical images recorded for these systems is displayed in Figure 4.8, with the average of several of these images (across various samples) giving an average roughness (R_a) value of 2.95 nm and a root mean square deviation (R_q) of 3.73 nm. The ratio of the two (R_q / R_a) resulted in a factor of 1.264, indicating a Gaussian asperity height distribution, due to its proximity to the ideal value of 1.253 for such a distribution.

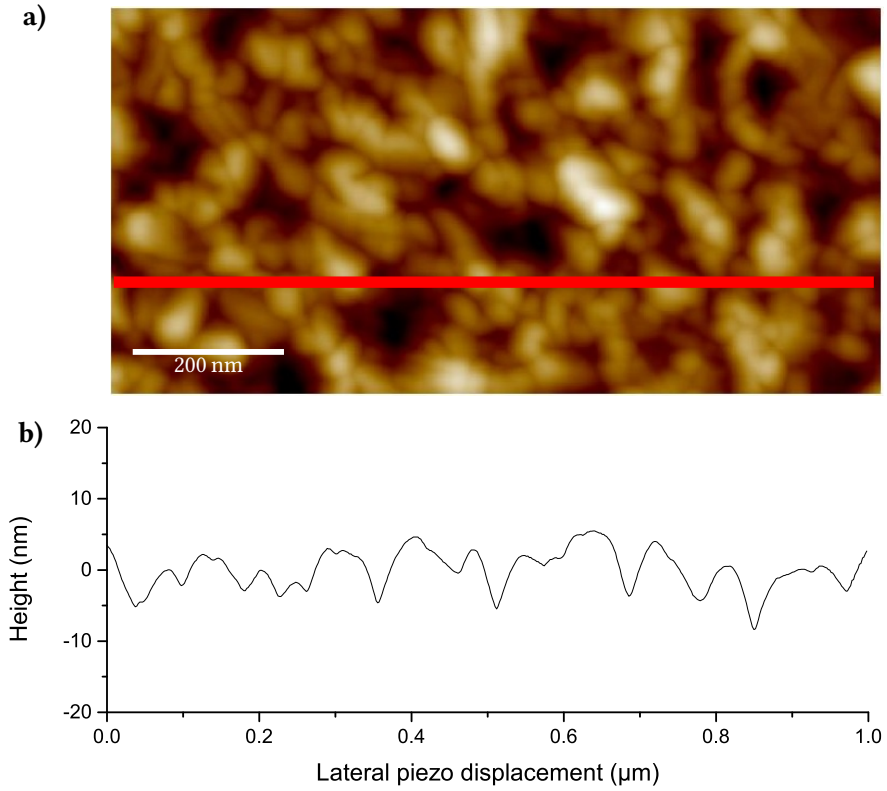

Figure 4.8: **a)** Height image of a DDT sample on gold imaged using a tapping mode AFM probe (image area 0.5 × 1 µm^2). **b)** Sample line section profile extracted from the same image (red line).

For silane SAMs, the radius of the tip used was measured to be 27 ± 2 nm. The average roughness for these samples was determined to be 0.510 nm nm, while the average root mean square deviation was 0.645 nm. An example image of the surface topography and line section can be seen in Figure 4.9. While these values are much smaller than those found

for gold surfaces, due a much smoother glass surface compared to an evaporated gold surface, the ratio of the two roughness factors was calculated to be 1.265, also implying a Gaussian asperity height distribution. Finally, for phosphonic acid SAMs on aluminium surfaces, the radius of the tip used was 37 ± 2 nm, and the average roughness and root mean square deviation were found to be 2.88 nm and 3.67 nm, respectively. This leads to a ratio of 1.274, once again indicating a Gaussian asperity height distribution. As with the gold surfaces, the aluminium surfaces are expected to be rougher than the underlying glass substrate due to the nature of the thermal metal evaporation technique.

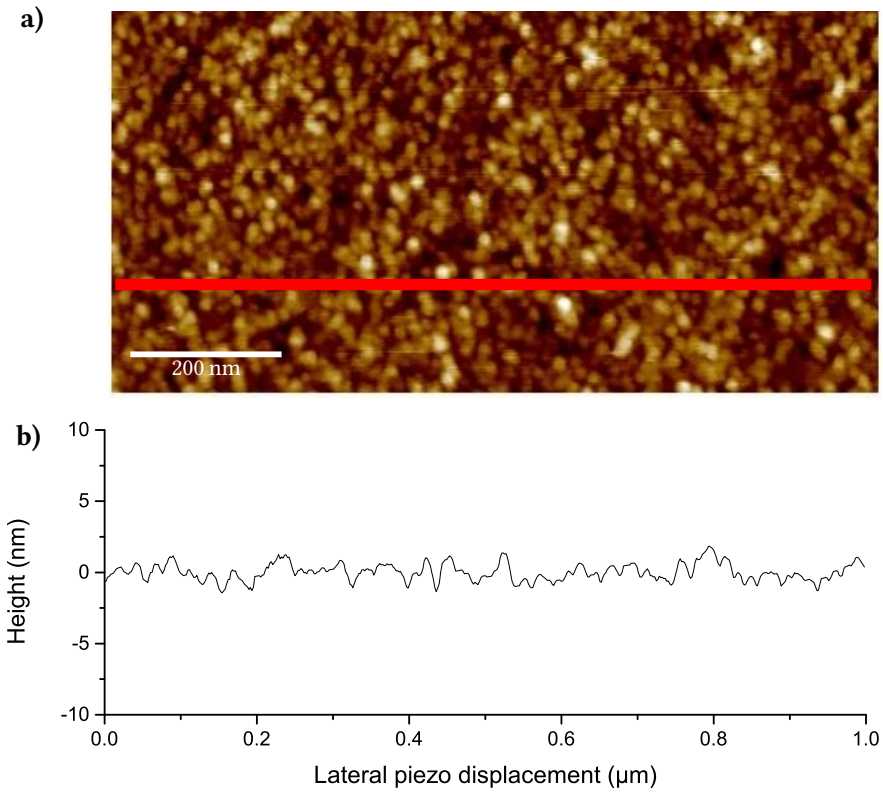

Figure 4.9: **a)** Height image of a DTS SAM on glass imaged using a tapping mode AFM probe (image area $0.5 \times 1\,\mu m^2$). **b)** Sample line section profile extracted from the same image (red line).

4.3.4 Pull-off Forces

Table 4.2: Refractive indices (n_D, measured at sodium D line), dielectric constants (ε), experimental AFM pull-off forces normalized by tip radius (F_{po}/R), experimental work of adhesion (W_{exp}), calculated Lifshitz work of adhesion (W_{calc}), and Hunter model free energy of complexation ($\Delta G°$) obtained in different pure liquids for gold surfaces with adsorbed dodecanethiol SAMs. Bulk values for dodecanethiol included for reference.

Medium	$\mathbf{n_D}^*$	ε^*	$\mathbf{F_{po}/R}$ ($\mathbf{mN\,m^{-1}}$)	$\mathbf{W_{exp}}$ ($\mathbf{mJ\,m^{-2}}$)	$\mathbf{W_{calc}}$ ($\mathbf{mJ\,m^{-2}}$)	$\mathbf{\Delta G°}$ ($\mathbf{mJ\,m^{-2}}$)
dodecanethiol	1.420	2.00	—	—	—	—
water	1.333	78.36	292 ± 12	46.5 ± 1.9	4.98	37.08
methanol	1.327	32.66	41 ± 4	6.52 ± 0.53	4.95	7.19
ethanol	1.359	24.55	34 ± 4	5.41 ± 0.63	3.26	5.61
nitromethane	1.379	35.87	30 ± 3	4.77 ± 0.51	2.91	3.80
perfluorodecalin	1.313	1.98	24 ± 3	3.82 ± 0.48	3.40	0.31
benzyl alcohol	1.538	12.70	8.3 ± 2.1	1.32 ± 0.33	5.31	3.28
benzonitrile	1.525	25.20	4.2 ± 1.6	0.67 ± 0.25	5.11	2.03
n-heptane	1.385	1.92	2.8 ± 1.0	0.45 ± 0.16	0.39	0.72
n-decane	1.410	1.99	3.8 ± 1.1	0.60 ± 0.18	0.04	0.73
n-dodecane	1.420	2.00	2.4 ± 0.9	0.38 ± 0.14	0.00	0.78
n-hexadecane	1.433	2.05	1.7 ± 1.0	0.27 ± 0.16	0.04	0.81
1,2,4-trichloro-benzene	1.571	4.15	2.7 ± 1.4	0.43 ± 0.22	6.36	0.81

* ε, n_D: average values at 20 °C obtained from Marcus et al.[329] and Lide et al.[274]

Pull-off forces obtained via force spectroscopy, normalized to the calibrated tip radius (on average between 50 – 60 nm), for dodecanethiol SAMs on gold surfaces are presented in Table 4.2, alongside the theoretical values for the Lifshitz work of adhesion and normalized Hunter free energy of complexation calculated using the methods described in Sections 2.2.1 and 2.2.3. The pull-off forces collected are a measure of the force required to break all short-range interactions within (e.g., hydrogen bonds), and long-range interactions (such as dispersion forces) outside the area of contact. The experimental work

of adhesion was determined under the assumption that the critical load (L_c) at which the AFM tip jumps out of contact with the surface follows the TCCM model (Section 1.3.5), and is defined to occur at $L_c = -2\pi RW$. This transition occurs regardless of which model of contact mechanics best describes the system, and by using $L_c = F_{po}$ the work of adhesion can be calculated as follows:

$$W_{exp} = \frac{F_{po}}{2\pi R} \tag{4.2}$$

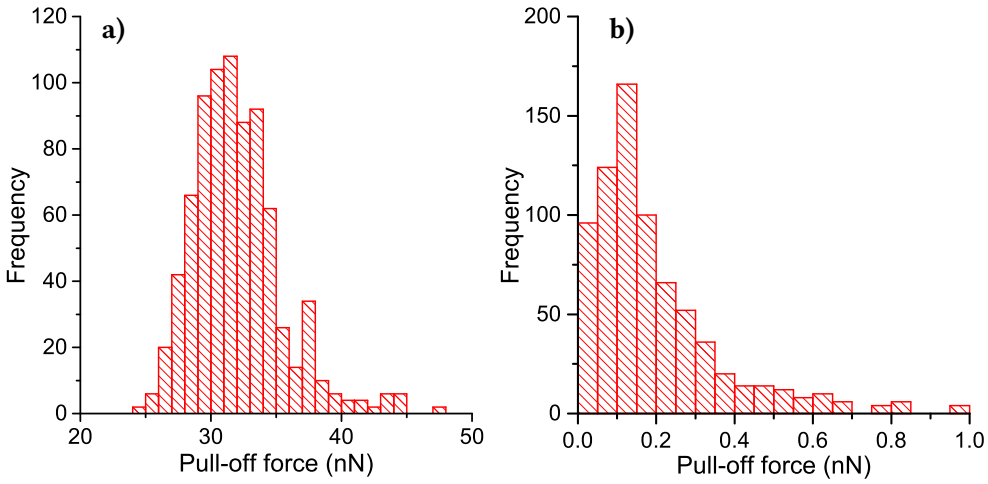

Figure 4.10: Example histograms showing distribution of pull-off forces obtained in **a)** water and **b)** heptane.

To better visualize the differences between the two theoretical approaches in calculating interaction energies between DDT SAMs, the experimentally obtained work of adhesion was compared with the Lifshitz work of adhesion and the normalized Hunter free energy of complexation (Figure 4.11). Uncertainties in the experimental values were calculated from the standard error in the mean of all recorded pull-off forces, while the error in the theoretical values was assigned a conservative value of 20 %. This is due to the intrinsic uncertainties in the bulk properties used in Eq. 3.4, as well as the simplifications it makes in the derivation from the exact Lifshitz equation.[6] With regards to the Hunter model, it was developed for calculations in the solution phase, and therefore does not account for the restrictions imposed on the degrees of freedom in the spatial motion of the monolayer molecules.

It can be seen in Table 4.2 that some of the standard errors in the experimental work of adhesion are moderately large, especially for systems with low measured interaction energies. This is attributed to the roughness of the surface leading to contacts of greater than expected area (e.g., a tip in a valley between two crystal grains) and thus to a "tail" in the distribution of measured pull-off forces, as seen in Figure 4.10. A slight shift of the mean towards greater values is therefore expected, as well as a larger standard deviation (and thus standard error) in the experimental work of adhesion. The variation in pull-off forces between samples, after normalizing for the tip radius, was found to be 10 – 15 % on average (with one exception where it was found to be 19 %). Therefore, combining data from different samples to give a larger dataset was deemed appropriate.

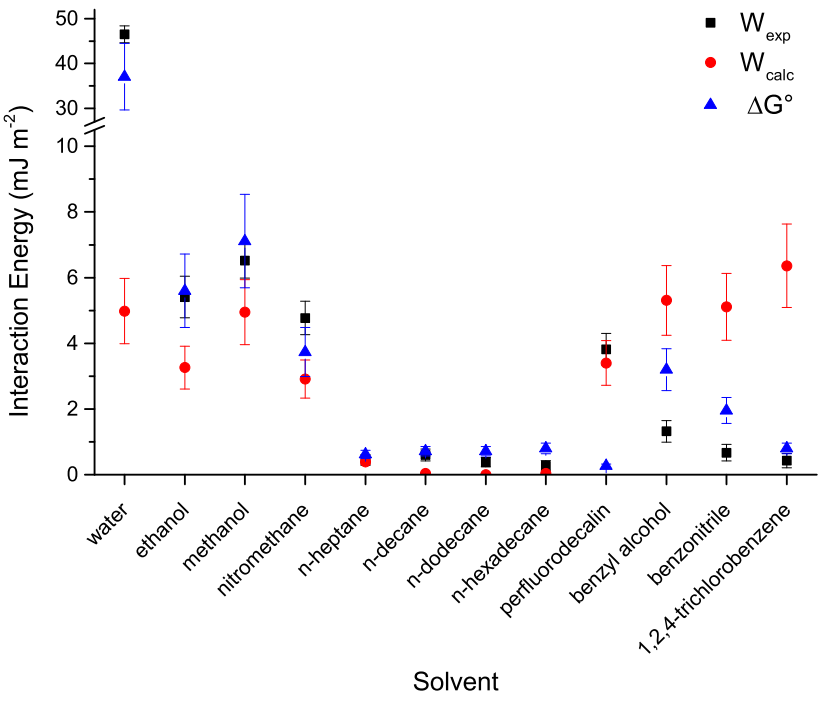

Figure 4.11: Comparison between experimental work of adhesion (W_{exp}) and calculated values from Lifshitz theory (W_{calc}) and the Hunter model ($\Delta G°$) for a system of hydrocarbon surfaces in a number of liquids. Error bars for experimental values correspond to the standard error in the mean, while the theoretical results were assigned a 20 % error.

As Figure 4.11 shows, there are discrepancies between the predictions of Lifshitz theory and measured works of adhesion for a series of different liquids, ranging from polar to non-polar. For the non-polar alkanes and perfluorodecalin, calculated values of the

work of adhesion are somewhat closer to the experimental results, being a little lower than measured. The solvents of greater polarity (ethanol, methanol, and nitromethane) demonstrate that the experimentally obtained values are being underestimated by Lifshitz theory. Finally, the three solvents previously identified in Chapter 3 to be potential outliers (benzyl alcohol, benzonitrile, and 1,2,4-trichlorobenzene), show an extremely poor correlation between experimental and theoretical values. Possible reasons for this will be addressed at a later stage.

A closer correlation was generally obtained between the normalized free energy of the Hunter model and experimentally derived work of adhesion values, including for water but excluding perfluorodecalin. The Hunter model approaches the interaction between non-polar surfaces from the perspective of molecular-scale electrostatic interactions (via the use of hydrogen bond parameters) reaching a thermodynamic equilibrium. The calculated free energy of complexation between the surface and liquid SSIPs consequently provides a measure on the competition between the different molecular species and can thus be used to predict the interaction energy between surfaces.

The work required per unit area to separate two identical materials S in a medium M can be described by the following equation:

$$W_{\mathrm{SMS}} = W_{\mathrm{SS}} + W_{\mathrm{MM}} - 2W_{\mathrm{SM}} \tag{4.3}$$

The work done in separating the two surfaces (W_{SS}) and the medium molecules (W_{MM}) is countered, in part, by the energy released in the creation of the interface of the surfaces and medium molecules (W_{SM}). As the only variable is the change in medium, the change in $W_{\mathrm{MM}} - 2W_{\mathrm{SM}}$ should correspond to the differences in W_{exp}. From a hydrogen bonding point of view, if the hydrogen bond acceptor and donor ability of the medium is increased compared to that of the surface (which for alkanes is weak), then the surface interaction energy should increase correspondingly as the medium-medium complex would have to be broken with an energetic surplus. Conversely, if the hydrogen bond acceptor and donor strengths of the surface and medium are comparable, a negligible pull-off force should be observed as any work done to separate two medium molecules would be regained by the formation of equal strength hydrogen bonds between the surfaces and medium.

For the liquid alkanes investigated, the hydrogen bond donor and acceptor characteristics are similar to those of the adsorbed dodecane monolayer ($\alpha = 0.5$, $\beta = -0.5$). The main contribution to adhesive interactions between the two surfaces comes from dispersion forces, which are well accounted for by both W_{calc} and ΔG°. Interestingly, the experimental interaction energy in perfluorodecalin is noticeably greater than what is predicted by the Hunter model. From the point of view of thermodynamics, perfluoroalkanes ($\alpha = 1.1$, $\beta = -0.2$) have hydrogen bonding donor and acceptor abilities similar to dodecane and therefore the energy required to separate a medium-medium complex should be comparable to the formation of a surface-medium interface. However, the experimental result, which is well described by Lifshitz theory, indicates that the interaction is dominated by dispersion forces (which only have a static contribution of $5.6\,\text{kJ}\,\text{mol}^{-1}$ in the Hunter model), mirroring observations made in previous studies.[165,377] Although the omission of hydrogen bond contributions in the Lifshitz theory is of little consequence when predicting the interactions in non-polar liquids, the same cannot be said for surfaces in polar liquids.

For ethanol ($\alpha = 2.8$, $\beta = -5.6$), methanol ($\alpha = 2.9$, $\beta = -5.6$), and nitromethane ($\alpha = 1.8$, $\beta = -3.2$), the measured W_{exp} values were $30 - 60\,\%$ larger than W_{calc}, which can be attributed to an increase in W_{MM}. This rise would largely be a result of the stronger hydrogen bond donor and acceptor abilities of these polar liquids, and would not lead to an equivalent increase in the magnitude of the surface-medium interfacial energy, W_{SM}, as there is no corresponding change in the monolayer's donor or acceptor strength. Thus, Lifshitz theory is unable to account for these hydrogen bonding interactions (being limited to the use of the bulk dielectric constant in determining the effect of polar media on the van der Waals forces), and underestimates the surface adhesion. This limitation does not apply to the calculation of ΔG° which can, perhaps unsurprisingly, predict this increase in the surface adhesion quite well. The situation becomes even more problematic for Lifshitz theory when considering the adhesion in water, as the predicted work of adhesion is $8\times$ smaller than the experimental one.

That van der Waals interactions are unable to fully explain the full magnitude of the attractive forces between non-polar molecules in water is not new knowledge,[378] and has been attributed to the hydrophobic effect for some time now.[335] The remarkable ability

of the Hunter model to account for such a significant rise in the interaction energy for this system suggests that the hydrophobic effect could be understood by the competition of hydrogen bonding interactions; the inability of non-polar surfaces to bind to water molecules is thought to disrupt the latter's ability to form hydrogen bonds, yielding an enthalpic force.[379] The Hunter model, in using a test molecule of small surface area, would indicate a dominance in the entropic contribution to the free energy change (due to increased order of the water surrounding a non-polar molecule). The confinement energy term, ΔG_c, correlates with $-T\Delta S$ and the origin of the solvophobic effect visible in the results obtained for $\Delta G°$ is not entirely accurate.

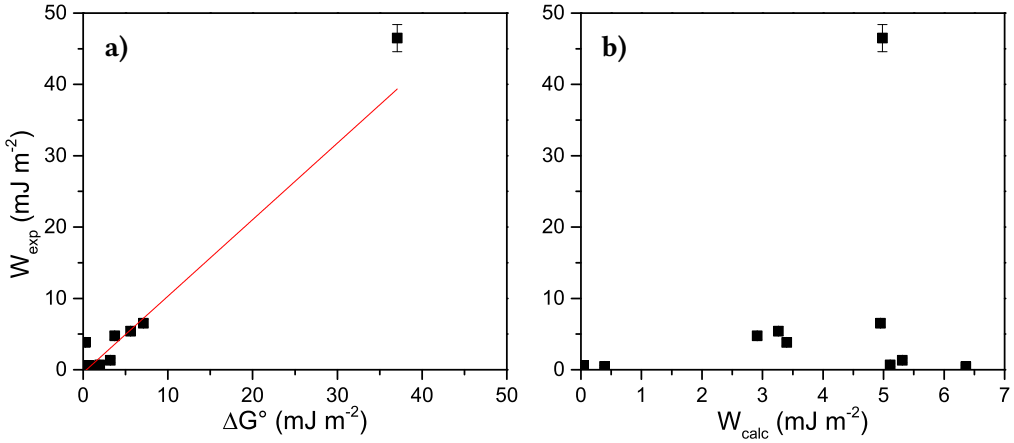

Figure 4.12: Graphs of interaction energies between surfaces of dodecanethiol SAMs on gold. **a)** Experimentally derived work of adhesion (W_{exp}) against the predicted free energy of complexation ($\Delta G°$). R^2 of applied linear fit found to be 0.84. **b)** Experimentally derived work of adhesion against the predicted Lifshitz interaction (W_{calc}). No clear correlation present.

The final three liquids in Figure 4.11 are benzyl alcohol ($\alpha = 2.7, \beta = -4.9$), benzonitrile ($\alpha = 1.4, \beta = -3.6$), and 1,2,4-trichlorobenzene ($\alpha = 0.6, \beta = -1.9$), which were previously recognized for their considerably large predicted Lifshitz work of adhesion compared to the free energy of complexation value, the former suggesting larger adhesive interactions than in polar solvents such as water and methanol. While neither approach offers a perfect match for the experimental values, results obtained via Lifshitz theory diverge by a much greater degree than the free energy (especially for 1,2,4-trichlorobenzene where $\Delta G°$ and W_{exp} are low, unlike W_{calc}). This overestimation in the work of adhesion was previously

attributed to the use of the bulk dielectric constant and refractive index, the latter of which is responsible for the dispersion force contribution to the van der Waals interaction. As the difference in the refractive index of the dodecane and intermediary phases in these three liquids is particularly large, this dispersion interaction becomes the dominant term in Eq. 3.4. Dispersion plays a smaller role in the Hunter model (as seen for perfluorodecalin) and thus avoids the suggestion that the interaction would be greater than in water. Plotting W_{exp} against ΔG° results in a relation that is moderately well fitted by a linear regression ($R^2 = 0.84$), presented in Figure 4.12a, while no such correlation can be found for the Lifshitz theory predictions (Figure 4.12b).

However, it is possible that the 3-medium model and bulk properties of dodecane to simulate the monolayer are not fully appropriate, and may account for some of the discrepancies in the three liquids just mentioned. The assumption that the monolayer would share the same bulk properties as the liquid is not entirely correct, as the dielectric constant is dependent on the density of the medium (see Eq. 2.12). Additionally, it is possible that the underlying gold may affect the interaction between the surfaces as well, as per Eq. 2.3. Therefore, the Lifshitz work of adhesion was recalculated for benzyl alcohol, benzonitrile, and 1,2,4-trichlorobenzene to ascertain whether this may be the source of the discrepancy with the experimentally obtained values.

This was achieved by using bulk properties for a denser medium ($\varepsilon = 2.1$ and $n = 1.45$),[380] while gold was accounted for using a 5-medium calculation. While the recalculated values of W_{ad} were reduced (benzyl alcohol: $3.61\,\text{mJ}\,\text{m}^{-2}$, benzonitrile: $3.65\,\text{mJ}\,\text{m}^{-2}$, 1,2,4-trichlorobenzene: $4.18\,\text{mJ}\,\text{m}^{-2}$), they are still much greater than those obtained via pull-off measurements. Unless there is some layering of the liquid occurring which reduces the interaction between phases due to increased separation (as is potentially seen for some of the systems in the friction experiments), it is likely that Lifshitz theory is unable to fully predict the interaction in highly polarizable liquids.

Based on the preceding discussion, mixtures of benzyl alcohol and methanol were selected for further investigation (there was no change seen in the relation between W_{ad} and [BA] other than a slight change in the magnitude of the interaction after the recalculation described above). Figure 4.13 shows the variation in the calculated work of adhesion and the interaction free energy with the composition of the mixture.

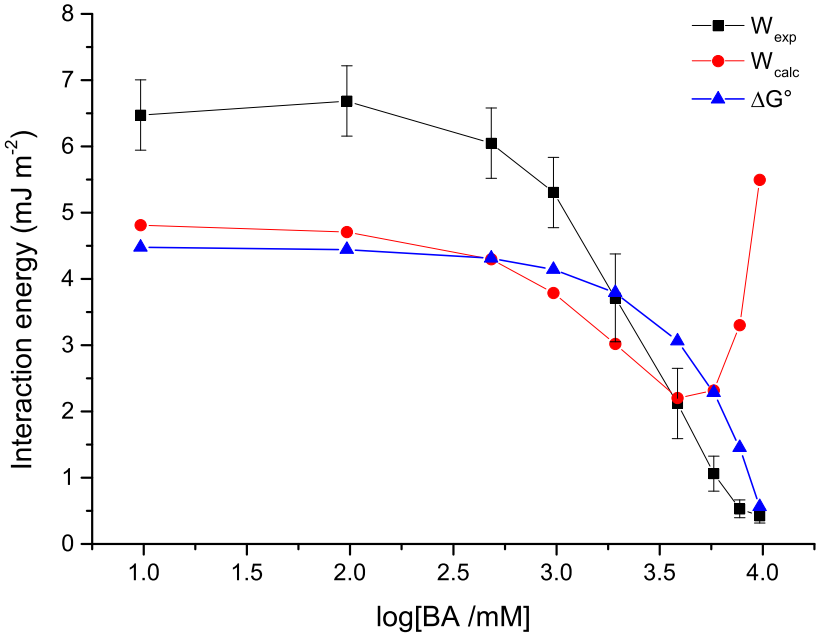

Figure 4.13: Experimental (black squares) and Lifshitz (red circles) works of adhesion, and free energy of complexation (blue triangles) for mixtures of benzyl alcohol and methanol between surfaces of dodecanethiol SAMs on gold, plotted against the log of the concentration of benzyl alcohol.

In contrast to the experimental data, which shows a smooth decline in W_{exp} with [BA], the values of W_{calc} decrease to a minimum and then increase with [BA] to reach a value of 5.31 mJ m^{-2} at [BA] = 4×10^{-3} M, larger than the experimental value at this concentration. However, ΔG° values calculated using the Hunter model decrease with increasing [BA]. The form of the relationship with the concentration of benzyl alcohol is very similar to that exhibited by W_{exp}/[BA], although the experimental value of W declines less sharply. For surfaces of 11-mercaptoundecanoic acid and 11-hydroxyundecyl thiol SAMs on gold, the Hunter model was also found to yield a relationship between ΔG° and concentration that was qualitatively similar to that between F_{a} and concentration.[37,41] Despite the fact that ΔG° decreases more rapidly than W_{exp}, and at a higher concentration, the data strongly suggests that the molecular-scale Hunter model describes the interactions of non-polar surfaces in mixtures of changing polarity more effectively than does Lifshitz theory.

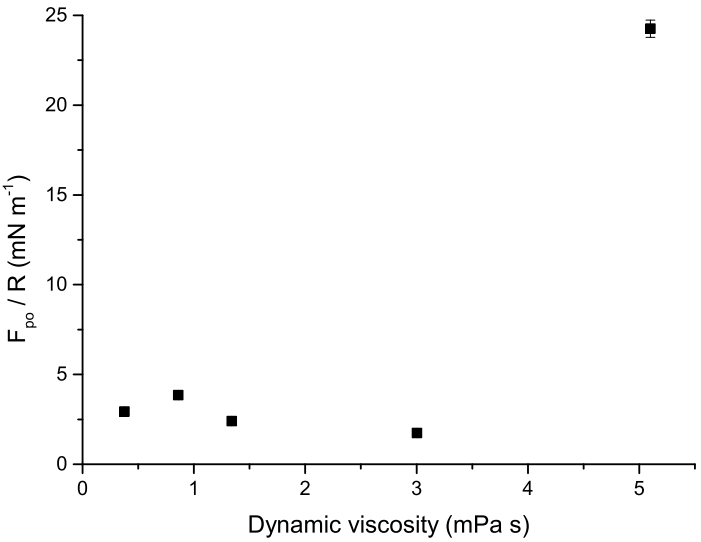

Figure 4.14: Tip radius normalized pull-off forces against dynamic viscosity for dodecanethiol SAMs on gold in various non-polar solvents. In order of increasing viscosity: heptane, decane, dodecane, hexadecane, perfluorodecalin.

To ensure the viscosity of the liquids used was not a factor in the experimental pull-off forces obtained, the pull-off forces (normalized with tip radius) were plotted against the dynamic viscosity; a measure of its resistance to shearing flows. Figure 4.14 shows that there is no positive correlation for the system of DDT surfaces (unlike the one found for hydrogen bonding MUA surfaces[41]), and as such the variation in pull-off values obtained, e.g., perfluorodecalin, are unlikely to be due to a difference in viscosity.

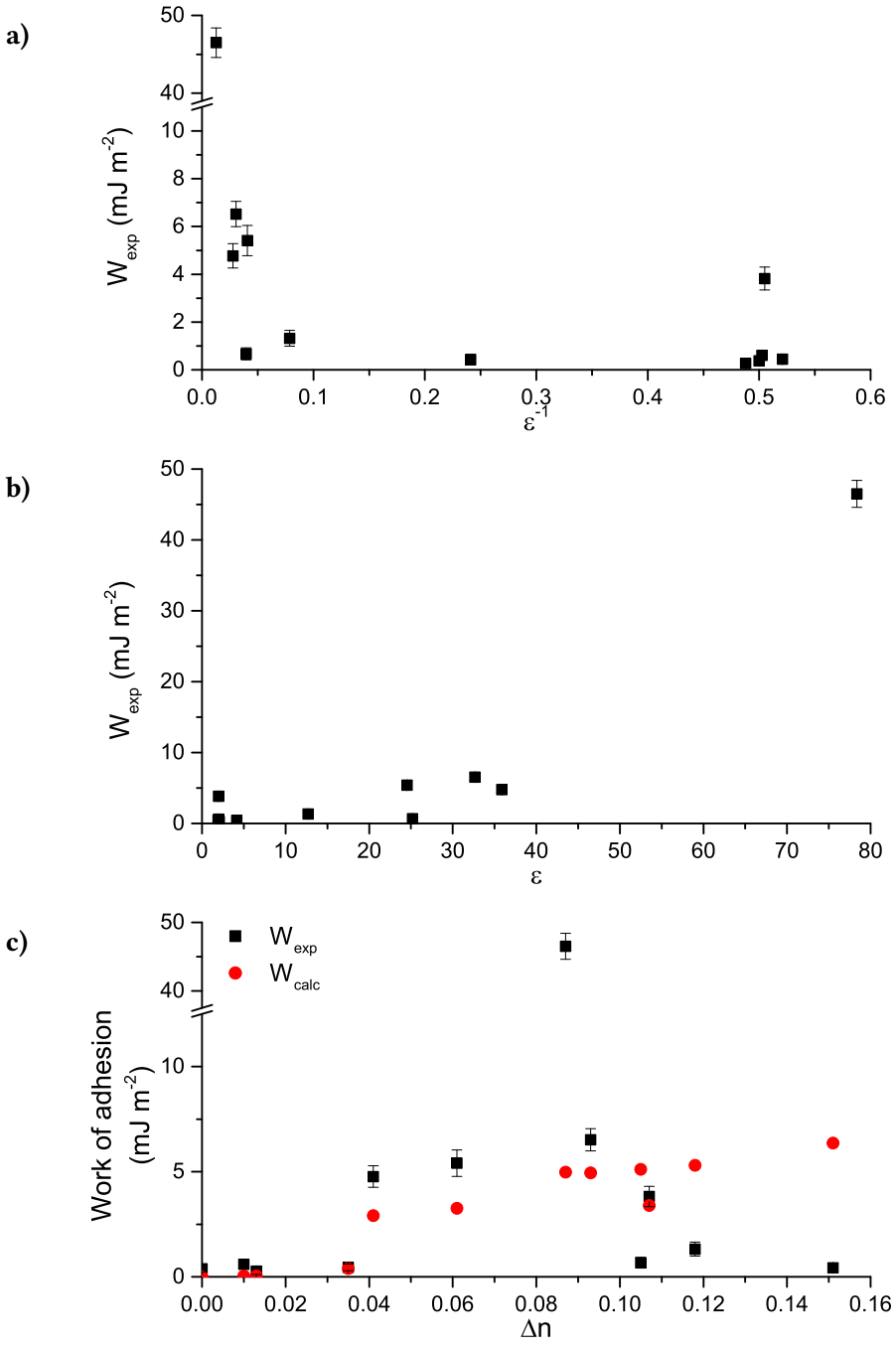

Figure 4.15: Experimental work of adhesion (W_{exp}) between surfaces of dodecanethiol SAMs on gold. **a)** W_{exp} against the inverse dielectric constant (ε^{-1}) of liquid media found in Table 4.2. **b)** W_{exp} against the dielectric constant (ε) of liquid media. **c)** W_{exp} and W_{calc} against the difference in refractive index (Δn) between liquid and surface.

As discussed in Section 3.3.1, the polarity of a liquid can be approximated by the value of its dielectric constant, and is therefore related to γ_{SM} in the Dupré equation (Eq. 3.15). As the polarity of a liquid increases, the contribution of Debye and Keesom interactions is expected to rise, and the energy required to separate two non-polar surfaces increases. Figure 4.15b shows a possible positive relation between W_{exp} and ε, although its exact form is difficult to discern (if one exists at all). Fitting an exponential curve yields an R^2 value of 0.8, but the true relation may be more complex and requires further data collection for liquids with dielectric constants between 40 and 80. The correlation between the interaction energy and ε^{-1} has frequently been used in the literature for systems of polar surfaces,[41,165,190] and a similar relation was found as seen in Figure 4.15a, albeit with greater variation than in the literature (e.g., at $\varepsilon^{-1} = 0.5$).

It was suggested above that the difference in the refractive index, responsible for the dispersion force, was the reason for the overestimation of the van der Waals interaction between DDT surfaces. Indeed, in Figure 4.15c it can be seen that the theoretical values gradually increase with Δn, which is not repeated in the experimental values. It is clear therefore that using the bulk dielectric constants and refractive indices of the media involved is a rather crude way of predicting the interactions between non-polar surfaces, as hydrogen bonding interactions and the large interaction energy in water are left completely unaccounted for, as seen in the results presented here.

A comparison of the normalized pull-off forces in water and ethanol for the various monolayers formed can be seen in Table 4.3. The pull-off forces in water remain largely unchanged in the different thiol and silane monolayers, indicating that the differences may be masked by experimental error. When recording the pull-off forces for samples of alkylphosphonic acids, an appreciable reduction in the measured pull-off over time was discovered. This was attributed to the poor stability of alkylphosphonic acid monolayers on oxide surfaces in water, as has been previously discovered for Al_2O_3 (0001) surfaces.[213] Therefore, pull-off and friction measurements in water for phosphonic acid SAMs were not performed beyond some preliminary pull-off measurements over time (Figure 4.16).

Table 4.3: Tip radius normalized pull-off forces (F_{po}/R) in water and ethanol between surfaces with various adsorbed monolayers on either gold, aluminium, or glass as indicated. Due to their instability, phosphonic acid pull-off forces in water were not recorded.

	F_{po}/R (mN m^{-1})	
Monolayer (substrate)	**water**	**ethanol**
DDT (Au)	292 ± 12	34 ± 4
ODT (Au)	298 ± 15	24 ± 6
DDPA (Al)	—	10 ± 5
ODPA (Al)	—	14 ± 5
DTS (SiO_2)	289 ± 35	9 ± 3
OTMS (SiO_2)	272 ± 29	11 ± 4

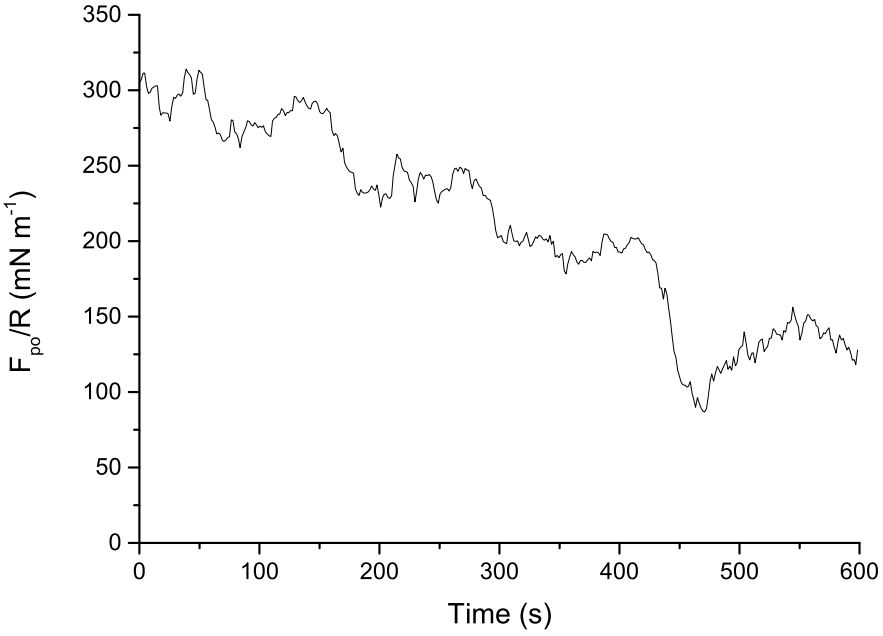

Figure 4.16: Normalized pull-off forces for dodecylphosphonic acid (DDPA) SAMs in water against time.

For ethanol, however, there was a difference in the normalized pull-off force measured for alkylthiols on gold and for analogous SAMs formed on other surfaces. Even amongst the thiols themselves ODT has a slightly reduced pull-off force in ethanol than DDT, which could be explained by the longer chain length increasing the separation between the underlying bulk gold surfaces ($F \sim 1/D^2$). This would imply that the gold substrate contributes to the interaction energy between the alkylthiol SAM surfaces in ethanol, and potentially other liquids as well. The size of the gold-gold interaction is over an order of magnitude lower than force exerted in the presence of water, and therefore would lie within the error values obtained for the related pull-off forces. The same effect of the underlying metal is not found between the phosphonic acid and silane SAMs. These results could be attributed to the lower experimentally obtained Hamaker constants between silica–water–silica ($A = 0.83 \times 10^{-20}$ J) or alumina–water–alumina ($A = 6.7 \times 10^{-20}$ J) and gold–water–gold ($A = 25 \times 10^{-20}$ J) interfaces.[6,381] However, further experiments on a wider range of SAMs with varying chain lengths would be required to verify these findings.

4.3.5 Friction Forces

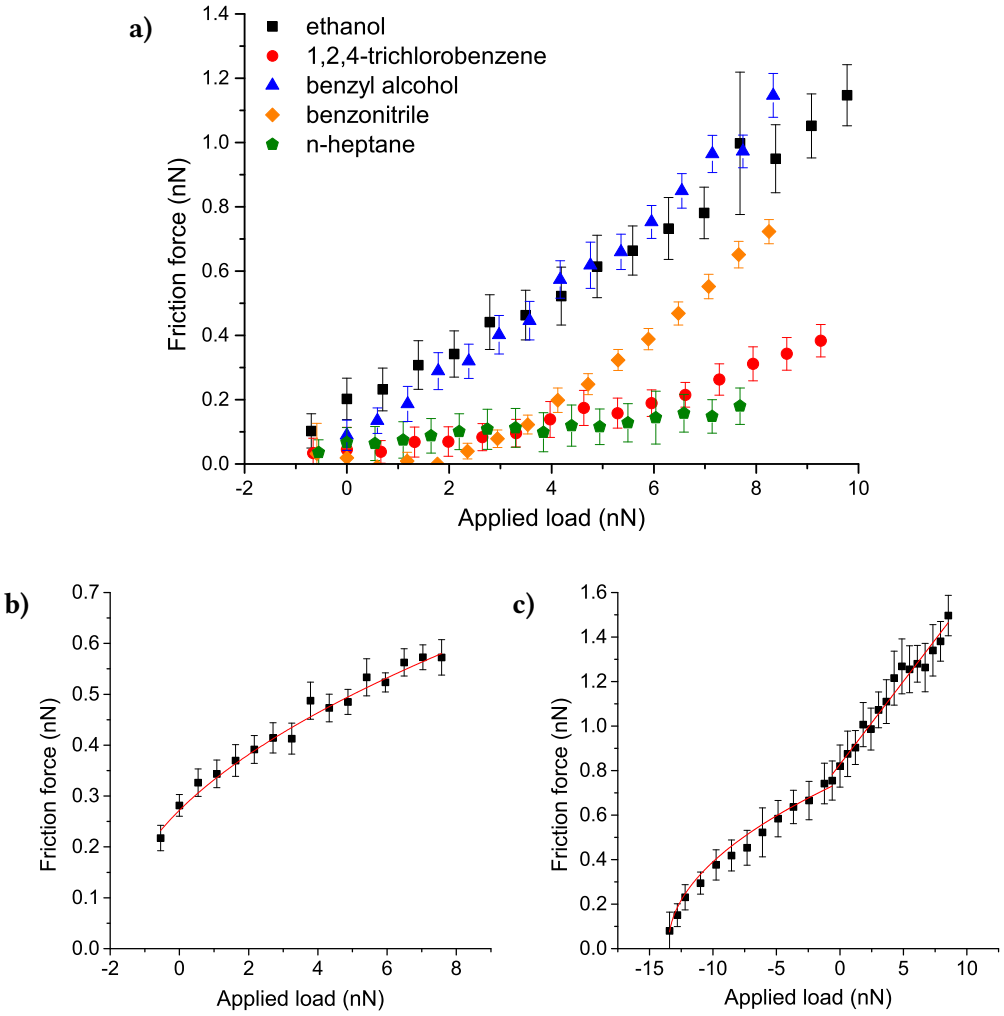

Figure 4.17: Friction-load plots for dodecanethiol SAM surfaces in sliding contact in various liquid media. **a)** Friction graphs for solvents demonstrating linear behavior. **b)** Friction graph showing sublinear behavior in methanol. **c)** Friction graph for water showing sublinear behavior at tensile loads and linear behavior under compressive loading.

The friction data collected via FFM for DDT surfaces in various liquids is presented in Figure 4.17. These were further subdivided into friction-load plots for liquids demonstrating linear friction behavior (Figure 4.17a), and those which demonstrated sublinear behavior in methanol and water (Figures 4.17b and 4.17c, respectively). Little

hysteresis was observed when ramping load up and down, and the plotted graphs show the friction-load behavior at decreasing loads. Coefficients of friction (μ) and normalized critical shear strengths ($\tau/K^{2/3}$) obtained from the fitting of the different plots can be found in Table 4.4.

Table 4.4: Coefficients of friction (μ) and critical shear strengths ($\tau/K^{2/3}$, via the GFE) for sliding contacts between gold-coated AFM probes and surfaces with adsorbed dodecanethiol monolayers in various liquid media.

Medium	μ	$\tau/\mathrm{K}^{2/3}$ **(Pa$^{1/3}$)**
ethanol	0.10 ± 0.01	—
methanol	—	2.17 ± 0.43
n-heptane	0.013 ± 0.010	—
benzyl alcohol	0.11 ± 0.02	—
L < 2 nN	0.005 ± 0.002	—
benzonitrile		
L ≥ 2 nN	0.10 ± 0.04	—
L < 3 nN	0.015 ± 0.020	—
1,2,4-trichlorobenzene		
L ≥ 3 nN	0.041 ± 0.010	—
L < 0 nN	—	2.09 ± 0.37
water		
L ≥ 0 nN	0.08 ± 0.02	—

Friction-load plots were normalized to zero when not in sliding contact, as friction forces when out of contact of ca. 0.1 – 0.15 nN were measured; an expected result due to the many sources of error in a liquid FFM environment: piezo drift, detector and laser noise, solvent volatility, and compatibility of solvent and O-ring. Within the group of friction-load plots demonstrating linear behavior, the majority pass through the origin. Ethanol and benzyl alcohol are exceptions to this as they possess a greater friction force at zero applied load, and ethanol continuing with a positive force into the tensile regime. Considering both ethanol and benzyl alcohol were found to result in greater adhesion

forces than other non-polar liquids in the previous section, this outcome is not entirely unexpected. However, it is also likely that the adhesive interaction is not sufficient to make the area-dependent term of the friction force—discussed at greater length later—be significant, as is the case for water and methanol.

In benzonitrile, and to a lesser extent 1,2,4-trichlorobenzene, a two-slope behavior was found, with the coefficient of friction rising from 0.005 to 0.1 after a threshold load of 2 – 3 nN was applied. In previous studies on the friction of methyl-terminated monolayers, a slope change was found at loads of ca. 10 nN, and was theorized to occur due to a change in the possible energy dissipation mechanisms such as the creation of gauche or other defects under a higher sliding strain.[382] However, as none of the other linear friction plots for DDT show this behavior, it is unlikely for this mechanism to occur as it would be expected to appear in all friction-load plots of DDT systems.

A two-slope behavior has also been observed in the author's laboratory for systems in n-octanol, and has been attributed to the formation of physisorbed layers at the monolayer–liquid interface.[21] Molecular dynamics (MD) simulations of various organic lubricants being compressed between sliding contacts have shown that the pressure required to squeeze out the last layer of molecules increases as the molecular size of the non-polar liquid increases, in the order of several hundred MPa.[383] It is therefore plausible that the benzonitrile physisorbs to the DDT surface through van der Waals interactions, and is removed at applied loads greater than 2 nN, corresponding to a pressure of ca. 100 MPa.

Methanol and water were found to yield the greatest adhesion strength (6.52 and 46.5 mJ m^{-2}, respectively), the effect of which is manifested as a sublinearity in the friction-load behavior seen in their corresponding graphs in Figure 4.17. To fit the sublinear sections of the graphs, the general fitting equation (GFE) developed by Carpick et al.[68] was used, providing the means to determine the transition parameter (α_T), the critical shear strength (τ), and an estimation of the bulk elastic modulus of the monolayers (K). To allow the shear strength to be used independently of different SAMs, it was normalized with respect to K (5 GPa from the derived Maugis parameter found using the GFE). The transition parameters obtained from the GFE fit of the two sublinear plots were 0.08 and 0.10 for water and methanol respectively, which corresponds to DMT-like

behavior. In water, however, this sublinear relationship exists solely in the tensile regime and transitions into a linear relation at applied loads greater than zero. The reason for this behavior is not immediately apparent.

The relationship between the coefficient of friction and the experimental and theoretical interaction energies is shown in Figure 4.18. If one compares the coefficient of friction to the work of adhesion obtained in the previous section (Figure 4.18a), there appears to be a rise (to an upper limit) in the sliding interaction in liquids generating greater adhesive forces. At adhesion energies below $1\,\mathrm{mJ\,m^{-2}}$, the coefficient of friction drops to 0.04 or lower, increasing to about 0.1 for liquids with moderately low observed work of adhesion. An invariance in the coefficient of friction has been previously demonstrated for both polar and non-polar liquids,[21,37,190] and is attributed to plowing of the monolayer by the AFM tip. It is therefore more likely that the decrease in the coefficients of friction for the two liquids generating the lowest interaction energies to be somewhat anomalous. A suggested reason for this phenomenon is that the liquid binds strongly to the surface, leading to a thin surface film of solvent molecules that is not removed when the tip is brought into contact with the surface. The energy dissipation during friction is therefore not through the plowing of the monolayer, but through a form of fluid film lubrication.

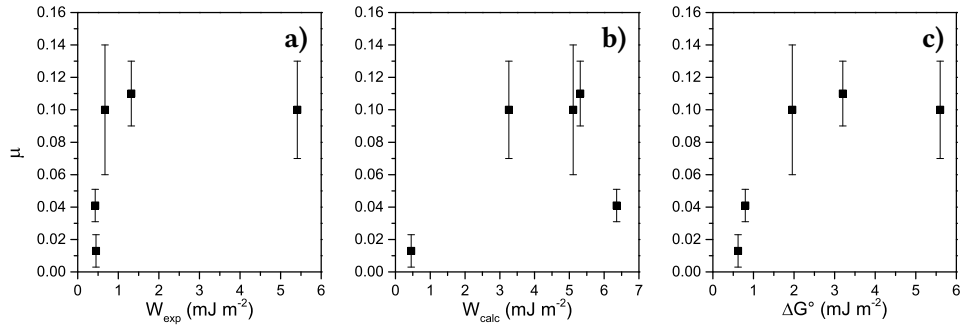

Figure 4.18: Coefficient of friction (μ) against experimental and theoretical adhesive interactions between dodecanethiol surfaces in various liquids. **a)** Experimental work of adhesion (W_{exp}). **b)** Lifshitz theory calculated work of adhesion (W_{calc}). **c)** Hunter model normalized free energy of complexation (ΔG°).

Comparing μ to the calculated Lifshitz work of adhesion and the Hunter free energy of complexation (Figures 4.18b and 4.18c, respectively) results in a similar relation for both approaches. An exception to this is benzonitrile, which once again demonstrates the potential weakness of Lifshitz in determining the adhesive energies between non-polar surfaces. The normalized critical shear strength of water and methanol are also comparable in magnitude, despite the large difference (40 mJ m^{-2}) in the adhesive interactions of both liquids.

Considering that the coefficient of friction remains constant after a threshold adhesive energy, and that the relation shifts from linear to sublinear, one may question whether the friction force originates from multiple sources rather than simply from the contact area. By considering the solvation state of the surface, in a similar fashion as for the pull-off forces, it may be possible to better understand the shift in the type of friction-load relation measured. It has previously been suggested that it may be appropriate to treat friction force as the sum of load-dependent and area-dependent terms,[112,384,385] using τ as the surface shear strength and A as the area of contact:[190]

$$F_{\mathrm{fr}} = \mu F_{\mathrm{N}} + \tau A \tag{4.1}$$

From DMT mechanics, the contact area between a sphere and a half-space is given by:

$$A = \pi \left(\frac{R}{K}\right)^{2/3} (F_{\mathrm{N}} + 4\pi\gamma R)^{2/3} \tag{4.4}$$

where R is the radius of the sphere (probe), K is the bulk modulus, γ is the surface free energy, and $F_{\mathrm{a}} = 4\pi\gamma R$. By combining the two equations, the following friction force relation is found:

$$F_{\mathrm{fr}} = \mu(F_{\mathrm{N}} + F_{\mathrm{a}}) + \tau \left(\frac{R}{K}\right)^{2/3} \pi(F_{\mathrm{N}} + F_{\mathrm{a}})^{2/3} \tag{4.5}$$

The same correction has been applied to the total load of both terms, in order to account for the addition load caused by adhesion. As the adhesive interaction between surfaces in various liquids decreases, the area-dependent term is expected to become insignificant, and has been experimentally verified by the linear results in Figure 4.17a for liquids with

low adhesion. Once the interactions between surfaces become significant, the rise in the area-dependent shear term causes the friction-load relationship to become non-linear, as seen for the DDT systems in water and methanol.

However, if one fits the friction-load plots with Eq. 4.5, the surface shear strengths increase as a function of adhesion, as seen in Figure 4.19a. The coefficient of friction remains largely invariant at ≈0.1 for adhesion energies above $1\,\mathrm{mJ\,m^{-2}}$, as seen before (the same reason is proposed for lower coefficients of friction for liquids yielding low interaction energies). Plotting these results against the values obtained via Lifshitz theory and the Hunter model, it is apparent that the change in the surface shear strength as a function of surface interaction is well predicted by hydrogen bond thermodynamics. The same cannot be said for Lifshitz theory which, perhaps predictably, fails to offer values similar to those obtained through experiment.

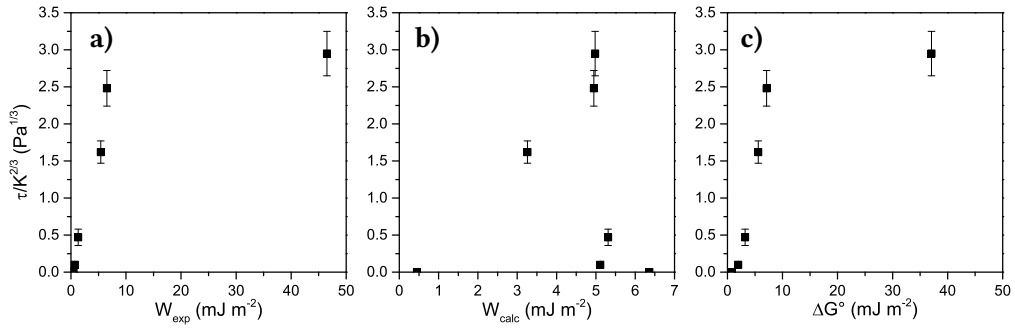

Figure 4.19: Normalized shear strength ($\tau/K^{2/3}$, from Eq. 4.5) against experimental and theoretical adhesive interactions between dodecanethiol surfaces in various liquids. **a)** Experimental work of adhesion (W_{exp}). **b)** Lifshitz theory calculated work of adhesion (W_{calc}). **c)** Hunter model normalized free energy of complexation (ΔG°).

Recent work by Brukman et al.[361] has suggested that there exist two primary mechanisms of energy dissipation in such systems of two surfaces with adsorbed SAMs in sliding contact: viscoelastic plowing and interfacial shearing. SAMs are not perfectly rigid solids, and are capable of being compressed, which leads an AFM tip to vertically deform the monolayer molecules directly at the point of contact by a height h, as shown diagrammatically in Figure 4.20. As the tip slides across the surface, it must therefore compress, deform, or tilt adjacent molecules to move, resulting in a frictional force. Increasing the load applied leads to deeper penetration into the SAM, and therefore a

greater friction force is experienced. For a parabolic tip of radius R penetrating the surface, the projected area (A_P) of the tip in the plane of movement is given by:

$$A_P \propto \sqrt{Rh^3} \tag{4.6}$$

For Hertzian or DMT contacts (which the data suggests), and using the TCCM model for a coating of thickness t, the load (L) is related to the penetration height (h) by:[57,81]

$$L = \frac{\pi E_u R h^2}{t} \tag{4.7}$$

Therefore, energy is dissipated in the lateral stresses applied to the individual chains of the monolayer as the tip plows through it. For the systems investigated in this project, at a maximum load of 10 nN the tip would penetrate 1.13 Å into the monolayer (approximately 10 % of the total thickness).

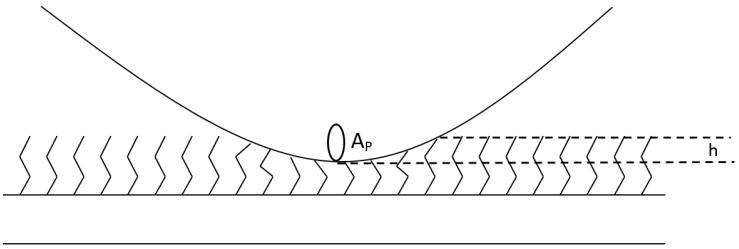

Figure 4.20: Diagram showing the compression effect of the AFM tip on the monolayer when applied under load to the surface.

This mechanism has been given further support by studies showing that this plowing effect, causing a linear friction-load plot, is only present for coated substrates and coated or uncoated tips.[386] Subsequent MD simulation studies have also confirmed that there exists penetration of monolayers by the AFM tip at applied loads well below 10 nN, without affecting the linearity of the friction-load plot obtained.[85,387] The simulations by Knippenberg et al.[387] in particular provide evidence of energy dissipation occurring during the plowing mechanism, as the sum of the force generated by monolayer chains pushing the tip in the direction of movement (i.e., behind the tip) is smaller than that required to compress/bend/tilt those in the forward direction.

The effect of adhesion on the plowing mechanism has not been confirmed, but was proposed by Brukman et al. to simply add to the total load experienced by the AFM probe (effectively increasing A_P), and therefore the linear dependence between the friction and the load is maintained. From the data presented in Figure 4.18, however, there does not appear to be much effect of adhesion on the coefficient of friction (and thus the load-dependent term) after a critical threshold, but instead it has a greater impact on the surface shear strength as seen in Figure 4.19. It is therefore suggested that the primary effect of adhesion for non-polar surfaces in sliding contact is on the area-dependent term, primarily through the increase in the surface shear strength and the effective contact area according to DMT mechanics (see Eq. 4.5).

In the case of two-slope friction-load plots, the plowing mechanism is likely not experienced until the physisorbed layer of liquid molecules is displaced at a threshold load, after which the tip is able to plow into the solid monolayer, thus increasing the friction force recorded. In effect, the monolayers of solvent in these systems are acting as a molecular lubricant. For the linear friction-load plots, an increase in the adhesive interaction also resulted in a rise in the friction force at zero applied loads, just as was observed in previous studies.[85,361]

The sublinearity of the friction-load plots obtained from liquids that yield greater tip–sample adhesion energies can therefore be attributed to a rising surface shear strength, causing the area-dependent term to dominate the dissipative pathway. Work is done breaking and making adhesive interactions at the interface between sample and tip, which in turn generates the shearing experienced by the AFM probe. While plowing still contributes to the overall friction force, the energy required to shear the interactions between the tip and the deformed monolayer within the area of contact increases. Conversely, as the shear contribution to friction tends to zero, the friction-load relationship becomes linear as $F_{fr} \propto (F_N + F_a)$. The fact that the friction relation in this limiting case is not Hertzian in nature (i.e., $F_{fr} \propto F_N^{2/3}$) gives further credence to the idea of friction being the sum of load- and area-dependence terms. The change in the relation at applied loads greater than zero (from sublinear to linear in the case of water) would then indicate that the plowing mechanism begins to dominate, either due to an increase in the energy dissipation due to plowing, or a decrease in the surface shear strength.

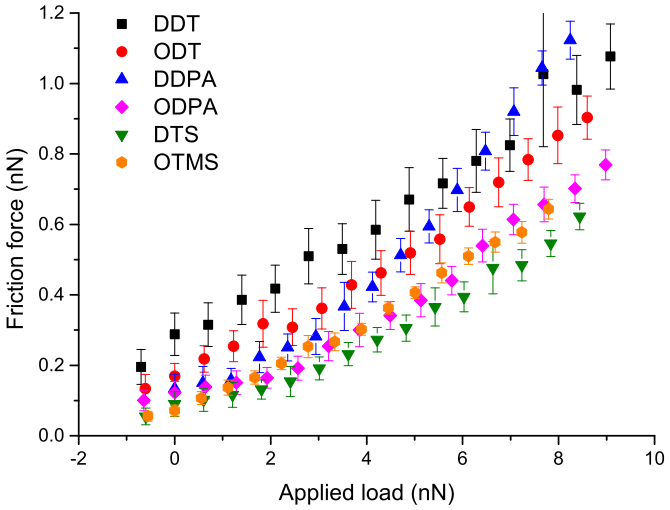

Figure 4.21: Friction-load plots obtained in ethanol for self-assembled monolayers of: dodecanethiol (DDT) and octadecanethiol (ODT) on gold, dodecylphosphonic acid (DDPA) and octadecylphosphonic acid (ODPA) on aluminium, and dodecyltrichlorosilane (DTS) and octadecyltrimethoxysilane (OTMS) on glass.

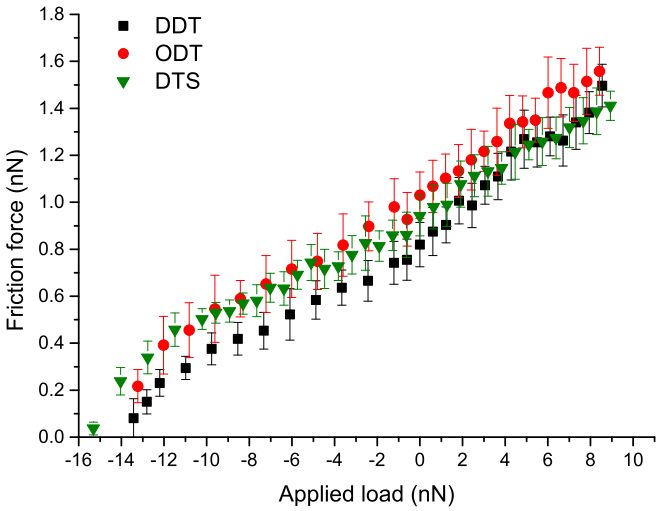

Figure 4.22: Friction-load plots obtained in water of self-assembled monolayers of: dodecanethiol (DDT) on gold, octadecanethiol (ODT) on gold, and dodecyltrichlorosilane (DTS) on glass.

Table 4.5: Coefficients of friction (μ) and critical shear strengths ($\tau/K^{2/3}$, via the GFE) for sliding contacts between AFM probes and surfaces with adsorbed hydrocarbon monolayers in water and ethanol.

	DDT		**ODT**		**DDPA**	
Medium	μ	$\tau/\mathrm{K}^{2/3}$ ($\mathrm{Pa}^{1/3}$)	μ	$\tau/\mathrm{K}^{2/3}$ ($\mathrm{Pa}^{1/3}$)	μ	$\tau/\mathrm{K}^{2/3}$ ($\mathrm{Pa}^{1/3}$)
L < 0 nN	—	2.09 ± 0.37	—	2.49 ± 0.29		
water					—	—
L ≥ 0 nN	0.08 ± 0.02	—	0.07 ± 0.01	—		
L < 3 nN					0.05 ± 0.01	
ethanol	0.10 ± 0.01	—	0.08 ± 0.01	—		—
L ≥ 3 nN					0.15 ± 0.02	
	ODPA		**DTS**		**OTMS**	
Medium	μ	$\tau/\mathrm{K}^{2/3}$ ($\mathrm{Pa}^{1/3}$)	μ	$\tau/\mathrm{K}^{2/3}$ ($\mathrm{Pa}^{1/3}$)	μ	$\tau/\mathrm{K}^{2/3}$ ($\mathrm{Pa}^{1/3}$)
L < 0 nN						
water	—	—	—	2.39 ± 0.27	—	—
L ≥ 0 nN						
L < 3 nN	0.02 ± 0.01		0.03 ± 0.01		0.05 ± 0.01	
ethanol		—		—		—
L ≥ 3 nN	0.09 ± 0.02		0.08 ± 0.01		0.10 ± 0.02	

The frictional properties of other alkane SAMs were also investigated in water, chosen for its strong sublinearity in the tensile region for DDT, and ethanol, due to its linear friction-load plot with a non-zero friction at zero applied load. The results of these friction experiments are presented in Figures 4.21 and 4.22 for ethanol and water, respectively. The coefficients of friction and normalized surface shear strength as obtained via the GFE are given in Table 4.5.

A decrease in the intercept value—and hence L_c—was observed for those systems with a lower measured adhesion energy in ethanol (see Table 4.3), effectively shifting the plot towards negative loads. This mirrors the observations made earlier for DDT surfaces in liquids of varying adhesive interactions and those of previous studies,[85,361,386] further corroborating the supposition of friction being the sum of load- and area-dependent terms. The fact that the monolayers of varying length and substrate demonstrate behavior indicative of lower adhesion gives confidence in the previously obtained adhesive energy values. As suggested earlier, it is possibly due to the interactions of the underlying substrates with each other and with the adsorbed monolayers (or relative lack thereof in the case of silanes on glass). However, there may be other factors that may lead to a change in the measured friction—and adhesion— force; the packing density in particular.

Both alkanethiol SAMs demonstrate the same friction-load behavior (albeit at a slight vertical offset to each other, commensurate with a greater F_a) with comparable coefficients of friction. A similar two-slope behavior to that observed for benzonitrile between DDT surfaces (Figure 4.17a) was obtained for the other families of monolayers. The threshold load for the transitions between slopes is roughly 3 nN in all of these monolayers, implying that there might be a similar change occurring at each surface. It was previously proposed that this effect may be due to the physisorption of the solvent to the surfaces, requiring a threshold amount of pressure in order to squeeze out the last layer of liquid.[383] The coefficients of friction below this threshold applied load are similar in magnitude for the plots affected, and above it they match those derived for DDT and ODT. An exception to this is DDPA, which shows a much sharper increase in the coefficient of friction after 3 nN load, which usually arises due to poorer packing or the presence of defects.

The friction-load plots in water (Figure 4.22) demonstrate similar behavior in the different monolayers investigated, and show a significant departure from the results obtained in ethanol (from linear to sublinear). Friction measurements were not performed for phosphonic acid SAMs due to their degradation in water, as described in the previous section. When fitted with the GFE, the transition parameter, α_T, was found to be 0.15 and 0.00 for ODT and DTS, respectively. Compared to the value for DDT surfaces (0.08), these would suggest pure DMT behavior for DTS and greater JKR behavior (while maintaining predominantly DMT character) for ODT. However, the transition parameters for the thiol

monolayers are still much closer to an ideal DMT system ($\alpha_T = 0$) than a JKR one ($\alpha_T = 1$), so the assumption of a DMT contact area in Eq. 4.5 remains valid. The transition to a more linear relation after the tensile region is also experienced for the ODT system in water, albeit to a lesser degree than seen in DDT, with a similar coefficient of friction determined from the linear section of the graph. Additionally, the surface shear strength, as derived from the fitting of the GFE, is greater for both ODT and DTS.

In contrast, fitting the plots using the load- and area-dependent friction equation results in normalized surface shear strengths of 2.9 and 2.7 $Pa^{1/3}$ for ODT and DTS, respectively; within error of the value 3.0 $Pa^{1/3}$ for DDT. As all three monolayer systems yielded equivalent pull-off forces and have similar surface shear strengths, the offset in the friction force measured is potentially due to the difference in the packing densities and defects in the monolayers (as in ethanol previously).

4.4 Conclusions

The adhesion between gold-coated AFM tips and substrates functionalized with non-polar 1-dodecanethiol (DDT) SAMs was investigated in number of liquids, and was found to increase roughly as the polarity of the liquid increased. When compared to the predictions of the interaction between DDT surfaces (alkane surfaces for the Hunter model) calculated in Chapter 3, there was a better agreement with Hunter's surface site interaction point (SSIP) model than with Lifshitz theory. The SSIP model assumes a molecule will interact through specific interaction sites of constant area and volume, with assigned hydrogen bond donor or acceptor parameters based on the maxima and minima of their molecular electrostatic potential surface. While interactions in non-polar liquids are generally well defined by both approaches, Lifshitz theory was found to consistently underestimate the adhesion energy in more polar liquids, and in the case of water the calculated work of adhesion was underestimated by an order of magnitude. Additionally, for the aromatic compounds Lifshitz theory overestimated the surface interactions by a considerable margin, due to the use of bulk properties in its calculations.

In contrast, good agreement was in general obtained between the Hunter model and the experimental data. The previous chapter identified benzyl alcohol and methanol mixtures as suitable candidates for further investigation, due to their extreme disagreement in the relation of the interaction energy with respect to the concentration of benzyl alcohol between the two theoretical approaches. The relation obtained using experimental pull-off force data strongly resembles the predictions offered by the Hunter model, providing further support for the validity of considering the importance of hydrogen bonding interactions in systems of non-polar surfaces in contact. The effect of the underlying substrate and chain length on adhesion was also explored, using 1-octadecanethiol (ODT) on gold, dodecyl and octadecylphosphonic acid (DDPA, ODPA) on aluminium, and n-dodecyltrichlorosilane (DTS) and n-octadecyltrimethoxysilane (OTMS) on glass. The results suggest there may be a minor influence by the substrate for measurements taken in ethanol, with gold causing greater adhesive interactions than aluminium or silica. However, in water these differences were effectively gone.

These finding are remarkable, as the SSIP model of hydrogen bond thermodynamics was developed to calculate the equilibrium free energies of complexation of molecules in solution, while the properties of the systems investigated and the conditions of the AFM experiments are quite removed from these ideal conditions. Instead of being completely unrestricted, the monolayer molecules have a greatly reduced range of motion (translation, rotation, etc.) with a variable area of contact (and hence number of interacting SSIPs) between surfaces. Furthermore, the interactions measured with an AFM are dynamic, with the tip constantly experiencing changes in acceleration, thus increasing the likelihood of time-dependent effects. Nonetheless, the data presented in this chapter suggests that the Hunter model is capable of predicting the nature of the interaction between non-polar surfaces in a number of liquids in more situations than by considering van der Waals interactions alone.

Friction-load plots were also obtained for systems of DDT surfaces in many of the same liquids, the relations of which were found to be dependent on the adhesive energies in the medium. Liquids causing a lower adhesive interaction (as measured using pull-off forces) resulted in linear friction-load relationships. At adhesion energies below 1 mJ m^{-2} Amonton's Law behavior was observed, while increasing adhesion shifted the friction-load

plots towards non-zero friction at zero applied load. Above 6 mJ m^{-2} the friction-load relationship became sublinear, with friction being measured well into the tensile region for systems in water. This behavior was explained by considering friction to be the sum of load- (μ) and area-dependent (τ) terms, caused by the energy dissipation through plowing through the monolayer and shearing the intermolecular interactions, respectively. The coefficient of friction, a measure of the plowing mechanism, remained independent of adhesion for the majority of liquids, except at adhesion energies below 1 mJ m^{-2} where it reduced close to zero. Conversely, τ was found to increase with the adhesion, thus becoming dominant as the interactions between surfaces increased and caused the friction-load plots to become non-linear.

The effect of chain length and substrates on friction between SAM coated surfaces was also examined. In ethanol, the difference in adhesion between the different monolayers was observed through the shift in the friction value at the intercept, as expected from the previous results. A two-slope friction-load behavior was also observed for the phosphonic acid and silane SAMs, with the coefficient of friction increasing considerably at loads greater than 3 nN. This effect was also observed in benzonitrile for DDT surfaces, and is suggested to occur due to the formation of physisorbed layers of the liquid at the surface, which require a threshold level of pressure to be fully "squeezed" out. The coefficients of friction above this threshold load were equal in all the monolayers, except for DDPA which exhibited a coefficient of friction greater by 50 %, which is attributed to the difference in the packing density and quality of the monolayer formed. In water, the friction-load behavior in DDT, ODT, and DTS were largely the same, but with slightly greater friction forces at lower loads. These are also credited to the difference in the molecular organization of the monolayers.

CHAPTER 5

Mechanochemical Nanopatterning

Selective Deprotection of OEG-NPEOC-APTES SAMs via AFM

In this chapter, the removal of the NPEOC protecting group of self-assembled monolayers (SAMs) formed by the adsorption of OEG-NPEOC-APTES on silicon is demonstrated by mechanochemical means, without requiring the UV exposure conventionally used in the photodeprotection of this molecule. A simplified schematic of the proposed proposed group removal mechanism is shown in Figure 5.1 below. The effect of the applied load, tip speed, and tip environment on the characteristics of the scribed features are examined. The fabrication of complex structures using this technique with a commercially available AFM instrument is also demonstrated. Finally, the results of density functional theory (DFT) simulations are presented with the aim of gaining a further understanding of the NPEOC photodeprotection mechanism, and how conversion of mechanical energy may be involved in this process.

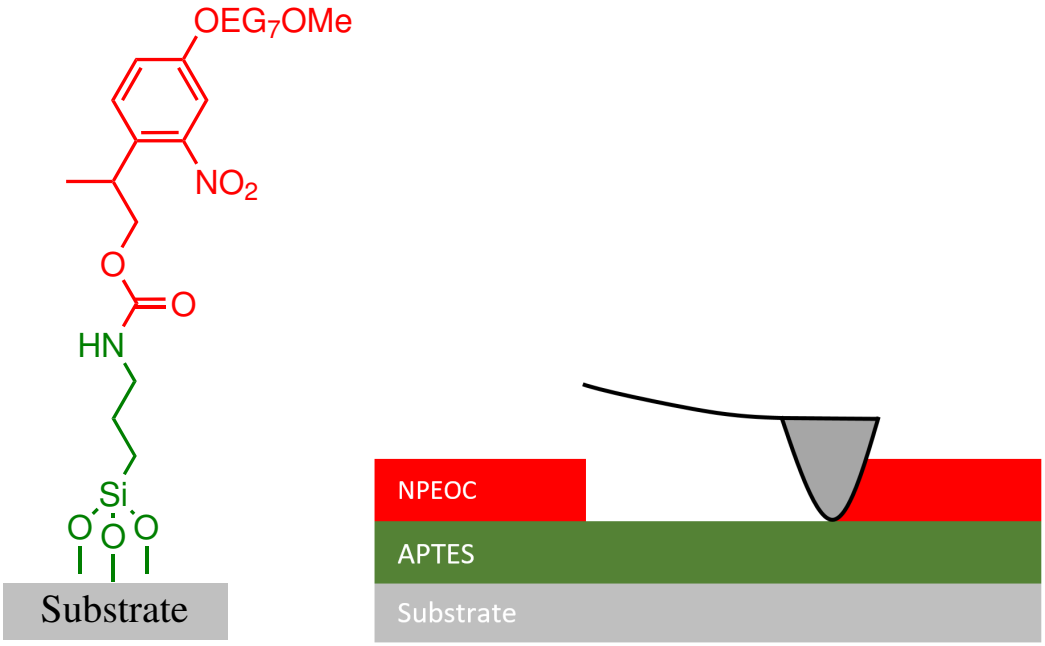

Figure 5.1: **Left)** Skeletal structure of a single OEG-NPEOC-APTES molecule adsorbed onto a clean silicon surface. **Right)** Schematic diagram showing region of OEG-NPEOC-APTES SAM that has been mechanochemically removed by an AFM tip.

5.1 Introduction

The surge of research into nanofabrication, specifically in top-down lithographic techniques (where the desired structures are formed from the removal of material), has allowed for a rapid expansion of many technological areas, such as electronics and sensing. These procedures are expected to lead to more advanced technologies, especially as bottom-up fabrication methods improve, in which smaller "building blocks" such as atoms or molecules are combined to create functional devices. Some of these applications include bio-sensor arrays,[388,389] tunable nanoelectronics,[390] and optical[223,391] or light harvesting[392] devices. However, the use of more conventional top-down methods combined with bottom-up synthetic procedures remains an area of great interest, as it allows for the direct chemical modification at the nanoscale (size ranges below 100 nm).

Initial work in this area was carried out by Sagiv et al.[253,254] by developing electro-oxidative lithography (originally coined "constructive lithography"), in which a positive bias was applied across an AFM probe and sample to oxidatively convert alkyl silanes into carboxyl-terminated ones. This method has since been used for the guided self-assembly of nanoscale structures by various groups.[393–395] Similarly to the oxidative lithography technique, scanning near-field optical microscopy (SNOM) (which is also a form of SPL) has been used to produce nanostructures through the chemical modification of surface monolayers by exposure to UV light.[255,396] SNOM operates by exploiting the evanescent field generated at an aperture of diameter much smaller than the wavelength of light directed towards it, as first suggested by Synge[397] for the characterization of biological samples. The use of this evanescent field, using a hollow AFM probe with aperture diameter ≈50 nm, has allowed for the repeatable production of 20 nm structures,[396] with sub-10 nm feature sizes also being achieved.[255,398]

In recent years, there has been an increased interest in the modification of surfaces with biological molecules such as proteins[119,399,400] and DNA.[401,402] Work in the author's laboratory has demonstrated the patterning of 3-aminotriethoxysilane (APTES) monolayers with 2-nitrophenylpropyloxycarbonyl (NPPOC) or 2-(4-nitrophenyl)ethoxycarbonyl (NPEOC) protecting groups attached (shown to have high photodeprotection efficiencies[403]), by directed synthesis at the surface via

micropatterning[404,405] and SNOM.[283,405–407] This was achieved by exposing the monolayer to UV light ($\lambda = 325\,\text{nm}$) cleaving the NPPOC group and leaving amine groups ($-NH_2$) free at the surface for further derivatization in the exposed regions. The goal of promoting protein adsorption solely within patterned regions (i.e., specific adsorption) has been to form a better understanding of the processes behind cell adhesion[408,409] and in developing more accessible methods for protein patterning at the nanoscale. This is in contrast to more costly techniques such as conventional lithography where masks can become exorbitantly expensive and only allow for the creation of identical patterns, and electron beam lithography which requires expensive equipment and maintenance.

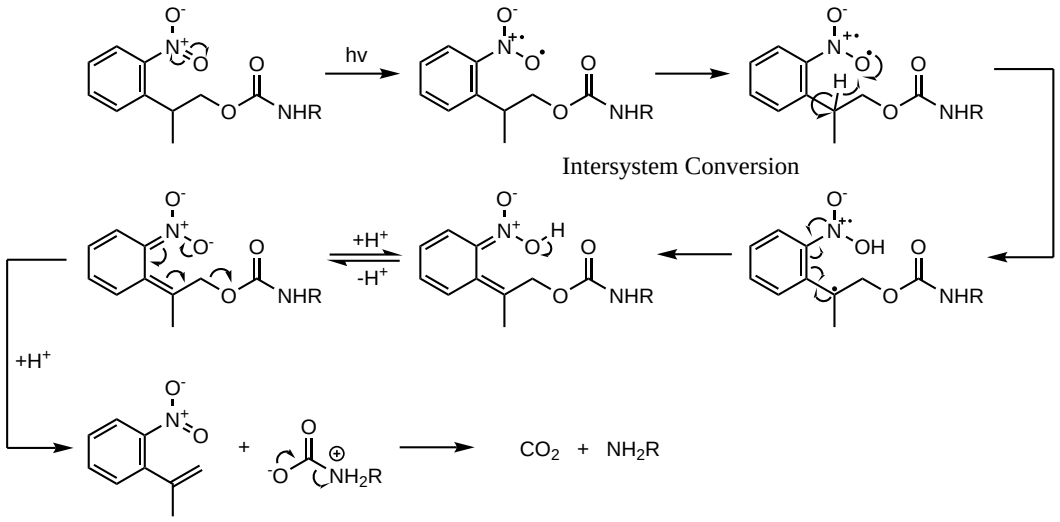

Figure 5.2: Proposed pathway for NPPOC photodeprotection by UV light.[283]

To improve the protein resistance of the OEG-NPEOC-APTES monolayer, with the aim of reducing nonspecific adsorption, an oligoethylene glycol (OEG) chain was attached to the NPPOC phenyl ring.[406] The mechanism proposed[283] for the photodeprotection of NPPOC under UV light is given in Figure 5.2, following the work by Hasan et al.[410] and Beier et al.[411] However, beyond the study of intramolecular sensitization of NPPOC,[412–414] not much research has been done on the precise nature of the photodeprotection mechanism. Thus, a brief investigation on the potential pathways via density functional theory, a method of modelling the electronic structure of the ground- and excited-states of molecules (see Section 1.7 for further details), is presented in this chapter.

There already exist many different SPM techniques for nanopatterning, such as dip-pen nanolithography,[252,415,416] nanoshaving,[417–419] or the aforementioned SNOM and oxidative lithography, to name a few. However, these require modified and/or special equipment (such as a 325 nm laser with a sensitive feedback loop to maintain an appropriate separation from the surface in the case of SNOM) or operate by modifying the surface by exclusively physical means. The goal of the work presented here was to examine whether an AFM probe could be used to cause mechanochemical deprotection of an adsorbate with a photoremovable protecting group, i.e., whether mechanical energy could be used to cause a specific chemical modification normally excited by adsorption of a photon.

Mechanochemistry, whereby mechanical stimulus is converted into energy used in the activation and acceleration of chemical reactions, is much less understood than other branches of chemistry such as photo- or electrochemistry, despite mechanochemical reactions being described as far back as ancient Greece.[420] Molecules of alkanethiol SAMs on gold have been shown to be reversibly displaced by the shear forces experienced between monolayer and AFM probe,[359] with DFT calculations showing these forces causing a shift in the lateral position of gold-thiol bonds and, to a lesser extent, the first gold surface layer.[421] Gaining a better understanding of the effect of pressure on the energy dissipation processes involved in AFM experiments, and how these may enable chemical reactions to occur at the surface is therefore of great interest.

This chapter will seek to provide a deeper insight into the potential mechanochemical processes involved with the deprotection of OEG-NPEOC-APTES by an AFM probe in contact mode. The mechanochemical technique demonstrated in this chapter allows for the patterning of NPPOC/OEG-NPEOC-APTES monolayers with an unmodified commercial AFM instrument and standard tapping mode AFM probes, with feature sizes reproducibly below 50 nm. To determine if the environment at the surface plays a role in the mechanochemical deprotection, the technique was performed in both non-polar and highly polar liquids. The effect of tip speed and applied load on the features created were examined, and the minimum load required to remove APTES from the silicon substrate was measured.

5.2 Experimental

5.2.1 Monolayer Formation and Characterization

Self-assembled monolayers to be mechanochemically deprotected were prepared using the procedure described in Section 2.3.4. Clean silicon substrates were placed into sample vials and immersed in a 1 mM solution of OEG-NPEOC-APTES for 48 hours. The samples were then rinsed in toluene and ethanol mixtures, and annealed in a vacuum oven before being placed in clean sample vials and wrapped in aluminum foil to prevent degradation of the monolayer by ambient light. Monolayers of APTES on silicon were prepared with the same method, but were not needed to be protected with aluminium foil. All silane samples were used within 1 month.

To test whether proper monolayer formation was being achieved, X-ray photoelectron spectroscopy (XPS, Section 2.6.2), secondary ion mass spectrometry (SIMS, Section 2.6.3), and contact angle goniometry (Section 2.6.1) were employed. Due to the sensitive nature of OEG-NPEOC-APTES monolayers (the nitro group has been shown to be reduced upon exposure to X-rays[186]), the XPS exposure time was reduced to 60 s, with a maximum current of 5 A. XPS and SIMS measurements were not performed on all samples due to cost considerations, however contact angles were measured for all samples. Samples failing to demonstrate water contact angles 45° for OEG-NPEOC-APTES and 60° for APTES were discarded.[283,406]

5.2.2 Mechanochemical Removal of NPEOC

Both mechanochemical deprotection and imaging were performed using a Digital Instruments NanoScope III MultiMode instrument with rectangular silicon tapping mode probes with an average tip radius of 7 nm. For friction measurements, V-shaped silicon nitride contact mode AFM tips with an average tip radius of 50 nm were used. To apply the correct load to the sample, the cantilevers' deflection sensitivity and normal spring constant were determined via the methods described in Section 2.5.4. Prior to mounting into the AFM, a mark was made in the center of the sample to allow each pattern to be

found again on subsequent mountings. All patterning and subsequent measurements were performed in a room with UV-filtered lighting, to prevent deprotection by conventional means.

To investigate the effect of different scratching parameters, the AFM software's nanolithography module was used. The module allows a user to compile input scripts with a number of different commands for changing instrumental settings, such as x-, y-, and z-axis translation position and speed. Using these input scripts various factors were examined, with more complex input scripts being created via a custom piece of software, AFMdraw. A liquid cell with O-ring was used to test the effect of solvent environment on the mechanical removal of NPEOC. Control experiments were performed with APTES, to identify at what load the APTES molecules were being cleaved from the surface. Further details can be found in Section 2.5.3.

Once a series of patterns had been written, the samples were soaked for 10 min and washed thoroughly in ethanol and dried with nitrogen, ready for imaging. A fresh tapping mode probe was used, and topographical images were obtained in soft-tapping mode. Friction images were recorded at very low loads (10 nN) to avoid further deprotection of the surface. All images were flattened using first-order plane fit and flatten commands in Bruker's AFM analysis software to eliminate sample tilt and improve presentation quality. Line sections (averaged across multiple lines of linear features) were exported to CSV files for further analysis in OriginPro.

5.2.3 Surface Modification

Following mechanochemical patterning, samples were rinsed with ethanol and placed under inert atmosphere in clean sample vials. The exposed amine groups were then reacted with trifluoroacetic anhydride (TFAA) in dry THF, using triethylamine as a catalyst. After 2 h under nitrogen, the samples were thoroughly rinsed and dried, ready for further analysis. More information on the reaction scheme followed can be found in Section 2.3.5.

5.2.4 UV-Visible Spectroscopy

In order to select the most appropriate functional and basis sets to be used in the DFT calculations, the UV-Vis spectrum of NPEOC in solution was obtained. An aprotic solvent, acetonitrile, was used in order to minimize the specific interaction between solvent and solute molecules,[270] making spectra more comparable to results obtained via DFT for the gas-phase.[271] A 0.1 mM solution of OEG-NPEOC-APTES in acetonitrile was prepared and measured with a UV-Vis spectrometer, details of which can be found in Section 2.6.4.

5.2.5 Density Functional Theory

The ground-state geometry of a simpler NPPOC molecule (without oligoethylene glycol sidechain, and with a methyl replacing the APTES group, see Figure 5.21) in the gas-phase and in water was calculated for a number of different functionals and basis sets using Gaussian 09.[298] From excited-state energy calculations, theoretical UV-Vis spectra were obtained and compared to the experimental value obtained in acetonitrile. The functional and basis set that resulted in spectra that most closely resembled empirical data were selected for use in further calculations.

The ground-state geometries for a variety of different conformations along the proposed NPEOC deprotection pathway were optimized. Additionally, geometries as various bonds in NPEOC were stretched by scanning across a range of separation values were also obtained. The resulting ground-state energy vs. bond length plots were fitted with a Morse oscillator potential to obtain a relative measure of the bond-dissociation energy. For more details on the parameters used, see Section 2.7.

Calculations in the excited-state geometry optimizations were performed using the "Optimization" job type and "TD-SCF" method, with 6 excited-state levels being investigated to arrive at a final geometry for the $n = 2$ energy level ($N = 6$, with state of interest root $N = 1$). UV-Vis spectra (and associated energy level transitions) were calculated using the "Energy" job type and "TD-SCF" method for 100 excited-state energy levels ($N = 100$), with resulting data exported into CSV files.

Some simulations were run in a water environment and were performed using the integral equation formulism polarizable continuum model (IEFPCM), the default self-consistent reaction field (SCRF) method in which the molecule to be solvated is placed

in a cavity within the solvent reaction field. In the IEFPCM model, originally developed by Tomasi et al.[422,423] and Pascual-Ahuir et al.,[424] a series of overlapping spheres are generated in order to determine the solute cavity.

5.3 Results and Discussion

5.3.1 X-ray Photoelectron Spectroscopy

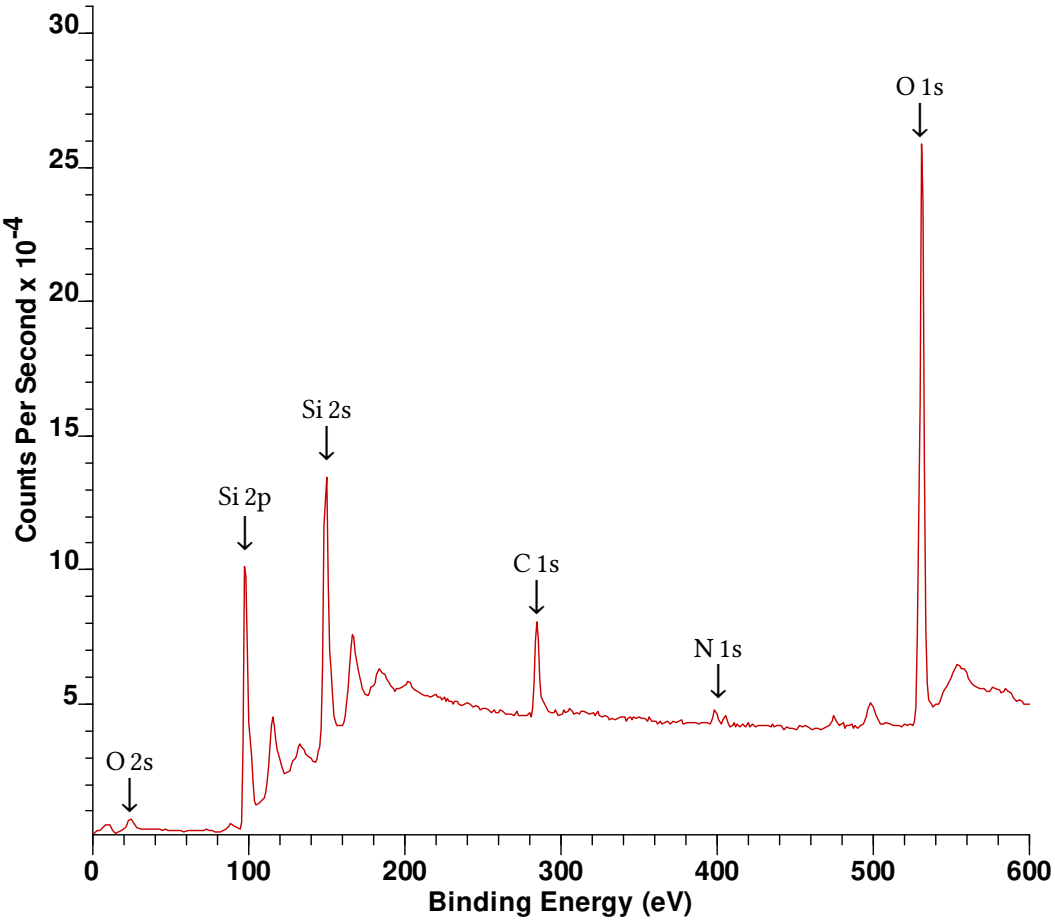

Figure 5.3: XPS wide scan spectrum of silicon substrate with OEG-NPEOC-APTES SAM.

The wide scan XPS spectrum of a fresh OEG-NPEOC-APTES self-assembled monolayer on silicon is presented in Figure 5.3 above, with all the expected elements present. High-resolution C 1s and N 1s spectra of OEG-NPEOC-APTES, before and after photodeprotection, can be seen in Figure 5.4. The total contribution as a % of the total peak areas before and after photodeprotection are summarized in Table 5.1.

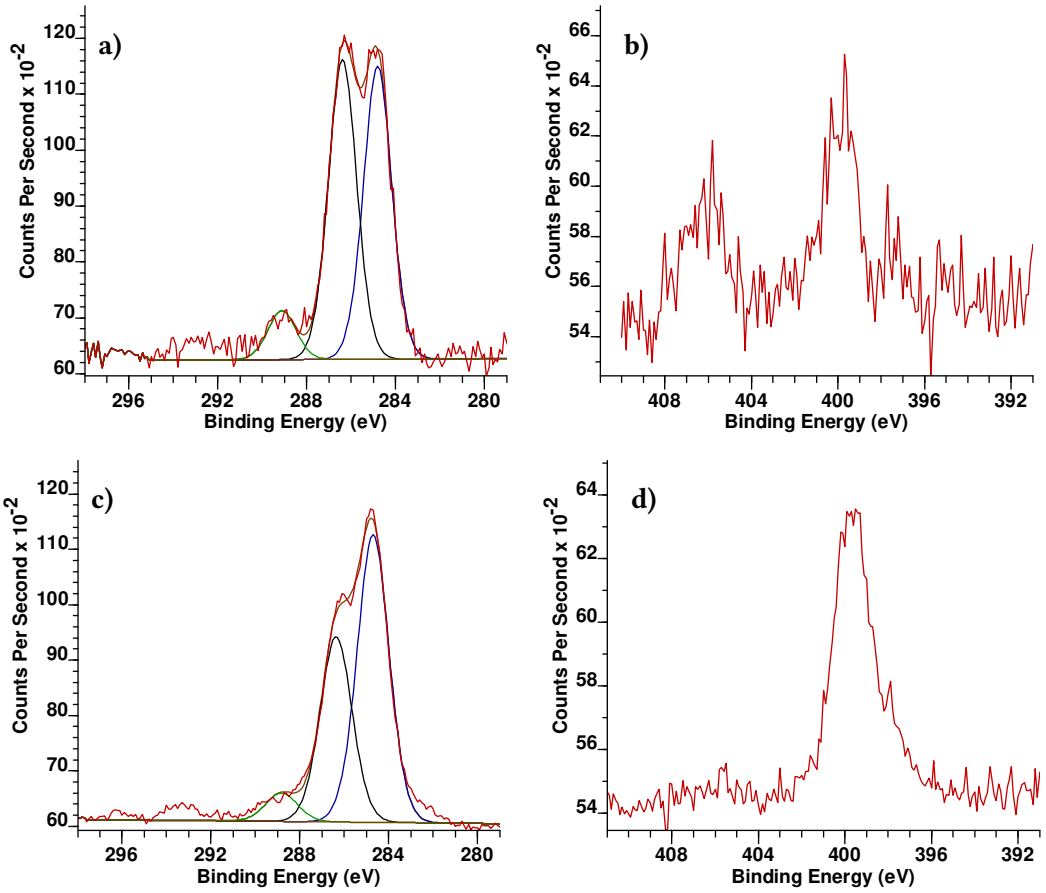

Figure 5.4: C 1s (left) and N 1s (right) high-resolution XPS spectra of OEG-NPEOC-APTES monolayers before (upper) and after (lower) photodeprotection.

In the C 1s spectrum of the undeprotected monolayer (Figure 5.4a), there is an equal contribution from the hydrocarbon sections (285.0 eV), and from carbon atoms in the oligoethylene glycol sidechain and adjacent to the carbamate (286.4 eV). Additionally, there exists a small contribution from the carbamate carbon, found at 289.2 eV. In the

N 1s spectrum of the unexposed SAM (Figure 5.4b), two peaks corresponding to nitrogen in the carbamate (400.0 eV) and nitro (406.2 eV) groups are observed, with a peak area ratio of 3:2; a deviation from the expected 1:1 ratio is attributed to partial deprotection.

Following deprotection, the NO_2 peak becomes undetectable (Figure 5.4d). In the C 1s spectrum of the exposed monolayer (Figure 5.4c), the areas of the ether and carbamate carbon peaks are reduced with respect to the hydrocarbon peak. The disappearance of the nitro peak, in conjunction with the reduction of the ether carbon peak, suggests that the NPEOC has been cleaved from the surface, leaving behind amine-terminated APTES. These results match those obtained in studies with similar OEG-NPEOC-APTES self-assembled monolayer,[405] and show that the expected monolayer has been formed correctly on the surface using the methodology described. Lower measured values compared to expected calculated values (see Table 5.1) is likely due to partial deprotection during mounting in the XPS instrument and exposure to X-rays during data collection.

Table 5.1: Contribution of different bonding environments as % of total area of C 1s and N 1s spectra for OEG-NPEOC-APTES monolayers before and after photodeprotection. Also included are calculated values for an expected unexposed monolayer.

	C 1s			**N 1s**	
	C−<u>C</u>−C	**C−<u>C</u>−O, C−<u>C</u>−N**	**O−<u>C</u>N=O**	**<u>N</u>H$_2$**	**<u>N</u>O$_2$**
Energy (eV)	285.0	286.4	289.2	400.0	406.2
Calculated	25.9	70.4	3.7	50	50
NPEOC-APTES	46 ± 2	47 ± 3	7.6 ± 0.5	60 ± 2	40 ± 2
Deprotected	59 ± 1	36 ± 2	4.6 ± 0.7	83 ± 2	—

5.3.2 Secondary Ion Mass Spectrometry

Samples were also characterized by SIMS following the methodology described in Section 2.3.4. The spectra obtained from these measurements are presented in the following pages.

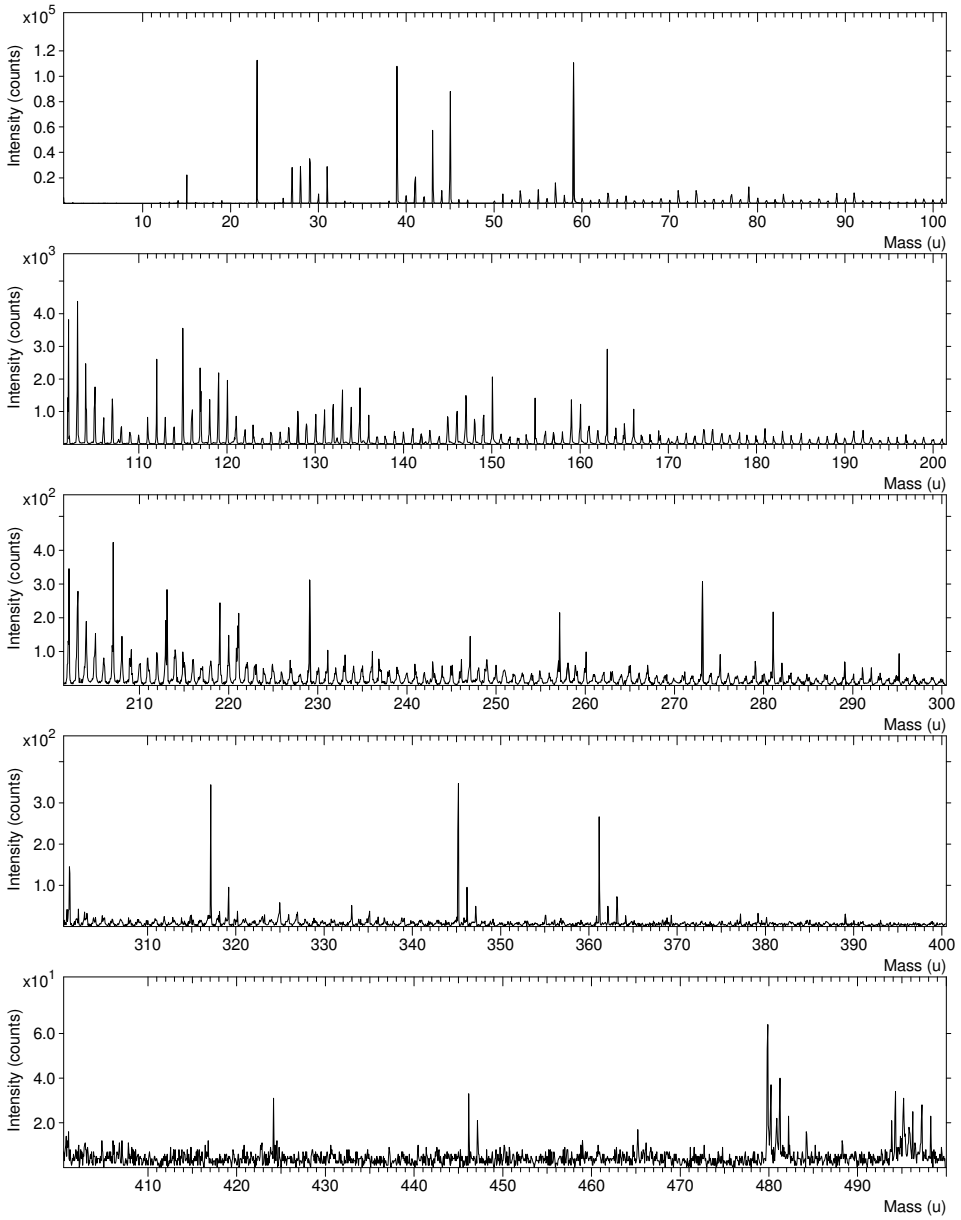

Figure 5.5: Positive ion spectrum of OEG-NPEOC-APTES self-assembled monolayer. m/z: 1 to 500.

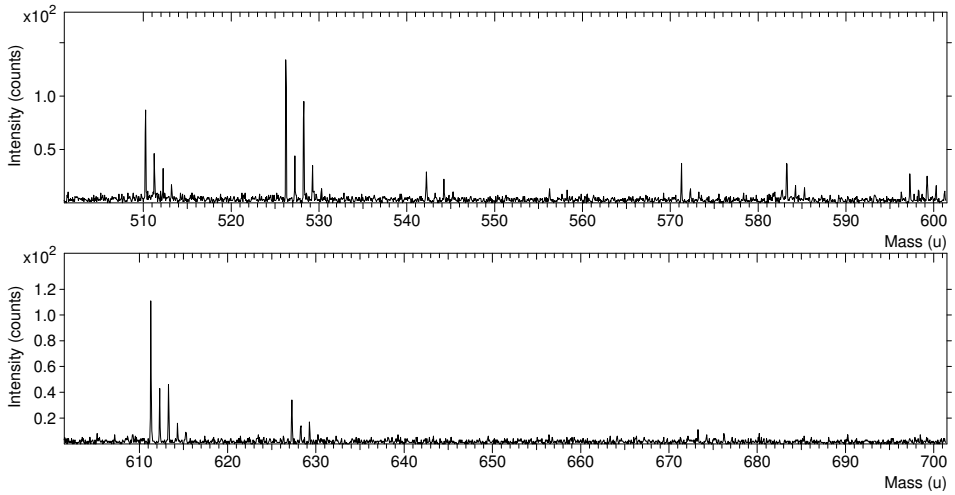

Figure 5.6: Positive ion spectrum of OEG-NPEOC-APTES self-assembled monolayer. m/z: 500 to 700.

In the low-mass section of the positive spectrum (Figure 5.5), strong peaks are observed for the cationic carbamate fragment ($COONH^+$) at 59 m/z, the end of the OEG sidechain ($CH_2OCH_3^+$) at 45 m/z, sections of the phenyl group ($C_3H_3^+$) at 39 m/z (alternatively due to K^+), and a sodium contamination peak at 23 m/z. Between m/z=200 and 370 there exist regular peaks separated by an m/z of 16 (O) and 28 (C_2H_2, CO), originating from fragments formed with different lengths of the OEG sidechain (missing from NPPOC spectra). The high m/z section of the positive spectrum of the OEG-NPEOC-APTES monolayer can be seen in Figure 5.6. The mass peak at 627 m/z corresponds to the ion of the OEG-NPEOC-APTES molecular ion (without ethoxy groups, actual m/z = 631) minus 4 hydrogens (peak for $C_{28}H_{43}N_2O_{12}Si^+$ fitted to within 50 ppm), with the peaks at greater m/z are due to fragments with fewer hydrogen losses. The peaks at 611 – 613 m/z therefore suggest the removal of an oxygen atom or CH_4 for the aforementioned fragments. The signal at ≈528 m/z is assigned to an ion formed by the cleavage of the C−N bond in the carbamate group, and a fragment with a further loss of the carbonyl center is seen at 510 m/z.

The negative spectrum is shown in Figure 5.7 overleaf, where the main low-mass peaks visible correspond to O^- (−16 m/z), $C_2H_2^-$ (−26 m/z), and the characteristic NO_2^- for NPEOC (−46 m/z). At −m/z greater than 100, regular peaks (similar to those seen in the

positive spectrum) due to fragments with varying OEG lengths are observed. The final peak visible at −475 m/z corresponds to the ion formed on cleavage at the α-carbon of the ethoxycarbonyl attached to the NPEOC phenyl group.

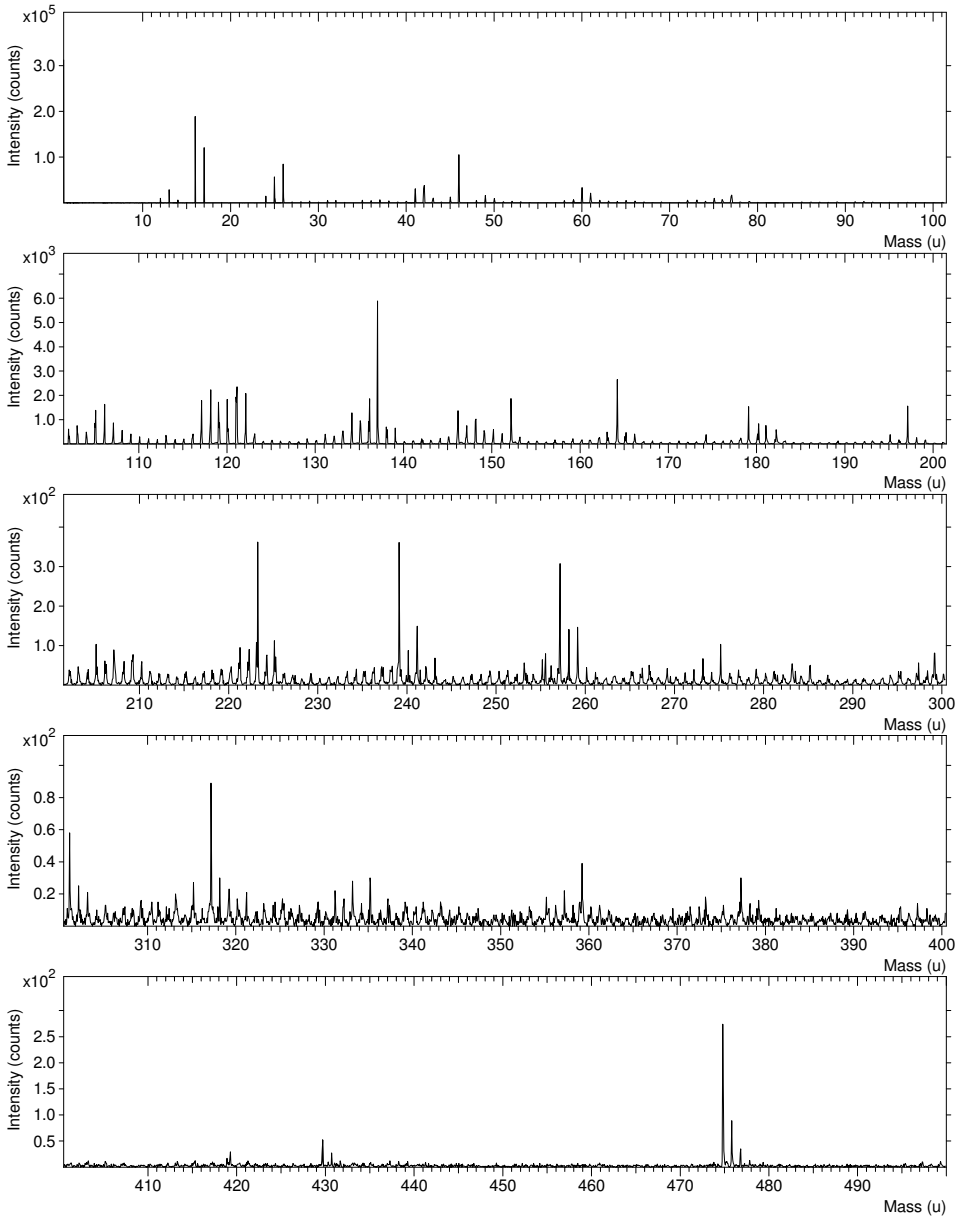

Figure 5.7: Negative ion spectrum of OEG-NPEOC-APTES self-assembled monolayer. −m/z: 1 to 500.

5.3.3 Mechanochemical Removal of NPEOC

Nanolithography was carried out by using an AFM probe at elevated load to modify the film surface. Figure 5.8 shows AFM tapping mode height and friction images of two representative patterns.

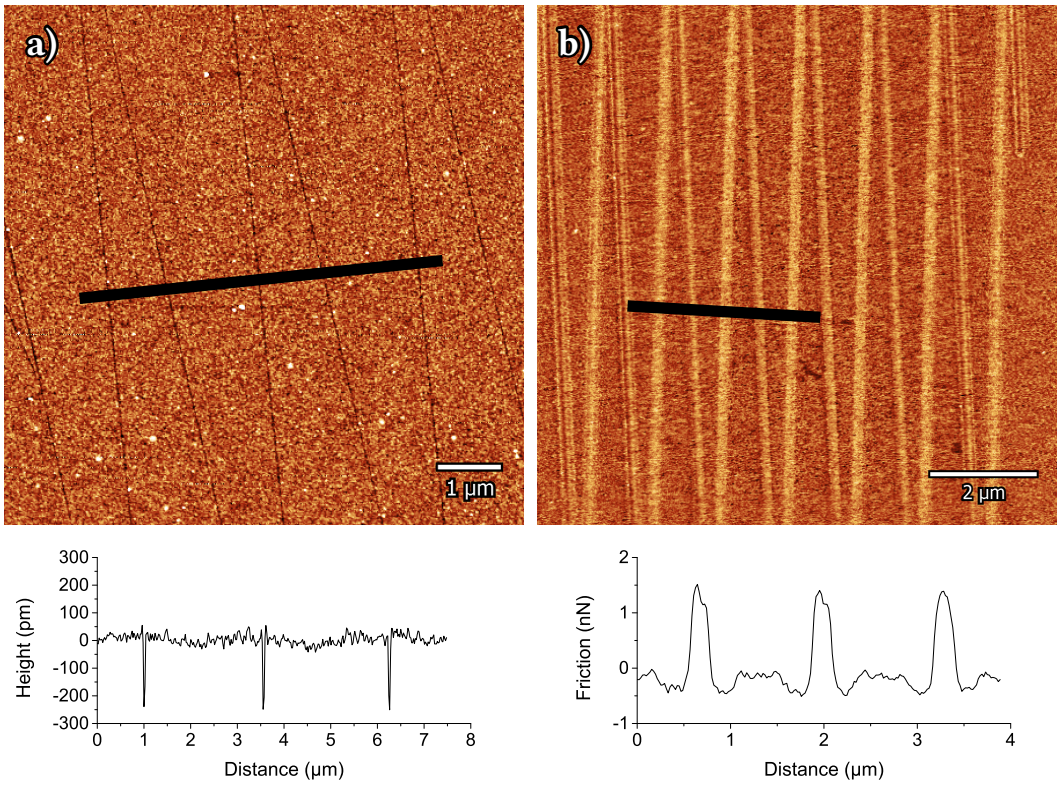

Figure 5.8: AFM images of nanoscale features fabricated via mechanochemical removal of NPEOC by an AFM tip. Included line profiles are taken from regions marked by the overlaid black rectangles. **a)** Height image obtained in tapping mode (write load: 500 nN). **b)** Friction image obtained via FFM (write load: 2000 nN).

The lines in Figure 5.8a were produced by applying a load of 500 nN to a tapping mode AFM probe ($R \approx 7$ nm, $k \approx 24\,\mathrm{N\,m^{-1}}$) moving in constant contact with the surface. Tapping mode AFM was used to obtain all height images, employing the same type of probe used to fabricate the nanoscale patterns. The features created have an average full width at half maximum (FWHM) of 30 nm and a depth of 0.25 nm, as determined from the fitting of line profiles (cross-sections) in OriginPro. There is no evidence of accumulation of material along the edges of the lines, which is commonly found in experiments where plowing of the thin film or monolayer is occurring.[425–427]

The friction image shown in Figure 5.8b was obtained using a V-shaped contact mode probe, where the final image is acquired by subtracting retrace channels from their related trace channels. Comparatively broad lines (ca. $2-3\times$ larger than the tip radius) were created by using an applied load of 2000 nN. Consequently the patterned structures are large compared to the nominal radius of the contact mode probe used to characterize the features (≈50 nm). As a result, the change in friction across the lines compared to the rest of the monolayer is not a consequence of edge-effects, but is determined by the different properties of the modified and unmodified materials. The small increase in the background signal between line profile peaks is attributed to the other set of lines at an angle between the line array being analyzed. An increase in the friction force of over 1 nN was measured between the center of a line and the surrounding monolayer, mirroring the result obtained by Alang Ahmad et al.[283] for lines fabricated via photodeprotection of NPPOC-APTES monolayers using SNOM.

This increase in friction is unexpected for the removal of the NPEOC protecting group, as the adhesive interaction (and thus friction due to shearing, as discussed in Chapter 4) for OEG-terminated SAMs is greater than that for amine-terminated APTES. From the combination of the Dupré (Eq. 3.15) and Young's equation[428] one obtains the Young-Dupré equation (valid for planar interfaces only):

$$W_{\mathrm{A}} = \gamma_L(1 + \cos\theta) \tag{5.1}$$

where W_{A} is the work of adhesion, and γ_L and θ are the surface tension and surface contact angle of the liquid, respectively. As the contact angle of OEG-NPEOC-APTES SAMs (45°) is lower than that of APTES SAMs (60°), the work of adhesion is expected to be higher for the former ($\cos 45^\circ > \cos 60^\circ$). Therefore, the friction force experienced within the deprotected regions should be reduced, as was discovered by Alang Ahmad et al.[406] for OEG-NPEOC-APTES monolayers deprotected by exposure to 325 nm light.

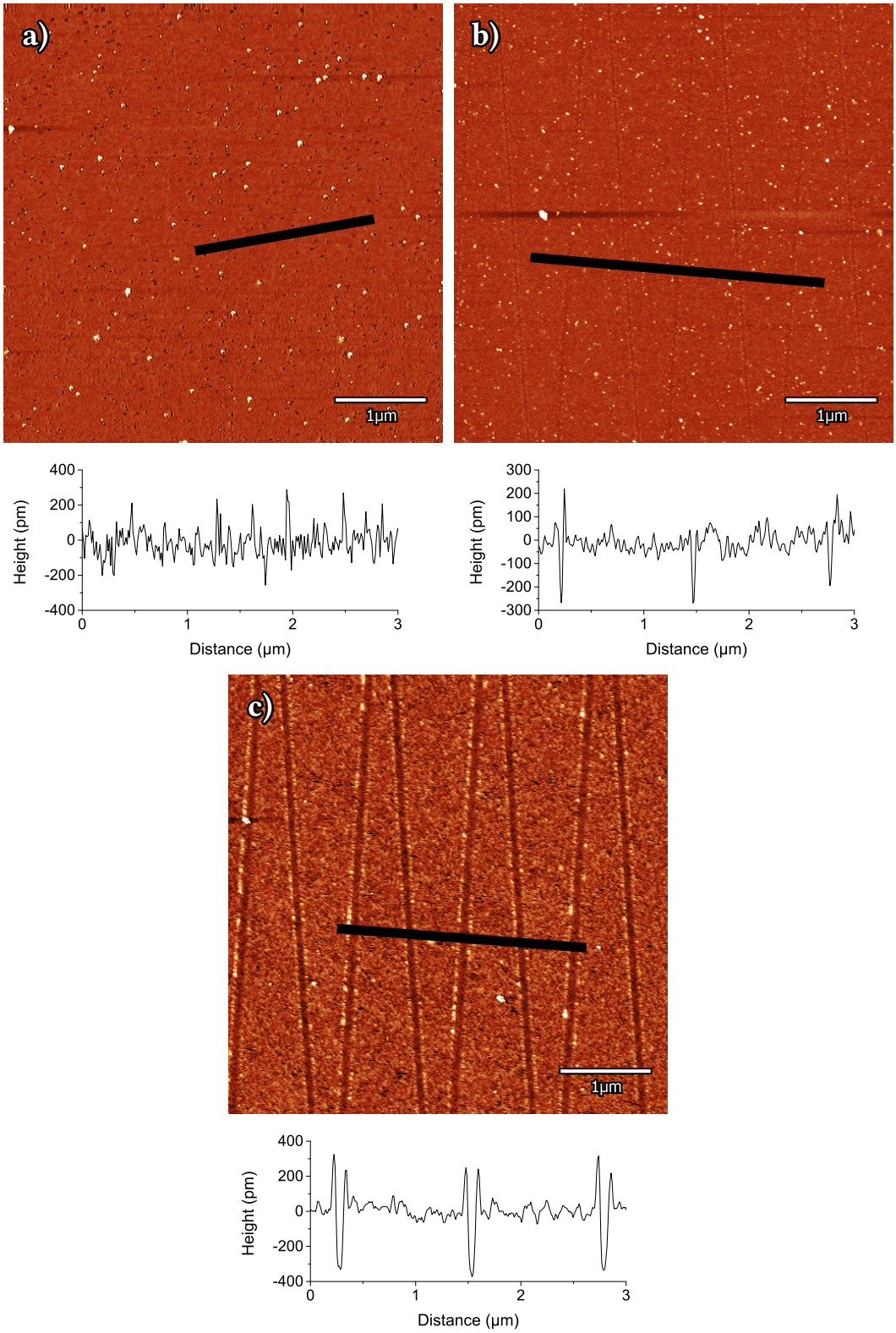

Figure 5.9: AFM height images and line profiles (corresponding to areas within black rectangles) after mechanochemical stimulation via AFM tip for various SAMs. **a)** APTES monolayer after an applied load of 500 nN **b)** APTES monolayer after an applied load of 10,000 nN **c)** OEG-NPEOC-APTES monolayer after an applied load of 10,000 nN.

The line sections in Figure 5.8 show that material is removed from the surface during pattern formation. There are thus two possible explanations for the observed increase in friction within the "scratched" areas that are consistent with this removal of material during the lithographic process. First, removal of the complete OEG-NPEOC-APTES molecules (exposing the polar silanol groups at the substrate surface); and second, the incomplete deprotection of the monolayer leading to a disordered layer. In the latter case, disordered lower density remnants of the protecting group would be expected to increase energy dissipation through plowing, hence causing the increase in the friction force.

The influence of the load on the lithographic process was investigated. APTES SAMs were modified using a tapping mode AFM probe (of comparable radius) at varying applied loads and imaged using tapping mode. As can be seen in Figure 5.9a, topographical features were not formed at applied loads of 500 nN, with height images being indistinguishable from virgin APTES monolayers. Loads of at least 10,000 nN were required to create lines in APTES (Figure 5.9b) with feature sizes much smaller than those achieved at similar loads for OEG-NPEOC-APTES (Figure 5.9c). This suggests that at lower applied loads, such as those used to form the structures in Figure 5.8, physical removal of material is unlikely. Also absent from the image in Figure 5.8a is any evidence of the accumulation of displaced material along the edges of features. However, such accumulation is clearly evident in Figure 5.9 as a result of purely mechanical surface modification. These considerations suggest that the increased friction contrast in the patterned regions in Figure 5.8b results from residual protecting groups, following cleavage of the carbamate N−C bond. Additionally, it is possible that there is incomplete deprotection of the monolayer within the rastered features, causing the monolayer inside the lines to become disordered. This lack of order has been shown to increase friction,[192,360,429,430] as the molecular organization of monolayers plays a critical role in the plowing contribution.[100] The energy dissipation via shearing could also remain significant in the case of incomplete removal of the NPEOC protecting group, as the remaining OEG groups on the surface may prevent a reduction in the shearing term.

Quantifying the extent of deprotection within the features is difficult, as their size is well below the in-plane spatial resolution limit of the XPS and SIMS instruments used. In the study by Alang Ahmad et al.[406] samples were deprotected by exposure to

UV light doses known to fully remove the NPEOC protecting group, determined from XPS and contact angle measurements at varying doses on macroscopic exposures.[283] These high-energy exposures were also likely large enough to cause localized heating at the point of exposure, promoting the lift-off of the protecting groups. In the case of mechanochemical deprotection, removal of the NPEOC group in an area large enough to be quantified via XPS or SIMS would be problematic. Using an AFM probe to sequentially remove individual lines to create a larger area would not guarantee that molecules at the interface between removed and intact regions would be properly deprotected on each pass. This is due to the additional space available for non-compressive deflection of the OEG-NPEOC-APTES molecules towards previously deprotected areas. Identifying the precise nature of the mechanochemical lithography is therefore beyond the scope of this chapter, and instead the suggestions presented were inferred via more indirect means.

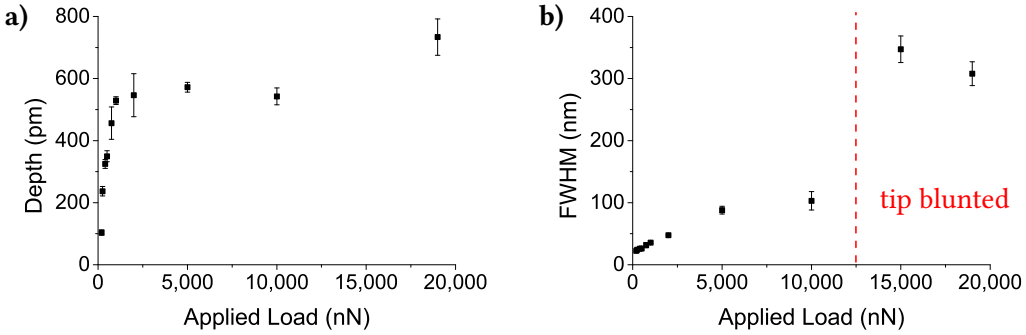

Figure 5.10: Graphs showing the effect of load applied to an AFM tip on the sizes of the fabricated features via mechanochemical deprotection, at a write speed of $1\,\mu m\,s^{-1}$. **a)** Applied load against depth. **b)** Applied load against FWHM. Feature sizes were determined from the fitting of a Gaussian curve to the troughs found in line profile troughs.

The effect of the applied load on the depth and FWHM of the features created via mechanochemical deprotection (determined from the fit of Gaussian curves on the troughs in the feature line profiles, $N = 25$) is presented in Figures 5.10a and 5.10b, respectively. Write speeds were kept constant at $1\,\mu m\,s^{-1}$ for all load experiments. A minimum load of ca. 200 nN was required to create features visible via tapping mode AFM with a depth of 0.1 nm and FWHM of 25 nm. However, these features are very faint and difficult to find after rinsing with ethanol. Applied loads of 500 nN or over were preferred in order to produce easily locatable features, with depths increasing in magnitude until plateauing at

≈0.5 nm under loads greater than a critical load of 2500 nN. Above this load, however, an increased amount of built-up material was found near feature edges, indicating a greater degree of plowing. The measured FWHM increased with the load applied up to a value of 12,500 nN, at which point the AFM tips used were immediately blunted when writing lines, tripling their corresponding widths. At loads greater than 10,000 nN, the measured feature depth was also increased by 0.2 nm, approximately the same as the depth of the lines scratched into the APTES monolayers at comparable loads (Figure 5.9b). This further confirms that APTES is not removed until exceptionally large loads are applied.

The Hertzian contact pressure[57] where the AFM probes ($R \approx 7$ nm) contact the OEG-NPEOC-APTES SAMs at a load of 200 nN (the minimum required to produce visible features) was calculated to be ≈2 GPa. Previous studies have shown that below a critical applied load, AFM tips with $R < 100$ nm move across the top of thiol SAMs on gold[431] and silane SAMs on mica;[217] the pressure is absorbed by reversible compression of the monolayer molecules. Once the surface pressure exceeds a critical amount, in the order of 1 GPa for all tip radii,[112] the tip penetrates through the upper surface of the monolayer. The loads required to produce clear structures in OEG-NPEOC-APTES films corresponds to pressures exceeding this critical amount, thus it is probable that the lateral compression of neighboring molecules (caused by the AFM tip pushing through the monolayer surface) is involved in the mechanochemical process. This may further support the hypothesis that partial deprotection occurs within the measured features, as the OEG-NPEOC-APTES molecules remaining within these are unable to be compressed against neighboring molecules. The minimum pressure required to completely cleave APTES was calculated to be ≈9 GPa. Figures 5.11a and 5.11b show the dependence of the depth and FWHM of the written features on the write speed (the speed of the AFM probe across the surface), at a constant applied load of 1000 nN. While the write speed has little effect on the average width of 25 nm (except for a slight reduction to 20 nm at 0.1 μm s^{-1}), speeds greater than 100 μm s^{-1} resulted in decreasing feature depths (from 0.35 nm to 0.25 nm). While slower write speeds result in the smallest possible features with the lowest size variance, the time taken to produce patterns at 0.1 μm s^{-1} can be prohibitively slow. Thus, write speeds of

1 µm s^{-1} at applied loads of 500 – 1000 nN were chosen as the best compromise between feature size with sufficient deprotection (while avoiding material build-up) and writing time.

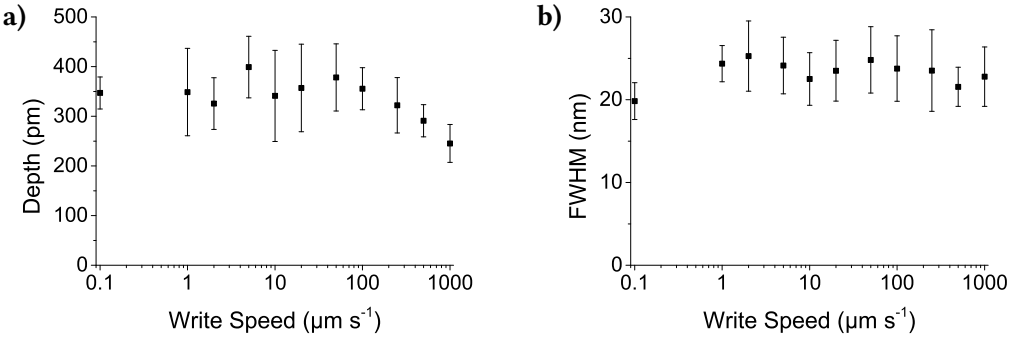

Figure 5.11: Graphs showing the effect of write speed on the sizes of the fabricated features via mechanochemical deprotection by an AFM tip, at an applied load of 1000 nN. **a)** Write speed against depth. **b)** Write speed against FWHM. Feature sizes were determined from the fitting of a Gaussian curve to the troughs found in line profile troughs.

Investigations were also performed to determine to what extent the tip and environment chemistry affects the mechanochemical removal of the NPEOC protecting group. Monolayers of OEG-NPEOC-APTES were patterned in water (Figure 5.12a) and heptane (Figure 5.12b) using the same procedure as in air, at a write speed of 1 µm s^{-1} and applied load of 1000 nN. These liquids were chosen to represent both highly polar (water) and non-polar (heptane) liquids. In both media, the features created are slightly wider than those created in air, although this can be attributed to variations in tip radius between different AFM probes. As with patterns created in air using similar parameters, there is little build-up of material at the feature edges. Therefore, solvent environment alone does not appear to have any significant impact on the mechanochemical deprotection of OEG-NPEOC-APTES monolayers.

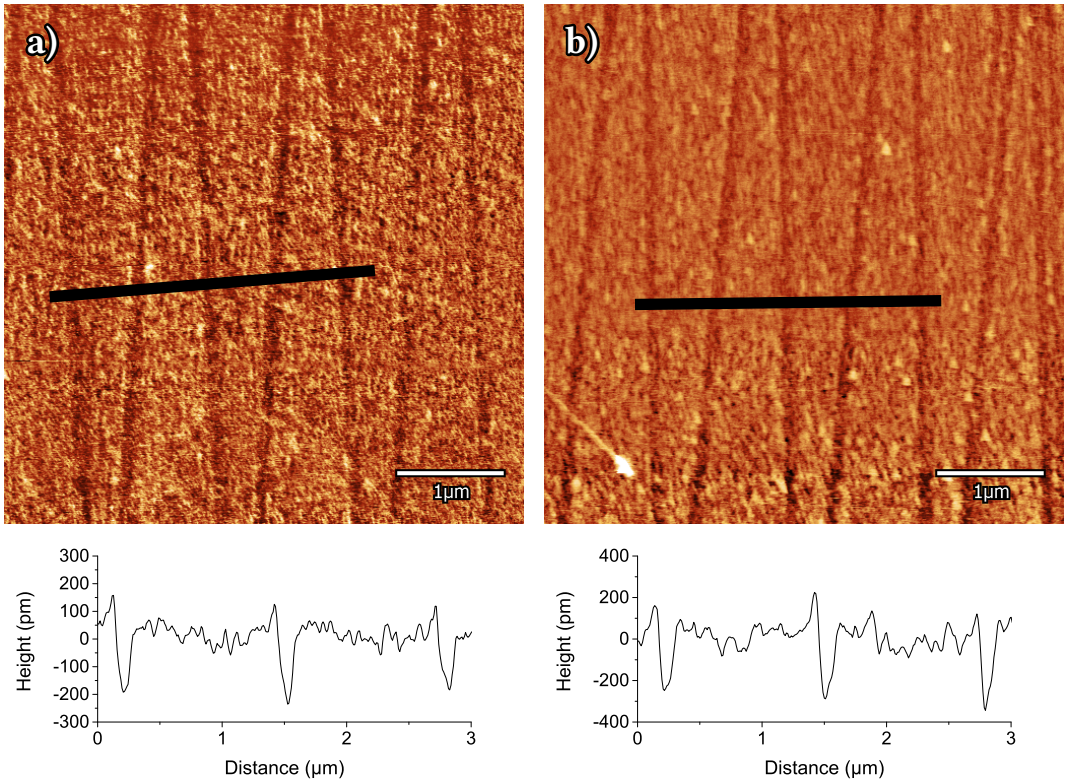

Figure 5.12: AFM height images and line profiles of regions within black rectangles of OEG-NPEOC-APTES monolayers deprotected via mechanochemical removal in liquid at an applied load of 1000 nN. **a)** NPEOC removal in water. **b)** NPEOC removal in heptane.

AFM probes were functionalized with n-octadecyltrichlorosilane (OTS) as per Section 2.4.3, in order to determine the role of tip chemistry on the mechanochemical process. Patterns fabricated at 1000 nN in water and heptane using these OTS functionalized probes are presented in Figures 5.13a and 5.13b. Although the feature sizes are as expected, there is a considerable amount of material build-up around edges of the lines created in heptane. This might suggest that the by-product of the mechanochemical deprotection mechanism is polar, as it is better removed by either a polar probe (e.g., an unfunctionalized silicon probe, Figure 5.12) or desorbs from the surface in the presence of polar solvent (Figure 5.13a). Alternatively, it is possible that the non-polar tip and solvent environment lead the deprotection to occur via a different pathway, favoring the production of the more polar nitrosobenzaldehyde by-product. However, while the former explanation is more likely, it is far from conclusive from the evidence presented, with further studies on the composition of the material agglomerations being required.

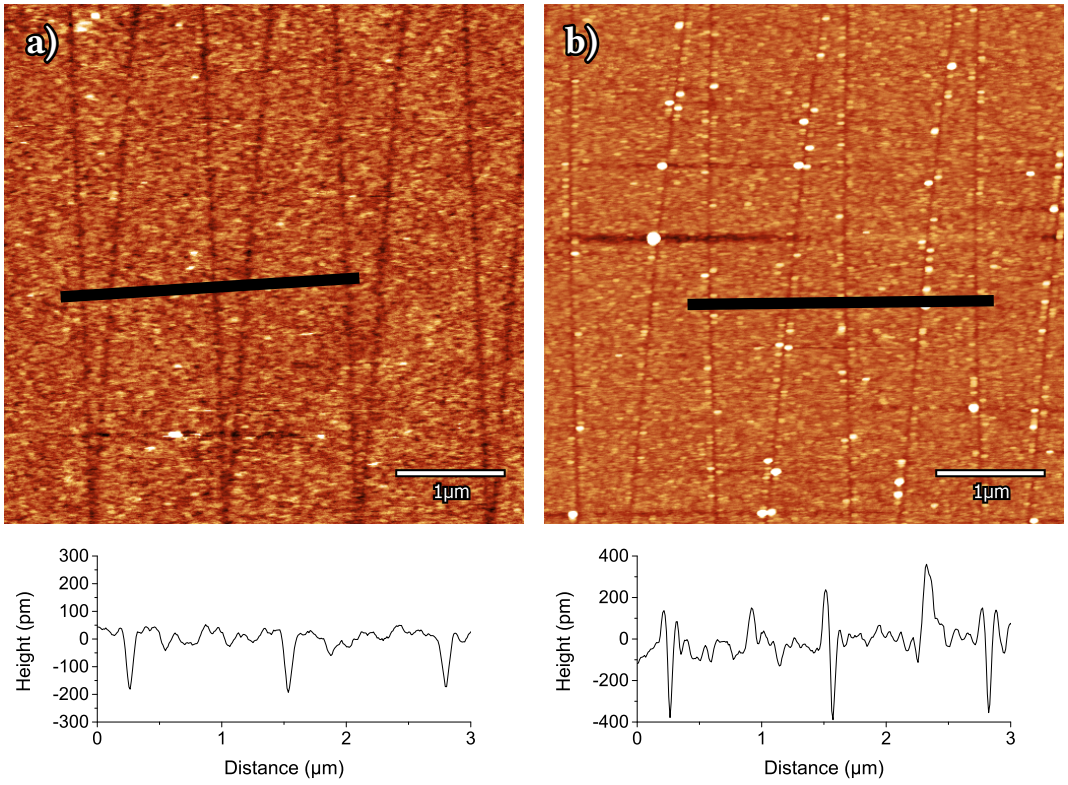

Figure 5.13: AFM height images and line profiles of regions within black rectangles of OEG-NPEOC-APTES monolayers deprotected via mechanochamical removal in liquid at an applied load of 1000 nN with an OTS functionalized AFM probe. **a)** NPEOC removal in water. **b)** NPEOC removal in heptane.

5.3.4 Surface Derivatization

The parameters affecting the width and depth of the features created by mechanochemical deprotection have been presented in the previous section. Additionally, it has been shown that the entire OEG-NPEOC-APTES molecule is not being cleaved from the surface. However, the viability of the technique as an alternative to photodeprotection is predicated on its ability to undergo surface reactions on the amine groups exposed by removal of the NPEOC protecting group. Surface reactions of the exposed amine groups with TFAA are presented, as well as work by Dr. Robert Ducker showing specific adsorption of green fluorescent protein (GFP) on mechanochemically patterned regions.

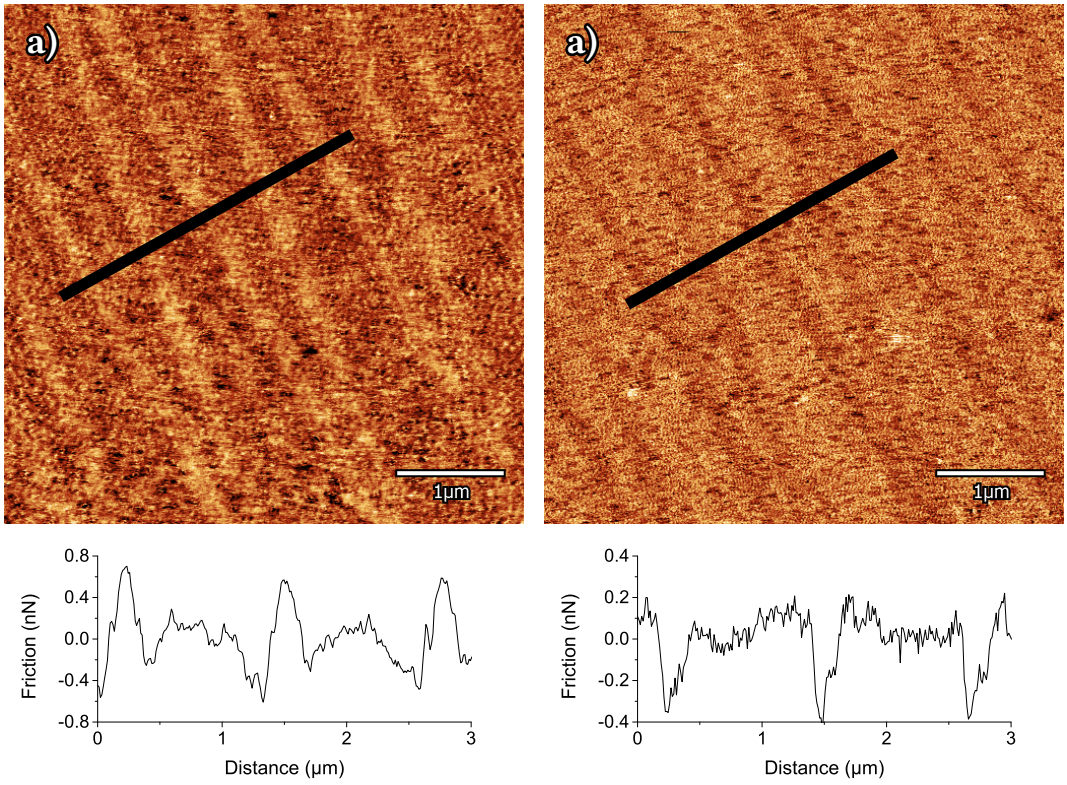

Figure 5.14: Friction images and line profiles corresonding to regions shown by black rectangles for OEG-NPEOC-APTES monolayers deprotected via mechanochemical stimulation by an AFM probe at an applied load of 2000 nN. **a)** Before reaction with TFAA. **b)** After reaction with TFAA.

Derivatization of NPPOC-APTES monolayers after photodeprotection with trifluoroacetic anhydride have been shown to cause a reduction in the friction measured within patterned features.[283] This is due to the decrease in the surface free energy of trifluoromethyl-terminated monolayers (water contact angle ≈120° for close-packed SAMs[432]) compared to those with either OEG- (45°) or amine-terminated (60°) groups, considerably decreasing the contribution of shearing to friction. Friction images obtained via FFM can be seen in Figure 5.14, before and after derivatization with TFAA, following the same method used by Alang Ahmad et al.[283] described in further detail in Section 2.3.5. Immediately apparent is the inversion in friction contrast within the deprotected features compared to the intact monolayer. A total reduction in friction of ≈1.1 nN between the centers the features pre- and post-derivatization was measured. This result demonstrates

the reactivity of the amine groups remaining on the surface after removal of the NPEOC protecting group, and confirms the ability of the technique to selectively deprotect the OEG-NPEOC-APTES monolayer.

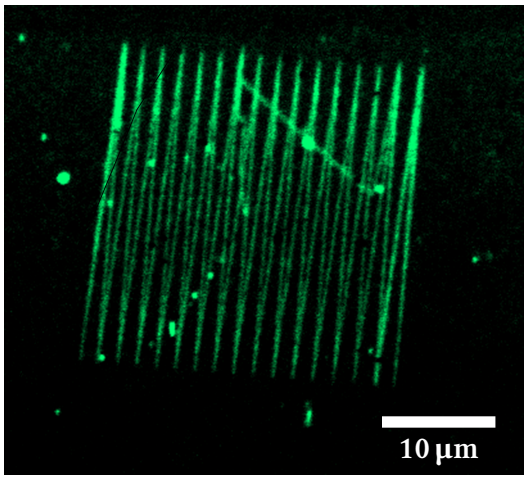

Figure 5.15: Confocal microscopy image of line array fabricated via mechanochemical stimulus, functionalized with GFP. Sample and image produced by Dr. Robert Ducker.

As the NPEOC protecting group was modified with OEG to promote specific protein adsorption,[405,406] Dr. Robert Ducker, a member of the author's laboratory, attempted the immobilization of GFP to the deprotected regions. This was done using the method used by Ul-Haq et al.,[433] whereby the deprotected samples were immersed in a solution of His-tagged GFP in phosphate-buffered saline (PBS). Figure 5.15 shows a confocal microscopy image of a line array produced by the mechanochemical technique described in this chapter. It is clear from the high contrast between the patterned region and the surrounding area that non-specific adsorption of protein is not an issue, with the quality of the pattern matching that of those produced via SNOM.[405,433] These surface derivatization results demonstrate that the mechanochemical deprotection of OEG-NPEOC-APTES (and NPPOC-APTES) by an unmodified AFM probe is a viable alternative to producing nanoscale patterns.

Compared to patterning via SNOM, which requires a 325 nm laser and special controller or feedback loop, the technique only requires a factory-standard AFM instrument and probes with cantilevers stiff enough to reach the required loads. Therefore, further investigation into the mechanics of the deprotection it provides, as well as gaining a better understanding of its limitations are of great interest.

5.3.5 Vector Image Patterning

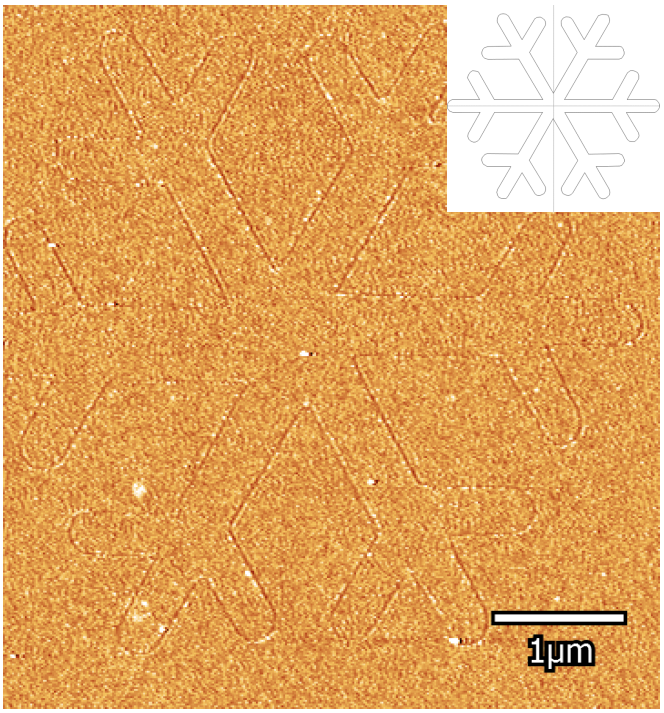

Figure 5.16: AFM height image of a snowflake pattern created via mechanochemical deprotection of OEG-NPEOC-APTES by an AFM tip. Overlaid image shows source image used to create pattern.

While arrays of lines offer a simple way to test how various parameters affect the features created via nanolithographic techniques, more complex structures possible via SPL are sometimes desirable.[250,434] Naturally, this approach is serial in nature and therefore much slower than parallel techniques such as IL.[435] However, some advances have been made in parallelizing SPL techniques, such as the the "Millipede"[436] (and analogous "Snomipede"[437] using SNOM technology) where more than a thousand AFM

tips write to the surface simultaneously. Nevertheless, complex patterns written via the mechanochemical deprotection of OEG-NPEOC-APTES monolayers are presented in this section, demonstrating the ease of creating such features with standard AFM control software. All patterns were fabricated using an applied load of 1000 nN at a write speed of $1\,\mu m\,s^{-1}$.

Figure 5.16 shows an AFM height image of a snowflake pattern generated via removal of the NPEOC protecting group by an AFM. The overlaid image shows the vector graphic used to generate the input file used by the AFM controller software's nanolithography module. These input files include, but are not limited to, commmands that control the lateral translation (position), tip move speed (write speed), and deflection setpoint (applied load) of an AFM probe. Using a piece of software called "AFMdraw" written by the author, vector drawings are converted into a set of translations and other instructions that are then saved to a working nanolithography input file. This allows for any user to rapidly generate complex structures, without the need to work out individual commands by hand. Figures 5.17 and 5.18 overleaf show several more examples of the complex structures created from "AFMdraw" input files. The former is an AFM height image of a schematic diagram of an AFM instrument in operation, while the latter is the University of Sheffield crest.

Due to lateral drift during writing and the use of an open-loop scanner to fabricate all patterns presented, the proportions of the images created do not always match up to the source image. While this could largely be alleviated by employing a closed-loop scanner, the images presented demonstrate the powerful ability of the technique presented in creating complex nanoscale patterns. These could also be further modified by derivatization with biological molecules, as demonstrated in the previous section.

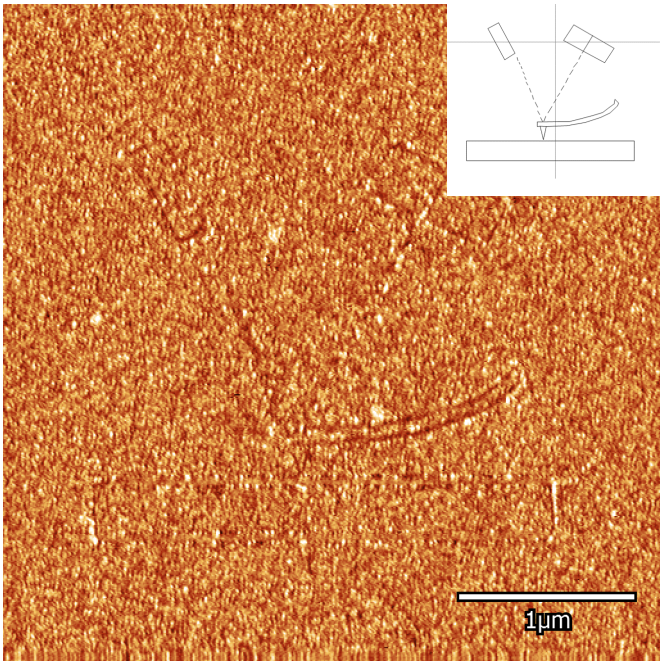

Figure 5.17: AFM height image of a schematic diagram of an AFM in operation created via mechanochemical deprotection of OEG-NPEOC-APTES by an AFM tip. Overlaid image shows source image used to create pattern.

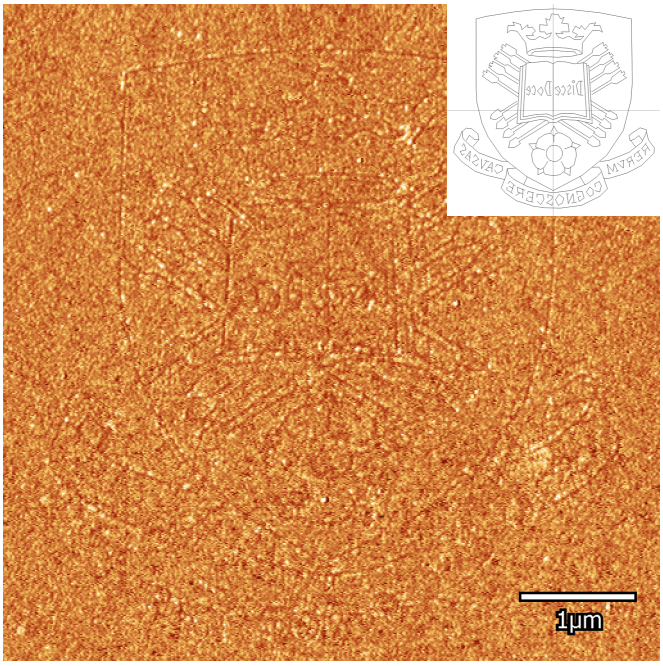

Figure 5.18: AFM height image of the University of Sheffield crest created via mechanochemical deprotection of OEG-NPEOC-APTES by an AFM tip. Overlaid image shows source image used to create pattern.

5.3.6 UV-Visible Spectroscopy

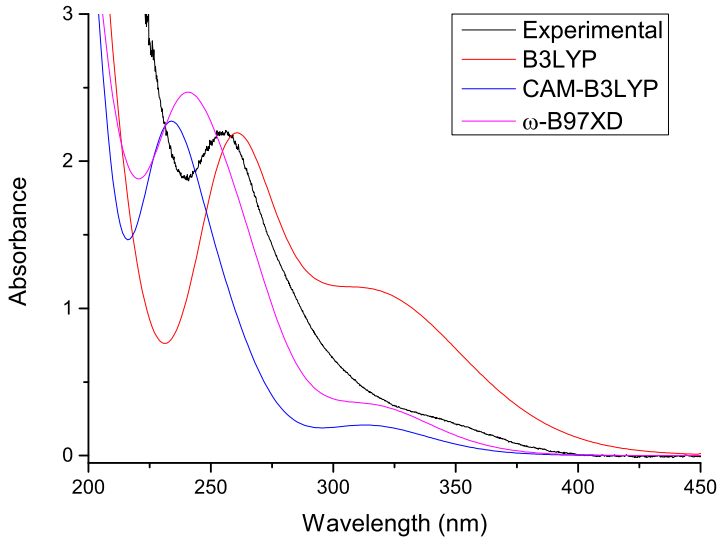

Figure 5.19: UV-Visible spectrum for OEG-NPEOC-APTES in acetonitrile obtained experimentally (black) versus spectra obtained via various DFT functionals and the 6-311G(d,p) basis set.

The results of the UV-Visible spectroscopy measurements of OEG-NPEOC-APTES in acetonitrile can be seen in Figures 5.19 and 5.20 (black line). An absorption peak is found at 265 nm, with a shoulder at 350 nm, thus allowing 325 nm light to interact with the molecule. Plotted on the same axes are the normalized results obtained via DFT time-dependent self-consistent field (TD-SCF) excited-state calculations. In Figure 5.19 above, the 6-311G(d,p) basis set was kept constant while three functionals were investigated: the widely used B3LYP,[259] CAM-B3LYP — a long-range corrected version of B3LYP,[438] and ω-B97XD which includes empirical dispersion parameters as well as long-range corrections.[299] An empirical contribution to dispersion was added by the keyword "empiricaldispersion=gd3bj" to the B3LYP and CAM-B3LYP functional calculations to better account for these forces. Despite no functional offering a perfect match, ω-B97XD was selected for further use due to its similarity to the experimental

spectrum's profile and its inclusion of dispersion, which is not internally accounted for in the CAM-B3LYP functional. With a functional selected, three possible basis sets were compared: 6-311G(d,p), 6-311++G(d,p), and aug-cc-pVTZ.

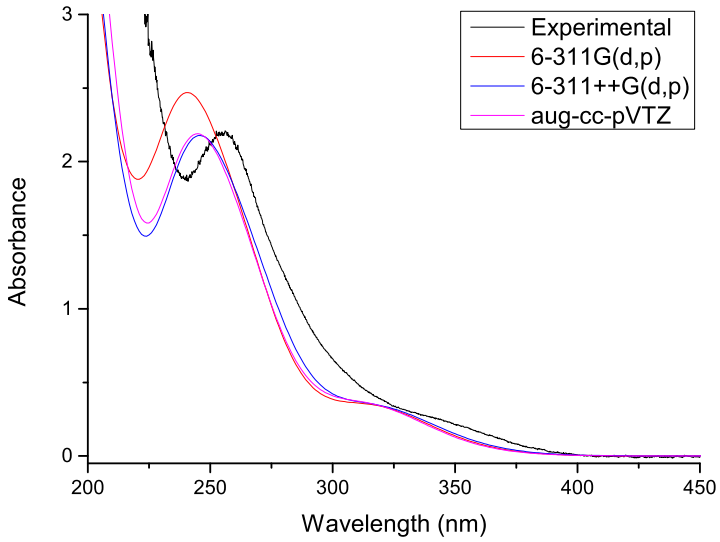

Figure 5.20: UV-Visible spectrum for OEG-NPEOC-APTES obtained experimentally (black) versus spectra obtained via various DFT basis sets and the ω-B97XD functional.

The 6-311++G(d,p) basis set includes the ++ diffuse function, compared to 6-311G(d,p), in order to better represent molecular orbitals further away from the nucleus (including those of lighter atoms).[300] Similarly, aug-cc-pVTZ, a triple-zeta basis set[439] based on Dunning's correlation consistent basis set,[440] also includes a diffuse function of each function type per atom, as denoted by the aug- term.[439,441] Figure 5.20 shows the results of the excited-state TD-SCF DFT calculations using these three basis sets with the ω-B97XD functional. Perhaps unsurprisingly, both triple-zeta basis sets with included diffuse functions offer almost identical theoretical UV-Vis spectra, both reducing the negative absorption peak wavelength offset from the experimental result to 250 nm in contrast with 6-311G(d,p). The position of the shoulder at 325 nm remained constant for all three basis sets; a blueshift of 25 nm compared to the experimental result. This offset is thought to occur due to the minor differences between the molecule under investigation via DFT and the OEG-NPEOC-APTES molecule used experimentally, as well as the solvent

environment. Therefore, the 6-311++G(d,p) basis set was selected for all future DFT calculations (favored to aug-cc-pVTZ due to reduced computational cost for similar results, as no heavy atoms present).

5.3.7 Density Functional Theory

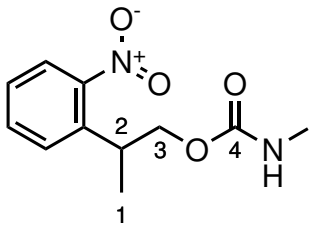

Figure 5.21: NPPOC molecule used in DFT simulations with labelled ethoxycarbonyl carbon atoms.

The proposed photodeprotection mechanism starting from two main conformations of the NPPOC molecule seen in Figure 5.21 (with the ethoxycarbonyl carbon atoms labelled 1 – 4) was investigated. Images of two starting conformations can be found in Figure 5.22, and are referred to as either "straight" or "folded", depending on the position of the amine with respect to the nitrophenyl group. While the images presented below were obtained in the gas-phase, these two conformations were also found in simulations to be stable for water.

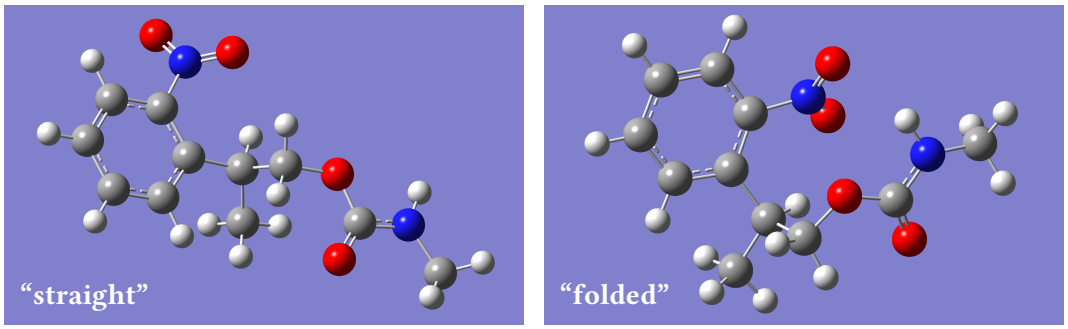

Figure 5.22: Optimized ground-states of the two main starting conformations. **Left)** "Straight" conformation, with ethoxycarbonyl chain positioned away from the nitrophenyl group. **Right)** "Folded" conformation, where amine is bent towards nitrophenyl group.

Table 5.2: Hartree energies (E_h) of optimized ground- and excited-state structures in the gas-phase at sequential steps on the proposed photodeprotection pathway (Figure 5.2) for the "folded" conformation. Also shown are the difference in energy at each step, as well as the sum of all steps compared to the initial position.

	Ground		Excited		
Pathway step	E_h	ΔE_h	E_h	ΔE_h	**Cumulative** ΔE_h
Initial conformation	−837.896	0.000	—		0.000
+*hν*	—		−837.779	0.116	0.116
H^+ transfer	—		−837.717	0.062	0.179
H^+ transfer (relax)	−837.827	−0.110	—		0.069
Decomposition (Final)	−837.857	−0.030	—		0.038

$1\,E_h = 27\,\text{eV} = 2600\,\text{kJ mol}^{-1} \equiv \lambda = 46\,\text{nm}$

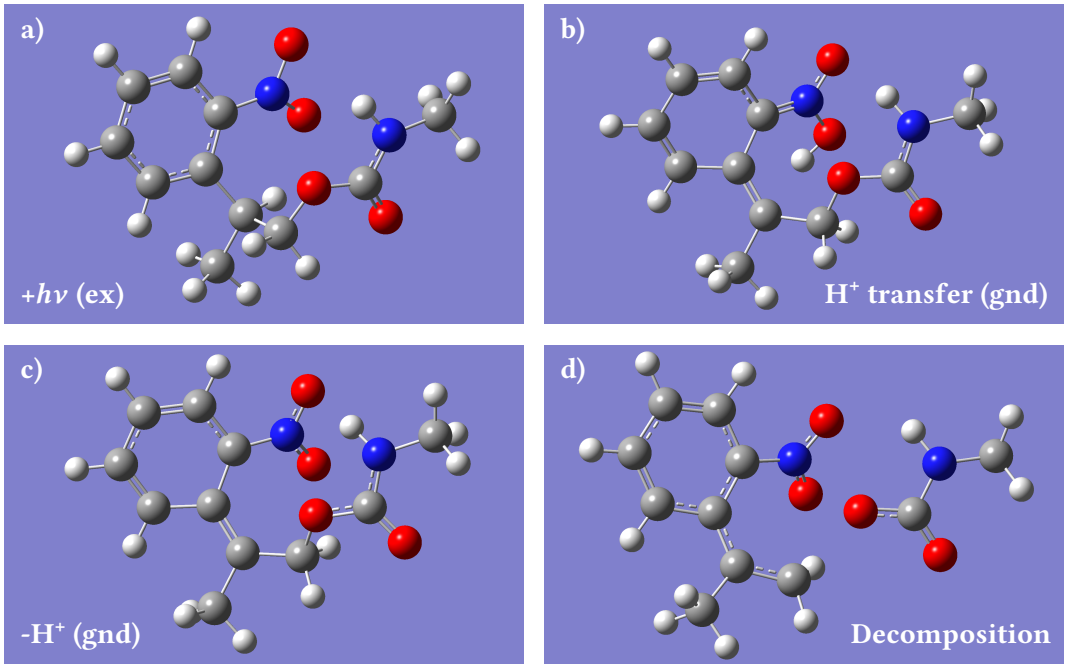

Figure 5.23: Optimized geometries at different steps along the proposed photodeprotection pathway. **a)** After irradiation with UV light. **b)** After proton transfer and relaxation (intermediate formation). **c)** After proton loss (ionic form). **d)** After decomposition of intermediate.

The energies of the optimized structures for the "folded" conformation along the proposed photodeprotection scheme can be found in Table 5.2. The initial photoirradiation step leads to an excited-state conformation with an increased energy of 0.116 E_h (3.15 eV) compared to the ground-state, achievable by irradiation with a 325 nm (3.81 eV) laser. From Figure 5.23a it can be seen that there is a conformational change in the nitro group. In the optimized ground-state geometry, the carbon, nitrogen, and oxygen atoms are in a planar arrangement to each other. However, upon excitation there is an elongation of both NO bonds (from 1.21 Å to 1.28 Å) and a change in the angles between the constituent atoms leading to an approximately tetrahedral configuration (∠ONO: 124.3° to 105.4°), suggesting a change in the local electronic configuration.

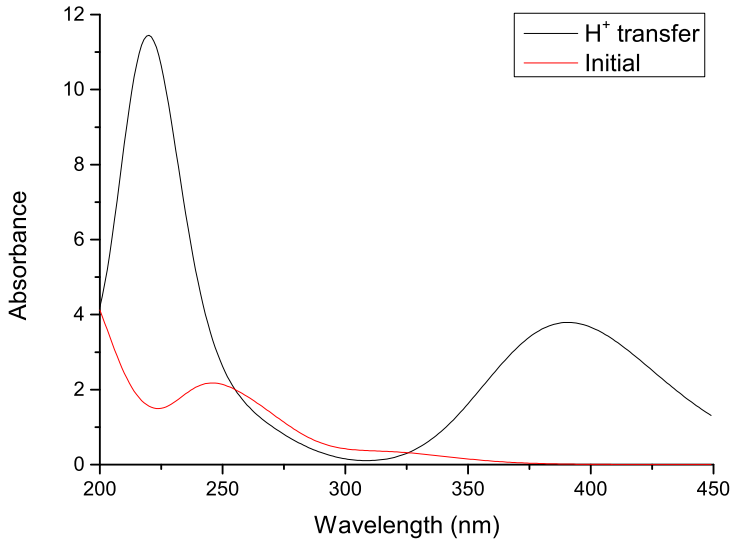

Figure 5.24: Theoretical UV-Visible spectra of initial and proton transfer conformations along photodeprotection mechanism.

A further 0.062 E_h (1.69 eV) is required to transfer a proton between C_2 and the nearest oxygen in the nitro group to create an *aci*-nitro intermediate, leading to a total change in energy from the ground-state of 0.179 E_h (4.87 eV). However, the ground-state energy of the *aci*-nitro is 0.110 E_h (2.99 eV) lower than in the excited-state and 0.047 E_h (1.28 eV) lower than the excited-state following UV radiation. Additionally, a calculation of the UV-Vis spectrum at this step of the proposed pathway (Figure 5.24) shows a redshift in

the $\pi\pi^*$ transition, in which an electron is excited from the highest occupied molecular orbital (HOMO) to the lowest unoccupied molecular orbital (LUMO). The lowest energy absorbance peak appears at 390 nm with an oscillator strength of 0.178, compared to the NPPOC ground-state where the $\pi\pi^*$ transition occurs at 320 nm with an oscillator strength of 0.015 (seen as an increase in the calculated absorbance). This $S_0 \rightarrow S_1$ transition has a strength an order of magnitude greater than in the the initial ground-state conformation, albeit at a lower energy, but is unlikely to be a factor in subsequent steps in the decomposition of the molecule.

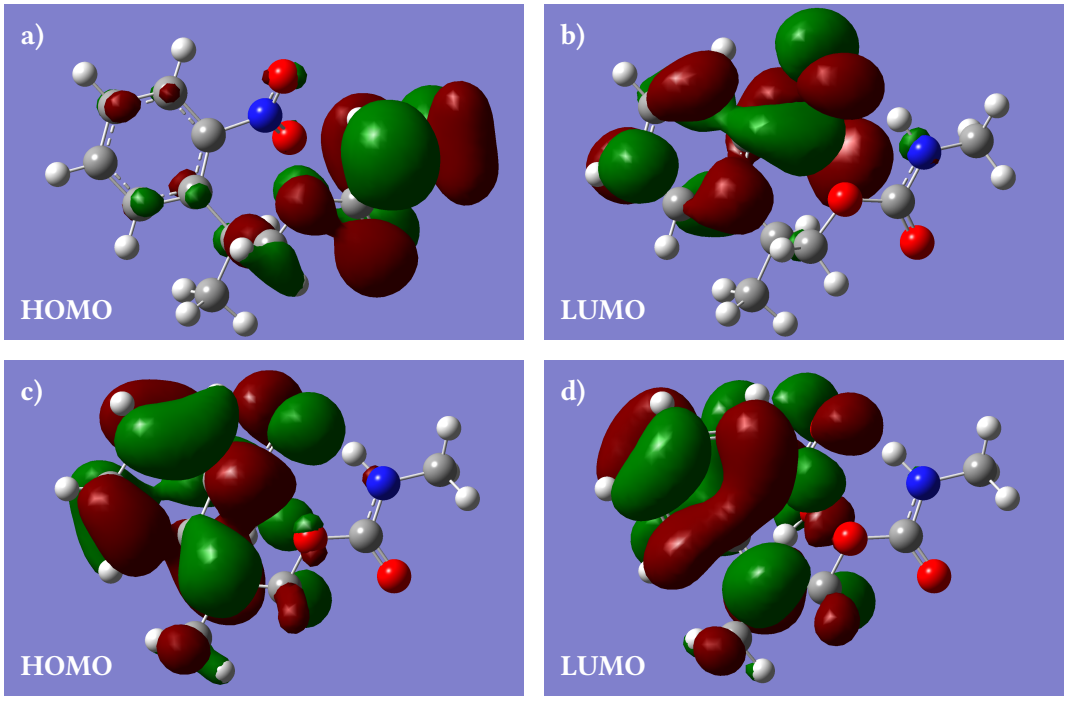

Figure 5.25: HOMO and LUMO of the ground-state geometry for the initial conformation (**a**, **b**) and following proton transfer (**c**, **d**).

The molecular orbitals of the initial and post-proton transfer forms of NPPOC were calculated as part of the geometry optimizations. In the initial form, the HOMO (Figure 5.25a) is localized predominantly over the carbamate section at the end of the tail group, while the LUMO (Figure 5.25b) is found on the nitrophenyl; more specifically on the nitro group itself. Therefore, the HOMO-LUMO transition to the S_1 energy state can be assumed to incorporate intramolecular charge-transfer (ICT). Thus, due to the electron density of the LUMO on the nitro group oxygen atoms and the lower ground-state energy

relative to the initial NPPOC molecule ($-0.110\,E_h$), it is plausible that a proton transfer could occur upon photoirradiation.[272] Combined with a proton transfer, it is likely that this ICT character is responsible for the calculated redshift in the first electronic transition of the new form. It can be seen from Figures 5.25c and 5.25d that this ICT behavior is not present for the $\pi\pi^*$ transition, as both the HOMO and LUMO are localized across the nitrophenyl group.

Table 5.3: Hartree energies (E_h) of optimized ground- and excited-state structures in water at sequential steps on the proposed photodeprotection pathway (Figure 5.2) for the "folded" conformation. Also shown are the difference in energy at each step, as well as the sum of all steps compared to the initial position.

	Ground		Excited		
Pathway step	E_h	ΔE_h	E_h	ΔE_h	**Cumulative ΔE_h**
Initial conformation	−837.909	0.000	—		0.000
+$h\nu$	—		−837.779	0.129	0.129
H^+ transfer	—		−837.721	0.059	0.188
H^+ transfer (relax)	−837.835	−0.114	—		0.074
Decomposition (Final)	−837.874	−0.039	—		0.035

$1\,E_h = 27\,\text{eV} = 2600\,\text{kJ mol}^{-1} \equiv \lambda = 46\,\text{nm}$

The formation of an *aci*-nitro compound via proton transfer after UV radiation has been postulated for many years.[410,442] Previous studies have shown that transient absorption spectra of *o*-nitrobenzyl (*o*NB)[443] and various NPPOC derivatives[444,445] show an absorbance peak at 400 nm after UV exposure. These results are mirrored in the theoretical spectra obtained for the *aci*-nitro intermediate in the gas-phase (Figure 5.24). Formation of the anionic form (via proton loss) has been observed by an increase of the absorption band at 450 nm, controllable via the pH of the environment. The decomposition of the NPEOC *aci*-nitro intermediate into a nitrosobenzaldehyde product, as is the case for the *o*NB intermediate,[443] has also been demonstrated.[444] However, studies have shown that the β-elimination pathway (leading to a nitrostyrene product) can be favored by the presence of water or an aprotic base.[411,412,444,446] To determine the effect of water on the

ground- and excited-state energies, simulations were run using the parameters described in Section 5.2.5 and are presented in Table 5.3. The results show no significant deviation in the energies of the optimized ground- and excited-state geometries, and therefore the overall photodeprotection mechanism is unlikely to be considerably affected.

The difference in energy between the initial NPPOC molecule and the final products is merely 100 kJ mol^{-1}, with an initial excitation occurring via UV irradiation at 325 nm. The main energetic barrier in the photodeprotection scheme is therefore in the initial $S_0 \rightarrow S_1$ transition, which leads to a proton being abstracted by the nitro group. However, whether this mechanism is feasible via mechanochemical means, or if the deprotection proceeds via a different pathway is difficult to ascertain. With this aim, the C_3—O and C_4—N bonds were artificially stretched by freezing the bond lengths at increasing 0.05 Å intervals, on both sides of their corresponding optimized bond length.

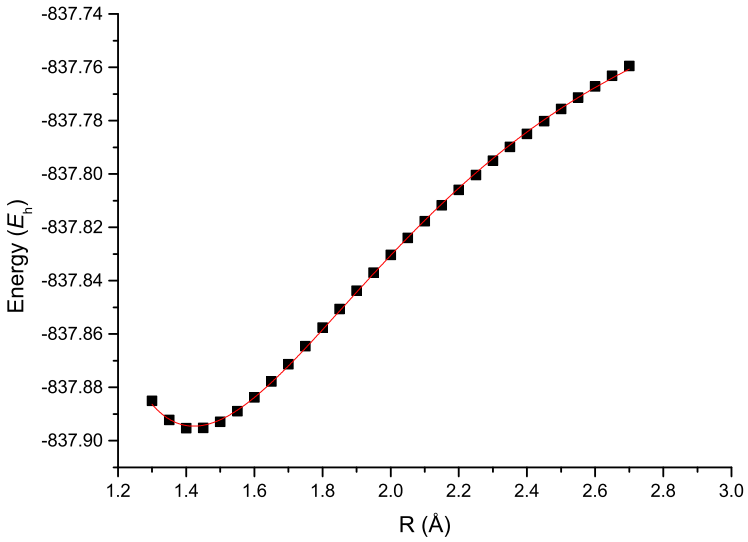

Figure 5.26: Plot of energy (E_h) against bond length (R) for the initial NPPOC ground-state conformation for the C_3O bond, fitted with the Morse potential. ($R^2 = 0.99$).

The resulting bond length to energy plots, an example of which can be seen in Figure 5.26, were fitted with the Morse oscillator potential:

$$V(R) = D_e\left(1 - e^{-a(R-R_e)}\right)^2 \tag{5.2}$$

where D_e is the well depth (equivalent to the bond-dissociation energy), a is a parameter that defines the width of the well, R is the separation between atoms (corresponding to the frozen bond lengths), and R_e is the equilibrium bond length.

Table 5.4: Equilibrium bond lengths (R_e) and bond-dissociation energies (D_e) for a number of different bonds in the initial and ionic forms of the NPPOC molecule in the gas-phase and water, determined from the fitting of the Morse potential.

	Gas-phase				**Water**			
Bond:	**C_3−O**	**C_3−O (-)**	**C_4−N**	**C_4−N (+)**	**C_3−O**	**C_3−O (-)**	**C_4−N**	**C_4−N (+)**
R_e (Å):	1.422	1.442	1.353	1.512	1.435	1.443	1.350	1.496
D_e (E_h):	0.177	0.024	0.233	0.087	0.132	0.033	0.225	0.084

The results of the fits to the Morse oscillator potential for the C_3−O and C_4−N bonds in their initial and ionic forms can be found in Table 5.4. Other than the anionic *aci*-nitro form, a cation with the positive charge on the carbamate nitrogen was also investigated. It was found that a proton transfer to said nitrogen led to a spontaneous decomposition of the NPPOC molecule into nitrostyrene, carbon dioxide, and methylamine products upon geometry optimization. It is clear that in the neutral form, decomposition via the elongation of the C_3−O bond is favorable, as the derived dissociation energy is 25 % to 40 % greater for C_4−N in the gas-phase and water, respectively. In the case of the ionic forms, a longer equilibrium bond length was obtained, with a corresponding decrease in both bond dissociation energies. Additionally, UV-Vis spectra of conformations with HOMO (carbamate) and LUMO (nitro) regions forced into close proximity (≈1.6 Å) were calculated.

At these constrained conformations, the $S_0 \rightarrow S_1$ transition occurs at lower energies, possible at near-infrared wavelengths (up to 1000 nm). The positions of the HOMO and LUMO were calculated and are presented in Figure 5.27. Unlike the initial conformation, the HOMO is now positioned over the nitro group which would account for the change in the absorption spectrum, while the LUMO is now also shared across the carbamate group. An AFM uses 650 nm laser light to detect the deflection of the cantilever, flooding the surface with light of this energy. It is therefore possible that the compressive energy simply causes a redshift in absorption band of the $\pi\pi^*$ transition causing a lower energy photon to be absorbed, thus leading to a proton transfer and the deprotection follows as usual. However, the oscillator strength of the transition is reduced by an order of magnitude and $\approx$0.15 E_h (4.08 eV) of energy is required to compress the molecule sufficiently.

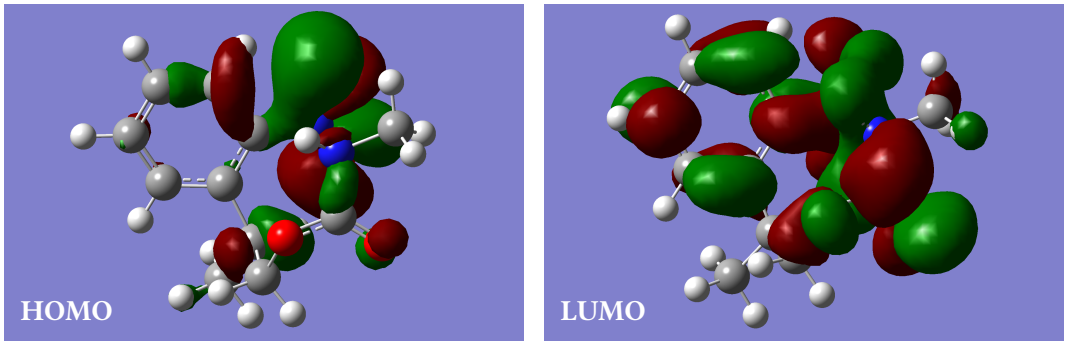

Figure 5.27: HOMO and LUMO of the ground-state geometry of the compressed NPPOC conformation (N−N distance frozen at 1.5 Å).

Assuming a coefficient of friction of 0.1 (similar to those achieved in Chapter 4 for stronger surface interactions, and within the order of magnitude expected for non-polar alkylsilane monolayers[218]), a normal force of 500 nN would lead to a friction force of 50 nN. The work done to move the tip over 1 µm on the surface is thus 5×10^{-14} J, covering a total area of 2×10^6 Å^2 (taking 20 nm contact width from feature FWHM). The packing density of an alkylsilane on silicon is approximately 20 Å^2/molecule,[216] likely denser than that of the OEG-NPEOC-APTES monolayer, leading to a total energy of 5×10^{-19} J (3.12 eV) per molecule. This result is extremely close to the 4.08 eV required according to DFT and makes the possibility of a redshift in the absorption spectrum of NPPOC more plausible, especially

considering the conservative assumptions made. Kinetic friction is converted into thermal energy through a dissipation process into phonons—quasiparticles representing atomic vibrations (i.e., heat)—at the surface.[447,448]

In this phononic model, kinetic energy is transferred from the moving AFM tip into the surface by coupling to the vibration frequencies of the adsorbate.[448] Therefore, if one or more vibrational modes exist that bring the two nitrogen atoms in the NPPOC molecule closer, it would be conceivable that the lateral work done by the AFM tip leads to a redshift in the absorption. Analysis of the IR spectrum computed via DFT revealed that several of these modes are present for the molecule at energies between 88 and 383 cm^{-1}, with such low-energy modes being favored for the transfer of mechanical energy into phononic excitation.[449]

If mechanochemical stimulus is sufficient to promote proton transfer within the molecule—whether directly or via the absorption of a lower energy photon—the *aci*-nitro intermediate (and hence the anionic form) may be formed. Alternatively, it may allow the carbamate nitrogen to abscond a proton from a nearby molecule, and therefore decomposition of NPPOC into nitrostyrene or nitrosobenzaldehyde would be possible without the absorption of a high energy photon. The latter by-product would not be favorable for patterning, as it would leave behind a carbamate end-group[450] rather than the desired amine. Previous photopatterning studies in the author's laboratory have shown the existance of trace amounts of nitroso by-product after UV photodeprotection, with the majority of the exposed area proceding via the β-elimination route.[405]

Molecular dynamics simulations may provide further insight into the effect of compressive force on the conformation of individual OEG-NPEOC-APTES molecules and their neighbors as part of a self-assembled monolayer, and would be a good starting point for future work.

5.4 Conclusions

The deprotection of OEG-NPEOC-APTES self-assembled monolayers via the mechanochemical removal of the NPEOC protecting group was demonstrated using an AFM probe rastered across the surface above a critical applied load. The features

created were easily reproducible, with depths of 0.2 – 0.6 nm and FWHM of 20 – 100 nm depending on the applied load and write speed. Evidence that the full monolayer molecules were not being cleaved from the surface by attempting the same experiments on fresh APTES SAMs. At lower loads (high enough to create features in OEG-NPEOC-APTES), height images were indistinguishable from virgin monolayers, with features only becoming visible at loads exceeding 9000 nN. Friction images obtained show an increase in the friction within the fabricated nanostructures, suggesting the incomplete removal of the NPEOC protecting group and/or the presence of by-products not removed by the rinsing process. These have the effect of increasing the friction force measured due to an increase in disorder, leading to a rise in the plowing contribution, and maintaining enough oligoethylene glycol (OEG) groups at the surface to prevent a significant reduction in the shearing term.

Tip chemistry and solvent environment were also investigated, to determine whether the mechanochemical lithography process is aided or hindered by external factors. AFM probes were functionalized with non-polar n-octadecyltrichlorosilane (OTS) SAMs and were used to write features into OEG-NPEOC-APTES monolayers. Features created using these probes were indistinguishable from those created with unmodified polar silicon probes, and as such tip chemistry alone is not believed to affect the mechanochemical deprotection. Nanostructures were also fabricated in polar (water) and non-polar (heptane) liquids, with feature sizes being identical to those created in air. The only difference observed was for features written in heptane with OTS functionalized probes, which showed discrete accumulations of material at the edges of the lines drawn. This has been explained by the inability of the non-polar tip and liquid to remove the polar by-products of the deprotection mechanism, causing them to agglomerate at the surface as the AFM probe moves across the surface.

To show that the protecting group is being properly removed to expose an amine group, samples were reacted with trifluoroacetic anhydride (TFAA) after patterning. A successful reaction was achieved, as evidenced by the reduction in friction within the nanostructures after derivatization. As the $-CF_3$ groups resulting from a reaction with the exposed amine groups are usually well ordered and lead to a lower surface free energy, a reduction in the measured friction strongly suggests removal of the NPEOC protecting

group is indeed occurring. Additionally, a fellow member of the author's research group was successfully able to selectively immobilize green fluorescent protein (GFP) to the deprotected regions' amine groups using well established methods and image the resulting samples with confocal microscopy.

The pathway proposed for the photodeprotection of OEG-NPEOC-APTES and NPPOC-APTES self-assembled monolayers (SAMs) was investigated using density functional theory (DFT). The ground- and excited-state geometries of a simplified NPPOC molecule were optimized for "straight" and "folded" initial conformations in the gas-phase and water. A number of functionals and basis sets were used to calculate theoretical UV-Visible spectra of NPPOC in solution. From these, the functional and besis set generating spectra most closely resembling those of experimentally obtained ones were used in all future simlations.

The main barrier in the photodeprotection pathway was found to be in the transfer of a proton to the nitro group, forming an *aci*-nitro intermediate. The UV-Visible spectrum of this intermediate structure was determined, and was found to match that of transient spectra obtained experimentally in the literature. From this intermediate, the molecule is able to decompose into either a nitrostyrene or nitrosobenzaldehyde by-product, depending on the basicity of the environment. A photon at an energy of 3.81 eV ($\lambda = 325$ nm) is sufficient to allow a $\pi\pi^*$ transition within the molecule, which has intramolecular charge-transfer (ICT) nature. This is due to the highest occupied molecular orbital (HOMO) and lowest unoccupied molecular orbital (LUMO) being located on different parts of the molecule (carbamate and nitro group, respectively), and therefore promoting proton transfer within the molecule upon further relaxation.

To simulate the possible effect of a compressive force on the protecting group's molecular structure, and how this may lead to deprotection without the need for UV exposure, the ground- and excited-state geometries for constrained conformations were optimized. When both nitrogen atoms were brought into close proximity, which may occur upon compression by an AFM probe at high loads, the UV-Visible absorption peaks were found to redshift. This could lead to a lower-energy photon being absorbed and allow the photodeprotection pathway to proceed as normal. However, further molecular

dynamics simulations would need to be carried out in order to better predict the potential conformational changes of a OEG-NPEOC-APTES monolayer upon compression by an AFM tip.

All the data presented in this chapter is strong evidence to support the hypothesis that the deprotection is occurring via mechanochemical means. The technique offered is novel, and offers a highly accessible method to pattern OEG-NPEOC-APTES monolayers, without the need for a UV light source. However, further work to understand the exact nature of the mechanochemical process is of great interest, with molecular dynamics simulations and analysis of the by-products created being a good starting point for future studies.

CHAPTER 6

Conclusions and Future Work

The adhesive energies between surfaces in liquids were calculated using two different approaches: Lifshitz theory of continuum mechanics and the surface site interaction point (SSIP) Hunter model of hydrogen bond thermodynamics. The predicted adhesive interactions between hydrocarbon surfaces were obtained for over 200 liquids, and the values of both theories were compared. Relatively good agreement was found between Lifshitz theory and the Hunter model for alkanes, amines, and primary alcohols, but diverged considerably for liquids containing heavier atoms or aromatic rings. The use of bulk solvent properties was suggested as the cause for this disparity between the theoretical interfacial energies, in particular due the difference in the refractive index between the interacting phases yielding a greater predicted dispersion force in Lifshitz theory. Binary mixtures of non-polar and polar liquids were also modelled, where the presence of aromatic rings also led to disagreement between the models. Benzyl alcohol/methanol mixtures, in addition to a pure liquids with a range of predicted values, were selected for experimental investigation in a later chapter.

By assuming polar surfaces to consist of a thin polar film on a thicker non-polar phase, Lifshitz theory calculations were expanded to determine the interactions between alcohol-, acid-, and amine-terminated surfaces. Both models were capable of accurately predicting the interactions between alcohol- and acid-terminated surfaces in liquids previously measured in the literature. However, Lifshitz theory arriving at a similar work of adhesion as found experimentally was considered to be potentially coincidental and would warrant further investigation. The calculations presented for the Lifshitz theory employed an approximated form of the Hamaker constant equation, and therefore determining this quantity from the exact relation would be a potential avenue for further research. Naturally, this requires the complete absorption spectrum of the interacting media (available for some liquids from various synchrotron sources such as DESY), and therefore a reduced set of liquids would be available. Additionally, it would be interesting to calculate the potential interactions between mixed monolayer and asymmetric polar (e.g., acid–amine) surfaces, both in pure liquid and in binary mixtures.

Force spectroscopy and friction force microscopy (FFM) was used to measure the tribological properties of several hydrocarbon self-assembled monolayers (SAMs), with the aim of verifying the predicted Lifshitz work of adhesion and Hunter free energy of complexation. Pull-off forces of 1-dodecanethiol (DDT) monolayers adsorbed onto gold were obtained in various liquids having previously been identified as showing either consistencies or discrepancies between the two theoretical models. The experimental work of adhesion between non-polar surfaces in alkanes was found to be well described by both approaches. However, Lifshitz theory consistently underestimated the interaction energies in more polar liquids—water in particular—and greatly overestimated adhesion in aromatic solvents. This is in contrast to the Hunter model, which, despite being concerned with the thermodynamic equilibrium of unconstrained molecules rather than fixed interaction sites, was able to predict the magnitude of the interactions with remarkable accuracy. The extremely high interaction energies in water are also well defined by the Hunter model, suggesting that the experienced "hydrophobic effect" could be understood from the equilibrium electrostatic competition of binding between non-polar interaction sites and water. Measurements in ethanol and water were repeated for alkylphosphonic acid SAMs on aluminium oxide and alkylsilanes SAMs on glass, showing the effect of monolayer packing and the underlying substrate on the forces experienced. Finally, pull-off force measurements in binary mixtures of benzyl alcohol and methanol showed that the form of the relation of W_{ad} on the concentration of benzyl alcohol was well accounted for by the Hunter model while being completely misrepresented by Lifshitz theory.

Friction-load plots of DDT SAMs were recorded for a subset of liquids showing adhesion measurements representative of the agreements and differences in the predicted values obtained from the Hunter model and Lifshitz theory. In liquids with low measured adhesive energies (below $1\,\mathrm{mJ\,m^{-2}}$), linear relationships between the friction force and the applied load were obtained, demonstrating Amontons-like behavior. At interfacial adhesion between $1 - 6\,\mathrm{mJ\,m^{-2}}$ a linear friction-load relation was maintained, but with a non-zero intercept value proportional to the measured work of adhesion. For methanol and water, which yielded the greatest experimental interaction energies ($6.52\,\mathrm{mJ\,m^{-2}}$ and $46.5\,\mathrm{mJ\,m^{-2}}$), sublinear character was observed in its friction-load plots with friction being measured further into the tensile range. This change in behavior over the range of

adhesive interactions has been attributed to the friction force being the sum of load- (μ) and area-dependent (τ) terms. The former arises from the tip plowing through the surface monolayer, penetrating further (and thus displacing more molecules) as the applied load is increased, with adhesion acting as a constant addition to the normal force. On the other hand, the area-dependence originates from the shearing of the surface monolayers as the effective contact area increases in accordance to the appropriate contact mechanical model (i.e., JKR or DMT) for the system, as determined from the calculation of a transition parameter.

Values of μ were found to be independent of adhesive energy, with the exception of liquids yielding a work of adhesion approaching zero, in which a reduced coefficient of friction was observed. An increase in the value of τ was seen as W_{ad} increased up to a threshold value, the form of this rise being correctly predicted by the Hunter model. Due to the overestimation in the work of adhesion, Lifshitz theory did not present the same relationship between the shear strength and the interaction energy. Measuring the work of adhesion and friction for liquids with dielectric constants between those of water and methanol would provide further insight into the relation between it and adhesion of hydrocarbon surfaces. Similar experiments could also be performed to verify the results of any expanded calculations to include polar and mixed monolayers. Additionally, further friction-load plots could be obtained to elucidate the source of lower coefficients of friction obtained in liquids yielding lower adhesive forces between hydrocarbon surfaces.

In the final results chapter, a novel technique for the mechanochemical deprotection of meta-heptaethyleneglycol 2-(4-nitrophenyl)ethoxycarbonyl (3-aminopropyl)triethoxysilane (OEG-NPEOC-APTES) SAMs using a tapping mode AFM probe is presented. Where excitation by UV light is usually required to cause the removal of the NPEOC protecting group—exposing an amine group for derivatization—it is shown that the transfer of mechanical energy from an AFM probe to the surface is sufficient to circumvent this requirement. The technique allows for well-defined patterns to be formed reproducibly, with feature sizes of 20 nm being readily achievable. Applied loads and write speeds were systematically changed to determine the effect on the resulting feature widths and depths. Greater loads were found to create wider and

deeper features (up to a critical point, before tip blunting), while the write speed had no appreciable effect on the written features. Changing the tip chemistry and environment, by adsorbing different monolayers and repeating the nanolithography in polar and non-polar liquids, also had no effect on the features formed. It was shown that the patterns formed were not simply a result of the cleavage of the complete monolayer, as APTES SAMs required applied loads several orders of magnitude greater to be visibly removed than the minimum load necessary for OEG-NPEOC-APTES. In addition, it was demonstrated that only the NPEOC group was being removed through the reaction of TFAA with the remaining amine at the surface, yielding a decrease in the friction force measured within the features.

Density functional theory (DFT) was employed to model the photodeprotection pathways of OEG-NPEOC-APTES through UV exposure, with the aim of elucidating potential mechanochemical deprotection mechanisms. The photodeprotection is believed to proceed through a proton transfer that is promoted by the intramolecular charge-transfer ocurring when a high energy photon is absorbed. This leads to the formation of an *aci*-nitro intermediate which further decomposes into the desired products, depending on the basicity of the environment. To simulate the effect of an AFM probe compressing the molecule, the ground- and excited-state conformations of a constrained geometry were optimized. The resulting energies and predicted UV/Visible spectra suggest a redshift in the absorption spectrum could occur, offsetting the energy requirement for the critical proton transfer in the deprotection pathway. Conversion of thermal energy into specific vibrational modes are therefore a presented as a possible mechanism for the mechanochemical removal of the NPEOC protecting group. Repeating the experiments with an AFM instrument that employs an infrared laser for tip position sensing would therefore be a logical step for future work. Additionally, molecular dynamics simulations may also provide further insight into the mechanistic effects of a tip plowing into the monolayer at increasing applied loads.

References

1. H. Nathanson, W. Newell, R. Wickstrom and J. Davis, "The resonant gate transistor", *IEEE Trans. Electron Devices*, 1967, **14**, 117.
2. B. Bhushan, *Handbook of micro/nano tribology*, CRC Press, 2nd Editio, 1998.
3. C. M. Mate, *Tribology on the small scale: a bottom up approach to friction, lubrication, and wear*, OUP Oxford, 2007.
4. G. Amontons, "De la resistance causée dans les machines", *Hist. l'Académie R. des Sci. avec les Mémoires Mathématique Phys.*, 1699, 206.
5. R. Maboudian, W. R. Ashurst and C. Carraro, "Self-assembled monolayers as anti-stiction coatings for MEMS: Characteristics and recent developments", *Sensors Actuators, A Phys.*, 2000, **82**, 219.
6. J. Israelachvili, *Intermolecular & surface forces*, Academic Press Limited, 1992.
7. V. A. Parsegian, *Van der Waals forces: a handbook for biologists, chemists, engineers, and physicists*, Cambridge University Press, 2005.
8. W. H. Keesom, "On the deduction of the equation of state from Boltzmann's entropy principle", *KNAW Proc.*, 1912, **15**, 240.
9. P. Debye, "Molekularkräfte und ihre Elektrische Deutung", *Phys. Z.*, 1921, **22**, 302.
10. F. London, "The general theory of molecular forces", *Trans. Faraday Soc.*, 1937, **33**, 8b.
11. H. Hamaker, "The London—van der Waals attraction between spherical particles", *Physica*, 1937, **4**, 1058.
12. M. Planck, "Entropie und Temperatur strahlender Wärme", *Ann. Phys.*, 1900, **306**, 719.
13. M. Planck, "Über das Gesetz der Energieverteilung im Normalspectrum", *Ann. Phys.*, 1901, **309**, 553.
14. A. Einstein, "Über einen die Erzeugung und Verwandlung des Lichtes betreffenden heuristischen Gesichtspunkt", *Ann. Phys.*, 1905, **322**, 132.
15. H. Casimir, "On the attraction between two perfectly conducting plates", *Proc. K. Ned. Akad.*, 1948, **360**, 793.
16. S. K. Lamoreaux, "Demonstration of the Casimir force in the 0.6 to 6 μm range", *Phys. Rev. Lett.*, 1997, **78**, 5.
17. H. B. G. Casimir and D. Polder, "The influence of retardation on the London-van der Waals forces", *Phys. Rev.*, 1948, **73**, 360.
18. M. Boström, B. E. Sernelius, I. Brevik and B. W. Ninham, "Retardation turns the van der Waals attraction into a Casimir repulsion as close as 3 nm", *Phys. Rev. A*, 2012, **85**, 010701.
19. B. Derjaguin, "Untersuchungen über die Reibung und Adhäsion, IV", *Kolloid-Zeitschrift*, 1934, **69**, 155.
20. E. M. Lifshitz, "The theory of molecular attractive forces between solids", *Sov. Phys. JETP*, 1954, **97**, 73.
21. N. Nikogeorgos and G. J. Leggett, "The relationship between contact mechanics and adhesion in nanoscale contacts between non-polar molecular monolayers", *Tribol. Lett.*, 2013, **50**, 145.
22. W. J. Miller and N. L. Abbott, "Influence of van der Waals forces from metallic substrates on fluids supported on self-assembled monolayers formed from alkanethiols", *Langmuir*, 1997, **13**, 7106.
23. G. A. Jeffrey and W. Saenger, *Hydrogen bonding in biological structures*, Springer Berlin Heidelberg, Berlin, Heidelberg, 1991, p. 569.
24. M. D. Joesten and L. J. Schaad, *Hydrogen bonding*, M. Dekker, 1974.
25. A. Werner, "Ueber Haupt- und Nebenvalenzen und die Constitution der Ammoniumverbindungen", *Justus Liebig's Ann. der Chemie*, 1902, **322**, 261.

26. A. Hantzsch, "Über die Isomerie-Gleichgewichte des Acetessigesters und die sogen. Isorrhopesis seiner Salze", *Berichte der Dtsch. Chem. Gesellschaft*, 1910, **43**, 3049.
27. W. M. Latimer and W. H. Rodebush, "Polarity and ionization from the standpoint of the lewis theory of valance", *J. Am. Chem. Soc.*, 1920, **42**, 1419.
28. D. Quane, "The reception of hydrogen bonding by the chemical community: 1920-1937", *Bull. Hist. Chem*, 1990, **7**, 3.
29. L. Pauling, "The nature of the chemical bond", 1939.
30. M. A. Spackman, "A simple quantitative model of hydrogen bonding", *J. Chem. Phys.*, 1986, **85**, 6587.
31. T. Steiner, "The hydrogen bond in the solid state", *Angew. Chemie Int. Ed.*, 2002, **41**, 48.
32. C. A. Hunter, "Quantifying intermolecular interactions: guidelines for the molecular recognition toolbox." *Angew. Chemie Int. Ed.*, 2004, **43**, 5310.
33. Y. Zhao and D. G. Truhlar, "Hybrid meta density functional theory methods for thermochemistry, thermochemical kinetics, and noncovalent interactions: The MPW1B95 and MPWB1K models and comparative assessments for hydrogen bonding and van der Waals interactions", *J. Phys. Chem. A*, 2004, **108**, 6908.
34. J. L. Cook, C. A. Hunter, C. M. R. Low, A. Perez-Velasco and J. G. Vinter, "Solvent effects on hydrogen bonding", *Angew. Chemie Int. Ed.*, 2007, **46**, 3706.
35. J. L. Cook, C. A. Hunter, C. M. R. Low, A. Perez-Velasco and J. G. Vinter, "Preferential solvation and hydrogen bonding in mixed solvents", *Angew. Chemie Int. Ed.*, 2008, **47**, 6275.
36. N. J. Buurma, J. L. Cook, C. A. Hunter, C. M. R. Low and J. G. Vinter, "The role of functional group concentration in solvation thermodynamics", *Chem. Sci.*, 2010, **1**, 242.
37. N. Nikogeorgos, C. A. Hunter and G. J. Leggett, "Relationship between molecular contact thermodynamics and surface contact mechanics." *Langmuir*, 2012, **28**, 17709.
38. M. H. Abraham and J. a. Platts, "Hydrogen bond structural group constants", *J. Org. Chem.*, 2001, **66**, 3484.
39. M. J. S. Dewar, E. G. Zoebisch, E. F. Healy and J. J. P. Stewart, "Development and use of quantum mechanical molecular models. 76. AM1: a new general purpose quantum mechanical molecular model", *J. Am. Chem. Soc.*, 1985, **107**, 3902.
40. R. Cabot and C. A. Hunter, "Non-covalent interactions between iodo-perfluorocarbons and hydrogen bond acceptors", *Chem. Commun.*, 2009, 2005.
41. K. Busuttil, M. Geoghegan, C. A. Hunter and G. J. Leggett, "Contact mechanics of nanometer-scale molecular contacts: correlation between adhesion, friction, and hydrogen bond thermodynamics." *J. Am. Chem. Soc.*, 2011, **133**, 8625.
42. C. A. Hunter, "A surface site interaction model for the properties of liquids at equilibrium", *Chem. Sci.*, 2013, **4**, 1687.
43. C. H. Scholz, "Earthquakes and friction laws", *Nature*, 1998, **391**, 37.
44. V. Bormuth, V. Varga, J. Howard and E. Schäffer, "Protein friction limits diffusive and directed movements of kinesin motors on microtubules." *Science*, 2009, **325**, 870.
45. N. S. Tambe and B. Bhushan, "Scale dependence of micro/nano-friction and adhesion of MEMS/NEMS materials, coatings and lubricants", *Nanotechnology*, 2004, **15**, 1561.
46. I. L. Singer and H. M. Pollock, *Fundamentals of friction: macroscopic and microscopic processes*, Springer Netherlands, 1992.
47. B. Bhushan, J. N. Israelachvili and U. Landman, "Nanotribology: friction, wear and lubrication at the atomic scale", *Nature*, 1995, **374**, 607.
48. D. Dowson, *History of tribology*, Professional Engineering Publishing, 1998.
49. F. P. Bowden and D. Tabor, *Friction and lubrication of solids*, Oxford University Press, 1950.
50. C.-A. de Coulomb, *Théorie des machines simples en ayant égard au frottement de leurs parties et à la roideur des cordages*, Bachelier, 1821, pp. 161–342.
51. *Handbook of materials behavior models: nonlinear models and properties*, ed. J. Lemaitre, Academic Press, 2001, p. 705.
52. J. T. Desaguliers, *A course of experimental philosophy*, W. Innys, 1745.

53. B. Derjaguin, "Molekulartheorie der äußeren Reibung", *Zeitschrift für Phys.*, 1934, **88**, 661.
54. F. P. Bowden and D. Tabor, "The area of contact between stationary and between moving surfaces", *Proc. R. Soc. A Math. Phys. Eng. Sci.*, 1939, **169**, 391.
55. J. Gao, W. D. Luedtke, D. Gourdon, M. Ruths, J. N. Israelachvili and U. Landman, "Frictional forces and Amontons' law: from the molecular to the macroscopic scale", *J. Phys. Chem. B*, 2004, **108**, 3410.
56. J. A. Greenwood and J. B. P. Williamson, "Contact of nominally flat surfaces", *Proc. R. Soc. A Math. Phys. Eng. Sci.*, 1966, **295**, 300.
57. K. L. Johnson, *Contact mechanics*, Cambridge University Press, 1987.
58. H. Hertz, "Über die Berührung fester elastischer Körper", *J. reine und Angew. Math.*, 1881, 156.
59. V. L. Popov, *Contact mechanics and friction*, Springer Berlin Heidelberg, Berlin, Heidelberg, 2010.
60. A. Berman, C. Drummond and J. Israelachvili, "Amontons' law at the molecular level", *Tribol. Lett.*, 1998, **4**, 95.
61. G. Adams and M. Nosonovsky, "Contact modeling — forces", *Tribol. Int.*, 2000, **33**, 431.
62. K. L. Johnson, K. Kendall and a. D. Roberts, "Surface energy and the contact of elastic solids", *Proc. R. Soc. A Math. Phys. Eng. Sci.*, 1971, **324**, 301.
63. B. Derjaguin, V. Muller and Y. Toporov, "Effect of contact deformations on the adhesion of particles", *J. Colloid Interface Sci.*, 1975, **53**, 314.
64. V. M. Muller, B. V. Derjaguin and Y. P. Toporov, "On two methods of calculation of the force of sticking of an elastic sphere to a rigid plane", *Colloids and Surfaces*, 1983, **7**, 251.
65. V. Vadillo-Rodríguez, H. J. Busscher, H. C. Van Der Mei, J. De Vries and W. Norde, "Role of lactobacillus cell surface hydrophobicity as probed by AFM in adhesion to surfaces at low and high ionic strength", *Colloids Surfaces B Biointerfaces*, 2005, **41**, 33.
66. C. Polaczyk, T. Schneider, J. Schöfer and E. Santner, "Microtribological behavior of Au(001) studied by AFM/FFM", *Surf. Sci.*, 1998, **402-404**, 454.
67. J. Han, J. Yeom, G. Mensing, D. Joe, R. I. Masel and M. A. Shannon, "Surface energy approach and AFM verification of the (CF) n treated surface effect and its correlation with adhesion reduction in microvalves", *J. Micromechanics Microengineering*, 2009, **19**, 085017.
68. R. W. Carpick, D. Ogletree and M. Salmeron, "A general equation for fitting contact area and friction vs load measurements", *J. Colloid Interface Sci.*, 1999, **211**, 395.
69. B. Cappella and G. Dietler, "Force-distance curves by atomic force microscopy", *Surf. Sci. Rep.*, 1999, **34**, 1.
70. D. Tabor, "Surface forces and surface interactions", *J. Colloid Interface Sci.*, 1977, **58**, 2.
71. D. Maugis, "Adhesion of spheres: The JKR-DMT transition using a dugdale model", *J. Colloid Interface Sci.*, 1992, **150**, 243.
72. E. Barthel, "On the description of the adhesive contact of spheres with arbitrary interaction potentials", *J. Colloid Interface Sci.*, 1998, **200**, 7.
73. E. Barthel, "Modelling the adhesion of spheres: when the form of the interaction is complex", *Colloids Surfaces A Physicochem. Eng. Asp.*, 1999, **149**, 99.
74. M. a. Lantz, S. J. O'Shea, M. E. Welland and K. L. Johnson, *Atomic-force-microscope study of contact area and friction on NbSe2*, 1997.
75. R. W. Carpick, D. F. Ogletree and M. Salmeron, "Lateral stiffness: A new nanomechanical measurement for the determination of shear strengths with friction force microscopy", *Appl. Phys. Lett.*, 1997, **70**, 1548.
76. K. Holmberg and A. Mathews, "Coatings tribology: a concept, critical aspects and future directions", *Thin Solid Films*, 1994, **253**, 173.
77. K. Holmberg, H. Ronkainen and A. Matthews, "Tribology of thin coatings", *Ceram. Int.*, 2000, **26**, 787.

78. G. Jennings and P. E. Laibinis, "Self-assembled monolayers of alkanethiols on copper provide corrosion resistance in aqueous environments", *Colloids Surfaces A Physicochem. Eng. Asp.*, 1996, **116**, 105.
79. F. Zhang, L. Zhao, H. Chen, S. Xu, D. G. Evans and X. Duan, "Corrosion resistance of superhydrophobic layered double hydroxide films on aluminum", *Angew. Chemie Int. Ed.*, 2008, **47**, 2466.
80. E. Barthel, A. Perriot, D. Dalmas, E. Sondergard and P. Nael, "Surface mechanics of functional thin films on glass surfaces", *Surf. Coatings Technol.*, 2006, **200**, 6181.
81. E. Reedy, "Thin-coating contact mechanics with adhesion", *J. Mater. Res.*, 2006, **21**, 2660.
82. E. D. Reedy, "Contact mechanics for coated spheres that includes the transition from weak to strong adhesion", *J. Mater. Res.*, 2007, **22**, 2617.
83. Y. Yang, A. C. Jamison, D. Barriet, T. R. Lee and M. Ruths, "Odd–even effects in the friction of self-assembled monolayers of phenyl-terminated alkanethiols in contacts of different adhesion strengths", *J. Adhes. Sci. Technol.*, 2010, **24**, 2511.
84. Y. Yang, J. Singh and M. Ruths, "Friction of aromatic thiol monolayers on silver: SFA and AFM studies of adhesive and non-adhesive contacts", *RSC Adv.*, 2014, **4**, 18801.
85. M. Chandross, C. D. Lorenz, M. J. Stevens and G. S. Grest, "Simulations of nanotribology with realistic probe tip models", *Langmuir*, 2008, **24**, 1240.
86. X. Jiang, P. Scott, D. Whitehouse and L. Blunt, "Paradigm shifts in surface metrology. Part I. Historical philosophy", *Proc. R. Soc. A Math. Phys. Eng. Sci.*, 2007, **463**, 2049.
87. K. Stout, P. Sullivan, W. Dong, E. Mainsah, N. Luo, T. Mathia and H. Zahouani, *The development of methods for the characterisation of roughness in three dimensions*, European Report EUR 15178N, 1993, p. 358.
88. L. Blunt and X. Jiang, *Advanced techniques for assessment surface topography: development of a basis for 3D surface texture standards "Surfstand"*, Kogan Page Science, 2003, p. 340.
89. *Geometrical product specifications (GPS) – Surface texture: Areal – Part 1: Indication of surface texture*, Standard, International Organization for Standardization, Geneva, CH, 2016.
90. *Geometrical product specifications (GPS) – Surface texture: Areal – Part 2: Terms, definitions and surface texture parameters*, Standard, International Organization for Standardization, Geneva, CH, 2012.
91. M. M. Khonsari and E. R. Booser, *Applied tribology: bearing design and lubrication*, Wiley, 2008.
92. G. Binnig and H. Rohrer, "Scanning tunneling microscopy", *Surf. Sci.*, 1983, **126**, 236.
93. G. Binnig and H. Rohrer, "Scanning tunneling microscopy", *IBM J. Res. Dev.*, 2000, **44**, 279.
94. J. W. G. Wilder, L. C. Venema, A. G. Rinzler, R. E. Smalley and C. Dekker, "Electronic structure of atomically resolved carbon nanotubes", *Nature*, 1998, **391**, 59.
95. F. J. Giessibl, "Advances in atomic force microscopy", *Rev. Mod. Phys.*, 2003, **75**, 949.
96. L. A. Bottomley, J. E. Coury and P. N. First, "Scanning probe microscopy", *Anal. Chem.*, 1996, **68**, 185.
97. G. Binnig, C. F. Quate and C. Gerber, "Atomic Force Microscope", *Phys. Rev. Lett.*, 1986, **56**, 930.
98. F. J. Giessibl, "AFM's path to atomic resolution", *Mater. Today*, 2005, **8**, 32.
99. M. Pierce, J. Stuart, A. Pungor, P. Dryden and V. Hlady, "Adhesion Force Measurements Using an Atomic Force Microscope Upgraded with a Linear Position Sensitive Detector", *Langmuir*, 1994, **10**, 3217.
100. G. J. Leggett, "Friction force microscopy of self-assembled monolayers: probing molecular organisation at the nanometre scale", *Anal. Chim. Acta*, 2003, **479**, 17.
101. Y. Martin, C. C. Williams and H. K. Wickramasinghe, "Atomic force microscope–force mapping and profiling on a sub 100-Å scale", *J. Appl. Phys.*, 1987, **61**, 4723.
102. G. Neubauer, S. R. Cohen, G. M. McClelland, D. Horne and C. M. Mate, "Force microscopy with a bidirectional capacitance sensor", *Rev. Sci. Instrum.*, 1990, **61**, 2296.
103. E. Meyer, "Atomic force microscopy", *Prog. Surf. Sci.*, 1992, **41**, 3.

104. L. Chen, C. L. Cheung, P. D. Ashby and C. M. Lieber, "Single-walled carbon nanotube AFM probes: optimal imaging resolution of nanoclusters and biomolecules in ambient and fluid environments", *Nano Lett.*, 2004, **4**, 1725.
105. V. Freger, J. Gilron and S. Belfer, "TFC polyamide membranes modified by grafting of hydrophilic polymers: An FT-IR/AFM/TEM study", *J. Memb. Sci.*, 2002, **209**, 283.
106. S. B. Velegol and B. E. Logan, "Contributions of bacterial surface polymers, electrostatics, and cell elasticity to the shape of AFM force curves", *Langmuir*, 2002, **18**, 5256.
107. T. J. Young, M. A. Monclus, T. L. Burnett, W. R. Broughton, S. L. Ogin and P. A. Smith, "The use of the PeakForce quantitative nanomechanical mapping AFM-based method for high-resolution Young's modulus measurement of polymers", *Meas. Sci. Technol.*, 2011, **22**, 125703.
108. J. J. Sáenz, N. García, P. Grütter, E. Meyer, H. Heinzelmann, R. Wiesendanger, L. Rosenthaler, H. R. Hidber and H. Güntherodt, "Observation of magnetic forces by the atomic force microscope", *J. Appl. Phys.*, 1987, **62**, 4293.
109. P. I. Oden, A. Majumdar, B. Bhushan, A. Padmanabhan and J. J. Graham, "AFM imaging, roughness analysis and contact mechanics of magnetic tape and head surfaces", *J. Tribol.*, 1992, **114**, 666.
110. T. D. Stowe, K. Yasumura, T. W. Kenny, D. Botkin, K. Wago and D. Rugar, "Attonewton force detection using ultrathin silicon cantilevers", *Appl. Phys. Lett.*, 1997, **71**, 288.
111. C. Quate, "The AFM as a tool for surface imaging", *Surf. Sci.*, 1994, **299-300**, 980.
112. R. W. Carpick and M. Salmeron, "Scratching the surface: fundamental investigations of tribology with atomic force microscopy", *Chem. Rev.*, 1997, **97**, 1163.
113. N. Gadegaard, "Atomic force microscopy in biology: technology and techniques", *Biotech. Histochem.*, 2006, **81**, 87.
114. T. R. Albrecht, P. Grütter, D. Horne and D. Rugar, "Frequency modulation detection using high- Q cantilevers for enhanced force microscope sensitivity", *J. Appl. Phys.*, 1991, **69**, 668.
115. F. J. Giessibl, "Atomic resolution of the silicon (111)-(7x7) surface by atomic force microscopy", *Science*, 1995, **267**, 68.
116. Q. Zhong, D. Inniss, K. Kjoller and V. Elings, "Fractured polymer/silica fiber surface studied by tapping mode atomic force microscopy", *Surf. Sci. Lett.*, 1993, **290**, L688.
117. R. Höper, T. Gesang, W. Possart, O. D. Hennemann and S. Boseck, "Imaging elastic sample properties with an atomic force microscope operating in the tapping mode", *Ultramicroscopy*, 1995, **60**, 17.
118. Y. Joseph, I. Besnard, M. Rosenberger, B. Guse, H.-g. Nothofer, J. M. Wessels, U. Wild, A. Knop-Gericke, D. Su, R. Schlögl, A. Yasuda and T. Vossmeyer, "Self-assembled gold nanoparticle/alkanedithiol films: preparation, electron microscopy, XPS-analysis, charge transport, and vapor-sensing properties", *J. Phys. Chem. B*, 2003, **107**, 7406.
119. Z. Shi, K. G. Neoh, E. T. Kang, C. K. Poh and W. Wang, "Surface functionalization of titanium with carboxymethyl chitosan and immobilized bone morphogenetic protein-2 for enhanced osseointegration", *Biomacromolecules*, 2009, **10**, 1603.
120. L. G. Rosa and J. Liang, "Atomic force microscope nanolithography: dip-pen, nanoshaving, nanografting, tapping mode, electrochemical and thermal nanolithography." *J. Phys. Condens. Matter*, 2009, **21**, 483001.
121. R. S. McLean and B. B. Sauer, "Tapping-mode AFM studies using phase detection for resolution of nanophases in segmented polyurethanes and other block copolymers", *Macromolecules*, 1997, **30**, 8314.
122. N. A. Burnham, R. J. Colton and H. M. Pollock, "Interpretation issues in force microscopy", *J. Vac. Sci. Technol. A*, 1991, **9**, 2548.
123. O. Marti, B. Drake and P. K. Hansma, "Atomic force microscopy of liquid-covered surfaces: Atomic resolution images", *Appl. Phys. Lett.*, 1987, **51**, 484.
124. A. L. Weisenhorn, P. K. Hansma, T. R. Albrecht and C. F. Quate, "Forces in atomic force microscopy in air and water", *Appl. Phys. Lett.*, 1989, **54**, 2651.

125. T. Rayment, R. McKendry, M.-e. Theoclitou and C. Abell, "Chiral discrimination by chemical force microscopy", *Nature*, 1998, **391**, 566.
126. T. Nakagawa, K. Ogawa, T. Kurumizawa and S. Ozaki, "Discriminating molecular length of chemically adsorbed molecules using an atomic force microscope having a tip covered with sensor molecules (an atomic force microscope having chemical sensing function)", *Jpn. J. Appl. Phys.*, 1993, **32**, L294.
127. C. D. Frisbie, L. F. Rozsnyai, A. Noy, M. S. Wrighton and C. M. Lieber, "Functional-group imaging by chemical force microscopy", *Science*, 1994, **265**, 2071.
128. A. Noy, C. D. Frisbie, L. F. Rozsnyai, M. S. Wrighton and C. M. Lieber, "Chemical Force Microscopy: Exploiting Chemically-Modified Tips To Quantify Adhesion, Friction, and Functional Group Distributions in Molecular Assemblies", *J. Am. Chem. Soc.*, 1995, **117**, 7943.
129. S. C. Clear and P. F. Nealey, "Chemical force microscopy study of adhesion and friction between surfaces functionalized with self-assembled monolayers and immersed in solvents", *J. Colloid Interface Sci.*, 1999, **213**, 238.
130. B. D. Beake and G. J. Leggett, "Friction and adhesion of mixed self-assembled monolayers studied by chemical force microscopy", *Phys. Chem. Chem. Phys.*, 1999, **1**, 3345.
131. D. V. Vezenov, A. Noy, L. F. Rozsnyai and C. M. Lieber, "Force titrations and ionization state sensitive imaging of functional groups in aqueous solutions by chemical force microscopy", *J. Am. Chem. Soc.*, 1997, **119**, 2006.
132. A. Noy, D. V. Vezenov and C. M. Lieber, "Chemical force microscopy", *Annu. Rev. Mater. Sci.*, 1997, **27**, 381.
133. A. Noy, D. V. Vezenov, J. F. Kayyem, T. J. Maade and C. M. Lieber, "Stretching and breaking duplex DNA by chemical force microscopy", *Chem. Biol.*, 1997, **4**, 519.
134. E. W. van der Vegte and G. Hadziioannou, "Scanning Force Microscopy with Chemical Specificity: An Extensive Study of Chemically Specific TipSurface Interactions and the Chemical Imaging of Surface Functional Groups", *Langmuir*, 1997, **13**, 4357.
135. H. Hillborg, N. Tomczak, A. Olàh, H. Schönherr and G. J. Vancso, "Nanoscale hydrophobic recovery: a chemical force microscopy study of UV/ozone-treated cross-linked poly(dimethylsiloxane)", *Langmuir*, 2004, **20**, 785.
136. A. Ashkin, K. Schütze, J. M. Dziedzic, U. Euteneuer and M. Schliwa, "Force generation of organelle transport measured in vivo by an infrared laser trap", *Nature*, 1990, **348**, 346.
137. S. Smith, L. Finzi and C. Bustamante, "Direct mechanical measurements of the elasticity of single DNA molecules by using magnetic beads", *Science*, 1992, **258**, 1122.
138. T. Hugel and M. Seitz, "The study of molecular interactions by AFM force spectroscopy", *Macromol. Rapid Commun.*, 2001, **22**, 989.
139. M. L. Hughes and L. Dougan, "The physics of pulling polyproteins: a review of single molecule force spectroscopy using the AFM to study protein unfolding", *Reports Prog. Phys.*, 2016, **79**, 076601.
140. Y. L. Chen, C. a. Helm and J. N. Israelachvili, "Molecular mechanisms associated with adhesion and contact angle hysteresis of monolayer surfaces", *J. Phys. Chem.*, 1991, **95**, 10736.
141. J. B. Pethica and A. P. Sutton, "On the stability of a tip and flat at very small separations", *J. Vac. Sci. Technol. A*, 1988, **6**, 2490.
142. U. Landman, W. D. Luedtke, N. A. Burnham and R. J. Colton, "Atomistic mechanisms and dynamics of adhesion, nanoindentation, and fracture", *Science*, 1990, **248**, 454.
143. M. Lemeshko and H. Weimer, "Dissipative binding of atoms by non-conservative forces." *Nat. Commun.*, 2013, **4**, 2230.
144. J. Zlatanova, S. M. Lindsay and S. H. Leuba, "Single molecule force spectroscopy in biology using the atomic force microscope", *Prog. Biophys. Mol. Biol.*, 2000, **74**, 37.
145. C. M. Mate, G. M. McClelland, R. Erlandsson and S. Chiang, "Atomic-scale friction of a tungsten tip on a graphite surface", *Phys. Rev. Lett.*, 1987, **59**, 1942.

146. A. R. Burns and R. W. Carpick, "Directional shear force microscopy", *Appl. Phys. Lett.*, 2001, **78**, 317.
147. R. Overney and E. Meyer, "Tribological investigations using friction force microscopy", *MRS Bull.*, 1993, **18**, 26.
148. S. Grafstrom, M. Neitzert, T. Hagen, J. Ackermann, R. Neumann, O. Probst and M. Wortge, "The role of topography and friction for the image contrast in lateral force microscopy", *Nanotechnology*, 1993, **4**, 143.
149. J. L. Hutter and J. Bechhoefer, "Calibration of atomic-force microscope tips", *Rev. Sci. Instrum.*, 1993, **64**, 1868.
150. G. J. Leggett, N. J. Brewer and K. S. L. Chong, "Friction force microscopy: towards quantitative analysis of molecular organisation with nanometre spatial resolution", *Phys. Chem. Chem. Phys.*, 2005, **7**, 1107.
151. J. L. Hazel and V. V. Tsukruk, "Friction force microscopy measurements: normal and torsional spring constants for V-shaped cantilevers", *J. Tribol.*, 1998, **120**, 814.
152. J. L. Hazel and V. V. Tsukruk, "Spring constants of composite ceramic/gold cantilevers for scanning probe microscopy", *Thin Solid Films*, 1999, **339**, 249.
153. H.-J. Butt, P. Siedle, K. Seifert, K. Fendler, T. Seeger, E. Bamberg, A. L. Weisenhorn, K. Goldie and A. Engel, "Scan speed limit in atomic force microscopy", *J. Microsc.*, 1993, **169**, 75.
154. J. P. Cleveland, S. Manne, D. Bocek and P. K. Hansma, "A nondestructive method for determining the spring constant of cantilevers for scanning force microscopy", *Rev. Sci. Instrum.*, 1993, **64**, 403.
155. N. a. Burnham, X. Chen, C. S. Hodges, G. a. Matei, E. J. Thoreson, C. J. Roberts, M. C. Davies and S. J. B. Tendler, "Comparison of calibration methods for atomic-force microscopy cantilevers", *Nanotechnology*, 2003, **14**, 1.
156. G. A. Matei, E. J. Thoreson, J. R. Pratt, D. B. Newell and N. A. Burnham, "Precision and accuracy of thermal calibration of atomic force microscopy cantilevers", *Rev. Sci. Instrum.*, 2006, **77**, 083703.
157. N. Wiener, *The fourier integral and certain of its applications*, Cambridge University Press, 1988.
158. H. .-.-J. Butt and M. Jaschke, "Calculation of thermal noise in atomic force microscopy", *Nanotechnology*, 1995, **6**, 1.
159. R. W. Stark, T. Drobek and W. M. Heckl, "Thermomechanical noise of a free v-shaped cantilever for atomic-force microscopy", *Ultramicroscopy*, 2001, **86**, 207.
160. A. D. Slattery, A. J. Blanch, V. Ejov, J. S. Quinton and C. T. Gibson, "Spring constant calibration techniques for next-generation fast-scanning atomic force microscope cantilevers", *Nanotechnology*, 2014, **25**, 335705.
161. R. S. Gates, W. A. Osborn and J. R. Pratt, "Experimental determination of mode correction factors for thermal method spring constant calibration of AFM cantilevers using laser Doppler vibrometry", *Nanotechnology*, 2013, **24**, 255706.
162. R. Proksch, T. E. Schäffer, J. P. Cleveland, R. C. Callahan and M. B. Viani, "Finite optical spot size and position corrections in thermal spring constant calibration", *Nanotechnology*, 2004, **15**, 1344.
163. M. L. B. Palacio and B. Bhushan, "Normal and lateral force calibration techniques for AFM cantilevers", *Crit. Rev. Solid State Mater. Sci.*, 2010, **35**, 73.
164. M. Munz, "Force calibration in lateral force microscopy: a review of the experimental methods", *J. Phys. D. Appl. Phys.*, 2010, **43**, 063001.
165. T. J. Colburn and G. J. Leggett, "Influence of solvent environment and tip chemistry on the contact mechanics of tip-sample interactions in friction force microscopy of self-assembled monolayers of mercaptoundecanoic Acid and dodecanethiol." *Langmuir*, 2007, **23**, 4959.
166. C. R. Hurley and G. J. Leggett, "Quantitative investigation of the photodegradation of polyethylene terephthalate film by friction force microscopy, contact-angle goniometry, and X-ray photoelectron spectroscopy." *ACS Appl. Mater. Interfaces*, 2009, **1**, 1688.

167. D. F. Ogletree, R. W. Carpick and M. Salmeron, "Calibration of frictional forces in atomic force microscopy", *Rev. Sci. Instrum.*, 1996, **67**, 3298.
168. M. Varenberg, I. Etsion and G. Halperin, "An improved wedge calibration method for lateral force in atomic force microscopy", *Rev. Sci. Instrum.*, 2003, **74**, 3362.
169. F. Zenhausern, M. Adrian, B. T. Heggeler-Bordier, L. M. Eng and P. Descouts, "DNA and RNA polymerase/DNA complex imaged by scanning force microscopy: Influence of molecular-scale friction", *Scanning*, 1992, **14**, 212.
170. P. Markiewicz and M. C. Goh, "Atomic force microscope tip deconvolution using calibration arrays", *Rev. Sci. Instrum.*, 1995, **66**, 3186.
171. A. Yacoot and L. Koenders, "Aspects of scanning force microscope probes and their effects on dimensional measurement", *J. Phys. D. Appl. Phys.*, 2008, **41**, 103001.
172. Y. Martin and H. K. Wickramasinghe, "Toward accurate metrology with scanning force microscopes", *J. Vac. Sci. Technol. B*, 1995, **13**, 2335.
173. V. Garcia, L. Martinez, J. Briceno-Valero and C. Schilling, "Dimensional metrology of nanometric spherical particles using AFM I, model development", *Probe Microsc.*, 1997, **1**, 107.
174. H. O. Finklea, L. R. Robinson, A. Blackburn, B. Richter, D. Allara and T. Bright, "Formation of an organized monolayer by solution adsorption of octadecyltrichlorosilane on gold: electrochemical properties and structural characterization", *Langmuir*, 1986, **2**, 239.
175. J. Gun and J. Sagiv, "On the formation and structure of self-assembling monolayers", *J. Colloid Interface Sci.*, 1986, **112**, 457.
176. G. Carson and S. Granick, "Self-assembly of octadecyltrichlorosilane films on mica", *J. Appl. Polym. Sci.*, 1989, **37**, 2767.
177. K. Mathauer and C. W. Frank, "Binary self-assembled monolayers as prepared by successive adsorption of alkyltrichlorosilanes", *Langmuir*, 1993, **9**, 3446.
178. N. S. Tambe and B. Bhushan, "Nanotribological characterization of self-assembled monolayers deposited on silicon and aluminium substrates", *Nanotechnology*, 2005, **16**, 1549.
179. A. Ulman, "Formation and structure of self-assembled monolayers", *Chem. Rev.*, 1996, **96**, 1533.
180. D. K. Schwartz, "Mechanisms and kinetics of self-assembled monolayer formation", *Annu. Rev. Phys. Chem.*, 2001, **52**, 107.
181. F. Schreiber, "Self-assembled monolayers: from simple model systems to biofunctionalized interfaces", *J. Phys. Condens. Matter*, 2004, **16**, R881.
182. J. C. Love, L. A. Estroff, J. K. Kriebel, R. G. Nuzzo and G. M. Whitesides, "Self-assembled monolayers of thiolates on metals as a form of nanotechnology", *Chem. Rev.*, 2005, **105**, 1103.
183. R. M. Wallace, D. A. Webb and B. E. Gnade, *Self-assembled monolayer coating for micro-mechanical devices*, 1996.
184. C. R. Yonzon, E. Jeoung, S. Zou, G. C. Schatz, M. Mrksich and R. P. Van Duyne, "A comparative analysis of localized and propagating surface plasmon resonance sensors: The binding of Concanavalin A to a monosaccharide functionalized self-assembled monolayer", *J. Am. Chem. Soc.*, 2004, **126**, 12669.
185. W. Geyer, V. Stadler, W. Eck, M. Zharnikov, A. Gölzhäuser and M. Grunze, "Electron-induced crosslinking of aromatic self-assembled monolayers: Negative resists for nanolithography", *Appl. Phys. Lett.*, 1999, **75**, 2401.
186. W. Eck, V. Stadler, W. Geyer, M. Zharnikov, A. Gölzhäuser and M. Grunze, "Generation of surface amino groups on aromatic self-assembled monolayers by low energy electron beams—a first step towards chemical lithography", *Adv. Mater.*, 2000, **12**, 805.
187. V. Chechik, R. M. Crooks and C. J. M. Stirling, "Reactions and reactivity in self-assembled monolayers", *Adv. Mater.*, 2000, **12**, 1161.

188. M. L. Wallwork, D. A. Smith, J. Zhang, J. Kirkham and C. Robinson, "Complex chemical Force titration behavior of amine-terminated self-assembled monolayers", *Langmuir*, 2001, **17**, 1126.
189. H. Cheng and Y. Hu, "Influence of chain ordering on frictional properties of self-assembled monolayers (SAMs) in nano-lubrication", *Adv. Colloid Interface Sci.*, 2012, **171-172**, 53.
190. K. Busuttil, N. Nikogeorgos, Z. Zhang, M. Geoghegan, C. A. Hunter and G. J. Leggett, "The mechanics of nanometre-scale molecular contacts", *Faraday Discuss.*, 2012, **156**, 325.
191. F. Schreiber, "Structure and growth of self-assembling monolayers", *Prog. Surf. Sci.*, 2000, **65**, 151.
192. X. Xiao, J. Hu, D. H. Charych and M. Salmeron, "Chain length dependence of the frictional properties of alkylsilane molecules self-assembled on mica studied by atomic force microscopy", *Langmuir*, 1996, **12**, 235.
193. M. D. Malinsky, K. L. Kelly, G. C. Schatz and R. P. Van Duyne, "Chain length dependence and sensing capabilities of the localized surface plasmon Resonance of Silver Nanoparticles Chemically Modified with Alkanethiol Self-Assembled Monolayers", *J. Am. Chem. Soc.*, 2001, **123**, 1471.
194. P. T. Mikulski, L. A. Herman and J. A. Harrison, "Odd and even model self-assembled monolayers: links between friction and structure", *Langmuir*, 2005, **21**, 12197.
195. C. D. Bain, E. B. Troughton, Y. T. Tao, J. Evall, G. M. Whitesides and R. G. Nuzzo, "Formation of monolayer films by the spontaneous assembly of organic thiols from solution onto gold", *J. Am. Chem. Soc.*, 1989, **111**, 321.
196. R. G. Nuzzo, F. a. Fusco and D. L. Allara, "Spontaneously organized molecular assemblies. 3. Preparation and properties of solution adsorbed monolayers of organic disulfides on gold surfaces", *J. Am. Chem. Soc.*, 1987, **109**, 2358.
197. R. G. Nuzzo, B. R. Zegarski and L. H. Dubois, "Fundamental studies of the chemisorption of organosulfur compounds on gold(111). Implications for molecular self-assembly on gold surfaces", *J. Am. Chem. Soc.*, 1987, **109**, 733.
198. C. A. Widrig, C. Chung and M. D. Porter, "The electrochemical desorption of n-alkanethiol monolayers from polycrystalline Au and Ag electrodes", *J. Electroanal. Chem. Interfacial Electrochem.*, 1991, **310**, 335.
199. M. M. Walczak, C. Chung, S. M. Stole, C. a. Widrig and M. D. Porter, "Structure and interfacial properties of spontaneously adsorbed n-alkanethiolate monolayers on evaporated silver surfaces", *J. Am. Chem. Soc.*, 1991, **113**, 2370.
200. M. Hasan, D. Bethell and M. Brust, "The tate of sulfur-bound hydrogen on formation of self-assembled thiol monolayers on gold: 1 H NMR spectroscopic evidence from solutions of gold clusters", *J. Am. Chem. Soc.*, 2002, **124**, 1132.
201. P. Fenter, P. Eisenberger and K. S. Liang, "Chain-length dependence of the structures and phases of CH3(CH2)n1 SH self-assembled on Au(111)", *Phys. Rev. Lett.*, 1993, **70**, 2447.
202. P. E. Laibinis, C. D. Bain, R. G. Nuzzo and G. M. Whitesides, "Structure and wetting properties of .omega.-alkoxy-n-alkanethiolate monolayers on gold and silver", *J. Phys. Chem.*, 1995, **99**, 7663.
203. X. Torrelles, E. Barrena, C. Munuera, J. Rius, S. Ferrer and C. Ocal, "New insights in the c(4×2) reconstruction of hexadecanethiol on Au(111) revealed by grazing incidence X-ray diffraction", *Langmuir*, 2004, **20**, 9396.
204. U. K. Sur and V. Lakshminarayanan, "A study of the hydrophobic properties of alkanethiol self-assembled monolayers prepared in different solvents", *J. Electroanal. Chem.*, 2004, **565**, 343.
205. J. Huang and J. C. Hemminger, "Photooxidation of thiols in self-assembled monolayers on gold", *J. Am. Chem. Soc.*, 1993, **115**, 3342.
206. W. Gao, L. Dickinson, C. Grozinger, F. G. Morin and L. Reven, "Self-assembled monolayers of alkylphosphonic acids on metal oxides", *Langmuir*, 1996, **12**, 6429.

207. C. Yee, G. Kataby, A. Ulman, T. Prozorov, H. White, A. King, M. Rafailovich, J. Sokolov and A. Gedanken, "Self-assembled monolayers of alkanesulfonic and -phosphonic acids on amorphous iron oxide nanoparticles", *Langmuir*, 1999, **15**, 7111.
208. M. Textor, L. Ruiz, R. Hofer, A. Rossi, K. Feldman, G. Hähner and N. D. Spencer, "Structural chemistry of self-assembled monolayers of octadecylphosphoric acid on tantalum oxide surfaces", *Langmuir*, 2000, **16**, 3257.
209. B. Adolphi, E. Jähne, G. Busch and X. Cai, "Characterization of the adsorption of ω-(thiophene-3-yl alkyl) phosphonic acid on metal oxides with AR-XPS", *Anal. Bioanal. Chem.*, 2004, **379**, 646.
210. M. J. Pellerite, T. D. Dunbar, L. D. Boardman and E. J. Wood, "Effects of fluorination on self-assembled monolayer formation from alkanephosphonic acids on aluminum: Kinetics and structure", *J. Phys. Chem. B*, 2003, **107**, 11726.
211. B. Bhushan, M. Cichomski, E. Hoque, J. A. DeRose, P. Hoffmann and H. J. Mathieu, "Nanotribological characterization of perfluoroalkylphosphonate self-assembled monolayers deposited on aluminum-coated silicon substrates", *Microsyst. Technol.*, 2006, **12**, 588.
212. R. Luschtinetz and A. Oliveira, "Self-assembled monolayers of alkylphosphonic acids on aluminum oxide surfaces–a theoretical study", *Zeitschrift für Anorg. und Allg. Chemie*, 2010, **8**, 1506.
213. P. Thissen, M. Valtiner and G. Grundmeier, "Stability of phosphonic acid self-assembled monolayers on amorphous and single-crystalline aluminum oxide surfaces in aqueous solution", *Langmuir*, 2010, **26**, 156.
214. E. S. Gawalt, M. J. Avaltroni, N. Koch and J. Schwartz, "Self-assembly and bonding of alkanephosphonic acids on the native oxide surface of titanium", *Langmuir*, 2001, **17**, 5736.
215. H. Dietrich, T. Schmaltz, M. Halik and D. Zahn, "Molecular dynamics simulations of phosphonic acid–aluminum oxide self-organization and their evolution into ordered monolayers", *Phys. Chem. Chem. Phys.*, 2017, **19**, 5137.
216. C. R. Kessel and S. Granick, "Formation and characterization of a highly ordered and well-anchored alkylsilane monolayer on mica by self-assembly", *Langmuir*, 1991, **7**, 532.
217. X.-D. Xiao, G.-y. Liu, D. H. Charych and M. Salmeron, "Preparation, structure, and mechanical stability of alkylsilane monolayers on mica", *Langmuir*, 1995, **11**, 1600.
218. C. D. Lorenz, M. Chandross, G. S. Grest, M. J. Stevens and E. B. Webb, "Tribological properties of alkylsilane self-assembled monolayers", *Langmuir*, 2005, **21**, 11744.
219. S. Onclin, B. J. Ravoo and D. N. Reinhoudt, "Engineering silicon oxide surfaces using self-assembled monolayers", *Angew. Chemie Int. Ed.*, 2005, **44**, 6282.
220. D. L. Angst and G. W. Simmons, "Moisture absorption characteristics of organosiloxane self-assembled monolayers", *Langmuir*, 1991, **7**, 2236.
221. C. P. Tripp and M. L. Hair, "An infrared study of the reaction of octadecyltrichlorosilane with silica", *Langmuir*, 1992, **8**, 1120.
222. M. E. McGovern, K. M. R. Kallury and M. Thompson, "Role of solvent on the silanization of glass with octadecyltrichlorosilane", *Langmuir*, 1994, **10**, 3607.
223. B. D. Gates, Q. Xu, M. Stewart, D. Ryan, C. G. Willson and G. M. Whitesides, "New approaches to nanofabrication: molding, printing, and other techniques", *Chem. Rev.*, 2005, **105**, 1171.
224. *Samsung Starts Industry's First Mass Production of System-on-Chip with 10-Nanometer FinFET Technology – Samsung Global Newsroom*, `https://news.samsung.com/global/samsung-starts-industrys-first-mass-production-of-system-on-chip-with-10-nanometer-finfet-technology`.
225. *ASML*, `https://www.asml.com/`.
226. S. H. Zaidi, "Multiple-exposure interferometric lithography", *J. Vac. Sci. Technol. B*, 1993, **11**, 658.

227. B. Päivänranta, A. Langner, E. Kirk, C. David and Y. Ekinci, "Sub-10 nm patterning using EUV interference lithography", *Nanotechnology*, 2011, **22**, 375302.
228. F. Watt, A. A. Bettiol, J. A. Van Kan, E. J. Teo and M. B. H. Breese, "Ion beam lithography and nanofabrication: a review", *Int. J. Nanosci.*, 2005, **04**, 269.
229. V. R. Manfrinato, L. Zhang, D. Su, H. Duan, R. G. Hobbs, E. A. Stach and K. K. Berggren, "Resolution limits of electron-beam lithography toward the atomic scale", *Nano Lett.*, 2013, **13**, 1555.
230. A. N. Abbas, G. Liu, B. Liu, L. Zhang, H. Liu, D. Ohlberg, W. Wu and C. Zhou, "Patterning, characterization, and chemical sensing applications of graphene nanoribbon arrays down to 5 nm using helium ion beam lithography", *ACS Nano*, 2014, **8**, 1538.
231. a. Gölzhäuser, W. Geyer, V. Stadler, W. Eck, M. Grunze, K. Edinger, T. Weimann and P. Hinze, "Nanoscale patterning of self-assembled monolayers with electrons", *J. Vac. Sci. Technol. B*, 2000, **18**, 3414.
232. G.-J. Zhang, T. Tanii, T. Zako, T. Hosaka, T. Miyake, Y. Kanari, T. Funatsu and I. Ohdomari, "Nanoscale patterning of protein using electron beam lithography of organosilane self-assembled monolayers", *Small*, 2005, **1**, 833.
233. J. Rundqvist, J. H. Hoh and D. B. Haviland, "Directed immobilization of protein-coated nanospheres to nanometer-scale patterns fabricated by electron beam lithography of poly(ethylene glycol) self-assembled Monolayers", *Langmuir*, 2006, **22**, 5100.
234. G.-J. Zhang, T. Tanii, T. Funatsu and I. Ohdomari, "Patterning of DNA nanostructures on silicon surface by electron beam lithography of self-assembled monolayer", *Chem. Commun.*, 2004, 786.
235. W. Hu, K. Sarveswaran, M. Lieberman and G. Bernstein, "High-resolution electron beam lithography and DNA nano-patterning for molecular QCA", *IEEE Trans. Nanotechnol.*, 2005, **4**, 312.
236. P. M. Mendes, S. Jacke, K. Critchley, J. Plaza, Y. Chen, K. Nikitin, R. E. Palmer, J. A. Preece, S. D. Evans and D. Fitzmaurice, "Gold nanoparticle patterning of silicon wafers using chemical e-beam lithography", *Langmuir*, 2004, **20**, 3766.
237. Y. Xia and G. M. Whitesides, "Soft lithography", *Angew. Chemie Int. Ed.*, 1998, **37**, 550.
238. J. L. Tan, J. Tien and C. S. Chen, "Microcontact printing of proteins on mixed self-assembled monolayers", *Langmuir*, 2002, **18**, 519.
239. S. G. Ricoult, M. Pla-Roca, R. Safavieh, G. M. Lopez-Ayon, P. Grütter, T. E. Kennedy and D. Juncker, "Large dynamic range digital nanodot gradients of biomolecules made by low-cost nanocontact printing for cell haptotaxis", *Small*, 2013, **9**, n/a.
240. M. Husemann, D. Mecerreyes, C. J. Hawker, J. L. Hedrick, R. Shah and N. L. Abbott, "Surface-initiated polymerization for amplification of self-assembled monolayers patterned by microcontact printing", *Angew. Chemie Int. Ed.*, 1999, **38**, 647.
241. R. R. Shah, D. Merreceyes, M. Husemann, I. Rees, N. L. Abbott, C. J. Hawker and J. L. Hedrick, "Using atom transfer radical polymerization to amplify monolayers of initiators patterned by microcontact printing into polymer brushes for pattern transfer", *Macromolecules*, 2000, **33**, 597.
242. G. Csucs, R. Michel, J. W. Lussi, M. Textor and G. Danuser, "Microcontact printing of novel co-polymers in combination with proteins for cell-biological applications", *Biomaterials*, 2003, **24**, 1713.
243. M. Mannini, D. Bonacchi, L. Zobbi, F. M. Piras, E. A. Speets, A. Caneschi, A. Cornia, A. Magnani, B. J. Ravoo, D. N. Reinhoudt, R. Sessoli and D. Gatteschi, "Advances in single-molecule magnet surface patterning through microcontact printing", *Nano Lett.*, 2005, **5**, 1435.
244. H. Singh, P. E. Laibinis and T. A. Hatton, "Synthesis of flexible magnetic nanowires of permanently linked coreshell magnetic beads tethered to a glass surface patterned by microcontact printing", *Nano Lett.*, 2005, **5**, 2149.

245. H.-W. Li, B. V. O. Muir, G. Fichet and W. T. S. Huck, "Nanocontact printing: a route to sub-50-nm-scale chemical and biological patterning", *Langmuir*, 2003, **19**, 1963.
246. N. Koo, U. Plachetka, M. Otto, J. Bolten, J.-H. Jeong, E.-S. Lee and H. Kurz, "The fabrication of a flexible mold for high resolution soft ultraviolet nanoimprint lithography", *Nanotechnology*, 2008, **19**, 225304.
247. M. D. Austin, H. Ge, W. Wu, M. Li, Z. Yu, D. Wasserman, S. A. Lyon and S. Y. Chou, "Fabrication of 5nm linewidth and 14nm pitch features by nanoimprint lithography", *Appl. Phys. Lett.*, 2004, **84**, 5299.
248. A. a. Tseng, A. Notargiacomo and T. P. Chen, "Nanofabrication by scanning probe microscope lithography: A review", *J. Vac. Sci. Technol. B*, 2005, **23**, 877.
249. M. Ringger, H. R. Hidber, R. Schlögl, P. Oelhafen and H. Güntherodt, "Nanometer lithography with the scanning tunneling microscope", *Appl. Phys. Lett.*, 1985, **46**, 832.
250. G.-Y. Liu, S. Xu and Y. Qian, "Nanofabrication of self-assembled monolayers using scanning probe lithography", *Acc. Chem. Res.*, 2000, **33**, 457.
251. N. Li, T. Yoshinobu and H. Iwasaki, "Low energy electron beam stimulated surface reaction: selective etching of SiO 2/Si using scanning tunneling microscope", *Jpn. J. Appl. Phys.*, 1998, **37**, L995.
252. R. D. Piner, J. Zhu, F. Xu, S. Hong and C. A. Mirkin, ""Dip-pen" nanolithography", *Science*, 1999, **283**, 661.
253. R. Maoz, E. Frydman, S. R. Cohen and J. Sagiv, ""Constructive nanolithography": inert monolayers as patternable templates for in-situ nanofabrication of metal-semiconductor-organic surface structures—a generic approach", *Adv. Mater.*, 2000, **12**, 725.
254. R. Maoz, E. Frydman, S. R. Cohen and J. Sagiv, "Constructive nanolithography: site-defined silver self-assembly on nanoelectrochemically patterned monolayer templates", *Adv. Mater.*, 2000, **12**, 424.
255. G. J. Leggett, "Scanning near-field photolithography-surface photochemistry with nanoscale spatial resolution", *Chem. Soc. Rev.*, 2006, **35**, 1150.
256. H. J. Mamin, "Thermal writing using a heated atomic force microscope tip", *Appl. Phys. Lett.*, 1996, **69**, 433.
257. A. Szabo and N. S. Ostlund, *Modern quantum chemistry: introduction to advanced electronic structure theory*, 1989.
258. W. Koch and M. C. Holthausen, *A chemist's guide to density functional theory*, 2nd Ed., 2001.
259. U. von Barth, "Basic density-functional theory an overview", *Phys. Scr.*, 2004, **T109**, 9.
260. W. Kohn, "Nobel lecture: electronic structure of matter—wave functions and density functionals", *Rev. Mod. Phys.*, 1999, **71**, 1253.
261. P.-O. Löwdin, "Scaling problem, virial theorem, and connected relations in quantum mechanics", *J. Mol. Spectrosc.*, 1959, **3**, 46.
262. P. Hohenberg and W. Kohn, "Inhomogeneous Electron Gas", *Phys. Rev.*, 1964, **136**, B864.
263. W. Kohn and L. J. Sham, "Self-Consistent Equations Including Exchange and Correlation Effects", *Phys. Rev.*, 1965, **140**, A1133.
264. R. G. Parr and Y. Weitao, *Density-functional theory of atoms and molecules*, Oxford University Press, 1994.
265. D. M. Ceperley and B. J. Alder, "Ground state of the electron gas by a stochastic method", *Phys. Rev. Lett.*, 1980, **45**, 566.
266. J. P. Perdew and Y. Wang, "Accurate and simple analytic representation of the electron-gas correlation energy", *Phys. Rev. B*, 1992, **45**, 13244.
267. J. P. Perdew, K. Burke and M. Ernzerhof, "Generalized gradient approximation made simple", *Phys. Rev. Lett.*, 1996, **77**, 3865.
268. Y. Zhao and D. G. Truhlar, "Comment on "More accurate generalized gradient approximation for solids"", *Phys. Rev. B*, 2008, **78**, 197101.

269. A. D. Becke, "Density-functional thermochemistry. III. The role of exact exchange", *J. Chem. Phys.*, 1993, **98**, 5648.
270. D. Jacquemin, E. A. Perpète, I. Ciofini and C. Adamo, "On the TD-DFT UV/vis spectra accuracy: the azoalkanes", *Theor. Chem. Acc.*, 2008, **120**, 405.
271. D. Jacquemin, B. Mennucci and C. Adamo, "Excited-state calculations with TD-DFT: from benchmarks to simulations in complex environments", *Phys. Chem. Chem. Phys.*, 2011, **13**, 16987.
272. G.-Y. Li, G.-J. Zhao, Y.-H. Liu, K.-L. Han and G.-Z. He, "TD-DFT study on the sensing mechanism of a fluorescent chemosensor for fluoride: Excited-state proton transfer", *J. Comput. Chem.*, 2010, **31**, 1759.
273. N. E. Hill, *Dielectric properties and molecular behaviour*, Van Nostrand Reinhold, 1969.
274. D. R. Lide, *CRC Handbook of Chemistry and Physics*, Taylor & Francis, 84th edn., 2003.
275. a. D. Sen, V. G. Anicich and T. Arakelian, "Dielectric constant of liquid alkanes and hydrocarbon mixtures." *J. Phys. D. Appl. Phys.*, 1992, **25**, 516.
276. A. Jouyban, S. Soltanpour and H.-K. Chan, "A simple relationship between dielectric constant of mixed solvents with solvent composition and temperature", *Int. J. Pharm.*, 2004, **269**, 353.
277. R. Mehra, "Application of refractive index mixing rules in binary systems of hexadecane and heptadecane with n-alkanols at different temperatures", *J. Chem. Sci.*, 2003, **115**, 147.
278. A. Z. Tasic, B. D. Djordjevic, D. K. Grozdanic and N. Radojkovic, "Use of mixing rules in predicting refractive indexes and specific refractivities for some binary liquid mixtures", *J. Chem. Eng. Data*, 1992, **37**, 310.
279. R. S. Neyband, A. Yousefi and H. Zarei, "Experimental and computational thermodynamic properties of (benzyl alcohol + alkanols) mixtures", *J. Chem. Eng. Data*, 2015, **60**, 2291.
280. J. J. Cras, C. a. Rowe-Taitt, D. a. Nivens and F. S. Ligler, "Comparison of chemical cleaning methods of glass in preparation for silanization", *Biosens. Bioelectron.*, 1999, **14**, 683.
281. S. Pillai and R. K. Pai, "Controlled growth and formation of SAMs investigated by atomic force microscopy", *Ultramicroscopy*, 2009, **109**, 161.
282. J. Sagiv, "Organized monolayers by adsorption. 1. Formation and structure of oleophobic mixed monolayers on solid surfaces", *J. Am. Chem. Soc.*, 1980, **102**, 92.
283. S. A. Alang Ahmad, L. S. Wong, E. Ul-Haq, J. K. Hobbs, G. J. Leggett and J. Micklefield, "Micrometer- and nanometer-scale photopatterning using 2-nitrophenylpropyloxycarbonyl-protected aminosiloxane monolayers", *J. Am. Chem. Soc.*, 2009, **131**, 1513.
284. J. S. Villarrubia, "Algorithms for scanned probe microscope image simulation, surface reconstruction, and tip estimation", *J. Res. Natl. Inst. Stand. Technol.*, 1997, **102**, 425.
285. P. M. Williams, "Blind reconstruction of scanning probe image data", *J. Vac. Sci. Technol. B*, 1996, **14**, 1557.
286. P. Atkins and J. de Paula, *Atkins' Physical Chemistry*, OUP Oxford, 10th Ed, 2010.
287. J. F. Watts and J. Wolstenholme, *An introduction to surface analysis by XPS and AES*, Wiley, 2003.
288. I. Tilinin, "Quantitative surface analysis by Auger and x-ray photoelectron spectroscopy", *Prog. Surf. Sci.*, 1996, **52**, 193.
289. S. Tougaard, "Quantitative XPS: non-destructive analysis of surface nano-structures", *Appl. Surf. Sci.*, 1996, **100-101**, 1.
290. K. Siegbahn and K. V.-s. i Uppsala, *ESCA; Atomic, molecular and solid state structure studied by means of electron spectroscopy*, Almqvist & Wiksells, 1967.
291. R. Castaing and G. Slodzian, "Microanalyse par émission ionique secondaire", *J. Microsc. (Paris).*, 1962, **1**, 395.
292. A. M. Belu, D. J. Graham and D. G. Castner, "Time-of-flight secondary ion mass spectrometry: techniques and applications for the characterization of biomaterial surfaces", *Biomaterials*, 2003, **24**, 3635.

293. S. G. Boxer, M. L. Kraft and P. K. Weber, "Advances in Imaging Secondary Ion Mass Spectrometry for Biological Samples", *Annu. Rev. Biophys.*, 2009, **38**, 53.
294. J.-L. Guerquin-Kern, T.-D. Wu, C. Quintana and A. Croisy, "Progress in analytical imaging of the cell by dynamic secondary ion mass spectrometry (SIMS microscopy)", *Biochim. Biophys. Acta - Gen. Subj.*, 2005, **1724**, 228.
295. C. J. May, H. E. Canavan and D. G. Castner, "Quantitative X-ray photoelectron spectroscopy and time-of-flight secondary ion mass spectrometry characterization of the components in DNA", *Anal. Chem.*, 2004, **76**, 1114.
296. J.-B. Lhoest, M. S. Wagner, C. D. Tidwell and D. G. Castner, "Characterization of adsorbed protein films by time of flight secondary ion mass spectrometry", *J. Biomed. Mater. Res.*, 2001, **57**, 432.
297. P. Kingshott, S. McArthur, H. Thissen, D. G. Castner and H. J. Griesser, "Ultrasensitive probing of the protein resistance of PEG surfaces by secondary ion mass spectrometry", *Biomaterials*, 2002, **23**, 4775.
298. M. J. Frisch, G. W. Trucks, H. B. Schlegel, G. E. Scuseria, M. A. Robb, J. R. Cheeseman, G. Scalmani, V. Barone, B. Mennucci, G. A. Petersson, H. Nakatsuji, M. Caricato, X. Li, H. P. Hratchian, A. F. Izmaylov, J. Bloino, G. Zheng, J. L. Sonnenberg, M. Hada, M. Ehara, K. Toyota, R. Fukuda, J. Hasegawa, M. Ishida, T. Nakajima, Y. Honda, O. Kitao, H. Nakai, T. Vreven, J. Montgomery, J. A., J. E. Peralta, F. Ogliaro, M. Bearpark, J. J. Heyd, E. Brothers, K. N. Kudin, V. N. Staroverov, R. Kobayashi, J. Normand, K. Raghavachari, A. Rendell, J. C. Burant, S. S. Iyengar, J. Tomasi, M. Cossi, N. Rega, J. M. Millam, M. Klene, J. E. Knox, J. B. Cross, V. Bakken, C. Adamo, J. Jaramillo, R. Gomperts, R. E. Stratmann, O. Yazyev, A. J. Austin, R. Cammi, C. Pomelli, J. W. Ochterski, R. L. Martin, K. Morokuma, V. G. Zakrzewski, G. A. Voth, P. Salvador, J. J. Dannenberg, S. Dapprich, A. D. Daniels, Ö. Farkas, J. B. Foresman, J. V. Ortiz, J. Cioslowski and D. J. Fox, *Gaussian 09*, Wallingford, CT, USA, 2009.
299. J.-D. Chai and M. Head-Gordon, "Long-range corrected hybrid density functionals with damped atom-atom dispersion corrections", *Phys. Chem. Chem. Phys.*, 2008, **10**, 6615.
300. T. Clark, J. Chandrasekhar, G. W. Spitznagel and P. V. R. Schleyer, "Efficient diffuse function-augmented basis sets for anion calculations. III. The 3-21+G basis set for first-row elements, Li-F", *J. Comput. Chem.*, 1983, **4**, 294.
301. P. E. Laibinis, G. M. Whitesides, D. L. Allara, Y. T. Tao, A. N. Parikh and R. G. Nuzzo, "Comparison of the structures and wetting properties of self-assembled monolayers of n-alkanethiols on the coinage metal surfaces, copper, silver, and gold", *J. Am. Chem. Soc.*, 1991, **113**, 7152.
302. V. DePalma and N. Tillman, "Friction and wear of self-assembled trichlorosilane monolayer films on silicon", *Langmuir*, 1989, **5**, 868.
303. C. E. D. Chidsey, C. R. Bertozzi, T. M. Putvinski and a. M. Mujsce, "Coadsorption of ferrocene-terminated and unsubstituted alkanethiols on gold: electroactive self-assembled monolayers", *J. Am. Chem. Soc.*, 1990, **112**, 4301.
304. T. Wink, S. J. van Zuilen, A. Bult and W. P. van Bennekom, "Self-assembled monolayers for biosensors", *Analyst*, 1997, **122**, 43R.
305. T. Böcking, K. A. Kilian, K. Gaus and J. J. Gooding, "Single-step DNA immobilization on antifouling self-assembled monolayers covalently bound to silicon (111)", *Langmuir*, 2006, **22**, 3494.
306. W. Senaratne, L. Andruzzi and C. K. Ober, "Self-assembled monolayers and polymer brushes in biotechnology: current applications and future perspectives", *Biomacromolecules*, 2005, **6**, 2427.
307. J. L. Wilbur, A. Kumar, E. Kim and G. M. Whitesides, "Microfabrication by microcontact printing of self-assembled monolayers", *Adv. Mater.*, 1994, **6**, 600.
308. U. Srinivasan, M. R. Houston, R. T. Howe and R. Maboudian, "Alkyltrichlorosilane-based self-assembled monolayer films for stiction reduction in silicon micromachines", *J. Microelectromechanical Syst.*, 1998, **7**, 252.

309. B. Bhushan, "Adhesion and stiction: Mechanisms, measurement techniques, and methods for reduction", *J. Vac. Sci. Technol. B*, 2003, **21**, 2262.
310. R. Maboudian, "Surface processes in MEMS technology", *Surf. Sci. Rep.*, 1998, **30**, 207.
311. K. Komvopoulos, "Surface engineering and microtribology for microeleetromechanical systems", *Wear*, 1996, **200**, 305.
312. P. R. Scheeper, J. A. Voorthuyzen, W. Olthuis and P. Bergveld, "Investigation of attractive forces between PECVD silicon nitride microstructures and an oxidized silicon substrate", *Sensors Actuators A. Phys.*, 1992, **30**, 231.
313. In, *IUPAC Compend. Chem. Terminol.* IUPAC.
314. In, *IUPAC Compend. Chem. Terminol.* IUPAC.
315. A. D. McLachlan, "Retarded dispersion forces in dielectrics at finite temperatures", *Proc. R. Soc. A Math. Phys. Eng. Sci.*, 1963, **274**, 80.
316. A. D. McLachlan, "Effect of the medium on dispersion forces in liquids", *Discuss. Faraday Soc.*, 1965, **40**, 239.
317. P. Richmond, B. Ninham and R. Ottewill, "A theoretical study of hydrocarbon adsorption on water surfaces using Lifshitz theory", *J. Colloid Interface Sci.*, 1973, **45**, 69.
318. J. N. Israelachvili, "The calculation of van der Waals dispersion forces between macroscopic bodies", *Proc. R. Soc. A Math. Phys. Eng. Sci.*, 1972, **331**, 39.
319. A. V. Parsegian and B. W. Ninham, "Application of the Lifshitz theory to the calculation of Van der Waals forces across thin lipid films." *Nature*, 1969, **224**, 1197.
320. U. Landman, W. D. Luedtke and M. W. Ribarsky, "Structural and dynamical consequences of interactions in interfacial systems", *J. Vac. Sci. Technol. A*, 1989, **7**, 2829.
321. N. B. Larsen, H. Biebuyck, E. Delamarche and B. Michel, "Order in microcontact printed self-assembled monolayers", *J. Am. Chem. Soc.*, 1997, **119**, 3017.
322. J. Mahanty and B. W. Ninham, *Dispersion forces*, Academic Press, 1976.
323. H.-J. Schneider, "Binding mechanisms in supramolecular complexes", *Angew. Chemie Int. Ed.*, 2009, **48**, 3924.
324. L. M. Salonen, M. Ellermann and F. Diederich, "Aromatic rings in chemical and biological recognition: energetics and structures", *Angew. Chemie Int. Ed.*, 2011, **50**, 4808.
325. M. C. R. Symons, J. M. Harvey and S. E. Jackson, "Spectroscopic studies of water—aprotic-solvent interactions in the water-rich region", *J. Chem. Soc. Faraday Trans. 1 Phys. Chem. Condens. Phases*, 1980, **76**, 256.
326. C. A. Hunter, "van der Waals interactions in non-polar liquids", *Chem. Sci.*, 2013, **4**, 834.
327. G. Wypych, *Handbook of Solvents*, ChemTec, 2001.
328. G. Maroulis, *Computational aspects of electric polarizability calculations : Atoms , molecules and clusters*, IOS Press, 2004.
329. Y. Marcus, *The properties of solvents*, Wiley, 1998, pp. 95–102.
330. A. Dupré and P. Dupré, *Théorie mécanique de la chaleur*, Gauthier-Villars, Paris, 1869.
331. T. Han, J. M. Williams and T. P. Beebe, "Chemical bonds studied with functionalized atomic force microscopy tips", *Anal. Chim. Acta*, 1995, **307**, 365.
332. C. R. Hurley and G. J. Leggett, "Influence of the solvent environment on the contact mechanics of tipsample interactions in friction force microscopy of poly(ethylene terephthalate) films", *Langmuir*, 2006, **22**, 4179.
333. A. Amirjahed and M. Blake, "Deviation of dielectric constant from ideality for certain binary solvent systems", *J. Pharm. Sci.*, 1975, **64**, 1569.
334. A. Chmielewska, M. Żurada, K. Klimaszewski and A. Bald, "Dielectric properties of methanol mixtures with ethanol, isomers of propanol, and butanol", *J. Chem. Eng. Data*, 2009, **54**, 801.
335. E. E. Meyer, K. J. Rosenberg and J. Israelachvili, "Recent progress in understanding hydrophobic interactions." *Proc. Natl. Acad. Sci.*, 2006, **103**, 15739.
336. R. C. Thomas, J. E. Houston, R. M. Crooks, T. Kim and T. A. Michalske, "Probing adhesion forces at the molecular scale", *J. Am. Chem. Soc.*, 1995, **117**, 3830.

337. D. LeNeveu and R. Rand, "Measurement and modification of forces between lecithin bilayers", *Biophys. J.*, 1977, **18**, 209.
338. T. Kuhl, Y. Guo, J. L. Alderfer, A. D. Berman, D. Leckband, J. Israelachvili and S. W. Hui, "Direct measurement of polyethylene glycol induced depletion attraction between lipid bilayers", *Langmuir*, 1996, **12**, 3003.
339. T. Van Vliet and J. Lyklema, "Rheology of polyelectrolyte-stabilized emulsions", *J. Colloid Interface Sci.*, 1978, **63**, 97.
340. T. W. Kelley, P. a. Schorr, K. D. Johnson, M. Tirrell and C. D. Frisbie, "Direct force measurements at polymer brush surfaces by atomic force microscopy", *Macromolecules*, 1998, **31**, 4297.
341. G. S. Grest, "Interfacial sliding of polymer brushes: a molecular dynamics simulation", *Phys. Rev. Lett.*, 1996, **76**, 4979.
342. M. Rief, F. Oesterhelt, B. Heymann and H. E. Gaub, "Single molecule force spectroscopy on polysaccharides by atomic force microscopy", *Science*, 1997, **275**, 1295.
343. D. Tabor and R. H. S. Winterton, "The direct measurement of normal and retarded van der Waals forces", *Proc. R. Soc. A Math. Phys. Eng. Sci.*, 1969, **312**, 435.
344. J. N. Israelachvili and D. Tabor, "The measurement of van der Waals dispersion forces in the range 1.5 to 130 nm", *Proc. R. Soc. A Math. Phys. Eng. Sci.*, 1972, **331**, 19.
345. J. N. Israelachvili and G. E. Adams, "Measurement of forces between two mica surfaces in aqueous electrolyte solutions in the range 0–100 nm", *J. Chem. Soc. Faraday Trans. 1 Phys. Chem. Condens. Phases*, 1978, **74**, 975.
346. J. Israelachvili and D. Tabor, "The shear properties of molecular films", *Wear*, 1973, **24**, 386.
347. P. M. Claesson, C. E. Blom, P. C. Herder and B. W. Ninham, "Interactions between water—stable hydrophobic Langmuir—Blodgett monolayers on mica", *J. Colloid Interface Sci.*, 1986, **114**, 234.
348. Y. H. Tsao, D. F. Evans and H. Wennerstroem, "Long-range attraction between a hydrophobic surface and a polar surface is stronger than that between two hydrophobic surfaces", *Langmuir*, 1993, **9**, 779.
349. R. Horn, D. Smith and W. Haller, "Surface forces and viscosity of water measured between silica sheets", *Chem. Phys. Lett.*, 1989, **162**, 404.
350. Y. Liu, T. Wu and D. F. Evans, "Lateral force microscopy study on the shear properties of self-assembled monolayers of dialkylammonium surfactant on mica", *Langmuir*, 1994, **10**, 2241.
351. O. Marti, J. Colchero and J. Mlynek, "Combined scanning force and friction microscopy of mica", *Nanotechnology*, 1990, **1**, 141.
352. W. A. Ducker, T. J. Senden and R. M. Pashley, "Measurement of forces in liquids using a force microscope", *Langmuir*, 1992, **8**, 1831.
353. M. Salmeron, G. Neubauer, A. Folch, M. Tomitori, D. F. Ogletree and P. Sautet, "Viscoelastic and electrical-properties of self-assembled monolayers on Au(111) films", *Langmuir*, 1993, **9**, 3600.
354. J. Ruan and B. Bhushan, "Atomic-scale and microscale friction studies of graphite and diamond using friction force microscopy", *J. Appl. Phys.*, 1994, **76**, 5022.
355. B. Bhushan and V. N. Koinkar, "Tribological studies of silicon for magnetic recording applications (invited)", *J. Appl. Phys.*, 1994, **75**, 5741.
356. B. Bhushan and S. Sundararajan, "Micro/nanoscale friction and wear mechanisms of thin films using atomic force and friction force microscopy", *Acta Mater.*, 1998, **46**, 3793.
357. V. N. Koinkar and B. Bhushan, "Microtribological studies of unlubricated and lubricated surfaces using atomic force/friction force microscopy", *J. Vac. Sci. Technol. A*, 1996, **14**, 2378.
358. Z. Rymuza, "Control tribological and mechanical properties of MEMS surfaces. Part 1: critical review", *Microsyst. Technol.*, 1999, **5**, 173.

359. a. Lio, C. Morant, D. F. Ogletree and M. Salmeron, "Atomic force microscopy study of the pressure-dependent structural and frictional properties of n-alkanethiols on gold", *J. Phys. Chem. B*, 1997, **101**, 4767.
360. a. Lio, D. H. Charych and M. Salmeron, "Comparative atomic force microscopy study of the chain length dependence of frictional properties of alkanethiols on gold and alkylsilanes on mica", *J. Phys. Chem. B*, 1997, **101**, 3800.
361. M. J. Brukman, G. Oncins, T. D. Dunbar, L. D. Boardman and R. W. Carpick, "Nanotribological properties of alkanephosphonic acid self-assembled monolayers on aluminum oxide: effects of fluorination and substrate crystallinity", *Langmuir*, 2006, **22**, 3988.
362. M. T. McDermott, J.-B. D. Green and M. D. Porter, "Scanning force microscopic exploration of the lubrication capabilities of n-alkanethiolate monolayers chemisorbed at gold: structural basis of microscopic friction and wear", *Langmuir*, 1997, **13**, 2504.
363. S. S. Perry, S. Lee, Y.-S. Shon, R. Colorado, Jr. and T. R. Lee, "The relationships between interfacial friction and the conformational order of organic thin films", *Tribol. Lett.*, 2001, **10**, 81.
364. M. Ruths, "Friction of mixed and single-component aromatic monolayers in contacts of different adhesive strength", *J. Phys. Chem. B*, 2006, **110**, 2209.
365. A. Marti, G. Haehner and N. D. Spencer, "Sensitivity of frictional forces to pH on a nanometer scale: a lateral force microscopy study", *Langmuir*, 1995, **11**, 4632.
366. Y. W. Yang and L. J. Fan, "High-resolution XPS study of decanethiol on Au(111): single sulfurgold bonding interaction", *Langmuir*, 2002, **18**, 1157.
367. H. Rieley, G. K. Kendall, F. W. Zemicael, T. L. Smith and S. Yang, "X-ray studies of self-assembled monolayers on coinage metals. 1. Alignment and photooxidation in 1,8-octanedithiol and 1-octanethiol on Au", *Langmuir*, 1998, **14**, 5147.
368. K. Heister, M. Zharnikov, M. Grunze and L. S. O. Johansson, "Adsorption of alkanethiols and biphenylthiols on Au and Ag substrates: a high-resolution X-ray photoelectron spectroscopy study", *J. Phys. Chem. B*, 2001, **105**, 4058.
369. T. Hauffman, O. Blajiev, J. Snauwaert, C. van Haesendonck, A. Hubin and H. Terryn, "Study of the self-assembling of n-octylphosphonic acid layers on aluminum oxide", *Langmuir*, 2008, **24**, 13450.
370. S. E. Creager and J. Clarke, "Contact-angle titrations of mixed .omega.-mercaptoalkanoic acid/alkanethiol monolayers on gold. reactive vs nonreactive spreading, and chain length effects on surface pKa values", *Langmuir*, 1994, **10**, 3675.
371. J. A. M. Sondag-Huethorst and L. G. J. Fokkink, "Potential-dependent wetting of octadecanethiol-modified polycrystalline gold electrodes", *Langmuir*, 1992, **8**, 2560.
372. D.-R. Chiou, K.-Y. Yeh and L.-J. Chen, "Adjustable pretilt angle of nematic 4-n-pentyl-4'-cyanobiphenyl on self-assembled monolayers formed from organosilanes on square-wave grating silica surfaces", *Appl. Phys. Lett.*, 2006, **88**, 133123.
373. S. R. Wasserman, G. M. Whitesides, I. M. Tidswell, B. M. Ocko, P. S. Pershan and J. D. Axe, "The structure of self-assembled monolayers of alkylsiloxanes on silicon: a comparison of results from ellipsometry and low-angle x-ray reflectivity", *J. Am. Chem. Soc.*, 1989, **111**, 5852.
374. A. Dhotel, Z. Chen, J. Sun, B. Youssef, J.-M. Saiter, A. Schönhals, L. Tan and L. Delbreilh, "From monomers to self-assembled monolayers: the evolution of molecular mobility with structural confinements", *Soft Matter*, 2015, **11**, 719.
375. H. Sugimura, A. Hozumi, T. Kameyama and O. Takai, "Organosilane self-assembled monolayers formed at the vapour/solid interface", *Surf. Interface Anal.*, 2002, **34**, 550.
376. T. T. Foster, M. R. Alexander, G. J. Leggett and E. McAlpine, "Friction force microscopy of alkylphosphonic acid and carboxylic acids adsorbed on the native oxide of aluminum", *Langmuir*, 2006, **22**, 9254.
377. K. Feldman, T. Tervoort, P. Smith and N. D. Spencer, "Toward a force spectroscopy of polymer surfaces", *Langmuir*, 1998, **14**, 372.

378. W. D. McElroy and B. Glass, *A symposium on the mechanism of enzyme action*, Johns Hopkins Press, 1954.
379. D. Chandler, "Interfaces and the driving force of hydrophobic assembly", *Nature*, 2005, **437**, 640.
380. J. Christopher Love, D. B. Wolfe, R. Haasch, M. L. Chabinyc, K. E. Paul, G. M. Whitesides and R. G. Nuzzo, "Formation and structure of self-assembled monolayers of alkanethiolates on palladium", *J. Am. Chem. Soc.*, 2003, **125**, 2597.
381. S. Biggs and P. Mulvaney, "Measurement of the forces between gold surfaces in water by atomic force microscopy", *J. Chem. Phys.*, 1994, **100**, 8501.
382. J. E. Houston, C. M. Doelling, T. K. Vanderlick, Y. Hu, G. Scoles, I. Wenzl and T. R. Lee, "Comparative study of the adhesion, friction, and mechanical properties of CF3- and CH3-terminated alkanethiol monolayers", *Langmuir*, 2005, **21**, 3926.
383. I. Sivebaek, V. Samoilov and B. Persson, "Squeezing molecularly thin alkane lubrication films: layering transitions and wear", *Tribol. Lett.*, 2004, **16**, 195.
384. E. Meyer, "Site-specific friction force spectroscopy", *J. Vac. Sci. Technol. B*, 1996, **14**, 1285.
385. U. D. Schwarz, W. Allers, G. Gensterblum and R. Wiesendanger, "Low-load friction behavior of epitaxial C60 monolayers under Hertzian contact", *Phys. Rev. B*, 1995, **52**, 14976.
386. E. E. Flater, W. R. Ashurst and R. W. Carpick, "Nanotribology of octadecyltrichlorosilane monolayers and silicon: self-mated versus unmated interfaces and local packing density effects", *Langmuir*, 2007, **23**, 9242.
387. M. T. Knippenberg, P. T. Mikulski, B. I. Dunlap and J. A. Harrison, "Atomic contributions to friction and load for tip–self-assembled monolayers interactions", *Phys. Rev. B*, 2008, **78**, 235409.
388. A. P. F. Turner, "Biosensors: sense and sensibility", *Chem. Soc. Rev.*, 2013, **42**, 3184.
389. V. Canalejas-Tejero, S. Herranz, A. Bellingham, M. C. Moreno-Bondi and C. A. Barrios, "Passivated aluminum nanohole arrays for label-free biosensing applications", *ACS Appl. Mater. Interfaces*, 2014, **6**, 1005.
390. W. Hoenlein, G. S. Duesberg, A. P. Graham, F. Kreupl, M. Liebau, W. Pamler, R. Seidel and E. Unger, "Nanoelectronics beyond silicon", *Microelectron. Eng.*, 2006, **83**, 619.
391. S. A. Maier, M. L. Brongersma, P. G. Kik, S. Meltzer, A. A. G. Requicha and H. A. Atwater, "Plasmonics-a route to nanoscale optical devices", *Adv. Mater.*, 2001, **13**, 1501.
392. M. Escalante, Y. Zhao, M. J. W. Ludden, R. Vermeij, J. D. Olsen, E. Berenschot, C. N. Hunter, J. Huskens, V. Subramaniam and C. Otto, "Nanometer arrays of functional light harvesting antenna complexes by nanoimprint lithography and hostguest interactions", *J. Am. Chem. Soc.*, 2008, **130**, 8892.
393. D. Meroni, S. Ardizzone, U. S. Schubert and S. Hoeppener, "Probe-based electro-oxidative lithography of OTS SAMs deposited onto transparent ITO substrates", *Adv. Funct. Mater.*, 2012, **22**, 4376.
394. S. Hoeppener, A. S. Susha, A. L. Rogach, J. Feldmann and U. S. Schubert, *Guided self-assembly of Fe3O4 nanoparticles on chemically active surface templates generated by electro-oxidative nanolithography*, 2006.
395. C. Haensch, S. Hoeppener and U. S. Schubert, "'Clicking' on the nanoscale: 1,3-dipolar cycloaddition of terminal acetylenes on azide functionalized, nanometric surface templates with nanometer resolution." *Nanotechnology*, 2009, **20**, 135302.
396. S. Sun and G. J. Leggett, "Matching the resolution of electron beam lithography by scanning near-field photolithography", *Nano Lett.*, 2004, **4**, 1381.
397. E. Synge, "XXXVIII. A suggested method for extending microscopic resolution into the ultra-microscopic region", *London, Edinburgh, Dublin Philos. Mag. J. Sci.*, 1928, **6**, 356.
398. M. Montague, R. E. Ducker, K. S. L. Chong, R. J. Manning, F. J. M. Rutten, M. C. Davies and G. J. Leggett, "Fabrication of biomolecular nanostructures by scanning near-field photolithography of oligo(ethylene glycol)-terminated self-assembled monolayers", *Langmuir*, 2007, **23**, 7328.

399. M. Mikhaylova, D. K. Kim, C. C. Berry, A. Zagorodni, M. Toprak, A. S. G. Curtis and M. Muhammed, "BSA immobilization on amine-functionalized superparamagnetic iron oxide nanoparticles", *Chem. Mater.*, 2004, **16**, 2344.
400. H.-w. He, H.-j. Liu, K.-c. Zhou, W. Wang and P.-f. Rong, "Characteristics of magnetic Fe3O4 nanoparticles encapsulated with human serum albumin", *J. Cent. South Univ. Technol.*, 2006, **13**, 6.
401. R. Mout, D. F. Moyano, S. Rana and V. M. Rotello, "Surface functionalization of nanoparticles for nanomedicine", *Chem. Soc. Rev.*, 2012, **41**, 2539.
402. T. Strother, W. Cai, X. Zhao, R. J. Hamers and L. M. Smith, "Synthesis and characterization of DNA-modified silicon (111) surfaces", *J. Am. Chem. Soc.*, 2000, **122**, 1205.
403. K. R. Bhushan, C. DeLisi and R. A. Laursen, "Synthesis of photolabile 2-(2-nitrophenyl)propyloxycarbonyl protected amino acids", *Tetrahedron Lett.*, 2003, **44**, 8585.
404. P. Chapman, R. E. Ducker, C. R. Hurley, J. K. Hobbs and G. J. Leggett, "Fabrication of two-component, brush-on-brush topographical microstructures by combination of atom-transfer radical polymerization with polymer end-functionalization and photopatterning", *Langmuir*, 2015, **31**, 5935.
405. S. Xia, M. Cartron, J. Morby, D. A. Bryant, C. N. Hunter and G. J. Leggett, "Fabrication of nanometer- and micrometer-scale protein structures by site-specific immobilization of histidine-tagged proteins to aminosiloxane films with photoremovable protein-resistant protecting groups", *Langmuir*, 2016, **32**, 1818.
406. S. A. Alang Ahmad, L. S. Wong, E. Ul-Haq, J. K. Hobbs, G. J. Leggett and J. Micklefield, "Protein micro- and nanopatterning using aminosilanes with protein-resistant photolabile protecting groups", *J. Am. Chem. Soc.*, 2011, **133**, 2749.
407. Z. J. Zhang, M. Moxey, A. Alswieleh, S. P. Armes, A. L. Lewis, M. Geoghegan and G. J. Leggett, "Nanotribological investigation of polymer brushes with lithographically defined and systematically varying grafting densities", *Langmuir*, 2017, **33**, 706.
408. E. A. Cavalcanti-Adam, A. Micoulet, J. Blümmel, J. Auernheimer, H. Kessler and J. P. Spatz, "Lateral spacing of integrin ligands influences cell spreading and focal adhesion assembly", *Eur. J. Cell Biol.*, 2006, **85**, 219.
409. E. A. Cavalcanti-Adam, T. Volberg, A. Micoulet, H. Kessler, B. Geiger and J. P. Spatz, "Cell spreading and focal adhesion dynamics are regulated by spacing of integrin ligands", *Biophys. J.*, 2007, **92**, 2964.
410. A. Hasan, K.-P. Stengele, H. Giegrich, P. Cornwell, K. R. Isham, R. A. Sachleben, W. Pfleiderer and R. S. Foote, "Photolabile protecting groups for nucleosides: Synthesis and photodeprotection rates", *Tetrahedron*, 1997, **53**, 4247.
411. M. Beier and J. D. Hoheisel, "Production by quantitative photolithographic synthesis of individually quality checked DNA microarrays", *Nucleic Acids Res.*, 2000, **28**, e11.
412. D. Wöll, J. Smirnova, M. Galetskaya, T. Prykota, J. Bühler, K.-P. Stengele, W. Pfleiderer and U. E. Steiner, "Intramolecular sensitization of photocleavage of the photolabile 2-(2-nitrophenyl)propoxycarbonyl (NPPOC) protecting group: photoproducts and photokinetics of the release of nucleosides", *Chem. - A Eur. J.*, 2008, **14**, 6490.
413. D. Wöll, S. Laimgruber, M. Galetskaya, J. Smirnova, W. Pfleiderer, B. Heinz, P. Gilch and U. E. Steiner, "On the mechanism of intramolecular sensitization of photocleavage of the 2-(2-nitrophenyl)propoxycarbonyl (NPPOC) protecting group", *J. Am. Chem. Soc.*, 2007, **129**, 12148.
414. M. C. Pirrung, T. M. Dore, Y. Zhu and V. S. Rana, "Sensitized two-photon photochemical deprotection", *Chem. Commun.*, 2010, **46**, 5313.
415. K.-B. Lee, S.-J. Park, C. A. Mirkin, J. C. Smith and M. Mrksich, "Protein nanoarrays generated by dip-pen nanolithography", *Science*, 2002, **295**, 1702.
416. K. B. Lee, J. H. Lim and C. A. Mirkin, "Protein nanostructures formed via direct-write dip-pen nanolithography", *J. Am. Chem. Soc.*, 2003, **125**, 5588.

417. S. Xu and G.-y. Liu, "Nanometer-scale fabrication by simultaneous nanoshaving and molecular self-assembly", *Langmuir*, 1997, **13**, 127.
418. J. Shi, J. Chen and P. S. Cremer, "Sub-100 nm patterning of supported bilayers by nanoshaving lithography", *J. Am. Chem. Soc.*, 2008, **130**, 2718.
419. L. G. Rosa, J. Jiang, O. V. Lima, J. Xiao, E. Utreras, P. Dowben and L. Tan, "Selective nanoshaving of self-assembled monolayers of 2-(4-pyridylethyl)triethoxysilane", *Mater. Lett.*, 2009, **63**, 961.
420. M. K. Beyer and H. Clausen-Schaumann, "Mechanochemistry: the mechanical activation of covalent bonds", *Chem. Rev.*, 2005, **105**, 2921.
421. P. Seema, J. Behler and D. Marx, "Force-induced mechanical response of molecule-metal interfaces: molecular nanomechanics of propanethiolate self-assembled monolayers on Au(111)", *Phys. Chem. Chem. Phys.*, 2013, **15**, 16001.
422. S. Miertuš, E. Scrocco and J. Tomasi, "Electrostatic interaction of a solute with a continuum. A direct utilizaion of AB initio molecular potentials for the prevision of solvent effects", *Chem. Phys.*, 1981, **55**, 117.
423. S. Miertuš and J. Tomasi, "Approximate evaluations of the electrostatic free energy and internal energy changes in solution processes", *Chem. Phys.*, 1982, **65**, 239.
424. J. L. Pascual-ahuir, E. Silla and I. Tuñon, "GEPOL: An improved description of molecular surfaces. III. A new algorithm for the computation of a solvent-excluding surface", *J. Comput. Chem.*, 1994, **15**, 1127.
425. B. Du, M. R. VanLandingham, Q. Zhang and T. He, "Direct measurement of plowing friction and wear of a polymer thin film using the atomic force microscope", *J. Mater. Res.*, 2001, **16**, 1487.
426. X. Xie, H. Chung, C. Sow and A. Wee, "Nanoscale materials patterning and engineering by atomic force microscopy nanolithography", *Mater. Sci. Eng. R Reports*, 2006, **54**, 1.
427. B. Vasić, M. Kratzer, A. Matković, A. Nevosad, U. Ralević, D. Jovanović, C. Ganser, C. Teichert and R. Gajić, "Atomic force microscopy based manipulation of graphene using dynamic plowing lithography", *Nanotechnology*, 2013, **24**, 015303.
428. T. Young, "An essay on the cohesion of fluids", *Philos. Trans. R. Soc. London*, 1805, **95**, 65.
429. A. B. Tutein, S. J. Stuart and J. A. Harrison, "Role of defects in compression and friction of anchored hydrocarbon chains on diamond", *Langmuir*, 2000, **16**, 291.
430. X. Yang and S. S. Perry, "Friction and molecular order of alkanethiol self-assembled monolayers on Au(111) at elevated temperatures measured by atomic force microscopy", *Langmuir*, 2003, **19**, 6135.
431. G.-y. Liu and M. B. Salmeron, "Reversible displacement of chemisorbed n-alkanethiol molecules on Au(111) surface: an atomic force microscopy study", *Langmuir*, 1994, **10**, 367.
432. T. Nishino, M. Meguro, K. Nakamae, M. Matsushita and Y. Ueda, "The lowest surface free energy based on CF3 alignment", *Langmuir*, 1999, **15**, 4321.
433. E. Ul-Haq, S. Patole, M. Moxey, E. Amstad, C. Vasilev, C. N. Hunter, G. J. Leggett, N. D. Spencer and N. H. Williams, "Photocatalytic nanolithography of self-assembled monolayers and proteins", *ACS Nano*, 2013, **7**, 7610.
434. S. Krämer, R. R. Fuierer and C. B. Gorman, "Scanning probe lithography using self-assembled monolayers", *Chem. Rev.*, 2003, **103**, 4367.
435. J. Adams, G. Tizazu, S. Janusz, S. R. J. Brueck, G. P. Lopez and G. J. Leggett, "Large-area nanopatterning of self-assembled monolayers of alkanethiolates by interferometric lithography." *Langmuir*, 2010, **26**, 13600.
436. P. Vettiger, M. Despont, U. Drechsler, U. Durig, W. Haberle, M. I. Lutwyche, H. E. Rothuizen, R. Stutz, R. Widmer and G. K. Binnig, "The "Millipede"—More than thousand tips for future AFM storage", *IBM J. Res. Dev.*, 2000, **44**, 323.
437. E. U. Haq, Z. Liu, Y. Zhang, S. A. A. Ahmad, L. S. Wong, S. P. Armes, J. K. Hobbs, G. J. Leggett, J. Micklefield, C. J. Roberts and J. M. R. Weaver, "Parallel scanning near-field photolithography: The snomipede", *Nano Lett.*, 2010, **10**, 4375.

438. T. Yanai, D. P. Tew and N. C. Handy, "A new hybrid exchange-correlation functional using the Coulomb-attenuating method (CAM-B3LYP)", *Chem. Phys. Lett.*, 2004, **393**, 51.
439. R. a. Kendall, T. H. Dunning and R. J. Harrison, "Electron affinities of the first-row atoms revisited. Systematic basis sets and wave functions", *J. Chem. Phys.*, 1992, **96**, 6796.
440. T. H. Dunning, "Gaussian basis sets for use in correlated molecular calculations. I. The atoms boron through neon and hydrogen", *J. Chem. Phys.*, 1989, **90**, 1007.
441. T. H. Dunning, K. A. Peterson and A. K. Wilson, "Gaussian basis sets for use in correlated molecular calculations. X. The atoms aluminum through argon revisited", *J. Chem. Phys.*, 2001, **114**, 9244.
442. H. Morrison and B. H. Migdalof, "Photochemical hydrogen abstraction by the nitro group", *J. Org. Chem.*, 1965, **30**, 3996.
443. H. Schupp, W. Wong and W. Schnabel, "Mechanistic studies of the photorearrangement of o-nitrobenzyl esters", *J. Photochem.*, 1987, **36**, 85.
444. S. Walbert, W. Pfleiderer and U. E. Steiner, "Photolabile protecting groups for nucleosides: mechanistic studies of the 2-(2-nitrophenyl)ethyl group", *Helv. Chim. Acta*, 2001, **84**, 1601.
445. M. Gaplovsky, Y. V. Il'ichev, Y. Kamdzhilov, S. V. Kombarova, M. Mac, M. A. Schwörer and J. Wirz, "Photochemical reaction mechanisms of 2-nitrobenzyl compounds: 2-Nitrobenzyl alcohols form 2-nitroso hydrates by dual proton transfer", *Photochem. Photobiol. Sci.*, 2005, **4**, 33.
446. H. Yi, S. Maisonneuve and J. Xie, "Synthesis, glycosylation and photolysis of photolabile 2-(2-nitrophenyl)propyloxycarbonyl (NPPOC) protected glycopyranosides", *Org. Biomol. Chem.*, 2009, **7**, 3847.
447. B. Persson, *Sliding friction: physical principles and applications*, Springer Berlin Heidelberg, 2000.
448. R. J. Cannara, M. J. Brukman, K. Cimatu, A. V. Sumant, S. Baldelli and R. W. Carpick, "Nanoscale friction varied by isotopic shifting of surface vibrational frequencies", *Science*, 2007, **318**, 780.
449. E. Gnecco and E. Meyer, *Fundamentals of friction and wear*, Springer Science & Business Media, 2007.
450. P. Prompinit, A. S. Achalkumar, X. Han, R. J. Bushby, C. Wälti and S. D. Evans, "Improved photoreaction yields for soft ultraviolet photolithography in organothiol self-assembled monolayers", *J. Phys. Chem. C*, 2009, **113**, 21642.

APPENDIX A

Tabular Lifshitz Theory and Hunter Model Data

Table A.1: Dielectric constants (ε), refractive indices (n), 3- and 5-medium Lifshitz work of adhesion ($W_{3\text{med}}$, $W_{5\text{med}}$), and normalized Hunter model free energy of complexation ($\Delta G°$) of all liquid media investigated for dodecanethiol surfaces.

Medium	ε	n	$W_{3\text{med}}$ (mJ m^{-2})	$W_{5\text{med}}$ (mJ m^{-2})	$\Delta G°$ (kJ mol^{-1})
tetramethylsilane	1.92	1.358	1.135	1.145	0.083
n-pentane	1.84	1.355	1.270	1.270	0.064
2-methylbutane	1.83	1.351	1.422	1.420	0.062
n-hexane	1.88	1.372	0.681	0.686	0.079
cyclohexane	2.02	1.424	0.002	0.000	0.063
n-heptane	1.92	1.385	0.368	0.378	0.076
n-octane	1.95	1.395	0.191	0.204	0.074
2_2_4-trimethylpentane	1.96	1.389	0.292	0.306	0.062
n-decane	1.99	1.410	0.036	0.055	0.076
n-dodecane	2	1.420	0.001	0.000	0.083
n-hexadecane	2.05	1.433	0.038	0.063	0.086
benzene	2.27	1.498	1.630	1.680	0.102
toluene	2.38	1.494	1.487	1.547	0.102
ortho-xylene	2.57	1.503	1.883	1.961	0.095
meta-xylene	2.37	1.495	1.505	1.565	0.102
para-xylene	2.27	1.493	1.445	1.495	0.097
ethylbenzene	2.40	1.493	1.453	1.516	0.091
isopropylbenzene	2.38	1.489	1.288	1.349	0.083
1_3_5-trimethylbenzene	2.28	1.497	1.585	1.636	0.091
styrene	2.43	1.544	4.097	4.162	0.090
1-chloro- 1_2_3_4-tetrahydronaphthalene	2.77	1.539	3.842	3.936	0.093
cis-decalin	2.20	1.479	0.927	0.970	0.061
water	78.36	1.333	4.984	5.026	4.167
methanol	32.66	1.327	4.945	5.034	0.804
ethanol	24.55	1.359	3.258	3.367	0.626
1-propanol	20.45	1.384	2.426	2.550	0.473
2-propanol	19.92	1.375	2.608	2.734	0.483
1-butanol	17.51	1.397	2.057	2.193	0.391
2-methyl-1-propanol	17.93	1.394	2.128	2.263	0.384
2-butanol	16.56	1.395	2.037	2.178	0.390
2-methyl-2-propanol	12.47	1.385	1.938	2.101	0.416
1-pentanol	13.90	1.408	1.731	1.886	0.317
3-methyl-1-butanol	15.19	1.405	1.840	1.988	0.318
2-methyl-2-butanol	5.78	1.402	0.812	0.996	0.358
1-hexanol	13.30	1.416	1.647	1.805	0.283
cyclohexanol	15	1.465	2.289	2.437	0.327
1-octanol	10.34	1.428	1.385	1.560	0.232
1-decanol	8.10	1.435	1.151	1.337	0.197
1-dodecanol	5.70	1.441	0.809	0.993	0.176
benzyl_alcohol	12.70	1.538	5.306	5.468	0.363
2-phenylethanol	12.31	1.533	4.918	5.081	0.299
allyl_alcohol	21.60	1.411	2.099	2.219	0.532
2-chloroethanol	25.80	1.442	2.327	2.432	0.476
2-cyanoethanol					0.566
2_2_2-trifluoroethanol	26.67	1.291	7.213	7.316	0.384
1_1_1_3_3_3-hexafluoro- 2-propanol	16.62	1.277	7.970	8.111	0.263
2-methoxyethanol	16.93	1.400	1.992	2.131	0.499
2-ethoxyethanol	29.60	1.406	2.359	2.454	0.385
ethylene_glycol	37.70	1.431	2.456	2.535	0.984

Continued on next page

Table A.1 continued from previous page

Medium	ε	n	W_{3med} (mJ m^{-2})	W_{5med} (mJ m^{-2})	$\Delta G°$ (kJ mol^{-1})
1_2-propanediol	32	1.431	2.370	2.460	0.761
1_3-propanediol	35	1.439	2.477	2.561	0.775
1_2-butanediol		1.437			0.605
2R_3S-butanediol	21.53	1.437	2.144	2.263	0.645
1_4-butanediol	30.20	1.444	2.456	2.550	0.897
1_5-pentanediol		1.448			0.745
diethylene_glycol	31.69	1.446	2.510	2.600	0.739
triethylene_glycol	23.69	1.454	2.447	2.559	0.544
glycerol	42.50	1.473	3.236	3.307	0.708
phenol	11.60	1.543	5.482	5.650	0.396
ortho-cresol	11.50	1.544	5.570	5.738	0.314
meta-cresol	12.44	1.540	5.360	5.523	0.360
para-cresol	11.07	1.539	5.205	5.376	0.352
2_6-dimethoxyphenol					0.341
6-amino-2_4-dimethylphenol	6.16	1.525	3.733	3.919	0.271
3-chlorophenol		1.563			0.350
diethyl_ether	4.20	1.350	1.852	2.013	0.096
di-n-propyl_ether	3.39	1.378	0.728	0.859	0.072
diisopropyl_ether	3.88	1.366	1.190	1.342	0.079
dibutyl_ether	3.08	1.397	0.302	0.417	0.068
bis2-chloroethyl_ether	21.20	1.455	2.385	2.506	0.068
1_2-dimethyoxyethane	7.20	1.378	1.486	1.673	0.187
diethylene_glycol_dimethyl_ether	5.80	1.406	0.779	0.963	0.149
furan	2.94	1.419	0.110	0.216	0.134
tetrahydrofuran	7.58	1.405	1.092	1.279	0.173
2-methyltetrahydrofuran	5.26	1.405	0.677	0.858	0.130
tetrahydropyran	5.61	1.419	0.678	0.861	0.116
1_3-dioxane	2.21	1.420	0.008	0.051	0.267
1_3-dioxolan		1.399			0.322
1_8-cineole	4.57	1.456	0.791	0.960	0.075
anisole	4.33	1.514	2.774	2.939	0.189
ethyl_phenyl_ether	4.22	1.505	2.304	2.465	0.164
diphenyl_ether	3.60	1.578	6.797	6.938	0.117
dibenzyl_ether	3.86	1.539	4.023	4.174	0.132
1_2-dimethoxybenzene	4.09	1.532	3.700	3.858	0.200
methyl_orthoformate		1.379			0.174
methyl_orthoacetate		1.381			0.147
propionaldehyde	18.50	1.359	3.041	3.172	0.295
butyraldehyde	13.40	1.377	2.210	2.367	0.235
benzaldehyde	17.80	1.544	5.963	6.098	0.287
p-methoxybenzaldehyde	15.50	1.573	7.933	8.079	0.354
cinnamaldehyde	16.90				0.303
acetone	20.56	1.356	3.249	3.372	0.438
2-butanone	18.11	1.377	2.484	2.618	0.318
2-pentanone	15.38	1.389	2.082	2.228	0.242
3-methyl-2-butanone	15.87				0.241
3-pentanone	17	1.390	2.146	2.285	0.217
cyclopentanone	14.45	1.435	1.779	1.931	0.257
4-methyl-2-pentanone	13.11	1.394	1.838	1.997	0.207
3_3-dimethyl-2-butanone	12.60	1.395	1.776	1.938	0.216
perfluorooctane					−0.005
cyclohexanone	15.50	1.450	2.023	2.169	0.239

Continued on next page

Table A.1 continued from previous page

Medium	ε	n	$W_{3\mathrm{med}}$ (mJ m^{-2})	$W_{5\mathrm{med}}$ (mJ m^{-2})	ΔG° (kJ mol^{-1})
2-heptanone	11.98	1.407	1.590	1.756	0.165
3-heptanone	12.88	1.407	1.665	1.826	0.154
2_2_4_4-tetramethyl-3-pentanone	14.50	1.420	1.725	1.876	0.111
acetophenone	17.39	1.532	5.227	5.364	0.257
ethyl_phenyl_ketone	15.50	1.527	4.829	4.975	0.204
benzyl_methyl_ketone		1.517			0.228
2_4_5-trimethylacetophenone		1.534			0.225
p-chloroacetophenone	9.60	1.555	6.099	6.277	0.223
diphenyl_ketone	11.40	1.606	10.467	10.636	0.202
2_4-pentanedione	25.70	1.447	2.381	2.487	0.546
2_3-butanedione		1.393			0.541
formic_acid	58.50	1.369	3.383	3.438	0.603
acetic_acid	6.15	1.370	1.530	1.716	0.493
propanoic_acid	3.37	1.384	0.579	0.710	0.510
butanoic_acid	2.90	1.396	0.282	0.385	0.437
pentanoic_acid	2.66	1.406	0.124	0.209	0.371
hexanoic_acid	2.63	1.415	0.067	0.149	0.330
heptanoic_acid	2.71	1.421	0.068	0.158	0.282
cis-perfluorodecalin	1.98	1.313	3.403	3.420	0.029
fluorobenzene	5.42	1.462	1.104	1.286	0.076
hexafluorobenzene	2.05	1.374	0.632	0.658	0.044
1_4-dichlorobutane	7.39	1.400	1.115	1.302	0.063
chlorobenzene	5.62	1.521	3.391	3.574	0.101
dichloromethane	8.93	1.421	1.208	1.390	0.062
1_1-dichloroethane	10	1.413	1.354	1.530	0.061
1_2-dichloroethane	10.36	1.442	1.498	1.673	0.066
trans-1_2-dichloroethylene	2.14	1.446	0.178	0.214	0.077
ortho-dichlorobenzene	9.93	1.549	5.725	5.902	0.095
meta-dichlorobenzene	5.04	1.543	4.564	4.742	0.105
chloroform	4.89	1.442	0.652	0.827	0.062
1_1_1-trichloroethane	7.25	1.435	1.023	1.210	0.064
1_1_2-trichloroethane	7.29	1.468	1.585	1.773	0.062
trichloroethylene	3.42	1.475	1.011	1.144	0.068
1_2_4-trichlorobenzene	4.15	1.571	6.356	6.516	0.086
carbon_tetrachloride	2.24	1.457	0.370	0.416	0.086
tetrachloroethylene	2.28	1.503	1.849	1.900	0.069
1_1_2_2-tetrachloroethane	8.20	1.491	2.454	2.639	0.053
pentachloroethane	3.73	1.500	1.980	2.126	0.055
iodobenzene	4.49	1.617	10.488	10.656	0.102
methylene_iodide	5.32	1.738	25.668	25.849	0.055
n-butylamine	4.88	1.398	0.677	0.852	0.218
benzylamine	4.60	1.538	4.156	4.326	0.252
ethylenediamine	12.90	1.454	1.911	2.071	0.595
diethylamine	3.78	1.382	0.719	0.867	0.187
di-n-butylamine	2.98	1.415	0.127	0.235	0.117
pyrrole	8.13	1.507	3.117	3.302	0.518
pyrrolidine		1.440			0.227
piperidine	5.80	1.452	0.981	1.165	0.197
morpholine	7.42	1.452	1.262	1.450	0.330
triethylamine	2.42	1.398	0.177	0.242	0.043
tri-n-butylamine	2.29	1.428	0.028	0.080	0.059
aniline	6.98	1.583	7.878	8.065	0.506

Continued on next page

Table A.1 continued from previous page

Medium	ε	n	W_{3med} (mJ m^{-2})	W_{5med} (mJ m^{-2})	$\Delta G°$ (kJ mol^{-1})
o-chloroaniline	13.40	1.585	8.767	8.925	0.339
methylphenylamine	6.06	1.568	6.521	6.707	0.326
N_N-dimethylaniline	4.91	1.556	5.412	5.588	0.174
aminoethanol	37.72	1.452	2.698	2.776	0.871
diethanolamine	25.19	1.473	2.933	3.040	0.682
triethanolamine	29.36	1.483	3.345	3.441	0.285
pyridine	12.91	1.507	3.626	3.786	0.232
2-methylpyridine	9.80	1.498	2.935	3.113	0.163
3-methylpyridine	11.35	1.506	3.445	3.614	0.177
4-methylpyridine	11.86	1.503	3.357	3.523	0.208
2_4-dimethylpyridine	9.60	1.498	2.912	3.091	0.158
2_6-dimethylpyridine	7.33	1.495	2.481	2.668	0.131
2_4_6-trimethylpyridine	12.02	1.495	3.035	3.200	0.118
2-cyanopyridine	93.80	1.529	5.914	5.949	0.441
pyrimidine		1.499			0.367
quinoline	8.95	1.624	11.957	12.139	0.184
acetonitrile	35.94	1.341	4.255	4.337	0.468
propionitrile	28.26	1.363	3.228	3.327	0.313
n-butyronitrile	24.83	1.382	2.610	2.718	0.189
3-methylbutanenitrile	19.71	1.395	2.192	2.318	0.191
acrylonitrile	33	1.388	2.667	2.755	0.352
phenylacetonitrile	18.70	1.520	4.615	4.746	0.240
benzonitrile	25.20	1.525	5.116	5.223	0.223
nitromethane	35.87	1.379	2.907	2.989	0.422
nitroethane	28.06	1.389	2.550	2.649	0.265
1-nitropropane	23.24	1.399	2.265	2.379	0.232
2-nitropropane	25.52	1.392	2.434	2.540	0.258
nitrobenzene	34.78	1.550	6.852	6.936	0.192
formamide	109.50	1.446	2.968	2.998	1.300
N-methylformamide	182.40	1.430	2.899	2.918	0.686
N_N-dimethylformamide	36.71	1.428	2.430	2.510	0.451
N_N-dimethylthioformamide	47.50	1.576	8.922	8.987	0.638
N_N-diethylformamide	29.02	1.434	2.327	2.424	0.306
N-methylacetamide	191.30	1.425	2.887	2.905	0.588
N_N-dimethylacetamide	37.78	1.435	2.486	2.565	0.445
N_N-diethylacetamide	31.33	1.439	2.418	2.509	0.302
2-pyrrolidinone	27.79	1.486	3.413	3.513	0.594
N-methyl_pyrrolidinone	32.20	1.467	2.929	3.018	0.345
N-methyl_thiopyrrolidinone	47.50	1.583	9.493	9.558	0.405
tetramethylurea	23.60	1.449	2.358	2.470	0.285
tetraethylurea	14.74	1.446	1.915	2.065	0.161
dimethylcyanamide	37.23	1.409	2.464	2.544	0.480
carbon_disulfide	2.64	1.624	10.804	10.888	0.287
dimethyl_sulfide	6.20	1.432	0.822	1.009	0.190
diethyl_sulfide	5.72	1.440	0.799	0.983	0.104
diisopropyl_sulfide	5.81	1.438	0.796	0.981	0.088
dibutyl_sulfide	4.41	1.450	0.659	0.825	0.066
tetrahydrothiophene	8.61	1.502	2.959	3.142	0.131
thiane	6.58	1.510	3.014	3.201	0.110
dimethylsulfoxide	46.45	1.477	3.394	3.460	0.634
dibutyl_sulfoxide					0.213
sulfolane	43.26	1.481	3.488	3.559	0.641

Continued on next page

Table A.1 continued from previous page

Medium	ε	n	W_{3med} (mJ m^{-2})	W_{5med} (mJ m^{-2})	$\Delta G°$ (kJ mol^{-1})
thiobis2-ethanol	27.84	1.519	4.860	4.960	0.702
diethyl_sulfite	15.60	1.415	1.805	1.950	0.318
dimethyl_sulfate	50.28	1.386	2.912	2.974	0.407
diethyl_sulfate	16.20	1.414	1.843	1.986	0.344
methanesulfonic_acid		1.432			0.867
trimethylphosphate	16.39	1.395	2.032	2.174	0.513
triethylphosphate	10.79	1.403	1.511	1.683	0.318
tri-n-butylphosphate	8.91	1.422	1.206	1.388	0.146
hexamethylphosphoric_triamide	39.50	1.507	4.470	4.546	0.213
hydrogen_peroxide	70.70	1.407	2.739	2.785	1.749
hydrogen_fluoride	84	1.340	4.629	4.669	1.074
sulfuric_acid	100	1.418	2.776	2.809	0.780
ammonia	22.38	1.325	4.778	4.894	0.653
hydrazine	52.90	1.469	3.220	3.280	1.062
sulfur_dioxide	11.90	1.357	2.702	2.868	0.348
thionyl_chloride	9.25	1.516	3.701	3.881	0.635
phosphorus_oxychloride	13.90	1.484	2.775	2.929	0.463

Concluded

Table A.2: Dielectric constants (ε), refractive indices (n), 3- and 5-medium Lifshitz work of adhesion (W_{3med}, W_{5med}), and normalized Hunter model free energy of complexation ($\Delta G°$) of all liquid media investigated for 11-mercapto-1-undecanol surfaces.

Medium	ε	n	W_{3med} (mJ m^{-2})	W_{5med} (mJ m^{-2})	$\Delta G°$ (kJ mol^{-1})
1_1_1_3_3_3-hexafluoro-2-propanol	16.62	1.277	8.924	8.304	5.528
1_1_1-trichloroethane	7.25	1.435	0.164	1.264	15.344
1_1_2_2-tetrachloroethane	8.20	1.491	0.892	1.764	15.360
1_1_2-trichloroethane	7.29	1.468	0.339	1.430	15.309
1_1-dichloroethane	10	1.413	0.647	1.116	15.280
1_2_4-trichlorobenzene	4.15	1.571	4.411	6.232	13.728
1_2-butanediol		1.437			7.214
1_2-dichloroethane	10.36	1.442	0.445	0.840	15.360
1_2-dimethoxybenzene	4.09	1.532	2.199	4.031	9.558
1_2-dimethyoxyethane	7.20	1.378	1.302	2.415	9.822
1_2-propanediol	32	1.431	1.716	0.033	6.879
1_3_5-trimethylbenzene	2.28	1.497	1.158	3.106	13.659
1_3-dioxane	2.21	1.420	0.502	2.441	9.287
1_3-dioxolan		1.399			9.415
1_3-propanediol	35	1.439	1.774	0.000	6.308
1_4-butanediol	30.20	1.444	1.628	0.000	6.682
1_4-dichlorobutane	7.39	1.400	0.659	1.725	15.356
1_5-pentanediol		1.448			6.944
1_8-cineole	4.57	1.456	0.050	1.789	9.670
1-butanol	17.51	1.397	1.584	0.858	7.723
1-chloro-1_2_3_4-tetrahydronaphthalene	2.77	1.539	2.715	4.689	13.627
1-decanol	8.10	1.435	0.242	1.137	9.440
1-dodecanol	5.70	1.441	0.034	1.515	9.775
1-hexanol	13.30	1.416	0.903	0.756	8.416
1-nitropropane	23.24	1.399	1.867	0.620	10.718

Continued on next page

Table A.2 continued from previous page

Medium	ε	n	W_{3med} (mJ m^{-2})	W_{5med} (mJ m^{-2})	$\Delta G°$ (kJ mol^{-1})
1-octanol	10.34	1.428	0.501	0.900	8.902
1-pentanol	13.90	1.408	1.084	0.841	8.077
1-propanol	20.45	1.384	2.164	1.139	7.381
2_2_2-trifluoroethanol	26.67	1.291	8.163	6.706	7.168
2_2_4_4-tetramethyl-3-pentanone	14.50	1.420	0.943	0.609	8.886
2_2_4-trimethylpentane	1.96	1.389	1.280	3.172	15.269
2_3-butanedione		1.393			9.156
2_4_5-trimethylacetophenone	1.53			10.963	
2_4_6-trimethylpyridine	12.02	1.495	1.363	1.437	7.127
2_4-dimethylpyridine	9.60	1.498	1.225	1.780	6.779
2_4-pentanedione	25.70	1.447	1.463	0.059	8.418
2_6-dimethoxyphenol				9.796	
2_6-dimethylpyridine	7.33	1.495	0.922	2.002	7.691
2-butanol	16.56	1.395	1.574	0.961	7.921
2-butanone	18.11	1.377	2.264	1.471	7.198
2-chloroethanol	25.80	1.442	1.461	0.052	7.393
2-cyanoethanol					7.303
2-cyanopyridine	93.80	1.529	4.503	2.705	8.513
2-ethoxyethanol	29.60	1.406	1.976	0.382	6.942
2-heptanone	11.98	1.407	0.947	1.028	8.057
2-methoxyethanol	16.93	1.400	1.477	0.818	6.751
2-methyl-1-propanol	17.93	1.394	1.704	0.930	8.046
2-methyl-2-butanol	5.78	1.402	0.488	1.949	8.179
2-methyl-2-propanol	12.47	1.385	1.550	1.544	7.796
2-methylbutane	1.83	1.351	2.929	4.788	15.308
2-methylpyridine	9.80	1.498	1.244	1.756	7.384
2-methyltetrahydrofuran	5.26	1.405	0.396	1.981	8.761
2-nitropropane	25.52	1.392	2.155	0.761	10.637
2-pentanone	15.38	1.389	1.683	1.224	7.441
2-phenylethanol	12.31	1.533	2.823	2.844	8.362
2-propanol	19.92	1.375	2.438	1.461	7.355
2-pyrrolidinone	27.79	1.486	2.069	0.555	4.538
2R_3S-butanediol	21.53	1.437	1.268	0.150	7.110
3_3-dimethyl-2-butanone	12.60	1.395	1.272	1.243	7.565
3-chlorophenol		1.563			7.612
3-heptanone	12.88	1.407	1.026	0.949	7.943
3-methyl-1-butanol	15.19	1.405	1.241	0.808	8.167
3-methyl-2-butanone	15.87				7.338
3-methylbutanenitrile	19.71	1.395	1.783	0.826	9.495
3-methylpyridine	11.35	1.506	1.648	1.846	6.691
3-pentanone	17	1.390	1.753	1.086	7.538
4-methyl-2-pentanone	13.11	1.394	1.354	1.238	8.194
4-methylpyridine	11.86	1.503	1.594	1.697	6.532
6-amino-2_4-dimethylphenol	6.16	1.525	1.935	3.303	7.682
acetic_acid	6.15	1.370	1.543	2.914	7.990
acetone	20.56	1.356	3.319	2.284	6.772
acetonitrile	35.94	1.341	4.720	2.928	8.345
acetophenone	17.39	1.532	3.196	2.483	8.352
acrylonitrile	33	1.388	2.538	0.823	8.941
allyl_alcohol	21.60	1.411	1.529	0.406	7.627
aminoethanol	37.72	1.452	1.868	0.038	5.592
ammonia	22.38	1.325	5.249	4.065	2.891

Continued on next page

Table A.2 continued from previous page

Medium	ε	n	$W_{3\text{med}}$ (mJ m^{-2})	$W_{5\text{med}}$ (mJ m^{-2})	ΔG° (kJ mol^{-1})
aniline	6.98	1.583	5.364	6.530	8.297
anisole	4.33	1.514	1.415	3.202	11.905
benzaldehyde	17.80	1.544	3.808	3.048	8.376
benzene	2.27	1.498	1.195	3.142	13.379
benzonitrile	25.20	1.525	3.290	1.915	9.714
benzyl_alcohol	12.70	1.538	3.147	3.101	8.689
benzyl_methyl_ketone	1.52			10.576	
benzylamine	4.60	1.538	2.468	4.200	6.884
bis2-chloroethyl_ether	21.20	1.455	1.293	0.203	10.833
butanoic_acid	2.90	1.396	0.755	2.727	8.192
butyraldehyde	13.40	1.377	1.930	1.767	8.381
carbon_disulfide	2.64	1.624	8.811	10.784	11.010
carbon_tetrachloride	2.24	1.457	0.420	2.363	15.601
chlorobenzene	5.62	1.521	1.712	3.211	13.442
chloroform	4.89	1.442	0.003	1.672	15.310
cinnamaldehyde	16.90				7.361
cis-decalin	2.20	1.479	0.745	2.682	15.643
cis-perfluorodecalin	1.98	1.313	5.289	7.186	14.229
cyclohexane	2.02	1.424	0.552	2.458	15.441
cyclohexanol	15	1.465	0.989	0.583	7.911
cyclohexanone	15.50	1.450	0.901	0.426	6.737
cyclopentanone	14.45	1.435	0.816	0.489	6.972
dibenzyl_ether	3.86	1.539	2.517	4.388	12.658
dibutyl_ether	3.08	1.397	0.693	2.656	11.204
dibutyl_sulfide	4.41	1.450	0.019	1.790	12.590
dibutyl_sulfoxide					3.425
dichloromethane	8.93	1.421	0.431	1.134	15.219
diethanolamine	25.19	1.473	1.699	0.325	6.444
diethyl_ether	4.20	1.350	2.452	4.264	10.046
diethyl_sulfate	16.20	1.414	1.154	0.586	9.311
diethyl_sulfide	5.72	1.440	0.037	1.512	11.843
diethyl_sulfite	15.60	1.415	1.095	0.606	8.301
diethylamine	3.78	1.382	1.047	2.931	4.978
diethylene_glycol	31.69	1.446	1.679	0.000	6.919
diethylene_glycol_dimethyl_ether	5.80	1.406	0.408	1.864	10.399
diisopropyl_ether	3.88	1.366	1.686	3.554	10.114
diisopropyl_sulfide	5.81	1.438	0.045	1.499	12.291
dimethyl_sulfate	50.28	1.386	2.968	1.005	9.580
dimethyl_sulfide	6.20	1.432	0.094	1.452	10.985
dimethylcyanamide	37.23	1.409	2.134	0.313	7.454
dimethylsulfoxide	46.45	1.477	2.355	0.413	3.876
di-n-butylamine	2.98	1.415	0.341	2.310	5.506
di-n-propyl_ether	3.39	1.378	1.229	3.165	10.750
diphenyl_ether	3.60	1.578	4.933	6.842	13.015
diphenyl_ketone	11.40	1.606	7.566	7.755	8.527
ethanol	24.55	1.359	3.352	2.017	6.884
ethyl_phenyl_ether	4.22	1.505	1.078	2.886	12.237
ethyl_phenyl_ketone	15.50	1.527	2.827	2.351	8.849
ethylbenzene	2.40	1.493	1.010	2.971	13.686
ethylene_glycol	37.70	1.431	1.876	0.046	6.603
ethylenediamine	12.90	1.454	0.716	0.635	4.999
fluorobenzene	5.42	1.462	0.130	1.677	13.582

Continued on next page

Table A.2 continued from previous page

Medium	ε	n	W_{3med} (mJ m^{-2})	W_{5med} (mJ m^{-2})	$\Delta G°$ (kJ mol^{-1})
formamide	109.50	1.446	2.544	0.850	7.332
formic_acid	58.50	1.369	3.690	1.717	6.311
furan	2.94	1.419	0.297	2.267	12.375
glycerol	42.50	1.473	2.209	0.305	7.606
heptanoic_acid	2.71	1.421	0.324	2.298	9.106
hexafluorobenzene	2.05	1.374	1.753	3.665	13.801
hexamethylphosphoric_triamide	39.50	1.507	3.027	1.164	0.921
hexanoic_acid	2.63	1.415	0.430	2.403	8.756
hydrazine	52.90	1.469	2.321	0.350	4.798
hydrogen_fluoride	84	1.340	5.397	3.536	0.010
hydrogen_peroxide	70.70	1.407	2.659	0.724	6.463
iodobenzene	4.49	1.617	7.964	9.719	12.376
isopropylbenzene	2.38	1.489	0.904	2.862	13.880
meta-cresol	12.44	1.540	3.186	3.185	7.460
meta-dichlorobenzene	5.04	1.543	2.733	4.369	13.398
meta-xylene	2.37	1.495	1.060	3.018	13.483
methanesulfonic_acid	1.43			12.862	
methanol	32.66	1.327	5.546	3.843	6.270
methyl_orthoacetate	1.38			9.103	
methyl_orthoformate	1.38			9.192	
methylene_iodide	5.32	1.738	21.758	23.328	10.334
methylphenylamine	6.06	1.568	4.262	5.654	9.783
morpholine	7.42	1.452	0.193	1.252	6.637
N_N-diethylacetamide	31.33	1.439	1.666	0.000	3.893
N_N-diethylformamide	29.02	1.434	1.603	0.034	4.602
N_N-dimethylacetamide	37.78	1.435	1.856	0.024	4.369
N_N-dimethylaniline	4.91	1.556	3.461	5.126	11.777
N_N-dimethylformamide	36.71	1.428	1.870	0.060	4.832
N_N-dimethylthioformamide	47.50	1.576	6.780	4.830	8.055
n-butylamine	4.88	1.398	0.547	2.219	5.906
n-butyronitrile	24.83	1.382	2.438	1.086	9.373
n-decane	1.99	1.410	0.764	2.663	15.539
n-dodecane	2	1.420	0.608	2.509	15.611
n-heptane	1.92	1.385	1.423	3.305	15.504
n-hexadecane	2.05	1.433	0.467	2.379	15.649
n-hexane	1.88	1.372	1.908	3.781	15.524
nitrobenzene	34.78	1.550	4.875	3.111	10.578
nitroethane	28.06	1.389	2.343	0.817	9.855
nitromethane	35.87	1.379	2.918	1.127	8.761
N-methyl_pyrrolidinone	32.20	1.467	1.862	0.173	3.768
N-methyl_thiopyrrolidinone	47.50	1.583	7.274	5.325	7.967
N-methylacetamide	191.30	1.425	2.810	1.558	5.708
N-methylformamide	182.40	1.430	2.757	1.466	5.948
n-octane	1.95	1.395	1.111	3.001	15.487
n-pentane	1.84	1.355	2.727	4.589	15.355
o-chloroaniline	13.40	1.585	6.101	5.937	9.236
ortho-cresol	11.50	1.544	3.343	3.513	7.023
ortho-dichlorobenzene	9.93	1.549	3.458	3.943	13.528
ortho-xylene	2.57	1.503	1.250	3.221	13.526
para-cresol	11.07	1.539	3.037	3.289	7.519
para-xylene	2.27	1.493	1.062	3.009	13.501
p-chloroacetophenone	9.60	1.555	3.771	4.326	8.068

Continued on next page

Table A.2 continued from previous page

Medium	ε	n	$W_{3\text{med}}$ (mJ m^{-2})	$W_{5\text{med}}$ (mJ m^{-2})	ΔG° (kJ mol^{-1})
pentachloroethane	3.73	1.500	0.946	2.838	15.379
pentanoic_acid	2.66	1.406	0.578	2.552	8.516
perfluorooctane					13.578
phenol	11.60	1.543	3.272	3.423	6.922
phenylacetonitrile	18.70	1.520	2.741	1.884	9.473
phosphorus_oxychloride	13.90	1.484	1.241	0.999	0.758
piperidine	5.80	1.452	0.068	1.524	3.454
p-methoxybenzaldehyde	15.50	1.573	5.421	4.946	7.590
propanoic_acid	3.37	1.384	1.013	2.950	7.843
propionaldehyde	18.50	1.359	3.037	2.202	8.012
propionitrile	28.26	1.363	3.334	1.799	8.797
pyridine	12.91	1.507	1.821	1.739	6.948
pyrimidine		1.499			7.793
pyrrole	8.13	1.507	1.376	2.264	7.791
pyrrolidine		1.440			4.169
quinoline	8.95	1.624	8.901	9.599	8.310
styrene	2.43	1.544	3.067	5.030	13.563
sulfolane	43.26	1.481	2.377	0.463	6.098
sulfur_dioxide	11.90	1.357	2.649	2.744	8.617
sulfuric_acid	100	1.418	2.655	0.898	0
tetrachloroethylene	2.28	1.503	1.351	3.299	14.800
tetraethylurea	14.74	1.446	0.831	0.462	6.334
tetrahydrofuran	7.58	1.405	0.564	1.584	8.176
tetrahydropyran	5.61	1.419	0.182	1.684	9.131
tetrahydrothiophene	8.61	1.502	1.254	2.030	11.351
tetramethylsilane	1.92	1.358	2.510	4.393	13.162
tetramethylurea	23.60	1.449	1.378	0.105	3.990
thiane	6.58	1.510	1.345	2.610	11.745
thiobis2-ethanol	27.84	1.519	3.141	1.626	7.399
thionyl_chloride	9.25	1.516	1.817	2.449	3.911
toluene	2.38	1.494	1.043	3.001	13.408
trans-1_2-dichloroethylene	2.14	1.446	0.405	2.333	14.091
trichloroethylene	3.42	1.475	0.363	2.296	14.352
triethanolamine	29.36	1.483	2.057	0.473	7.807
triethylamine	2.42	1.398	0.835	2.797	5.670
triethylene_glycol	23.69	1.454	1.409	0.130	7.388
triethylphosphate	10.79	1.403	0.913	1.221	4.656
trimethylphosphate	16.39	1.395	1.570	0.978	4.448
tri-n-butylamine	2.29	1.428	0.392	2.342	15.453
tri-n-butylphosphate	8.91	1.422	0.417	1.125	4.205
water	78.36	1.333	5.822	3.927	5.353

Concluded

Table A.3: Dielectric constants (ε), refractive indices (n), 3- and 5-medium Lifshitz work of adhesion ($W_{3\text{med}}$, $W_{5\text{med}}$), and normalized Hunter model free energy of complexation (ΔG°) of all liquid media investigated for 11-mercaptoundecanoic acid surfaces.

Medium	ε	n	$W_{3\text{med}}$ (mJ m^{-2})	$W_{5\text{med}}$ (mJ m^{-2})	ΔG° (kJ mol^{-1})
1_1_1_3_3_3-hexafluoro-2-propanol	16.62	1.277	6.946	3.541	12.759
1_1_1-trichloroethane	7.25	1.435	0.067	3.029	23.556
1_1_2_2-tetrachloroethane	8.20	1.491	1.340	5.789	23.587
1_1_2-trichloroethane	7.29	1.468	0.588	4.521	23.526
1_1-dichloroethane	10	1.413	0.216	2.037	23.495
1_2_4-trichlorobenzene	4.15	1.571	5.927	13.166	20.946
1_2-butanediol		1.437			10.238
1_2-dichloroethane	10.36	1.442	0.314	2.941	23.575
1_2-dimethoxybenzene	4.09	1.532	3.333	9.492	13.793
1_2-dimethyoxyethane	7.20	1.378	0.600	1.851	14.795
1_2-propanediol	32	1.431	1.427	1.333	9.898
1_3_5-trimethylbenzene	2.28	1.497	2.096	7.041	20.877
1_3-dioxane	2.21	1.420	0.642	3.308	13.971
1_3-dioxolan		1.399			14.300
1_3-propanediol	35	1.439	1.571	1.528	8.969
1_4-butanediol	30.20	1.444	1.470	1.872	10.398
1_4-dichlorobutane	7.39	1.400	0.182	2.068	23.574
1_5-pentanediol		1.448			10.621
1_8-cineole	4.57	1.456	0.348	4.263	13.611
1-butanol	17.51	1.397	0.906	1.091	11.018
1-chloro-1_2_3_4-tetrahydronaphthalene	2.77	1.539	4.043	10.313	20.804
1-decanol	8.10	1.435	0.107	2.924	12.852
1-dodecanol	5.70	1.441	0.095	3.477	13.245
1-hexanol	13.30	1.416	0.445	1.790	11.752
1-nitropropane	23.24	1.399	1.208	0.802	17.032
1-octanol	10.34	1.428	0.218	2.418	12.252
1-pentanol	13.90	1.408	0.537	1.556	11.362
1-propanol	20.45	1.384	1.337	0.752	10.714
2_2_2-trifluoroethanol	26.67	1.291	6.341	2.307	13.453
2_2_4_4-tetramethyl-3-pentanone	14.50	1.420	0.519	1.808	12.465
2_2_4-trimethylpentane	1.96	1.389	1.103	2.733	23.481
2_3-butanedione		1.393			14.497
2_4_5-trimethylacetophenone	1.53			11.238	
2_4_6-trimethylpyridine	12.02	1.495	1.754	5.653	9.188
2_4-dimethylpyridine	9.60	1.498	1.698	6.102	8.740
2_4-pentanedione	25.70	1.447	1.314	2.115	13.038
2_6-dimethoxyphenol				7.969	
2_6-dimethylpyridine	7.33	1.495	1.449	6.163	10.132
2-butanol	16.56	1.395	0.876	1.123	11.385
2-butanone	18.11	1.377	1.365	0.849	10.444
2-chloroethanol	25.80	1.442	1.267	1.928	10.752
2-cyanoethanol					12.606
2-cyanopyridine	93.80	1.529	5.363	7.101	12.869
2-ethoxyethanol	29.60	1.406	1.405	0.690	9.903
2-heptanone	11.98	1.407	0.408	1.695	11.262
2-methoxyethanol	16.93	1.400	0.830	1.176	9.828
2-methyl-1-propanol	17.93	1.394	0.987	1.012	11.609
2-methyl-2-butanol	5.78	1.402	0.126	2.317	11.728
2-methyl-2-propanol	12.47	1.385	0.775	1.331	11.223

Continued on next page

Table A.3 continued from previous page

Medium	ε	n	$W_{3\text{med}}$ (mJ m^{-2})	$W_{5\text{med}}$ (mJ m^{-2})	ΔG° (kJ mol^{-1})
2-methylbutane	1.83	1.351	2.349	2.759	23.525
2-methylpyridine	9.80	1.498	1.712	6.081	9.764
2-methyltetrahydrofuran	5.26	1.405	0.104	2.450	12.656
2-nitropropane	25.52	1.392	1.425	0.603	16.522
2-pentanone	15.38	1.389	0.917	1.123	10.644
2-phenylethanol	12.31	1.533	3.593	8.517	11.916
2-propanol	19.92	1.375	1.519	0.735	10.699
2-pyrrolidinone	27.79	1.486	2.340	4.138	5.790
2R_3S-butanediol	21.53	1.437	1.013	1.926	10.031
3_3-dimethyl-2-butanone	12.60	1.395	0.601	1.433	10.773
3-chlorophenol		1.563			13.494
3-heptanone	12.88	1.407	0.475	1.613	11.148
3-methyl-1-butanol	15.19	1.405	0.655	1.395	11.522
3-methyl-2-butanone	15.87				10.504
3-methylbutanenitrile	19.71	1.395	1.077	0.920	13.652
3-methylpyridine	11.35	1.506	2.164	6.493	8.696
3-pentanone	17	1.390	0.997	1.024	10.793
4-methyl-2-pentanone	13.11	1.394	0.661	1.368	11.684
4-methylpyridine	11.86	1.503	2.070	6.226	8.458
6-amino-2_4-dimethylphenol	6.16	1.525	2.838	8.608	13.958
acetic_acid	6.15	1.370	0.810	1.970	13.079
acetone	20.56	1.356	2.193	0.750	10.002
acetonitrile	35.94	1.341	3.474	0.419	12.818
acetophenone	17.39	1.532	3.926	8.086	11.862
acrylonitrile	33	1.388	1.789	0.327	13.695
allyl_alcohol	21.60	1.411	0.999	1.128	11.389
aminoethanol	37.72	1.452	1.816	2.042	7.629
ammonia	22.38	1.325	3.790	1.200	2.522
aniline	6.98	1.583	6.796	14.047	14.712
anisole	4.33	1.514	2.344	7.983	18.403
benzaldehyde	17.80	1.544	4.655	9.089	12.077
benzene	2.27	1.498	2.145	7.119	20.753
benzonitrile	25.20	1.525	3.954	7.081	14.158
benzyl_alcohol	12.70	1.538	3.972	8.999	12.925
benzyl_methyl_ketone	1.52			10.403	
benzylamine	4.60	1.538	3.615	9.913	8.563
bis2-chloroethyl_ether	21.20	1.455	1.228	2.714	15.441
butanoic_acid	2.90	1.396	0.574	2.657	12.371
butyraldehyde	13.40	1.377	1.052	1.195	12.232
carbon_disulfide	2.64	1.624	10.985	19.550	17.941
carbon_tetrachloride	2.24	1.457	0.947	4.715	23.810
chlorobenzene	5.62	1.521	2.607	8.323	20.739
chloroform	4.89	1.442	0.132	3.622	23.523
cinnamaldehyde	16.90				10.223
cis-decalin	2.20	1.479	1.503	5.900	23.883
cis-perfluorodecalin	1.98	1.313	4.289	3.592	22.420
cyclohexane	2.02	1.424	0.740	3.436	23.672
cyclohexanol	15	1.465	1.036	3.583	11.156
cyclohexanone	15.50	1.450	0.790	2.827	9.590
cyclopentanone	14.45	1.435	0.556	2.313	10.032
dibenzyl_ether	3.86	1.539	3.734	10.071	19.357
dibutyl_ether	3.08	1.397	0.505	2.641	15.859

Continued on next page

Table A.3 continued from previous page

Medium	ε	n	W_{3med} (mJ m^{-2})	W_{5med} (mJ m^{-2})	$\Delta G°$ (kJ mol^{-1})
dibutyl_sulfide	4.41	1.450	0.273	4.034	18.231
dibutyl_sulfoxide					3.954
dichloromethane	8.93	1.421	0.117	2.369	23.432
diethanolamine	25.19	1.473	1.827	3.453	8.778
diethyl_ether	4.20	1.350	1.650	2.377	14.558
diethyl_sulfate	16.20	1.414	0.657	1.519	14.041
diethyl_sulfide	5.72	1.440	0.082	3.422	17.445
diethyl_sulfite	15.60	1.415	0.612	1.588	12.172
diethylamine	3.78	1.382	0.634	2.362	5.997
diethylene_glycol	31.69	1.446	1.545	1.908	10.629
diethylene_glycol_dimethyl_ether	5.80	1.406	0.084	2.388	15.519
diisopropyl_ether	3.88	1.366	1.086	2.310	14.365
diisopropyl_sulfide	5.81	1.438	0.064	3.332	18.016
dimethyl_sulfate	50.28	1.386	2.250	0.091	14.900
dimethyl_sulfide	6.20	1.432	0.023	3.059	16.655
dimethylcyanamide	37.23	1.409	1.624	0.586	10.900
dimethylsulfoxide	46.45	1.477	2.591	3.247	4.836
di-n-butylamine	2.98	1.415	0.358	3.032	6.431
di-n-propyl_ether	3.39	1.378	0.810	2.401	15.320
diphenyl_ether	3.60	1.578	6.570	14.004	20.086
diphenyl_ketone	11.40	1.606	9.079	16.185	11.891
ethanol	24.55	1.359	2.269	0.535	10.188
ethyl_phenyl_ether	4.22	1.505	1.920	7.294	18.782
ethyl_phenyl_ketone	15.50	1.527	3.512	7.786	12.419
ethylbenzene	2.40	1.493	1.902	6.776	21.051
ethylene_glycol	37.70	1.431	1.598	1.188	9.780
ethylenediamine	12.90	1.454	0.668	3.220	6.618
fluorobenzene	5.42	1.462	0.429	4.458	21.362
formamide	109.50	1.446	2.561	1.915	9.922
formic_acid	58.50	1.369	2.813	0.000	12.185
furan	2.94	1.419	0.357	3.137	19.494
glycerol	42.50	1.473	2.392	3.053	12.215
heptanoic_acid	2.71	1.421	0.430	3.241	13.326
hexafluorobenzene	2.05	1.374	1.409	2.617	21.896
hexamethylphosphoric_triamide	39.50	1.507	3.552	5.310	0.594
hexanoic_acid	2.63	1.415	0.477	3.086	12.915
hydrazine	52.90	1.469	2.490	2.762	6.903
hydrogen_fluoride	84	1.340	4.248	0.362	7.163
hydrogen_peroxide	70.70	1.407	2.211	0.421	11.164
iodobenzene	4.49	1.617	9.899	18.371	20.133
isopropylbenzene	2.38	1.489	1.752	6.496	21.296
meta-cresol	12.44	1.540	4.027	9.129	13.440
meta-dichlorobenzene	5.04	1.543	3.894	10.297	20.609
meta-xylene	2.37	1.495	1.969	6.875	20.737
methanesulfonic_acid	1.43			11.441	
methanol	32.66	1.327	4.132	0.802	9.532
methyl_orthoacetate	1.38			7.853	
methyl_orthoformate	1.38			7.856	
methylene_iodide	5.32	1.738	24.735	36.198	18.259
methylphenylamine	6.06	1.568	5.600	12.577	15.369
morpholine	7.42	1.452	0.267	3.707	9.243
N_N-diethylacetamide	31.33	1.439	1.455	1.629	5.020

Continued on next page

Table A.3 continued from previous page

Medium	ε	n	$W_{3\text{med}}$ (mJ m^{-2})	$W_{5\text{med}}$ (mJ m^{-2})	$\Delta G°$ (kJ mol^{-1})
N_N-diethylformamide	29.02	1.434	1.332	1.508	6.042
N_N-dimethylacetamide	37.78	1.435	1.624	1.342	5.795
N_N-dimethylaniline	4.91	1.556	4.763	11.541	18.050
N_N-dimethylformamide	36.71	1.428	1.561	1.118	6.541
N_N-dimethylthioformamide	47.50	1.576	8.024	11.463	12.344
n-butylamine	4.88	1.398	0.209	2.377	6.932
n-butyronitrile	24.83	1.382	1.600	0.532	13.421
n-decane	1.99	1.410	0.807	3.076	23.755
n-dodecane	2	1.420	0.755	3.323	23.822
n-heptane	1.92	1.385	1.206	2.701	23.717
n-hexadecane	2.05	1.433	0.749	3.725	23.860
n-hexane	1.88	1.372	1.556	2.644	23.736
nitrobenzene	34.78	1.550	5.822	9.014	16.266
nitroethane	28.06	1.389	1.589	0.476	15.712
nitromethane	35.87	1.379	2.082	0.196	14.847
N-methyl_pyrrolidinone	32.20	1.467	1.949	2.899	5.032
N-methyl_thiopyrrolidinone	47.50	1.583	8.587	12.219	11.744
N-methylacetamide	191.30	1.425	2.652	1.714	7.250
N-methylformamide	182.40	1.430	2.648	1.822	7.896
n-octane	1.95	1.395	1.001	2.812	23.701
n-pentane	1.84	1.355	2.187	2.718	23.573
o-chloroaniline	13.40	1.585	7.382	13.588	14.455
ortho-cresol	11.50	1.544	4.244	9.634	13.419
ortho-dichlorobenzene	9.93	1.549	4.442	10.239	20.743
ortho-xylene	2.57	1.503	2.228	7.427	20.740
para-cresol	11.07	1.539	3.894	9.215	13.447
para-xylene	2.27	1.493	1.965	6.805	20.746
p-chloroacetophenone	9.60	1.555	4.824	10.847	11.235
pentachloroethane	3.73	1.500	1.783	7.021	23.604
pentanoic_acid	2.66	1.406	0.529	2.878	12.689
perfluorooctane					21.774
phenol	11.60	1.543	4.157	9.488	12.997
phenylacetonitrile	18.70	1.520	3.346	6.997	13.733
phosphorus_oxychloride	13.90	1.484	1.496	4.772	0
piperidine	5.80	1.452	0.235	3.921	3.781
p-methoxybenzaldehyde	15.50	1.573	6.568	12.129	10.653
propanoic_acid	3.37	1.384	0.663	2.445	12.046
propionaldehyde	18.50	1.359	1.947	0.844	11.852
propionitrile	28.26	1.363	2.301	0.379	12.970
pyridine	12.91	1.507	2.324	6.422	9.287
pyrimidine		1.499		0	11.464
pyrrole	8.13	1.507	1.991	6.915	13.520
pyrrolidine		1.440			4.821
quinoline	8.95	1.624	10.648	18.663	11.096
styrene	2.43	1.544	4.474	10.806	21.057
sulfolane	43.26	1.481	2.645	3.514	8.795
sulfur_dioxide	11.90	1.357	1.578	1.366	15.472
sulfuric_acid	100	1.418	2.369	0.877	6.301
tetrachloroethylene	2.28	1.503	2.353	7.477	22.631
tetraethylurea	14.74	1.446	0.681	2.711	8.579
tetrahydrofuran	7.58	1.405	0.132	2.137	11.906
tetrahydropyran	5.61	1.419	0.009	2.722	13.194

Continued on next page

Table A.3 continued from previous page

Medium	ε	n	W_{3med} (mJ m^{-2})	W_{5med} (mJ m^{-2})	$\Delta G°$ (kJ mol^{-1})
tetrahydrothiophene	8.61	1.502	1.800	6.495	16.831
tetramethylsilane	1.92	1.358	2.003	2.676	20.730
tetramethylurea	23.60	1.449	1.251	2.311	5.372
thiane	6.58	1.510	2.067	7.334	17.404
thiobis2-ethanol	27.84	1.519	3.752	6.498	11.424
thionyl_chloride	9.25	1.516	2.485	7.470	4.897
toluene	2.38	1.494	1.945	6.840	20.696
trans-1_2-dichloroethylene	2.14	1.446	0.823	4.234	21.597
trichloroethylene	3.42	1.475	0.971	5.469	21.993
triethanolamine	29.36	1.483	2.301	3.900	11.415
triethylamine	2.42	1.398	0.720	2.773	7.289
triethylene_glycol	23.69	1.454	1.336	2.538	10.989
triethylphosphate	10.79	1.403	0.358	1.739	5.934
trimethylphosphate	16.39	1.395	0.869	1.131	5.871
tri-n-butylamine	2.29	1.428	0.609	3.530	23.537
tri-n-butylphosphate	8.91	1.422	0.115	2.400	4.842
water	78.36	1.333	4.583	0.479	9.666

Concluded

Table A.4: Dielectric constants (ε), refractive indices (n), 3- and 5-medium Lifshitz work of adhesion (W_{3med}, W_{5med}), and normalized Hunter model free energy of complexation ($\Delta G°$) of all liquid media investigated for 11-amino-1-undecanethiol surfaces.

Medium	ε	n	W_{3med} (mJ m^{-2})	W_{5med} (mJ m^{-2})	$\Delta G°$ (kJ mol^{-1})
1_1_1_3_3_3-hexafluoro-2-propanol	16.62	1.277	12.389	7.961	8.931
1_1_1-trichloroethane	7.25	1.435	0.564	0.441	26.391
1_1_2_2-tetrachloroethane	8.20	1.491	0.162	0.968	26.369
1_1_2-trichloroethane	7.29	1.468	0.086	0.608	26.370
1_1-dichloroethane	10	1.413	1.421	0.397	26.324
1_2_4-trichlorobenzene	4.15	1.571	2.323	5.444	25.363
1_2-butanediol		1.437			18.422
1_2-dichloroethane	10.36	1.442	0.637	0.139	26.450
1_2-dimethoxybenzene	4.09	1.532	0.848	3.247	23.386
1_2-dimethyoxyethane	7.20	1.378	2.842	1.591	24.057
1_2-propanediol	32	1.431	2.097	0.363	18.085
1_3_5-trimethylbenzene	2.28	1.497	0.610	2.511	25.328
1_3-dioxane	2.21	1.420	1.465	1.857	23.301
1_3-dioxolan		1.399			22.888
1_3-propanediol	35	1.439	2.020	0.418	18.894
1_4-butanediol	30.20	1.444	1.749	0.284	17.551
1_4-dichlorobutane	7.39	1.400	1.753	0.905	26.445
1_5-pentanediol		1.448			17.874
1_8-cineole	4.57	1.456	0.164	0.980	24.875
1-butanol	17.51	1.397	2.623	0.566	19.760
1-chloro-1_2_3_4-tetrahydronaphthalene	2.77	1.539	1.319	4.024	25.344
1-decanol	8.10	1.435	0.617	0.338	21.194
1-dodecanol	5.70	1.441	0.370	0.679	21.520
1-hexanol	13.30	1.416	1.589	0.219	20.365
1-nitropropane	23.24	1.399	2.877	0.621	21.049

Continued on next page

Table A.4 continued from previous page

Medium	ε	n	$W_{3\text{med}}$ (mJ m^{-2})	$W_{5\text{med}}$ (mJ m^{-2})	$\Delta G°$ (kJ mol^{-1})
1-octanol	10.34	1.428	0.979	0.198	20.832
1-pentanol	13.90	1.408	1.919	0.339	20.207
1-propanol	20.45	1.384	3.477	1.005	19.318
2_2_2-trifluoroethanol	26.67	1.291	11.361	6.852	12.277
2_2_4_4-tetramethyl-3-pentanone	14.50	1.420	1.536	0.143	24.097
2_2_4-trimethylpentane	1.96	1.389	2.882	2.631	26.306
2_3-butanedione		1.393			21.041
2_4_5-trimethylacetophenone	1.53			10.707	
2_4_6-trimethylpyridine	12.02	1.495	0.494	0.826	23.855
2_4-dimethylpyridine	9.60	1.498	0.329	1.041	23.331
2_4-pentanedione	25.70	1.447	1.531	0.167	21.515
2_6-dimethoxyphenol				14.785	
2_6-dimethylpyridine	7.33	1.495	0.139	1.181	23.722
2-butanol	16.56	1.395	2.656	0.615	19.599
2-butanone	18.11	1.377	3.714	1.212	22.158
2-chloroethanol	25.80	1.442	1.617	0.164	19.297
2-cyanoethanol					12.613
2-cyanopyridine	93.80	1.529	3.067	3.541	20.218
2-ethoxyethanol	29.60	1.406	2.864	0.636	21.594
2-heptanone	11.98	1.407	1.824	0.414	23.291
2-methoxyethanol	16.93	1.400	2.460	0.493	21.184
2-methyl-1-propanol	17.93	1.394	2.812	0.661	19.194
2-methyl-2-butanol	5.78	1.402	1.603	1.113	19.765
2-methyl-2-propanol	12.47	1.385	2.853	0.959	19.715
2-methylbutane	1.83	1.351	5.305	4.271	26.367
2-methylpyridine	9.80	1.498	0.345	1.027	23.293
2-methyltetrahydrofuran	5.26	1.405	1.474	1.151	24.073
2-nitropropane	25.52	1.392	3.309	0.862	21.948
2-pentanone	15.38	1.389	2.903	0.809	22.711
2-phenylethanol	12.31	1.533	1.228	2.250	21.377
2-propanol	19.92	1.375	3.922	1.300	19.433
2-pyrrolidinone	27.79	1.486	1.365	0.745	21.013
2R_3S-butanediol	21.53	1.437	1.513	0.071	18.527
3_3-dimethyl-2-butanone	12.60	1.395	2.377	0.665	22.917
3-chlorophenol		1.563			12.714
3-heptanone	12.88	1.407	1.896	0.387	23.435
3-methyl-1-butanol	15.19	1.405	2.127	0.382	20.184
3-methyl-2-butanone	15.87				22.721
3-methylbutanenitrile	19.71	1.395	2.869	0.654	21.979
3-methylpyridine	11.35	1.506	0.572	1.198	23.024
3-pentanone	17	1.390	2.941	0.765	22.986
4-methyl-2-pentanone	13.11	1.394	2.483	0.690	22.820
4-methylpyridine	11.86	1.503	0.571	1.077	22.848
6-amino-2_4-dimethylphenol	6.16	1.525	0.607	2.466	12.569
acetic_acid	6.15	1.370	3.289	2.077	13.715
acetone	20.56	1.356	5.190	2.156	21.497
acetonitrile	35.94	1.341	6.925	3.365	19.360
acetophenone	17.39	1.532	1.588	2.184	22.407
acrylonitrile	33	1.388	3.789	1.183	19.742
allyl_alcohol	21.60	1.411	2.291	0.330	18.907
aminoethanol	37.72	1.452	1.855	0.517	19.643
ammonia	22.38	1.325	7.748	4.026	18.861

Continued on next page

Table A.4 continued from previous page

Medium	ε	n	W_{3med} (mJ m^{-2})	W_{5med} (mJ m^{-2})	$\Delta G°$ (kJ mol^{-1})
aniline	6.98	1.583	2.916	5.702	16.110
anisole	4.33	1.514	0.395	2.405	23.702
benzaldehyde	17.80	1.544	1.979	2.773	22.315
benzene	2.27	1.498	0.626	2.548	24.598
benzonitrile	25.20	1.525	1.825	2.003	21.618
benzyl_alcohol	12.70	1.538	1.437	2.529	18.809
benzyl_methyl_ketone	1.52			10.675	
benzylamine	4.60	1.538	0.977	3.391	21.262
bis2-chloroethyl_ether	21.20	1.455	1.180	0.107	25.258
butanoic_acid	2.90	1.396	2.165	2.047	16.671
butyraldehyde	13.40	1.377	3.399	1.236	22.973
carbon_disulfide	2.64	1.624	5.846	10.137	21.275
carbon_tetrachloride	2.24	1.457	0.653	1.774	26.782
chlorobenzene	5.62	1.521	0.493	2.377	24.817
chloroform	4.89	1.442	0.365	0.852	26.370
cinnamaldehyde	16.90				21.859
cis-decalin	2.20	1.479	0.552	2.100	26.753
cis-perfluorodecalin	1.98	1.313	8.423	6.642	23.941
cyclohexane	2.02	1.424	1.461	1.906	26.559
cyclohexanol	15	1.465	0.693	0.146	20.262
cyclohexanone	15.50	1.450	0.895	0.019	22.780
cyclopentanone	14.45	1.435	1.103	0.020	22.710
dibenzyl_ether	3.86	1.539	1.062	3.619	24.508
dibutyl_ether	3.08	1.397	2.070	1.955	25.418
dibutyl_sulfide	4.41	1.450	0.250	0.989	25.445
dibutyl_sulfoxide				11.058	
dichloromethane	8.93	1.421	1.065	0.366	26.290
diethanolamine	25.19	1.473	1.244	0.412	19.423
diethyl_ether	4.20	1.350	4.708	3.474	24.692
diethyl_sulfate	16.20	1.414	1.862	0.219	21.993
diethyl_sulfide	5.72	1.440	0.397	0.676	24.637
diethyl_sulfite	15.60	1.415	1.785	0.204	22.785
diethylamine	3.78	1.382	2.675	2.167	23.019
diethylene_glycol	31.69	1.446	1.769	0.328	19.481
diethylene_glycol_dimethyl_ether	5.80	1.406	1.446	1.028	24.387
diisopropyl_ether	3.88	1.366	3.639	2.784	24.866
diisopropyl_sulfide	5.81	1.438	0.441	0.662	24.999
dimethyl_sulfate	50.28	1.386	4.296	1.688	21.502
dimethyl_sulfide	6.20	1.432	0.592	0.615	23.372
dimethylcyanamide	37.23	1.409	2.974	0.781	21.008
dimethylsulfoxide	46.45	1.477	1.868	1.048	19.972
di-n-butylamine	2.98	1.415	1.361	1.620	23.744
di-n-propyl_ether	3.39	1.378	2.963	2.433	25.175
diphenyl_ether	3.60	1.578	2.748	6.093	24.336
diphenyl_ketone	11.40	1.606	4.602	7.109	23.108
ethanol	24.55	1.359	5.160	2.077	18.958
ethyl_phenyl_ether	4.22	1.505	0.246	2.095	24.169
ethyl_phenyl_ketone	15.50	1.527	1.320	1.944	22.985
ethylbenzene	2.40	1.493	0.525	2.357	25.056
ethylene_glycol	37.70	1.431	2.287	0.525	17.520
ethylenediamine	12.90	1.454	0.643	0.075	19.663
fluorobenzene	5.42	1.462	0.070	0.845	23.931

Continued on next page

Table A.4 continued from previous page

Medium	ε	n	$W_{3\text{med}}$ (mJ m^{-2})	$W_{5\text{med}}$ (mJ m^{-2})	$\Delta G°$ (kJ mol^{-1})
formamide	109.50	1.446	2.738	1.671	16.359
formic_acid	58.50	1.369	5.365	2.473	10.262
furan	2.94	1.419	1.246	1.583	22.913
glycerol	42.50	1.473	1.792	0.878	17.188
heptanoic_acid	2.71	1.421	1.242	1.641	17.325
hexafluorobenzene	2.05	1.374	3.653	3.108	23.616
hexamethylphosphoric_triamide	39.50	1.507	1.941	1.681	21.921
hexanoic_acid	2.63	1.415	1.478	1.757	17.204
hydrazine	52.90	1.469	2.002	1.060	19.046
hydrogen_fluoride	84	1.340	7.695	4.371	0
hydrogen_peroxide	70.70	1.407	3.596	1.538	12.723
iodobenzene	4.49	1.617	5.006	8.914	21.859
isopropylbenzene	2.38	1.489	0.503	2.252	25.209
meta-cresol	12.44	1.540	1.454	2.598	12.424
meta-dichlorobenzene	5.04	1.543	1.123	3.545	24.962
meta-xylene	2.37	1.495	0.549	2.409	24.996
methanesulfonic_acid	1.43			22.866	
methanol	32.66	1.327	8.036	4.192	18.566
methyl_orthoacetate	1.38			9.367	
methyl_orthoformate	1.38			9.605	
methylene_iodide	5.32	1.738	16.641	22.498	18.134
methylphenylamine	6.06	1.568	2.130	4.817	19.831
morpholine	7.42	1.452	0.251	0.433	22.072
N_N-diethylacetamide	31.33	1.439	1.895	0.316	22.076
N_N-diethylformamide	29.02	1.434	1.926	0.268	22.111
N_N-dimethylacetamide	37.78	1.435	2.179	0.505	21.573
N_N-dimethylaniline	4.91	1.556	1.611	4.305	24.029
N_N-dimethylformamide	36.71	1.428	2.330	0.517	21.499
N_N-dimethylthioformamide	47.50	1.576	4.397	5.479	20.400
n-butylamine	4.88	1.398	1.788	1.399	21.800
n-butyronitrile	24.83	1.382	3.792	1.158	21.958
n-decane	1.99	1.410	1.950	2.117	26.720
n-dodecane	2	1.420	1.598	1.961	26.842
n-heptane	1.92	1.385	3.105	2.772	26.677
n-hexadecane	2.05	1.433	1.196	1.822	26.910
n-hexane	1.88	1.372	3.850	3.254	26.703
nitrobenzene	34.78	1.550	2.955	3.519	21.550
nitroethane	28.06	1.389	3.563	1.017	20.437
nitromethane	35.87	1.379	4.357	1.563	18.210
N-methyl_pyrrolidinone	32.20	1.467	1.540	0.510	21.915
N-methyl_thiopyrrolidinone	47.50	1.583	4.761	5.974	21.666
N-methylacetamide	191.30	1.425	3.452	2.228	20.664
N-methylformamide	182.40	1.430	3.297	2.153	20.130
n-octane	1.95	1.395	2.592	2.462	26.651
n-pentane	1.84	1.355	5.025	4.070	26.443
o-chloroaniline	13.40	1.585	3.508	5.406	18.446
ortho-cresol	11.50	1.544	1.533	2.872	11.512
ortho-dichlorobenzene	9.93	1.549	1.578	3.220	25.050
ortho-xylene	2.57	1.503	0.564	2.583	25.042
para-cresol	11.07	1.539	1.328	2.625	12.665
para-xylene	2.27	1.493	0.582	2.415	25.021
p-chloroacetophenone	9.60	1.555	1.783	3.588	22.922

Continued on next page

Table A.4 continued from previous page

Medium	ε	n	W_{3med} (mJ m^{-2})	W_{5med} (mJ m^{-2})	$\Delta G°$ (kJ mol^{-1})
pentachloroethane	3.73	1.500	0.240	2.078	26.379
pentanoic_acid	2.66	1.406	1.800	1.901	16.965
perfluorooctane					22.807
phenol	11.60	1.543	1.489	2.789	11.567
phenylacetonitrile	18.70	1.520	1.364	1.658	21.251
phosphorus_oxychloride	13.90	1.484	0.573	0.497	20.552
piperidine	5.80	1.452	0.187	0.688	22.621
p-methoxybenzaldehyde	15.50	1.573	3.043	4.538	21.691
propanoic_acid	3.37	1.384	2.621	2.221	16.215
propionaldehyde	18.50	1.359	4.841	1.965	22.631
propionitrile	28.26	1.363	5.078	2.006	21.020
pyridine	12.91	1.507	0.712	1.179	22.567
pyrimidine		1.499			21.797
pyrrole	8.13	1.507	0.337	1.466	15.396
pyrrolidine		1.440			22.769
quinoline	8.95	1.624	5.646	8.832	23.098
styrene	2.43	1.544	1.602	4.411	24.501
sulfolane	43.26	1.481	1.805	1.050	20.302
sulfur_dioxide	11.90	1.357	4.524	2.126	16.330
sulfuric_acid	100	1.418	3.391	1.730	0.259
tetrachloroethylene	2.28	1.503	0.682	2.704	26.074
tetraethylurea	14.74	1.446	0.906	0.010	23.467
tetrahydrofuran	7.58	1.405	1.552	0.769	23.667
tetrahydropyran	5.61	1.419	0.973	0.850	24.267
tetrahydrothiophene	8.61	1.502	0.300	1.249	24.167
tetramethylsilane	1.92	1.358	4.734	3.859	23.388
tetramethylurea	23.60	1.449	1.392	0.123	22.280
thiane	6.58	1.510	0.298	1.776	24.453
thiobis2-ethanol	27.84	1.519	1.798	1.817	19.718
thionyl_chloride	9.25	1.516	0.580	1.695	19.963
toluene	2.38	1.494	0.541	2.391	24.798
trans-1_2-dichloroethylene	2.14	1.446	0.861	1.761	25.547
trichloroethylene	3.42	1.475	0.166	1.562	25.699
triethanolamine	29.36	1.483	1.415	0.718	22.645
triethylamine	2.42	1.398	2.231	2.180	24.301
triethylene_glycol	23.69	1.454	1.323	0.152	20.268
triethylphosphate	10.79	1.403	1.876	0.542	22.560
trimethylphosphate	16.39	1.395	2.658	0.623	21.734
tri-n-butylamine	2.29	1.428	1.198	1.745	26.581
tri-n-butylphosphate	8.91	1.422	1.032	0.357	23.232
water	78.36	1.333	8.266	4.757	14.593

Concluded

APPENDIX B

Source Code

Links to the source code of the programs written by the author can be found below, and are up to date as at the time of submission. MATLAB scripts are compilable without requiring any external libraries, while the Visual Studio projects provided for C# programs contain the required nuget packages. While the C# code was designed to be run on Windows computers with .NET Framework 4.5 or greater installed, it may be possible to run on *NIX systems if compiled using Mono: `http://www.mono-project.com/`. Documentation on software compilation or usage is not available outside of comments present in the code. All code is provided under the MIT license (see LICENSE in project repository for more information), with all other open source code used being attributed as per its license (see NOTICE in project repository).

MATLAB scripts

These allow calculation of Lifshitz work of adhesion with appropriate input files, using "combined.m" as an entry point. For Hunter model calculations, *phasetransfer* software is required. As *phasetransfer* was not written by the author, any queries relating to access to this program must be directed to the Hunter group: `http://www-hunter.ch.cam.ac.uk/` (accurate as of July 2017).

`https://gitlab.com/oscarsiles/LifshitzHunter`

TToolbox

Used mainly for determination of lateral calibration factor, pull-off forces, and friction forces. Can also be used to provide Lifshitz and Hunter results (based off of algorithms used in MATLAB scripts above).

`https://gitlab.com/oscarsiles/TToolbox`

AFMdraw

Able to produce scripts used by Bruker AFM control software (tested on NanoScope III) to produce complex patterns. More details on Bruker C++ extensions (NanoScript) can be found in their user manuals.

`https://gitlab.com/oscarsiles/AFMdraw`